

**Calorimetric Characterization of Phase Stability and
Phase Transformation Kinetics in Uranium Based
Alloys**

By

**ARUN KUMAR RAI
ENGG-02 2009 04020**

Indira Gandhi Centre for Atomic Research

***A thesis submitted to the
Board of Studies in Engineering Sciences
In partial fulfillment of requirements
For the Degree of***

DOCTOR OF PHILOSOPHY

of

HOMI BHABHA NATIONAL INSTITUTE

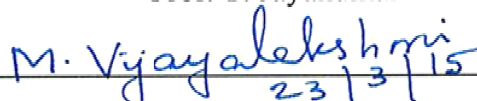


August, 2014

HOMI BHABHA NATIONAL INSTITUTE
Recommendations of the Viva Voce Board

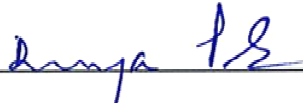
As members of the *viva voce* board, we certify that we have read the dissertation prepared by Mr. Arun Kumar Rai, entitled: "**Calorimetric Characterization of Phase Stability and Phase Transformation Kinetics in Uranium Based Alloys**" and recommend that it may be accepted as fulfilling the dissertation requirement for the degree of Doctor of Philosophy.


Date: 23 March 20

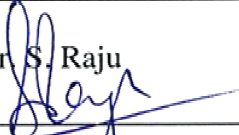
Chairman Prof. T. Jayakumar

Date: 23.3.15

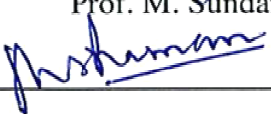
Guide / Convener Prof. M. Vijayalakshmi

Date: 23.3.15

Member 1 Prof. M. Sai Baba

Date: 23/3/2015

Member 2 Prof. B. K. Panigrahi
Date:

Technology Adviser Dr. S. Raju

Date: 23/03/15

Examiner Prof. M. Sundararaman

Date: 23-3-2015

Final approval and acceptance of this thesis is contingent upon the candidate's submission of the final copies of thesis to HBNI.

I, hereby certify that I have read this dissertation prepared under my direction and recommend that it may be accepted as fulfilling the thesis requirement.

Date: 23.3.15
Place: IGCAR, Kalpakkam


Signature of Guide

STATEMENT BY AUTHOR

This dissertation has been submitted in partial fulfillment of requirements for an advanced degree at Homi Bhabha National Institute (HBNI) and is deposited in the library, to be made available to borrowers under rules of the HBNI.

Brief quotations from this dissertation are allowed without special permission, provided that accurate acknowledgement of source is made. Requests for permission for extended quotation from or reproduction of this manuscript in whole or in part may be granted by the competent authority of HBNI, when in his or her judgment, the proposed use of the material is in the interest of scholarship. In all other instances, permission must be obtained from the author.



(Arun Kumar Rai)

Kalpakkam

23-03-2015

DECLARATION

I, hereby certify that the investigation presented in the thesis has been carried out by me. The work is original and has not been submitted earlier as a whole or in part for a degree/diploma at this or any other Institution / University.



(Arun Kumar Rai)

Kalpakkam

23-03-2015

List of publications arising from the thesis

Journal

1. Effect of heating and cooling rate on the kinetics of allotropic phase changes in uranium: A differential scanning calorimetry study **Arun Kumar Rai**, S. Raju, B. Jeyaganesh, E. Mohandas, R. Sudha and V. Ganesan, *J. Nucl. Mater.*, **2009**, 383, 215-225.
2. Measurement and Modelling of High Temperature Thermodynamic Properties of URh₃ Alloy, **Arun Kumar Rai**, Haraprasanna Tripathy, B. Jeya Ganesh and S. Raju, *J. Nucl. Mater.*, **2012**, 427, 378-383.
3. Phase Transformation Studies in U-xZr (x= 2, 5, 10 wt.%) Alloys Using Dynamic Calorimetry, **Arun Kumar Rai**, S. Raju, Haraprasanna Tripathy, R. N. Hajra and M. Vijayalakshmi, *Trans. Ind. Inst. Met.*, **2013**, 66, 387-390.
4. A Calorimetric Study of High Temperature Phase Stability in Fe-U Alloys, **Arun Kumar Rai**, S. Raju, and M. Vijayalakshmi, *J. Nucl. Mater.*, **2013**, 432, 520-528.
5. Measurement of Thermal Properties of UFe₂ by Calorimetry and Modelling Using Debye-Gruneisen Quasi-harmonic Formalism, **Arun Kumar Rai** and S. Raju, *J. Therm. Anal. Calorim.*, **2013**, 112, 73-82.
6. Calorimetric Study of Phase Stability and Phase Transformation in U-xZr (x = 2, 5, 10 wt.%) Alloys, **Arun Kumar Rai**, S. Raju, R. N. Hajra and Haraprasanna Tripathy, communicated to *Metallurgical and Materials Transactions A* (**2014**)

Conferences

1. Characterization of phase stability and phase change behavior in U-2wt.% Zr alloy: A differential scanning calorimetry study, **Arun Kumar Rai**, S. Raju, B. Jeyaganesh and V. Ganesan *Proc. of National Conf. on THERMANS 2010*, Kurukshetra University, March 8-10, 2010, pp. 77-79.
2. Measurement and modelling of high temperature thermodynamic properties of actinide alloys, S. Raju, **Arun Kumar Rai** and Haraprasanna Tripathy, *Proc. of the Second International Conf. on Advances in Nuclear Materials (ANM-2011)*, BARC Mumbai, 9-11 Feb. 2011, pp. 92-95.
3. Measurement of Thermal Properties of UFe₂ by Calorimetry and Modelling Using Debye-Gruneisen Quasi-harmonic Formalism, **Arun Kumar Rai** and S. Raju, *Proc. of International Conf. on THERMANS 2012*, BARC Mumbai, Jan 31-Feb 4, 2012, pp. 82-84.



(Arun Kumar Rai)

Dedicated
To
My Family

Acknowledgements

It's my pleasure to convey my gratitude to all of those, who have assisted me in preparing this Ph.D thesis. My humble acknowledgement is as follows;

First I would like to express my sincere gratitude to my advisor, Dr. M. Vijayalakshmi, Associate Director, Physical Metallurgy Group, IGCAR for her guidance and advice from the early stages of this research.

I am extremely thankful to Dr. S. Raju, Head CMMS, IGCAR for his valuable guidance and technical discussions at several occasions and his sincere involvement in reviewing the technical results of this thesis.

I am grateful to my doctoral committee, Chairman-Dr. T. Jayakumar and members-Dr. M. Sai Baba and Dr. B. K. Panigrahi for their valuable suggestions for the progress of the research work at various DC meetings

I would like to thank Dr. V. Ganesan, ROMG, Dr. P. Ch. Sahu, MSG, IGCAR, for providing the U-Zr and URh₃ samples.

I would like to sincerely thank Dr. Saroja Saibaba, Head, MTPD, IGCAR for providing consistent support for this project.

I would like to thank Dr. B. Jeyaganesh, for his support for carrying out the calorimetry experiments and useful discussions at early stages. I wish to thank Mr. Haraprasanna Tripathy, Mr. Raj Narayan Hajra and N. Vijayashanthi, MTPD, IGCAR for their timely help in the laboratory and the various useful discussions. I am also thankful to Mrs. A. Josephine Prabha and Dr. Madhusmita Bahera for their help in carrying out SEM experiments. I thank Dr. Joysurya Basu for his valuable comments, during preparation of this report. Further, I extend my thanks to all PMG members for providing the required facilities and their support during the course of research work.

I owe my sincere gratitude to my parents, brother and sister for their continual support and encouragement throughout my academic career. I wish to thank my beloved wife (Neetu) for her constant encouragement and support. I am very fortunate that, my wife had taken care of our God gifted twin babies (Dakshansh and Divyansh), especially, as I could not give much time for my family, during the course of this research work. I extend my thanks to my parent-in-laws and brother-in-laws for their support. I thank God, for showing way to come out of every difficult moment, which I have faces so far in my life.

Chapter 1

Introduction

1.1. Choice of U-Pu-Zr alloys as metal fuel for fast reactor application

Worldwide, in the history of nuclear reactor program, different varieties of nuclear fuels have been proposed and tested, which are either ceramic (oxide, carbide) or metal based [1-11]. However, it has been realized over a period of time and experience that none of the fuels have all the merits that are required for ideal reactor operation conditions [1-11]. The metallic fuels for example, have certain intrinsic merits over the other fuels for fast reactor applications [5, 10, 11]. In sixties, it was found that metallic fuels have excessive swelling [11]. But with appropriate fuel pin design, it has been found over a period of sustained operating experience, that it is possible to safely use metallic matrix as fuel by incorporating the space for swelling in the form of plenum and further, it has been found that metallic fuels can achieve very high burn up, of order of 200 GWd/ton. This is comparable to what has been proven for well known oxide fuels [1-11].

The concept of metallic fuel has emerged in a systematic fashion and the first metallic fuel proposed was uranium-fission (Fs) based alloy [11]. The uranium-fission alloy is nothing but the alloy formed between uranium and a conglomerate of fission products mostly of transition metals, such as Nb, Zr, Pd, Rh, Ru and Mo [2]. By using U-Fs alloys, many technological attributes of metallic fuels were discovered in early 1980's. Besides the U-Fs alloys, U-Pu binary combination has also been tested as candidate metal fuel [2]. However, the use of U-Pu binary alloy as nuclear fuel was found, not to be attractive due to the low melting temperature of alloy [11]. Thus an additive has been sought that would increase the melting temperature of the U-Pu alloy system [5-11]. Several elements that alloy well with this system have been explored, that include: chromium, molybdenum, titanium, zirconium etc. Addition of all these elements in controlled amounts resulted in an adequate increase in melting temperature [5-8, 11]. Further, certain alloying addition has been found to enhance the mechanical properties

and corrosion resistance as well [1, 2, 11]. Among different alloying elements, Zr is found to be more suitable because of following merits [5-8, 11]. The selection of Zr addition was unique as it improves the chemical compatibility between the fuel and austenitic/ferritic steel cladding materials by suppressing or minimizing the inter-diffusion of fuel and cladding components [9]. Without zirconium, the cladding elements like nickel and iron readily diffuse into the fuel and form low temperature eutectics that result in a lower solidus temperature (the temperature at which melting starts) adjacent to the cladding [9, 11]. Further, from the neutron economy point of view, Zr is more suitable because its absorption cross section is quite low when compared to other alloying elements [1, 11]. In addition Zr has 100% solid solubility in high temperature bcc uranium phase and hence the U-Pu-Zr ternary system can be made stable in cubic phase at probable reactor operating temperature zone like, 823-973 K (550-700°C) [11]. The concentration of zirconium in the U-Pu-Zr alloys was limited to about 10 wt.% for plutonium concentrations of up to 20 wt%, because too much zirconium would result in a higher liquidus temperature (the temperature at which melting is complete) that would exceed the softening point of the fused-quartz molds in the injection-casting fabrication equipment originally used for fabricating metallic fuel pencils [11]. Further, the addition of more Zr to fuel matrix leads to lower breeding gain of the fuel. In addition to U-Zr based metal fuel, U-Mo and U-Nb are also being considered in recent times as dispersion type fuel for advanced reactors [1-4]. In recent, U-Pu-Zr based metallic fuel appears to be the most suitable candidate because it promised superior performance due its following merits.

The metallic fuel (U-Pu-Zr) has the potential for the highest fissile atom density that will result in higher breeding ratio, in the range of 1.5 to 1.65 depending on actual Zr content. A higher breeding gain leads naturally to higher utilization potential of nuclear fuel [10, 11]. The reactors with high breeding gain can operate for longer times before

next refueling required [10, 11]. Therefore it would result in better utilization of fuel resources. Metallic fuel has high thermal conductivity leading to less steeper temperature gradients between fuel and cladding [11]. In addition, metallic fuel has favorable neutronic properties such as low neutron absorption cross section and a hard neutron spectrum. Moreover, U-Pu-Zr base metallic fuel has good compatibility with sodium coolant and this would result in better heat transfer [6, 7]. Finally, it has passive safety features during core off-normal events [6].

However, metallic fuels have some obvious demerits as well. Metallic fuel is known to exhibit appreciable swelling and irradiation growth [2, 11]. Swelling is basically due to the accumulation of fission gases such as Xe and Kr. In metallic fuel, swelling can occur up to a maximum of 33%; thereafter the gas bubbles become interconnected which leads to the release of trapped fission gases and swelling become less dominant [2,7]. On the other hand, irradiation induced growth caused owing to non uniform distribution of vacancies, when underlying matrix crystal structure is anisotropic. These two phenomena limit the in-pile performance of fuel.

The second most important issue with metal fuel is the fuel-cladding material chemical interaction. The chemical interaction with (steel) cladding is due to the solid state inter diffusion process. In this process, uranium, plutonium, and some lanthanide fission products can diffuse from fuel into the cladding, that would result in the formation of a brittle cladding layer between the fuel and cladding, and contribute to clad wall thickness reduction. Further the possible formation of low temperature eutectics can also limit the reactor operating temperature [2, 7].

Another major concern with metallic fuel is the redistribution of fuel constituents such as U and Zr in U-Pu-Zr type metallic fuel under thermal gradients [11]. The in-homogeneity associated with the restructuring of metallic fuel leads to the change in mechanical and neutronic properties of the fuel. It has been observed that it noticeably

affects the overall fuel lifetime. The restructuring of fuel also leads to a lowered solidus temperature in some portion of fuel.

In general, metallic fuel has a lower melting temperature than the nuclear ceramic fuels that limits the attainable reactor operating temperature. Finally depending on the fuel temperature and the Zr redistribution, the fuel could have multiple phase changes during reactor operation, causing alterations in both mechanical and neutronic properties.

To address all these concern associated with metallic fuels, a lot of research based on experiment and computation have been done and this field is currently experiencing a vast in-flux of research. *In order to ascertain the stability and performance of metal fuel at high temperature under service conditions, the study of phase stability and phase transformation characteristics is very important. This is a basic R&D issue set in the applied reactor engineering context.* In view of this, a brief description of the relevance and scope of present study on phase stability and phase transformation kinetics in uranium –transition metal based alloys is presented in the following section(s).

1.2. Relevance of study of phase stability and phase transformation kinetics in uranium–transition metal alloys in the context to the metallic fuel for fast reactor

As mentioned before, a study on the phase stability and phase transformation characteristics of uranium alloys is of interest on both basic and applied grounds [12-25]. With the revival of interest in metal-fuelled fast reactors, the knowledge of phase stability, transformation kinetics and thermo-physical properties aspects associated with developing uranium based metallic fuels assumes special significance [12-28]. Since any uranium based alloy fuel present inside the core is bound to experience numerous thermal transients and hence phase change cycles, a study of phase transformation is very important.

The phase transformation in uranium alloys have attracted considerable attention for several decades because the transformation sequence in uranium alloys involve many

metastable phases that form during cooling from high temperature phase [12-20]. The nature of various stable and metastable phases that emerge upon cooling from high temperature bcc phase is extremely sensitive to cooling rate, holding temperature and time and compositions of alloying elements [12-20]. In recent-past, there have been numerous studies reported in literature that are related to phase equilibria and phase transformation characteristics of uranium-transition metal alloys. These include U-Zr, U-Mo, U-Ti, U-Nb, U-Fe, U-Cr, U-Rh, U-Ru systems. [12-106]. It has also been observed that certain uranium alloys have been studied in fair detail; however, in most other instances, only an exploratory account is available. Although the broad phase diagram features have been established for many U-transition metal based alloys; finer aspects concerned with transformation thermo-kinetics still remain to be firmly established.

It is in this context that in the present study, three uranium-transition metal based alloys namely U-Zr, U-Fe and U-Rh have been chosen for investigating phase stability and phase transformation characteristics, using in particular calorimetry techniques. The motivation for this study in these three different alloy systems is given below.

In India, the emerging interest on metal fuelled and liquid metal cooled fast reactors has ushered in a spurt of research activities on diverse fronts related to materials processing and spent fuel reprocessing technologies [10]. As an integral part of this technology development initiative, it has been decided to investigate the physical metallurgy of some of the relevant uranium based metallic systems which are identified as potential fuel candidates. It is well known that the optimal choice of fuel depends on a host of factors such as, high temperature in-pile stability, irradiation induced swelling and elemental redistribution characteristics, thermal expansion and thermal conductivity behavior, compatibility with clad and coolant *etc.* [4-18]. In this context, it must be mentioned that among many probable candidates, the alloys based on U-Pu-Zr ternary combination are touted as potential fuel material, owing to certain intrinsic merits which

are mentioned in the previous section [5-11]. Thus for an example, the U-20Pu-10Zr (wt.%) alloy together with 9 wt.% Cr-based ferritic–martensitic steel as fuel clad and wrapper have been identified as a plausible fuel–core material combination [9].

In this regard, it is imperative that a comprehensive knowledge of high temperature phase stability of U-Zr alloys, especially their transformation characteristics as a function of composition and other thermal and processing history related variables, is of utmost importance in developing an insightful understanding of actual in-pile fuel behavior. As already mentioned above that there are several metallurgical issues associated with U-Pu-Zr based metal. For example, under normal reactor operating conditions, a U-Pu-Zr based metal fuel would experience a steep temperature gradient that may lead to rapid phase changes. These phase changes are accompanied by considerable dilatational strain. In addition, it is also known that one of the major issues related to the performance of metallic fuels is the temperature driven redistribution of elemental species across the fuel rod under neutron irradiation [19-23]. It is usually observed that the central portion of the fuel is preferentially enriched with zirconium, while it is depleted at the intermediate zone, and only slightly enriched at the outer surface of the fuel rod. Uranium on the other hand exhibits the opposite trend, while plutonium content remains fairly constant across the entire cross section fuel rod [20, 21]. There have been several studies on the mechanistic aspects of such distinct zone formation under irradiation in U-based metal fuels and valuable data have already been reported in the literature [15-18]. *However, there is still a relative paucity of information on factors related to basic thermo-kinetic stability of these alloys, which are essential from the point of view of elucidating the driving force for such compositional segregation [15-19]. In fact reliable experimental data on basic thermodynamic and kinetic quantities of different phases as a function of temperature and composition are required on all three binaries that constitute the ternary U-Pu-Zr metal fuel, namely U-Zr, U-Pu*

and Pu-Zr in that order. Among all the three alloy systems, U-Zr binary is most important and this has been taken up for detailed study here.

Further, since the fast reactors are employing U-Pu-Zr alloy as the fuel and austenitic or high chromium containing ferritic steels as the clad and or wrapper materials, there is a high possibility of chemical interaction of U and Pu with Fe, Cr and Ni derived from clad [24, 25]. This interaction leads to the formation of low temperature eutectics which limits the reactor operation temperature [24, 25]. In order to understand the chemical compatibility of metal fuel with clad material, we need to have reliable information related to phase equilibria on Fe-U, Ni-U, Cr-U, Fe-Pu, Cr-Pu and Ni-Pu systems. Within the spirit of CALPHAD methodology of phase stability assessment, more reliable assessment of the higher order system such as U-Pu-Fe-Zr will be possible only if reliable data are available on lower order systems [25]. *Therefore it is essential that periodic reinvestigation or reassessment of lower order binaries should be made, in order to develop a more comprehensive thermo-kinetic database on U-based metal fuel systems. In this respect, Fe-U binary is another important sub-binary system because both Fe and U constitute the base matrix for clad and fuel materials respectively.*

During fission, the composition of the fuel is not going to remain the same as fission products accumulate with burn-up [11]. During nuclear fission of U-Pu-Zr fuel, several fission products form and some of the important d-block transition elements like Pt, Rh, Ru, Pd, Ir, Zr, Mo *etc.*, are observed as fission products. These fission elements change the actual composition of fuel as a function of burn-up and play a vital role in deciding the performance capability of metal fuel. It has been experimentally found that for a burn up of about 10%, roughly around 16% of foreign Pt-group elements are generated in the fuel matrix and out of which Rh is 6% [11]. The presence of various foreign atoms influences the thermo-kinetic stability and performance of fuel [26-28]. In view of the restricted solubility of Pt-group elements in uranium, there is a very high

possibility of formation of UM_n intermetallics, where $M = Pd, Rh$ and Ru , and $n=3$. These compounds have very high melting temperature and are left as an insoluble residue after the dissolution of spent fuels during reprocessing [26-28]. Therefore, the knowledge of stability and phase equilibria of the uranium- fission product systems are also necessary to ascertain the usefulness of fuel during operating conditions [26-28]. *Among different uranium-fission products, the knowledge of phase stability and thermodynamics of U-Rh based intermetallics especially for URh_3 are of more important, because Rh is one of the dominant fission product in the case of U-Pu-Zr based metal fuel.*

It can be summarized therefore that an understanding of phase stability and phase transformation characteristics of uranium and its alloys with transition metals are of special interest in harnessing of the advantages of metallic fuel in fast reactor technology. In order to understand the phase stability and phase transformation characteristics in uranium-transition metal based alloys, the physics based finer aspects of alloying behavior of uranium with transition metals are required. In the next section a brief description about the alloying behavior with transition metal is presented.

1.3. Alloying behavior of uranium with transition metals

The electronic structure of uranium is $5f^36d^17s^2$, which makes it a highly active metal. Physical property wise it behaves like f-series transition metal; however during interaction and formation of alloys with other solutes, it shows a character like 6d transition series [16, 18]. Further because of the complexity of electronic configuration and four unpaired electrons in the outer shell, uranium ends up with complex crystal structure at low temperature [16, 18]. In reality, uranium exists in three polymorphic forms [16, 18]. The first polymorphic phase is α -U and has orthorhombic structure that is stable from below room temperature to 940 ± 5 K ($667 \pm 5^\circ\text{C}$). The second allotrope is β -U and has tetragonal structure, which is stable up to 1044 ± 5 K ($771 \pm 5^\circ\text{C}$). The third polymorph is γ -U which has cubic bcc structure up to 1408 K (1135°C) [16-18]. The

crystal structure orthorhombic α -U phase ($Cmcm$) with two atoms in the unit cell is shown in **figure 1.1**. In α -U phase, each U atom has four nearest neighbor. The lattice constant for this structure at room temperature are $a = 2.852 \text{ \AA}$, $b = 5.865 \text{ \AA}$, and $c = 4.945 \text{ \AA}$ [16, 18]. The complex orthorhombic structure as visualized from **figure 1.1** is a severely distorted closed packed hexagonal structure along $\langle 010 \rangle$ directions with $b/a=2.0570$ and $c/a=1.736$ [16, 18]

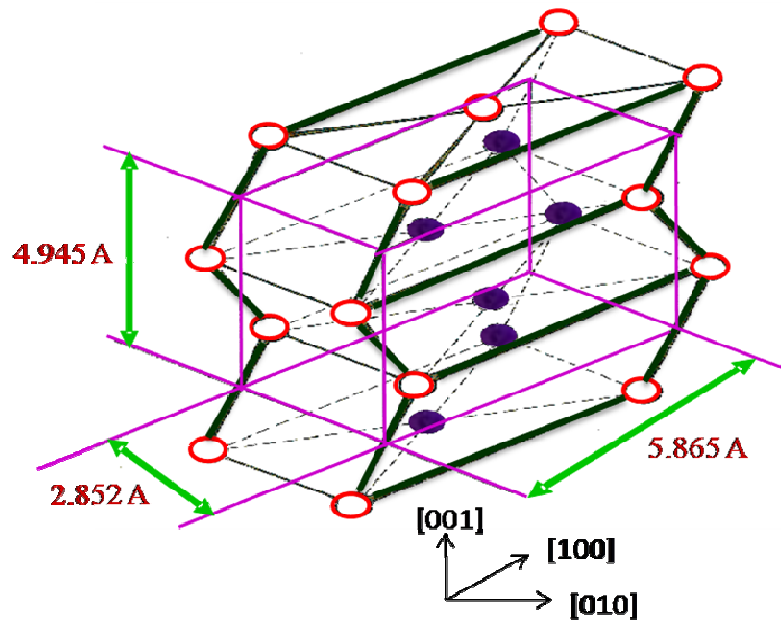


Fig. 1.1. Crystal Structure of α -uranium

The crystal structure of second intermediate β phase is complex tetragonal cell ($P4_2/mmm$) with $a=10.52 \text{ \AA}$ and $c=5.57 \text{ \AA}$ contain 30 atoms [16, 18]. The β phase structure is essentially a layer structure consisting of two types of layers referred to as main layer and subsidiary layer. This is shown in **figure 1.2**. Type ‘A’ layer is subsidiary and type ‘B’ and ‘C’ are main layers with different atomic arrangements [16, 18]. The stacking of these layers is of ABAC type which resembles like closed packed hexagonal structure. Finally the high temperature γ -phase has simple bcc structure ($Im\bar{3}m$) with $a=3.474 \text{ \AA}$ and displayed in **figure 1.3** [16, 18].

Uranium is very reactive in nature and has poor mechanical properties. Due to anisotropic structure α -uranium has highly textured microstructure that is not suitable for engineering applications [16-18]. Several thermo mechanical treatments have been tried

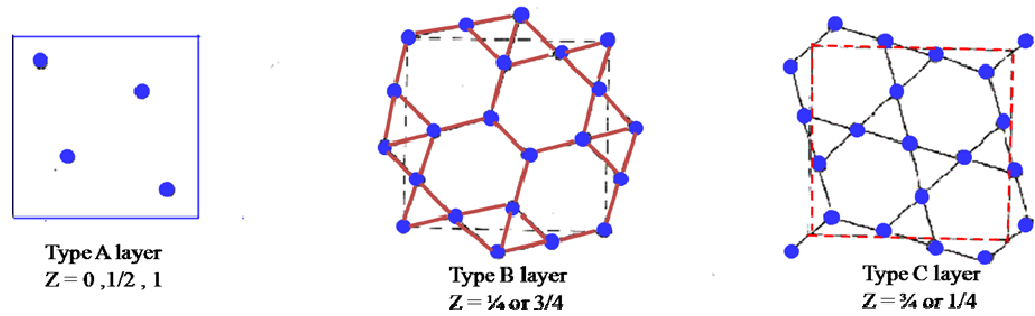


Fig.1.2. Three layer that constitute the crystal structure of β -uranium

by quenching from high temperature β and γ phase to get rid of preferred orientation in case of pure uranium; but the resulting improvement was not significant [13-18]. For

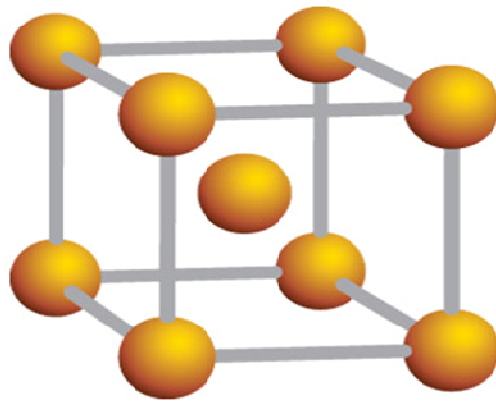


Fig. 1.3. BCC crystal structure of γ -uranium

employing uranium for technological application especially as nuclear fuel, it is required to enhance its mechanical properties, corrosion resistance and to get texture free microstructure. In this regard uranium metal has been frequently alloyed with a variety of elements namely transition metals such as Nb, Zr, Ti, Mo and Cr [13-18]. Alloying

additions have resulted in significant improvement of mechanical properties and corrosion resistance. In addition, the solubility of various alloying elements is found to be different in different phases of uranium depending on the size and crystal structure of the element [13-18]. It has been found that α -phase cannot dissolve any element beyond 0.3 wt% even at high temperature [18]. The intermediate β -phase can dissolve alloying elements to the maximum extent of 1 wt. % [18]. But many alloying elements have bcc structure at high temperature, like Mo, Nb, Ti, Zr can dissolve in the high temperature γ -phase with a high concentration ranging from 20 to 100 wt. % [18]. Experimentally and theoretically it has been observed that there are several transition metals, particularly of 3d, 4d and 5d series that form solid solutions with γ phase (bcc-U). This cubic phase can be retained in its metastable state upon cooling [18]. The γ stabilizing power of these elements increases with atomic number as d-electrons participate in bonding through hybridization with s and p atomic orbital [18]. However at the same time their solubility decreases as the size difference with uranium atoms becomes larger. Additionally the increased bond strength promotes intermetallic compound formation [18]. The first two elements in the 4d series, Zr and Nb, form complete solid solutions with γ bcc-U, but U-Zr cannot be completely retained in the γ phase, whereas U-Nb can be retained in the γ phase at room temperature only at rather large concentrations. This is due to large size difference between U and Nb which makes diffusion more difficult in γ phase [18]. On the other hand, elements like Pd and Pt have only ~2 wt% solubility and it has the propensity to form relatively stable compounds with uranium than other elements in the same group [18]. In the case of U-Zr alloy, Zr is 100% soluble in γ bcc-U. But in the case of U-Fe and U-Rh the solubility of both Fe and Rh is very limited in the three phases of uranium. The finer aspect related solubility in these alloy system will be discussed in the appropriate portions in this chapter.

1.4. Scope of the present study

The scope of present study is: Phase stability and phase transformation kinetics in U-Zr, U-Fe binary system and URh₃ intermetallic compounds. This is further elaborated in the ensuing section which also presents a brief summary of available literature information.

1.5. Study of phase equilibria and phase transformations in U-Zr System

1.5.1. General description of phases and equilibrium reactions

In **table 1.1**, the itemized listing of various studies related to phase equilibria, phase transformation and other related physical metallurgy aspects of U-Zr system has been presented [29-84]. It is very clear from **table 1.1** that there is extensive literature information available regarding to the phase equilibria and phase transformation studies on U-Zr system. Some of major findings are highlighted as follow.

Table 1.1 Listing of different related studies on U-Zr system		
Reference	Alloy composition	Important results reported
Summers-Smith (1954)	U-x Zr x=36.5 wt. %	Thermal analysis, metallography and X-ray diffraction study of solid state equilibria and liquidus temperatures. Confirmed the presence of $\beta \leftrightarrow \alpha + \gamma_2$ eutectoid at 935 ± 2 K ($662 \pm 2^\circ\text{C}$), Zr = 0.3 wt. %, and $\gamma \leftrightarrow \beta + \gamma_2$ monotectoid at 966 ± 3 K ($693 \pm 3^\circ\text{C}$), Zr = 6.1 wt. %. No δ -UZr ₂ phase is observed in this study
F. A. Rough <i>et al.</i> (1956)	U-xZr x= 44.9-52.1 wt. %	Formation δ UZr ₂ phase at 811 K (538°C) has been found. In addition, the three distinct phase regions of δ , $\gamma_2 + \delta$ and γ have been observed using metallography and XRD.
A.N. Holden (1956)	U-Zr	Using metallography established that the invariant reaction $\alpha + \gamma_2 \leftrightarrow \delta$ (peritectoid) occurs at 885 K (612°C) and $\gamma \leftrightarrow \alpha + \delta$ (eutectoid) at 868 K (859°C).

Howlett <i>et al.</i> (1958)	U-x Zr x= 11.3-50 wt. %	Reported the presence δ -UZr ₂ phase, established the miscibility gap for Zr content in the range of 6.1 to 33.7 wt. %. In addition, the presence of $\alpha+\gamma_2\leftrightarrow\delta$ peritectoid reaction at 893 K (620°C), Zr = 39.5 wt. %, and $\gamma\leftrightarrow\alpha+\delta$ eutectoid at 880 K (607°C); Zr =59 wt. % on Zr rich side. The eutectoid $\beta \leftrightarrow \alpha+\gamma_2$ decomposition temperature is reported to be around 943 K (670°C).
F. A. Rough <i>et al.</i> (1958)	Uranium rich side of U-Zr alloy	Reported the presence of peritectoid reaction at 973 K (700°C) on uranium rich side, i.e. $\beta + \gamma_1 \leftrightarrow\alpha$, rather than the eutectoid reaction as reported by others
J. F. Duffey <i>et al.</i> (1958)	U-x Zr x=33.7- 70.2 wt. %	Using thermal analysis, established the $\gamma_2+\delta$ phase boundary in the composition range, 40.5 to 60.5 wt.% of Zr. Reported the presence of $\alpha+\gamma_2\leftrightarrow\delta$ (peritectoid) at 890 K (617°C); Zr =39.5 wt.%, and $\gamma\leftrightarrow\alpha+\delta$ (eutectoid) at 879 K (606°C); Zr=54.8 wt.%.
H. H. Chiswick <i>et al.</i> (1958)	U-x Zr x=2-3 wt. %	Supported the Summers –Smith findings of eutectoid reaction on U rich side [xx] and ruled out the presence of peritectoid reaction reported by Rough et al. [1958].
D.L Douglass <i>et al.</i> (1958)	U-xZr x=60.5, 69.8, 77.3 & 79.7 wt. %	Phase transformation kinetics in Zr rich side of U-Zr alloys using XRD and metallography.
A. A. Bauer <i>et al.</i> (1959)	U-x Zr x=31.9-100 wt. %	Using DTA measurement confirmed the presence of $\alpha+\gamma_2\leftrightarrow\delta$ (peritectoid) at 880 K (607°C); Zr=40.5 wt.%, and $\gamma\leftrightarrow\alpha+\delta$ (eutectoid) at 868 K (595°C); Zr=62 wt.%. The composition for $\gamma_1\leftrightarrow\beta+\gamma_2$ (monotectoid) is 6.8 wt.% Zr.
S. T. Zegler <i>et al.</i> (1962)	U-xZr x=1.2-27.7 wt. %	Using thermal analysis, the presence of $\beta \leftrightarrow \alpha+\gamma_2$ (eutectoid) at 938 K (665°C); Zr=0.3 wt. %, and $\gamma_1\leftrightarrow\beta+\gamma_2$ (monotectoid) at 966 K (693°C); Zr=4.5 wt. % were reported. The solubility of Zr in α -U and β -U reported as 0.2 and 0.4 wt.% respectively. Effect of oxygen content on the stability of miscibility has also been reported.
A. Virot (1962)	U-xZr x=6 wt.%	Phase transformation kinetics study on U-6wt. % Zr using dilatometry, X-ray diffraction, metallography. It is reported that there is a possibility of direct $\gamma\rightarrow\alpha$ transformation under continuous cooling for higher cooling rates. M _s temperature for U-6 wt. % Zr estimated to be between 748-773 K (475-500°C). Suggested the possibility of monoclinic distortion of α under fast cooling.

G. Lagerberg <i>et al.</i> (1962)	U-xZr $x=0.5-5$ wt. %	Thermal analysis; the invariant reaction $\alpha+\gamma_2\leftrightarrow\delta$ is reported at 898 K (625°C). Using metallography and DTA phase transformation kinetics studied under isothermal and non-isothermal conditions. Both diffusional and martensitic mode of transformation kinetics have been observed. For U-2 wt.Zr alloy, experimental TTT diagram and $M_s = 763$ K (490°C) have been reported.
Y. Adda <i>et al.</i> (1962)	U-Zr alloys	Diffusion coefficient of uranium in γ phase of U- in the temperature range of 1073-1323 K (800-1050°C).
R. F. Hills <i>et al.</i> (1965)	U-xZr $x=0.97-27.7$ wt. %	Comprehensive end quench experiments performed for studying the decomposition behavior of γ -U (bcc) phase in U-Zr alloys with Zr ranging from 0.97 to 27.7 wt. % .
B. A. Hatt (1966)	U-xZr $x=10$ & 50 wt.%	Orientation relationship between high temperature γ -U (bcc) and α phase has been established. Development of banded microstructure upon $\gamma\rightarrow\alpha'$ transformation along all the crystallographically equivalent paths is shown.
G.B. Fedorov <i>et al.</i> (1968)	U-xZr $X=5.4, 21.1$ & 5.9 wt. %	Measurement of heat capacity data.
M. Kanno, <i>et al.</i> (1988)	U-xZr $x=0-100$ wt. %	Measurement of vapor pressure using Knudsen Effusion mass spectrometry in the temperature range of 1700-2600 K (1427-2327°C). From vapor pressure data, activity, partial molar Gibbs energy and integral molar free energies of mixing have been calculated. Further estimation of liquidus and solidus temperatures also made.
Y. Takahashi <i>et al.</i> (1988)	U-xZr $x=5.9, 17.1,$ 29.3, 49.6 & 79.5 wt. %	Measurement of thermal diffusivity in the temperature range of 300-1000 K (27-727°C).
Y. Takahashi <i>et al.</i> (1989)	U-xZr $x=15.9, 17.1,$ 29.3 & 79.5 wt. %	Measurement of heat capacity diffusivity in the temperature range of 300-1100 K (27-827°C).
R. R. Sheldon <i>et al.</i> (1989)	U-xZr $x=0-100$ wt. %	First comprehensive assessment of U-Zr system.
T. Matsui <i>et al.</i> (1989)	U-xZr $x=8.7$ wt.%	Measurement of heat capacity using direct heating pulse calorimetry in the temperature range of 300-1300 K (27-1027°C).

T. Ogawa <i>et al.</i> (1991)	U-xZr $x=0-100$ wt. %	Liquidus, solidus temperatures and activity have been calculated in light of available thermodynamic data on U-Zr system. The stability range of δ -UZr ₂ has been correctly reproduced by assuming that δ -UZr ₂ is similar to ω omega solid solution.
T. Ogawa <i>et al.</i> (1991)	U-Zr <i>diffusion couples</i>	Redistribution of the elemental species in U-Zr and U-Zr-Pu alloys studied under imposed steep temperature gradient.
M. Akabori <i>et al.</i> (1992)	U-xZr $x=34.6-77.5$ wt.%	Homogeneity range δ of phase established to lie in between 40.7 to 57.9 wt. % Zr at 873 K (600°C) and from 43.2 to 60.8 w.% Zr at 823 K (550°C) respectively.
A. Maeda <i>et al.</i> (1992)	U-xZr $x=11$ & 19.9 wt. %	Measurement of vapor pressure using Knudsen Effusion mass spectrometry in the temperature range of 1673-1873 K (1400-1600°C). From vapor pressure data, activity and liquidus point have been estimated. These data did not match with Kanno's earlier data at low temperatures; however, a fair agreement is found with the data of Ogawa.
D. D. Keiser <i>et al.</i> (1993)	U-Zr $x=10.3$ wt.%	Series of interdiffusion studies between U-10.3 wt. % Zr and pure Fe, Ni and binary Fe-Cr, Fe-Ni, Ni-Cr and ternary Fe-Ni-Cr alloys at 700°C.
M. Akabori <i>et al.</i> (1995)	U-xZr $x=1.9-87.9$ wt. %	UZr ₂ dissolution temperature has determined using DTA for various U-Zr alloys with Zr ranging from 1.9-87.9 wt. %. The dissolution temperature in U-1.9 wt. % Zr is found to be about 857 K (584°C), with a maximum of 885 K (612°C) observed for 30.7 wt. % Zr alloy. Enthalpy and entropy of transformation are also determined. Lattice parameter data for δ -UZr ₂ phase as function of temperature presented for 300-1000 K (27-727°C).
T. Ogata <i>et al.</i> (1996)	U-xZr $x=4.1-87.9$ wt.%	The interdiffusion coefficients in the γ - (bcc) U and β - (bcc) Zr solid solution have been measured in the temperature range of 973-1223 K (700-950°C) for the Zr content of 10 to 87.9 wt. % using EPMA.
G. L. Hofman <i>et al.</i> (1996)	U-xZr $x=9.6$ wt.%	U-9.6 wt. %Zr alloy has been irradiated to a burn up of 5 and 10 at.% and subsequent characterization done using metallography EPMA. The redistribution of elements has been modelled using mechanistic thermo-transport diffusion model.
T. Ogata <i>et al.</i> (1997)	U-Zr $x=10.3$ wt.%	Interdiffusion studies at 923 K (750°C) for U-10.3 wt. % Zr /Fe couple and U-10.3 wt.%Zr-1at.%Ce/ Fe couple.
M. Akabori,	U-xZr	Interdiffusion measurements in the δ -UZr ₂

<i>et al.</i> (1998)	$x=44.9, 53.5$ & 57.6 wt. %	composition in the temperature range 773-873 K (500-600°C). Activation energy for Zr inrerdiffusion in δ -UZr ₂ is found to be ~129 kJ mol ⁻¹ .
K. Nakamura <i>et al.</i> (1999)	U-Zr $x=10.3$ wt. %	Diffusion couple study on U-10.3 wt. % Zr / Fe and U-10.3 wt.% Zr / Fe-8 wt.% Cr at 908 K (635 °C), 923 K (723 °C), 953 K (680 °C), 988 K (715°C).
P. Y. Chevalier <i>et al.</i> (2004)	U- x Zr $x=0-100$ wt. %	Reassessment of U-Zr system: determined the temperature and composition for all the four invariant reactions based on CALPHAD methodology.
T. Murakami <i>et al.</i> (2009)	δ -UZr ₂ phase	Partial molar quantities estimated for δ -UZr ₂ phase from EMF measurement.
C. B. Basak <i>et al.</i> (2009)	U- x Zr $x=2$ wt. %	Phase transformation kinetics studies using dilatometry and SEM.
C. B. Basak <i>et al.</i> (2009)	U- x Zr $x=2$, wt. %	Study of martensitic transformation in U-2wt.%Zr alloys using metallography.
A. Landa <i>et al.</i> (2009)	U- x Zr $x=0-100$ wt. %	Ground state properties like atomic volume, bulk modulus, heat of formation, Debye temperature and Gruneisen constant are calculated as a function of Zr content at room temperature for bcc (γ -U, β -Zr) and δ phase using ab initio procedures.
M. Kurata <i>et al.</i> (2010)	U- x Zr $x=0-100$ wt. %	Reassessment of U-Zr system, determined the temperature and composition for all the four invariant reactions based on CALPHAD methodology.
W. Li <i>et al.</i> (2010)	U- x Zr $x=0-100$ wt. %	Experimental diffusion data were evaluated to assess the atomic mobility for the bcc phase of the U-Zr, Pu-Zr binaries and U-Pu-Zr ternary by using DICTRA simulations. The developed atomic mobility database, in conjunction with the CALPHAD-base thermodynamic description, have been successfully used to predict the outcome of a large number of binary and ternary diffusion-couple experiments.
C. B. Basak <i>et al.</i> (2010)	U- x Zr $x=50$ wt. %	Study of formation of δ -UZr ₂ phase form γ -U (bcc) under isothermal condition at 908 K (635 °C), 993 K (720 °C) & 1148 K (875°C).

G. Bozzolo <i>et al.</i> (2011)	U-xZr x=0-100 wt. %	Atomistic simulation of U-Zr alloys and their interaction with Fe, Ni and Cr.
R. R. Mohanty <i>et al.</i> (2011)	U-xZr x=0-100 wt. %	Simulation study of atomic transport in presence of temperature gradient.
C. B. Basak <i>et al.</i> (2011)	U-xZr x=7 & 35 wt. %	Phase transformation kinetics using XRD, TEM and SEM.
C. B. Basak <i>et al.</i> (2011)	U-xZr x=50 wt. %	Study of $\gamma \rightarrow \delta$ phase transformation using TEM and SEM.
S. Kaity <i>et al.</i> (2012)	U-xZr x=6 wt. %	Thermophysical property data on U-6wt.% Zr alloy.
W. Xei <i>et al.</i> (2012)	U-xZr x=0-100 wt. %	Density functional theory (DFT) based evaluation of enthalpy of formation.
W. Xiong <i>et al.</i> (2013)	U-xZr x=0-100 wt. %	Recent assessment of U-Zr system using a combination of CALPHAD approach and select ab initio results. A set of self-consistent thermodynamic parameters have been obtained.
T. Ogata <i>et al.</i> (2013)	U-Zr x=10.3 wt. %	Interdiffusion studies at 1023 K (750 °C) for U-10.3 wt.% Zr /Fe couple.
A. C. Bagchi <i>et al.</i> (2013)	U-xZr x=50, 60 & 70 wt. %	Phase transformation characteristics and microstructural behavior in δ -UZr ₂ phase region of U-Zr alloys.
A. K. Rai <i>et al.</i> (2013)	U-xZr x=2, 5 & 10 wt. %	Phase transformation studies in U-xZr (x=2, 5, 10 wt. %) alloys using dynamic calorimetry.
S. Ahn <i>et al.</i> (2014)	U-xZr x=0.1, 2, 5, 10, 20, 30, 40 & 50 wt. %	Phase transformation studies using DSC showing the anomalous behavior of transformation in U-10 wt.% Zr alloy.

In **figure 1.4**, the recently assessed U-Zr equilibrium diagram is shown [29]. It is clear that U-Zr binary is characterized by the presence of five phases. They are: α -U

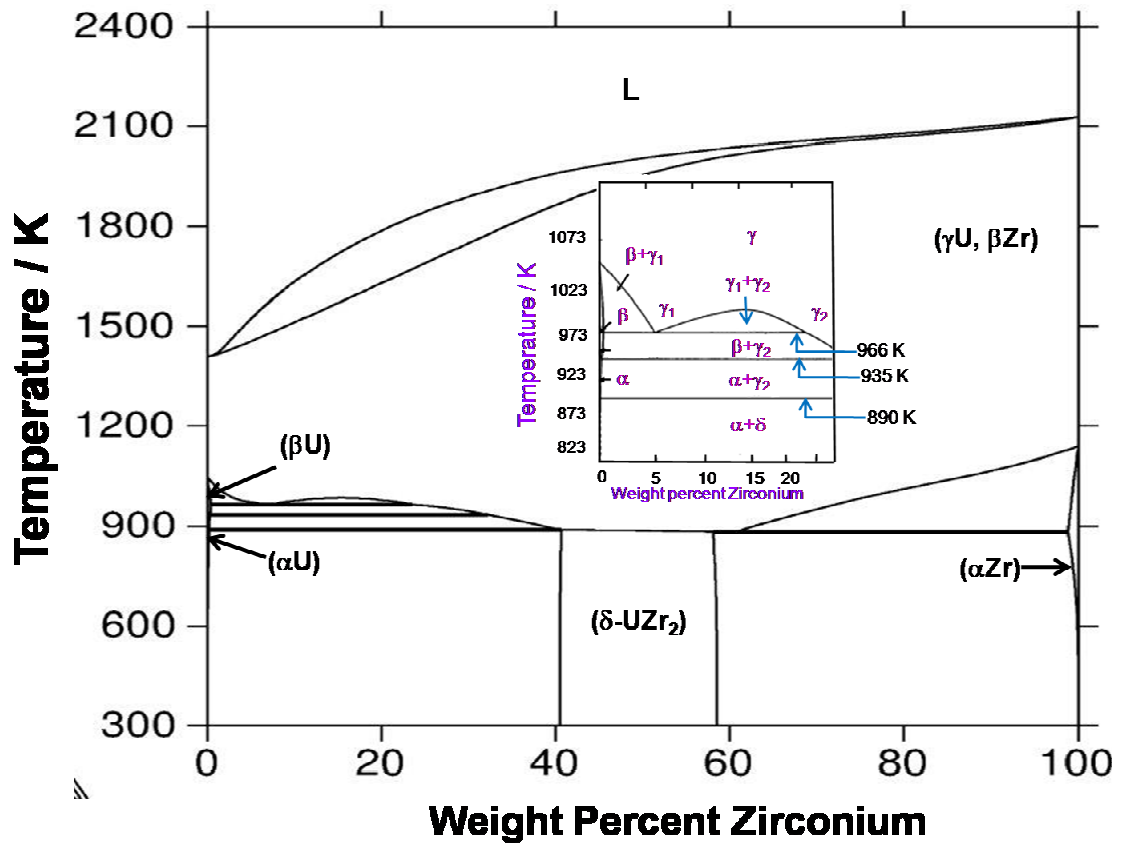


Fig. 1.4. Equilibrium phase diagram of U-Zr system given by Okamoto [29]

(orthorhombic), β -U (tetragonal), γ -U (bcc), α -Zr (hcp) and δ -UZr₂ intermetallic compound. In **table 1.2**, some additional crystallographic data on these phases is summarized. Further, the crystal structure of α -Zr phase is of hexagonal type with AB layer stacking and presented in **figure 1.5**. In addition the crystal structure of δ -UZr₂ is of AlB₂- ω type structure and it is shown in **figure 1.6**. According to the recent assessed diagram [29], the high temperature γ -U phase with bcc structure can dissolve 100 wt.% Zr, whereas the intermediate allotrope β -U exhibits a maximum solubility of about 0.42 wt% Zr at 965 K (692°C) [30-35]. The α -U on the other hand dissolves a maximum of

about 0.31 wt.% Zr at 935 K (662 °C) [30-35]. The only stable intermetallic reported in U-Zr binary is the δ -UZr₂ phase with a small range of homogeneity. In fact UZr₂ is found only between 45 to 62 wt % at 823K (550°C) [30-35]. Further, for alloys having a Zr content between 5 to 22 wt.% Zr, the high temperature γ phase exhibits a phase separation into two *bcc* phases, namely γ_1 (rich in uranium) and γ_2 (rich in Zr), below about 1023 K(750°C) [30-35]. Besides there is also the possibility of obtaining metastable α' (distorted orthorhombic) phase by means of a martensitic mode

Phase	Approximate Zr content at. %	Space Group	Pearson Symbol	Prototype
α -U	0-0.81	<i>Cmcm</i>	<i>oC4</i>	α U
β -U	0-1.2	<i>P4₂/mmm</i>	<i>tP30</i>	β U
γ (U,Zr)	0-100	<i>Im3m</i>	<i>cI2</i>	W
δ (UZr ₂)	63-78	<i>P6/mmm</i>	<i>hP3</i>	A1B2
α -Zr	99.9-100	<i>P6₃/mmc</i>	<i>hP2</i>	Mg

transformation upon fast cooling from the high temperature γ bcc phase [36, 37]. As compared to other related uranium-transition metal alloys, like U-Mo and U-Nb, the U-Zr system is not characterized by the presence of many metastable phases like α'' (monoclinic distortion of α -U), γ' (tetragonal distortion of γ -U), γ_s (distorted γ -U) etc. [38-43]. This is probably because of the fact that as compared to Mo and Nb, the atomic size of Zr is more close to that of uranium. This naturally leads to less distortion of the α

matrix, when the alloy is fast cooled from high temperature γ bcc phase [38-42]. In U-Zr system four invariant reactions are reported by many investigators and it is summarized in **table 1.3**. It is clear from this table that, the temperatures and compositions of these

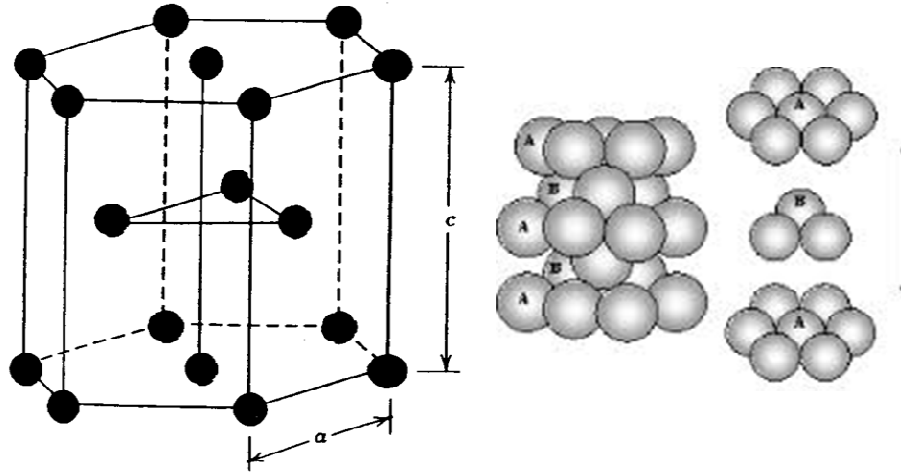


Fig. 1.5. Crystal structure of α -Zr with AB type layer stacking

invariant reactions reported so far are not fully unambiguous. Some of the key findings related to these invariant reactions are briefly discussed.

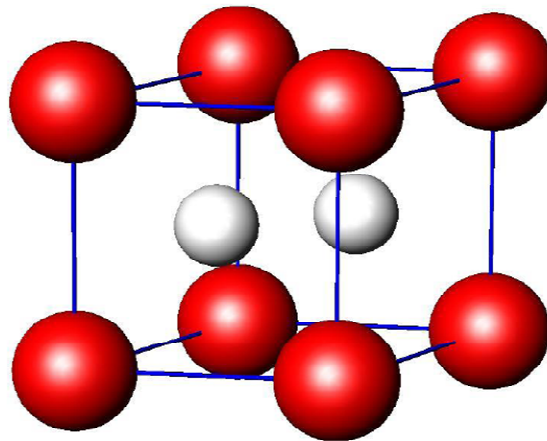


Fig. 1.6. Crystal structure of δ -UZr₂ phase

Summers-Smith was the first one to report the solvus, solidus and liquidus lines of U-Zr system for up to 36.5 wt. % Zr, by employing dilatometry, X-ray diffraction and metallography techniques [43]. However, the presence of δ -UZr₂ phase has not been

reported in this study. On uranium rich side, Summers-Smith [43] has predicted the eutectoidal decomposition of β phase in to $\alpha+\gamma_2$, that is, $\beta\rightarrow\alpha+\gamma_2$ at a temperature of about 935 ± 2 K ($662\pm 2^\circ\text{C}$) and at a composition of 0.31 wt.% Zr. The presence of $\delta\text{-UZr}_2$

Table 1.3						
Invariant reactions in U-Zr system						
Reaction	Composition of respective phases, at.% Zr			Temperature (K)	Type of reaction	Reference
$\gamma_1\leftrightarrow\gamma_2+\beta\text{-U}$	11.0	48.0	1.9	968	Monotectoid	[25]
	14.5	57.0	2.5	966		[33]
	11.2	44.0	1.2	965		[34]
	11.0	42.0	1.06	966		[30]
	9.7	47	-	961		[31]
	17.2	46.6	1.0	966		[43]
	11.0	42.4	1.2	966		[46]
	-	-	-	969		[49]
	-	-	-	968		[48]
$\beta\text{-U}\leftrightarrow\alpha\text{-U}+\gamma_2$	1.1	0.8	56.3	935	Eutectoid	[30]
	1.1	0.8	56.3	935		[34]
	1.9	1.7	62.6	937		[25]
	1.0	0.7	55.4	934		[33]
	1.1	-	57.0	932		[31]
	1.5	1.5	61.0	935		[43]
	-	0.55	-	935		[46]
	-	-	-	944		[49]
	-	-	-	945		[48]
$\gamma_2+\alpha\text{-U}\leftrightarrow\delta\text{-UZr}_2$	64.1	0.7	64.0	888	Peritectoid	[33]
	68.0	0.5	65.0	888		[25]
	67.7	0.69	63.6	893		[34]
	66.0	0.5	63.0	890		[30]
	77.9	0.5	65	885		[31]
	-	-	-	885		[32]
	-	-	62.5	890		[54]

	-	-	-	880		[45]
	-	-	-	885		[49]
$\gamma \leftrightarrow \delta$ -U _{Zr₂} + α -Zr	80.0	78.3	99.5	883	Eutectoid	[33]
	81.4	75.2	98.2	884		[25]
	81.3	79.3	98.7	877		[34]
	81.0	78.0	99.6	879		[30]
	78.0	76.0	99.6	883		[31]
	-	-	-	868		[32]
	76.1	-	-	879		[54]
	-	-	-	866		[45]

was established subsequently by Howlett *et al.*, [44] in the range 39.5 to 59.1 wt.% Zr. In addition, Howlett *et al.*, [44] noted that high temperature γ -bcc phase decomposes in to γ_1 (U-rich) + γ_2 (Zr-rich) bcc phases. The composition range of this miscibility gap has been established as 6.1 to 33.6 wt.% Zr by Howlett *et al.* [44]. The study of Rough *et al.* on the other hand has indicated the possibility of a peritectoid reaction $\beta + \gamma_2 \rightarrow \alpha$ taking place at 973 K (700°C) [45]. This suggestion differs markedly from that of Summers-Smith, who had proposed the eutectoid reaction [43]. But this finding of Rough *et al.*, [45] has been ruled out by the subsequent study of Chiswik *et al.* [13]. Further, it is also interesting to note that the same eutectoid reaction was placed at a lower temperature of 943 K (670°C) by Howlett *et al.*, using high temperature XRD data [44]. The occurrence of the eutectoid reaction was further supported by the study of Zegler [46], Lagerberg [47], Basak *et al.* [48] and Rai *et al.*, [49].

The other important invariant reaction in U-Zr system is the monotectoid, $\gamma_1 \leftrightarrow \beta + \gamma_2$, at 966 ± 3 K ($693 \pm 3^\circ\text{C}$) and at 6.1 wt.% Zr, according to the early report of Summers-Smith [43]. Nevertheless, the same reaction has been established at a slightly different composition, of about 6.8 wt.% Zr by Bauer *et al.*, [50] and at 4.5 wt.% Zr by Zegler *et al.* [46]. On Zr-rich side, the occurrence of two more invariant reactions has

been noted by Howlett *et al* [44]. One of these is the peritectoidal formation of δ -UZr₂ phase from α -U+ γ_2 two phase mixture at 893 K (620°C) and at 39.5 wt.% Zr. The second one is the eutectoidal decomposition of γ into α -Zr + δ -UZr₂ at 880 K (607°C) and at 59.1 wt.% Zr. The occurrence of these two invariant reactions is also supported by work of other investigators [46-49]. Later, the phase transformation study carried out on Zr-rich U-Zr alloys by Rough *et al.*, [51] clearly supported the presence of three distinct phase fields, namely δ -UZr₂, γ_2 + δ and γ_2 in the temperature range 823 K (550) to 923 K (650°C), and with Zr content varying between 44.9 to 52.2 wt.%.

Besides these, there have been several studies on the stability of δ -UZr₂ phase [52-58]. According to Akabori *et al.*, the homogeneity range of δ -UZr₂ corresponds to 38.5 to 57.9 wt.% Zr at 873 K (600°C) and 43.2 to 63.9 wt.% Zr at 823K (550°C) respectively [52]. The DTA study of Akabori showed that the dissolution temperature of δ -UZr₂ phase is found to vary between 857 K (584°C) to 885 K (612°C), depending on Zr content [52, 53]. On the other hand, the previous works of Howlett *et al.* [44], Lagerberg [47] and Duffey *et al.* [54] have shown that δ -UZr₂ dissolution occurs at around 890 K (617°C). Recently, Basak *et al.* [48, 55] have observed a similar type of phase transformation taking place at about 858 K (585°C) in U rich U-Zr alloys. They argued that it could be due to thermally activated relaxation of α' -martensite (that was obtained by fast cooling from high temperature γ -bcc phase) rather than arising from gradual dissolution of UZr₂. This finding of Basak *et al.*, [48] has further been supported by Kaity *et al.* [56] and Rai *et al* [49]. Very recently, Mckeown *et al.*, has clearly witnessed in their transmission electron microscopy study, the presence of δ -UZr₂ phase even in slow cooled as cast samples of U-10 wt.% Zr alloy [57]. Apart from these, the earlier studies of Bauer *et al.* and Zegler have suggested that the presence of oxygen and nitrogen impurities plays a vital role in deciding phase stability in U-Zr system [46, 58].

It has been observed that in the presence of oxygen and nitrogen, both α -U and α -Zr get stabilized relative to δ -UZr₂ phase. Zegler [46] has further observed that if oxygen content is less than about 150 mass ppm, then single phase γ_1 and γ_2 are found in the U-Zr samples that are annealed at 973 K (700) and 998K (725°C) respectively. However if oxygen content is in the range 160 to 300 mass ppm, then $\gamma_1+\gamma_2$ two phase field has been observed in samples subjected to same annealing treatment.

1.5.2. Solid state transformation kinetics

As for transformational kinetic aspects in U-Zr alloys are concerned, it is instructive to note that it was Lagerberg [47], who has reported for the first time, the possibility of having both diffusional and martensitic modes of decomposition of high temperature γ -bcc phase under varying cooling conditions. In the case of U-2 wt.% Zr alloy, the martensitic transformation start temperature (M_s) is estimated to be around 763 K (490°C) [47], and for U-6 wt.% Zr, the M_s has been predicted to be in the range of 748 K (475°C) to 773 K (500°C) by Virot [59]. The X-ray diffraction (XRD) and metallographic investigation on Zr rich Zr-U alloys with U content in range 3.2-8.8 wt.% showed that addition of U has made sluggish precipitation of α -Zr phase; while the formation of δ -UZr₂ has been enhanced [60]. Further, in a systematic study on decomposition of high temperature γ phase by Hills *et al* [61], it has been reported that the decomposition of γ can proceed *via* diffusional, martensitic or mixed modes depending on Zr content and cooling rates employed [61]. In case of alloys having Zr content up to 8.8 wt. %, fast cooling promotes α' -martensite formation through displacive mode, with the martensite possessing either acicular (Zr <4.1 wt.%) or banded structure (4.1<Zr≤8.820 wt. %). However, if Zr content is in the range 14.1-20.4 wt%, then the γ phase first transforms to an intermediate ω (hexagonal) phase which then transforms to martensitic α' . The $\gamma \rightarrow \omega$ transformation is reported to be martensitic in

nature for high Zr content alloys [61]. However in the case of Zr-lean alloys, the ω -phase can result from the diffusional decomposition of γ -bcc as well, and in such cases $\omega \rightarrow \alpha_{\text{eq}}$ diffusional transformation follows as the natural sequence. Therefore, it appears that bypassing of $\gamma \rightarrow \beta$ transformation upon cooling is possible in U-Zr alloys, by tailoring both composition and cooling rates. In the case of U-0.97 wt.% Zr, it has also been found that γ first transforms to β , which then undergoes another transition to produce $\gamma_2 + \alpha$ again through a diffusional mode. Note that γ_2 is the Zr rich bcc phase. Instead of precipitating equilibrium δ -UZr₂ phase, which requires appreciable diffusion, the γ_2 undergoes a displacive transformation $\gamma_2 \rightarrow \alpha'$ to yield distorted α' -martensite phase. In other words, the following reaction sequence, $\gamma \rightarrow \beta \rightarrow \gamma_2 + \alpha \rightarrow \alpha + \alpha'$ has been advocated by Hills *et al.* [61]. It may be recalled that according to equilibrium phase diagram given in **figure 1.4**, the equilibrium course of phase change for a U-0.97 wt.% Zr alloy would be: $\gamma \rightarrow \beta + \gamma_1 \rightarrow \beta + \gamma_2 \rightarrow \alpha + \gamma_2 \rightarrow \alpha + \delta$ -UZr₂. It is clear that the sluggish diffusion of both U and Zr with progressively lowering temperature and coupled to the fact that less time is available for the transformation to proceed at high cooling rates, enable the formation of martensitic α' in this case. It is only expected that with increasing Zr content, the diffusional transformation would further get inhibited, unless extremely slow cooling rates are imposed. It may also be added that the banded microstructure α' -martensite has been found to be composed of twins for high Zr containing U-Zr alloys indicating the role of transformational stresses [62]. In a series of studies, Basak *et al.*, have investigated the phase transformation character of U-Zr alloys with Zr content varying from 2 to 50 wt.% [48, 55, 63-66]. In one of their studies, Basak *et al.*, [64] have suggested the possibility of formation of α'' phase (a monoclinic distorted version of equilibrium orthorhombic α) at 870 K (597°C), that is just before $\gamma \rightarrow \alpha'$ phase change, which occurs at 826 K (553°C). However, it is not clear from their study whether the

formation of α'' proceeds through intermediate β or directly from γ phase through a displacive mode [64]. Thus, it is clear that there is a lack of clarity on the decomposition modes of high temperature γ -bcc phase, as influenced by cooling rate and Zr content.

1.5.3. Thermodynamic modelling of phase equilibria

In late eighties, there have been few studies on the determination of liquidus and solvus temperatures by both measurement and thermodynamic modeling [29-24, 67-71]. Leibowitz *et al.*, have measured and calculated the liquidus and solidus temperatures for the entire composition range using DTA technique and thermodynamic phase diagram optimization [67, 68]. Later on, the estimation of liquidus and solidus temperatures based on Knudsen effusion technique based activity measurements, has been carried out by Kanno and Maeda *et al.* [70, 71]. This is also continued by Ogawa *et al.*, who have also calculated the activity, liquidus and solidus temperatures in the light of then available data on U-Zr system [69]. This study reproduced the stability range of δ -UZr₂ by assuming it to be a ω -like phase [69]. In recent times, Xiong *et al.*, have again reassessed the U-Zr system using CALPHAD methodology, with some additional inputs coming from *ab-initio* theoretical calculations [34]. The *ab-initio* calculation of atomic volume, enthalpy of formation, cohesive energy, Debye temperature and Gruneisen constant at 0 K has also been carried out by Landa *et al.* and Xei *et al.* [72-75].

On the diffusion studies related area, there are only few studies related to the determination of diffusivity data in the high temperature γ -bcc phase of U-Zr alloys [76-79]. However, on a related front, there are several experimental measurements of thermophysical properties like thermal diffusivity, heat capacity and thermal expansivity [56, 80-84].

Summarizing the situation, it may be stated that although there is a broad based consensus with regard to the general nature of phase equilibria in U-Zr binary system,

there are still some issues of concern, especially with regard to the actual temperature and compositions of invariant reactions. Further, the nature of formation of metastable displacive α' -martensite either separately or in conjunction with δ -UZr₂ upon cooling from γ -bcc phase is yet to be clarified beyond doubt. It also appears that the kinetic aspects of various solid state transformations have also not been addressed clearly thus far. Rigorous computational modelling of phase equilibria and phase transformation kinetics is also hampered, partly due to the lack of reliable (recent) data on various mobility values for Zr and U in different allotropes of uranium. Thus, there is ample scope to reinvestigate diffusion behavior and kinetics of phase transformations in U-Zr system.

1.6. Phase equilibria and phase transformation studies on Fe-U system

The literature survey related to phase equilibria on Fe-U system is presented in **table 1.4**. It is instructive to note from **table 1.4** that there exists a fair amount of phase equilibria and thermochemistry related information on Fe-U system, which has been the subject of a recent assessment by Chatain *et al* [85]. The equilibrium solubility of uranium in α -iron and that of Fe in α -U at room temperature are negligible [86-92]. However,

Table 1.4		
Phase equilibria information of Fe-U system		
Reference	Composition wt% Fe	Equilibrium data
Paul Gordon <i>et. al.</i> (1950)	0-11.2	Measurement of different solvus line, liquidus and solidus points, allotropic phase change temperatures, eutectic points and melting temperature of UFe ₂
J. D. Grogan <i>et. al.</i> (1950)	0-11.2	Measurement of different solvus line, liquidus and solidus points, allotropic phase change temperatures, eutectic

		points and melting temperature of UFe ₂
J. A. Straatmann <i>et. al.</i> (1964)	0-0.48	Peritectic temperature, solidus line measurement on Fe rich side
G. G. Michaud (1966)	75.7-100	Measurement of allotropic phase transformations, melting temperature (UFe ₂) and eutectic point
M. Kannno (1974)	UFe ₂	EMF measurement
G. M. Campbell (1977)	UFe ₂	Enthalpy increments and heat capacity
L. R. Chapman <i>et. al.</i> (1984)	1.5-95.9	Measurement of allotropic transformations, eutectic, peritectic temperature, liquidus and solidus line
L. Leibowitz <i>et. al.</i> (1991)	0.2-95.9	Measurement of allotropic transformations, eutectic, peritectic temperature, liquidus and solidus line
P. Gardie <i>et. al.</i> (1992)	0.12-2.4	Activity measurement and computed liquidus line
D. Labroche <i>et. al.</i> (2000)	UFe ₂ and U ₆ Fe	High temperature heat capacity data in the temperature range of 300-1400 K
S. Chatain <i>et al.</i> (2003)	U-Fe	Assessment of phase diagram

at high temperatures, iron is soluble to some extent (~ 4 wt %) in γ -U (bcc) phase [92]. According to the currently accepted equilibrium diagram [85] given in **figure 1.7**, the U-Fe binary is characterised by the presence of two almost stoichiometric intermetallic phases, namely Fe₂U and FeU₆, which are connected to the high temperature liquid phase on either end by two eutectic reactions. On the Fe-rich side, the eutectic reaction involving liquid, Fe₂U and γ -Fe occurs at 1353±5 K (1080±5°C), whereas the other one involving FeU₆ and Fe₂U is relatively deep and is located at 998±5 K (725±5°C).

In literature, there is some uncertainty surrounding the correct compositional placement of the first eutectic involving Fe_2U [86-92]. Gordon and Kaufmann have reported the first comprehensive experimental data on liquidus, solvus and other phase transformation temperatures in Fe-U system for almost, the entire range of composition [86]. Subsequently, similar studies have also been carried out by Grogan on uranium rich

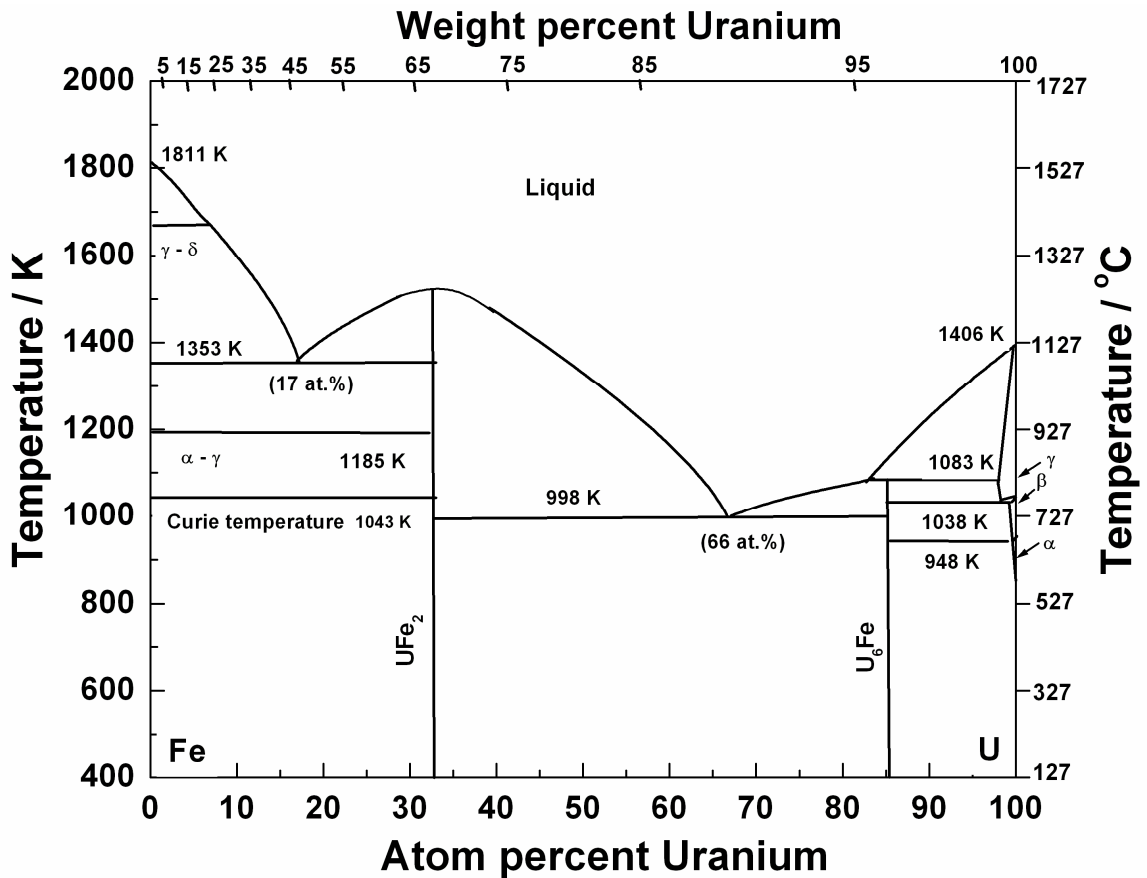


Fig. 1.7. Fe-U equilibrium phase diagram

side [87]. In addition, measurements of liquidus temperatures have also been made by Straatmann *et al.*, [90] and also by Michaud [91] on uranium and iron rich sides respectively. These different experimental data suffer from some scatter, as will be discussed in the later chapters of this thesis. This situation prompted further studies of liquidus temperature variation as a function of U content from Chapman *et al.*, [89] and also by Leibowitz *et al* [88]. The latter researchers have not only measured the

temperatures of phase changes using differential thermal analysis (DTA), but also made the first comprehensive thermodynamic calculation/assessment of Fe-U equilibrium diagram in terms of a critically assessed thermodynamic database [88, 93-100]. Meanwhile, Gardie *et al.*, have also made estimations of the uranium activity based on mass spectrometry measurements of vapour pressure [93]. Their estimated liquidus and solidus temperatures on Fe-rich side were found to be in reasonable agreement with the work of Leibowitz *et al* [88].

Notwithstanding all these developments, it may be mentioned that there is still some confusion among the reported experimental data related to $Fe_2U + \gamma Fe \rightarrow Liquid$, and $FeU_6 + Fe_2U \rightarrow Liquid$ transformation temperatures. In addition, no experimentally measured values of enthalpies of various solid state transformations are available as a function of alloy compositions in literature [85-100]. With a view to address these issues to some extent, an attempt has been made pertaining to a comprehensive differential scanning calorimetry (DSC) investigation of high temperature phase stability in Fe-U alloys as a function of composition in the present study.

1.7. Phase equilibria studies on U-Rh system.

Starting from the pioneering research of Chiswick and Parks [101, 102], the studies related to phase equilibria on U-Rh binary are very few. According to the recent assessed equilibrium phase diagram shown in **figure 1.8** [103], it is clear that both Rh and U exhibits limited solid solubility in each other even at high temperatures. However, the binary U-Rh system is characterized by the presence of four stoichiometric intermetallic compounds namely URh₃, U₃Rh₅, U₃Rh₄, and U₄Rh₃. Among all the four compounds URh₃ is the most stable compound with melting temperature of about 1973 K (1700°C). Except URh₃ all other compound in U-Rh system forms through peritectic reactions respectively at 1428 K (1155°C)-U₄Rh₃, 1723 K (1450°C)-U₃Rh₄ and 1823 K (1550°C)-U₃Rh₅. In addition, U₄Rh₃ undergoes a polymorphic transition at a temperature of about

993K (720°C). Besides these there are two more eutectic reactions. The first eutectic reaction occurs between U and U_4Rh_3 at 1138 K (865°C) for Rh content of 12.3 wt. %. The second eutectic occur between Rh and URh_3 at 1666 K (1393°C) for the Rh content of about 74 wt. %. Chiswick and Dwight *et al.* were the first to publish the partial phase diagram of U-Rh system with Rh content up to 50 wt. % [103]. In their study, it has been proposed that two intermetallic compounds U_2Rh and URh exist with limited solubility range. However, after this, Park has measured invariant reaction temperatures, liquidus and solidus temperature using metallography, XRD and thermal analysis [102]. The

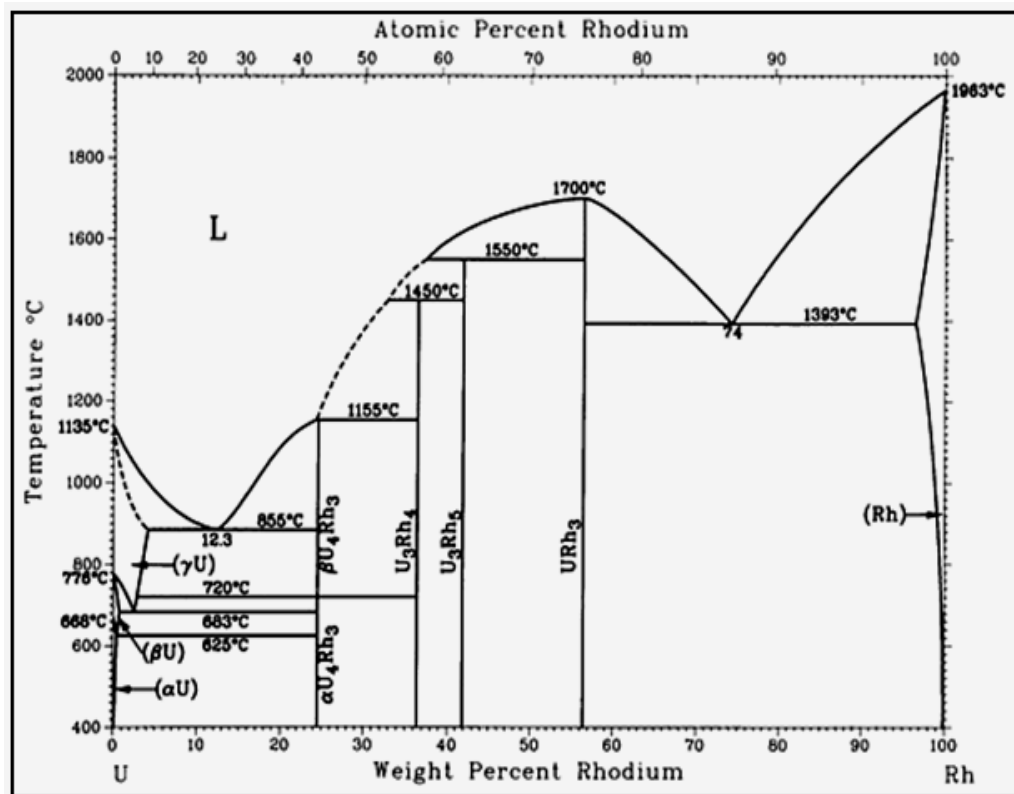


Fig. 1.8. Equilibrium phase diagram of U-Rh system

study of Park has established the presence of four line compounds URh_3 , U_3Rh_5 , U_3Rh_4 , and U_4Rh_3 rather U_2Rh and URh compounds [102]. According to Park [102], the maximum solid solubility of Rh in γ -uranium is near 3.6 wt. %, in β -uranium is about 0.7 wt. % and in α -uranium is about 0.1 wt. %. On the other hand, the solid solubility of

uranium in rhodium is about 6.9 wt. %. The reinvestigation of U-Rh phase diagram by Okamoto [103] has supported the findings of Park [102]. Apart from these, there have been some study related to the measurement of thermodynamic properties of URh₃ compound up to 840 K [105-106]. It can be seen from **figure 1.8** that still some of the portions of phase diagram are not established with a high degree of confidence and hence shown in dotted line.

Therefore, there is strong necessity to reinvestigate the phase equilibria and phase stability on U-Rh system. The measurement of thermodynamic properties of all the four intermetallic compounds will also be quite helpful in assessing the U-Rh phase diagram. However, in the present study, the scope is restricted to the evaluation of thermodynamic properties of one of the intermetallic compound URh₃ using calorimetry.

1.8 Organization of the Thesis

This present thesis is divided into eight chapters and these chapters are organized in the following manner.

Chapter 1: This introductory chapter began with a brief introduction to nuclear metal fuel in the context of fast reactor. Following this, the need of studying the phase stability and phase transformation in uranium-transition metal alloys with regard to nuclear metal fuel has been highlighted. Subsequently, a broad based literature surveys related to phase transformation and phase stability aspects on U-Zr, U-Fe and U-Rh system are presented.

Chapter 2: In this chapter the experimental methodology adopted in the present study has been discussed. This chapter begins with a brief description about the melting of different U based alloys used in the present study, basic compositional characterization and annealing treatment adopted. This is followed by detailed descriptions about instrumentation, calibration and experimental procedure for both differential scanning calorimetry (DSC) and inverse drop calorimetry that are employed in the present study.

In addition a very short description about X-ray diffraction, metallography and scanning electron microscopy are also presented.

Chapter 3: Under this chapter, the theoretical aspects related to phase transformation kinetics and quasi harmonic Debye-Gruneisen formalism are briefly highlighted. Under phase transformation kinetics, the development of Kolmogorov-Johnson-Mehl-Avrami (KJMA) formalism is elaborated in some detail for both isothermal and non-isothermal transformations. Further, in the context to Debye-Gruneisen quasi-harmonic formalism, a brief account of practical aspects is presented in order to obtain self consistent estimates of both heat capacity and thermal expansivity.

Chapter 4: In this chapter, calorimetric characterization of the effect of heating/cooling rates on kinetics of allotropic phase changes in uranium is discussed. The effect of heating/cooling rates on different allotropic phase changes has been studied primarily using DSC. It is shown that the transformation temperatures exhibited a strong non-linear variation with the heating or cooling rate. The DSC results obtained for the $\alpha \rightarrow \beta$ and $\beta \rightarrow \gamma$ transformations during heating have been modelled using standard Kolmogorov-Johnson-Mehl-Avrami (KJMA) model which confirm to a nucleation and growth mediated process. With the help KJMA model, it is possible to obtain kinetics parameters and these are discussed in the light of available diffusion data in α -U, β -U and γ -U phases. Further the kinetics of on-cooling transformations like $\gamma \rightarrow \beta$ and $\beta \rightarrow \alpha$ have been analyzed using an empirical model proposed by Kamamoto and Koistinen-Marburger. This analysis confirms that cooling induced transformations may follow a martensitic or massive mode.

Chapter 5: This chapter deals with the study on phase stability and phase transformation characteristics in U-xZr (x=0, 2, 5 & 10 wt. %) alloys using calorimetry. Using DSC, the sequence of various transformations that occur during heating and cooling cycles in U-2,

5 & 10 wt. Zr alloys is established. Further, the co-occurrence of martensitic relaxation and δ -UZr₂ dissolution in U-2, 5 & 10 wt. Zr alloys has been clearly confirmed using a combination of DSC and metallography. In addition, the effect of cooling rate and Zr content on the decomposition of high temperature γ phase has been studied. It has been observed that depending on Zr content and cooling rate, the decomposition of γ phase may adopt either diffusional or martensitic mode of transformation. The DSC data obtained as a function of heating/cooling rate have been used to construct continuous heating (CHT) and cooling transformation (CCT) diagrams.. With the help of these results, it is possible to determine the critical cooling rate for martensitic transformations. Finally, the kinetics of $\alpha \rightarrow \beta$ diffusional transformation that occurs on heating has been modelled in terms of Kolmogorov-Johnson-Mehl-Avrami (KJMA) formalism. It is found that the transformation is effectively controlled by the diffusion of Zr in α' -orthorhombic phase.

Chapter 6: In this chapter the reinvestigation of phase equilibria on Fe-U binary system using differential scanning calorimetry is presented. With the help of DSC, different solvus, solidus and liquidus temperatures as function of U content have been measured for Fe_{100-x}U_x binary alloys, with x varying from 0 to 95 mass % U. Further, the composition and temperature of two eutectic invariant reactions that occur in Fe-U binary system are correctly established from DSC results. The measured transformation temperatures have been used to construct the binary Fe-U phase diagram. Besides these, the heat of transformation for various invariant reactions and solid state transformations have also been obtained as a function of U content.

Chapter 7: This chapter deals with measurement and modelling of thermo physical properties of UFe₂ and URh₃ compounds. In this chapter, measurement of enthalpy increment data in the range of 300-1473 K using drop calorimetry for both compounds

are presented. Further, the enthalpy data obtained in the present study are modeled using quasi harmonic Debye-Grüneisen formalism in conjunction with literature information on low temperature capacity and thermal expansion data. The modeling exercise yielded dilatational contribution to heat capacity, and a consistent estimate of temperature dependent volume thermal expansivity for both URh₃ and UFe₂ compounds.

Chapter 8: This chapter summarizes the results of chapter 4 to chapter 7 and is devoted to exploring the further avenues of research that can be profitably continued from what limited data has been accrued in this study.

1.9. References

1. L.C. Walters, B .R. Seidel and J.H. Kittel, Nucl. Techno., 65 (1984) 179.
2. G. L. Hofman and L. C. Walters, "Metallic Fast Reactor Fuels" in: B.R.T. Frost, ed., Materials Science and Technology: A Comprehensive Treatment, Part 1, Vol. IOA (VCH, New York, 1994).
3. R. G. Pahl, D. L. Porter, D .C. Crawford and L. C. Walters, J. Nucl. Mater., 188 (1992) 3.
4. R. D. Leggett and L. C. Walters, J. Nucl. Mater., 204 (1993) 23
5. P. E. Potter, J. Nucl. Mater., 389 (2009) 29.
6. D. E. Burkes, R. S. Fielding, D. L. Porter, D. C. Crawford and M. K. Meyer, J. Nucl. Mater., 389 (2009) 458.
7. W. J. Carmack, D. L. Porter, Y. I. Chang, S. L. Hayes, M. K. Meyer, D. E. Burkes, C. B. Lee, T. Mizuno, F. Delage and J. Somers, J. Nucl. Mater., 392 (2009) 139.
8. D. E. Burkes, R. S. Fielding and D. L. Porter, J. Nucl. Mater., 392 (2009) 158-163.
9. C. R. F. Azevedo, Eng. Failure Analysis, 18 (2011) 1943.
10. A. Riyas and P. Mohanakrishnan, Ann. Nucl. Energy, 35 (2008) 87.
11. G. L. Hofman, L. C. Walters and T. H. Bauer, Prog. Nucl. Energy, 31 (1997) 83.
12. R. A. Vandermeer, Proceedings of the Third Army Materials Technology Conference held at Vall, Colorado, USA, February 1974, p. 259.
13. H. H. Chiswik, A. E. Dwight, L. T. Lloyd, M. V. Nevitt and S. T. Zegler, Proceedings of the Second United Nations International Conference on Peaceful Uses of Atomic Energy, June 1985, p. 1.
14. D. Blake and R. F. Hehemann, Proceedings of the Third Army Materials Technology Conference held at Vall, Colorado, USA, February 1974, p. 189.

15. J. J. Burke and P. H. Dixon, Symposium on Uranium & Graphite, London Inst. of Metals, 1962.
16. A. N. Holden, Physical Metallurgy of Uranium, Addison – Wesley Publishing Co. Inc. USA, 1958.
17. J. J. Burke, Physical Metallurgy of Uranium Alloys, Hill Publishing Co. Inc, USA, 1974.
18. O. S. Ivanov, Phase Diagram of Uranium Alloys, Nauka Publishers, Moscow, 1972.
19. Y. S. Kim, G. L. Hofman, S. L. Hayes and Y. H. Sohn, J. Nucl. Mater., 327 (2004) 27.
20. D. L. Porter, C. E. Lahm, and R. G. Pahl, Metall. Trans. A, 21 (1990) 1871.
21. G. L. Hofman, S. L. Hayes and M. C. Petri, J. Nucl. Mater., 227 (1996) 277.
22. T. Ogawa, T. Iwai and M. Kurata, J. Less. Comm. Met., 175 (1991) 59.
23. R. R. Mohanty, J. Bush, M. A. Okuniewski and Y. H. Sohn, J. Nucl. Mater., 414 (2011) 211.
24. K. Nakamura, T. Ogata, M. Kurata, T. Yokoo and M. A. Mignanelli, J. Nucl. Mater., 304 (2002) 63-72.
25. M. Kurata, T. Ogata, K. Nakamura and T. Ogawa, J. Alloys Compd., 271–273 (1998) 636.
26. H. Kleykamp, Pure & Appl. Chem., 63 (1991) 1401.
27. H. Kleykamp, J. Nucl. Mater., 201 (1993) 193.
28. H. Kleykamp, Proc. of the Symposium on Behavior and Chemical State of Irradiated Ceramic Fuels Vienna, IAEA, Vienna (1974) 157.
29. H. Okamoto, J. Phase Equilibria, 28 (2007) 499.
30. R. R. Sheldon and D. E. Peterson, Bulletin of Alloy Phase Diagram, 10 (1989) 165.

31. H. Baker, ASM Handbook, Alloy Phase Diagrams, 1992.
32. P.Y. Chevalier, E. Fischer and B. Cheynet, CALPHAD: Coupl. Phase Diag. Thermochem. 28 (2004) 15.
33. P.Y. Chevalier, E. Fischer, J. Nucl. Mater., 257 (1998) 213.
34. W. Xiong, W. Xie, C. Shen and D. Morgan, J. Nucl. Mater., 443 (2013) 331.
35. R. F. Hills, B. R. Butcher, B. W. Howlett and D. Stewart, J. Nucl. Mater., 16 (1965) 25.
36. V. K. Orlov and V. M. Teplinskaya, Atomic Energy, 86 (1999) 118.
37. K. Tangri and D. K. Chaudhuri, J. Nucl. Mater., 4 (1965) 278.
38. J. Lehmann and R. F. Hills, J. Nucl. Mater., 2 (1960) 261.
39. H. L. Yakel, The Physical Metallurgy of Uranium alloys Conference sponsored by the AEC Army Material and Mechanical Research Centre, Vail Colorado, February 1974.
40. H. L. Yakel, J. Nucl. Mater., 33 (1969) 286.
41. R. A. Vandermeer, Acta Metall., 28 (1979) 383.
42. J. G. Speer and D. V. Edmonds, Acta Metall., 36 (1988) 1015.
43. D. Summers-Smith, J. Inst. Met. 83 (1954-55) 277.
44. B. W. Howlett and A. G. Knapton, paper P/1469, Proc. 2nd U. N. International Conference on Peaceful use at GENEVA, SWITZERLAND, 6 (1958) 104.
45. F. A. Rough and A. A. Bauer, Battelle (USA) Report BMI – 1300, 1958.
46. S. T. Zegler, USAEC Rep. ANL-6055, 1962.
47. G. Lagerberg, J. Nucl. Mater., 9 (1962) 261.
48. C. B. Basak, G. J. Prasad, H. S. Kamath and N. Prabhu, J. Alloys Compd., 480 (2009) 857.
49. Arun Kumar Rai, S. Raju, Haraprasanna Tripathy, R. N. Hajra and M. Vijayalakshmi, Trans. Ind. Inst. Met., 66 (2013) 387.

50. A. A. Bauer, Battelle (USA) Report BMI-1350, 1959.
51. F. A. Rough, A. E. Austin, A. A. Bauer and J. R. Doig, Battelle (USA) Report BMI-1092, 1956.
52. M. Akabori, A. Itoh, T. Ogawa, F. Kobayashi and Y. Suzuki, *J. Nucl. Mater* 188 (1992) 249.
53. M. Akabori, , T. Ogawa, A. Itoh and Y. Morii, *J. Phys. Condens. Matter.*, 7 (19957) 8249.
54. J. F. Duffey, and C. A. Bruch, *Trans. AIME*, 212 (1958) 17.
55. C. B. Basak, R. Keswani, G. J. Prasad, H. S. Kamath and N. Prabhu, *J. Alloys Comp.*, 471 (2009) 544.
56. S. Kaity, J. Banerjee, M. R. Nair, K. Ravi, S. Das, T. R. G. Kutty, Arun Kumar and R. P. Singh, *J. Nucl. Mater.*, 427 (2012) 1.
57. T. Mckeown, S. Irukuvarghula, S. Ahn, M. A. Wall. L. L. Hsiung, S. McDeavitt and P. E. A. Turuchi, *J. Nucl. Mater.*, 436 (2013) 100.
58. A. A. Bauer, G. H. Beatty and F. A. Rough, *Trans. AIME*, 212 (1958) 801.
59. A. Viro, *J. Nucl. Mater.*, 5 (1962) 109.
60. D. L Douglass, L. L Marsh and G. K Manning, *Trans ASM*, 50 (1958) 305.
61. R. F. Hills, B. R. Butcher, B. W. Howlett and D. Stewart, *J. Nucl. Mater.*, 16 (1965) 25.
62. B. A. Hatt, *J. Nucl. Mater* 19 (1966) 133.
63. C. Basak, *J. Nucl. Mater.*, 416 (2011) 280.
64. C. Basak,R. Keswani, G. J. Prasad, H. S. Kamath N. Prabhu and S. Banerjee, *J. Nucl. Mater.*, 393 (2009) 146.
65. C. B. Basak, N. Prabhu and M. Krishnan, *Intermetallics*, 18 (2010) 1707.
66. C. B. Basak, S. Neogy, D. Srivastava, G. K. Dey, S. Banerjee, *Philos. Magz.*, 91 (2011) 3290.

67. L. Leibowitz, E. Veleckis, R. A. Blomquist and A. D. Pelton, *J. Nucl. Mater.*, 154 (1988) 145.
68. L. Leibowitz, R. A. Blomquist and A. D. Pelton, *J. Nucl. Mater.*, 167 (1989) 76.
69. T. Ogawa and T. Iwai, *J. Less. Comm. Met.*, 170 (1991) 101.
70. M. Kanno, M. Yamawaki, T. Koyama and N. Morika, *J. Nucl. Mater.*, 54 (1988).
71. A. Maeda, Y. Suzuki and T. Ohmichi, *J. Alloys Compd.* 179 (1992) 21.
72. A. Landa, P. Soderlind, P. E. A. Turchi, L. Vitos and A. Ruban, *J. Nucl. Mater.*, 393 (2009).
73. A. Landa, P. Söderlind, and P. E. A. Turchi, *J. Alloys Compd.*, 478 (2009) 103.
74. A. Landa, P. Söderlind and P. E. A. Turchi, *J. Nucl. Mater.*, 414 (2011) 132.
75. W. Xiong, W. Xie, C. Shen and D. Morgan, *J. Nucl. Mater.*, 443 (2013) 331.
76. Y. Adda and A. Kirianenko, *J. Nucl. Mater.*, 6 (1962) 135.
77. T. Ogata, M. Akabori, A. Itoh and T. Ogawa, *J. Nucl. Mater.*, 232 (1996) 125.
78. M. Akabori, A. Itoh, T. Ogawa and T. Ogata, *J. Alloys Comp.*, 271-273 (1998) 597.
79. W. Li, R. Hu, Y. W. Cui, H. Zhong, H. Chang, J. Li and L. Zhou, *J. Nucl. Mater.*, 407 (2010) 220.
80. G.B. Fedorov and E. A. Smirnov, *Sov. Atom. Energy*, 25 (1968) 795.
81. Y. Takahashi, M. Yamawaki and K. Yamamoto, *J. Nucl. Mater.*, 154 (1988) 141.
82. Y. Takahashi, K. Yamamoto, T. Ohsato, H. Shimada, T. Terai and M. Yamawaki, *J. Nucl. Mater.*, 167 (1989) 147.
83. T. Matsui, T. Natsume and K. Naito, *J. Nucl. Mater.*, 167 (1989) 152.
84. A. C. Bagchi, G. J. Prasad, K. B. Khan and R. P. Singh, *J. Mater. Sci. Eng.*, 2 (2013) 10000121.
85. S. Chatain, C. Guéneau, D. Labroche, J. Rogez, and O. Dugne, *J. Phase Equilibria*, 24 (2003) 122.

86. P. Gordon and A.R. Kaufmann, *Trans. AIME*, 188 (1950) 182.
87. J. D. Grogan, *J. Inst. Met.*, 77 (1950) 571.
88. L. Leibowitz and R.A. Blomquist, *J. Nucl. Mater.*, 184 (1991) 47.
89. L. R. Chapman and C. E. Holcombe, Jr., *J. Nucl. Mater.*, 126 (1984) 323.
90. J. A. Straatmann and N.F. Neumann, *Mallinckrodt Chem. Reports*, MCW-1487, Weldon Spring, MO, (1964).
91. G. G. Michaud, *Can. Met. Quarterly*, 5 (1966) 355.
92. N. Swindells, *J. Nucl. Mater.*, 18 (1966) 261.
93. P. Gardie, G. Bordier, J. J. Poupeau and J. Le Ny, *J. Nucl. Mater.*, 189 (1992) 85.
94. O. Kubaschewski, *Proceedings of the Symposium on Thermodynamics of Nuclear Materials*, IAEA, Vienna, (1962) p. 219.
95. D. Labroche, J. Rogez, S. Chatain, and O. Dugne: 10th IUPAC Conference on High Temperature Materials Chemistry, Jülich, Germany, (2000) p. 123.
96. M. P. Antony, R. Babu, C.K. Mathews and U.V. Varada Raju, *J. Nucl. Mater.*, 233 (1995) 213.
97. M .P. Antony, R. Babu, C.K. Mathews, and U.V. Varada Raju, *J. Nucl. Mater.*, 228 (1996) 154.
98. H. Okamoto, *Phase Diagrams of Binary Alloys*, (1993) 129.
99. T. B. Massalski, *Binary Alloy Phase Diagrams*, 2nd ed., ASM International, Materials Park, OH, (1990).
100. M. Kanno, *J. Nucl. Mater.*, 51 (1974) 24.
101. H. W. Chiswik; *Metallurgy and Fuels*, *Progress in Nuclear Energy*, Series V. Vol 3 Pergamon, New York (1961).p. 23.
102. J. J. Park, *J. Res. Nat. Bur. Stand.*, 72A (1968) 11.
103. H. Okamoto., *ASM International, Alloy Phase Diagram Section*, Materials Park, Ohio, U.S.A., (1990).

104. H. H. Chiswik, A. E. Dwight, L. T. Lloyd, M. V. Nevitt and S. T. Zegler, Proc. 2nd Int. Conf. Peaceful Uses of Atomic Energy, Vol. 6 (U.N., Geneva, 1958) p. 394.
105. E. H. P. Cordfunke, R. P. Muis, G. Wubenga, Ramon Burriel, TO. Michael (Wing Kei), Hanaa Zainel and E. F. Westrum., J. Chem. Thermodyn., 17 (1985) 1035.
106. G. Wjbenga and E. H. P. Cordfunke, J. Chem. Thermodyn., 14 (1982) 409.

Chapter 2

Experimental Methodology

This chapter deals basically with the detailed description of different techniques that have been employed as principal and supplementary tools for the characterization of phase stability and phase transformation studies in uranium alloys. In the present study two different types of calorimeters namely differential scanning calorimeter (DSC) and inverse drop calorimeter have been extensively employed. As it is clear from **chapter 1**, an accurate knowledge base of thermodynamic quantities such as transformation temperatures, enthalpy of transformation, heat capacity, Gibbs energy *etc.*, as a function of temperature as well composition are very much useful for assessing thermokinetic stability or kinetic phase diagrams. Once such data are known, it becomes quite easy to predict the stability of a phase at a desired temperature and composition under chosen thermal history. In addition if some data on transformation temperatures are known as a function of heating or cooling rate, then information on kinetics of phase transformation can also be obtained by employing appropriate models of transformation kinetics. In recent past, the computational techniques which are either based on ab-initio methods (density functional theory) and or empirical methods such as solution models have matured to a level that it becomes possible to predict phase stability of a system to a reasonable degree of confidence. But they still need some experimental information to validate any theoretical assessment. Hence one need to generate reliable experimental data in the first hand and these data can only be obtained by carrying out careful and time consuming experiments.

In the present study DSC has been employed to obtain data on phase transformation temperatures and enthalpy of transformation as a function of several heating and cooling rates. Further, using drop calorimetry the enthalpy increment or relative enthalpy ($H_T - H_{298.15}$) as a function of temperature (T) is measured and these data

are modelled suitably to obtain consistent estimates of thermal quantities like heat capacity, thermal expansivity *etc.*

In addition, other supplementary techniques are also employed for the microstructural characterization such as optical microscopy, scanning electron microscopy (SEM), microhardness measurements and X-ray diffraction (XRD). This chapter is organized in the following way.

The chapter begins with the short description about the melting of alloys used in the present study, compositional details and the different heat treatments given to these alloys before actual experiment. Following this, a concise description of dynamic (DSC) and static (inverse drop) calorimetry is provided. The instrument details, experimental and calibration procedures are discussed. Finally a brief description about the supplementary techniques such as microscopy, hardness measurement, SEM and XRD are provided.

2.1. Details about alloy synthesis, composition and heat treatment

In the present study three types of alloys based on uranium are chosen. They are: U-Zr, U-Fe and URh₃. The melting, compositional analysis and annealing treatment for the three alloys are presented below.

The U-Zr alloys used in this study have been made in Bhabha Atomic Research Centre (BARC), Mumbai, India. Reactor grade natural uranium and U-2, 5, 10wt.% Zr alloys used in this study have been prepared using vacuum induction melting (10^{-6} torr) followed by injection casting route [1-4]. The starting materials, uranium and zirconium used for melting have purity of the order of 99.90% and 99.95%, respectively. For minimizing the carbon pickup, the graphite crucible has been coated with yttria slurry prepared in alcoholic media. The scrap of the melt has been heated up to 1450°C under vacuum [3-4]. After ensuring the complete melting, quartz molds opened at one end have

been immersed in the melt. In order to push the molten liquid in the mold, the furnace chamber has been pressurized with inert gas. Finally the pencil shaped alloys removed from the quartz molds using de-molding set up. Typical diameter of the alloy slugs were about 5 & 10 mm.

Material /Element	Uranium	U-2wt.%Zr	U-5wt.%Zr	U-10wt.%Zr
Zr	-	1.98	5.03	9.99
Al	349	410	235	331
Cr	14.7	10.5	9.8	12.7
Fe	73.5	77	50.2	89.1
Mg	11	14	8.6	16.3
Mn	9.3	14.5	8.4	21.3
Ni	32	21.5	18.5	225.
Co	0.2	0.7	0.3	0.4
Cd	0.04	0.01	0.06	0.03
Ce	2.2	8.7	7.3	3.6
Sm	0.4	0.1	0.6	0.4
Gd	0.04	0.01	0.07	0.03
N	41	53	67	76
O	552	532	422	532
Si	615	450	322	543
U	Bal.	Bal.	Bal.	Bal.

The compositional analysis of all the four alloys has been carried out by the Inductively Coupled Plasma-Atomic Emission Spectroscopic (ICP-AES) analysis. Results of the chemical analysis are presented in **table 2.1**. For carrying out the calorimetric measurements on all the four alloy systems, small smooth-cut pieces of regular geometry have been annealed at 1273 K /1000°C for 10 h in high pure Ar atmosphere, followed by slow furnace cooling.

In case of Fe-U system, a series of $Fe_{100-x}U_x$ alloys with U content x varying from 0 to 95 mass % at an interval of roughly 5 mass % including the nearly stoichiometric ordered intermetallic compound UFe_2 , have been prepared in an electronically controlled

graphite resistance heating furnace under flowing high pure argon gas (50 mL min^{-1}) atmosphere maintained at 1300 mill bar pressure [5-6]. Recrystallized alumina crucibles are used for melting the alloys. The starting materials used are reactor grade uranium containing small amounts of carbon, oxygen and silicon as major impurities (**table 2.2**) and pure iron with less than 80 mass ppm of combined impurities (Aldrich Chemicals, U K). Before melting, the oxidized layer from the surface of both uranium and iron pieces have been removed by mild grinding. For ensuring compositional homogeneity, each alloy piece has been re-melted three times, after which they are slowly cooled to room temperature.

Table 2.2														
Chemical composition of reactor grade uranium and pure iron used in synthesis of Fe-U alloys														
Reactor grade Uranium (composition in mass ppm)														
Al	Cr	Fe	Mg	Ni	Co	Cd	Ce	S _m	C	N	O	Si	M _n	U
349	14.7	73.5	11	32	0.2	0.0 4	2. 2	0. 4	31 6	41	55 2	61 5	9.3	Bal.
Pure Fe (composition in mass ppm)														
Si	Cu	Ti	C	Fe										
13	1	0.6	14	Bal.										

After final melting, each alloy has been weighed to assess the weight loss if any, accrued during melting. It has been observed that the general weight loss is of the order 0.5 mass % for all these alloys. The as prepared alloys have been homogenized at 1273 K (1000°C) for about 10 hours in flowing pure Ar-atmosphere to ensure good compositional homogeneity.

In the case of U-Rh alloy only the ordered intermetallic compound URh_3 has been prepared by arc-melting under vacuum (10^{-6} torr) from the appropriately weighed pieces

of high pure Rh (99.99 mass percent purity, Aldrich chemicals, U.K) and reactor grade uranium [4,7]. The alloy buttons weighing about 2–3 g have been re-melted four to five times for ensuring complete melting and a fair degree of initial compositional homogeneity. The broken small pieces of as melted buttons have subsequently been given an annealing treatment at 1273 K for about 10 h in high pure flowing argon atmosphere (50 ml min^{-1}), before the commencement of actual experiments.

2.2. Major experimental techniques: Calorimetry

2.2.1. Principle of calorimeter

A calorimeter measures the relative change in heat energy, however heat cannot be measured directly, but its action, for example a change in temperature can be monitored accurately using suitable thermometry. The measured temperature (change in effect) can be converted in to heat after suitable calibration [8-10]. The general calibration equation for converting the temperature difference to its effective caloric value is given below

$$Q(T) = C_{\text{cal}} \times \Delta T \quad (2.1)$$

$Q(T)$ is the heat content at a given temperature T , C_{cal} calorimeter constant that has to be determined specifically for each calorimeter by using suitable standards. Temperature can be measured using a variety of thermometers such as thermocouples, platinum resistance thermometer, gas thermometer or Hg thermometer depending on the temperature range. Further the determination of the calorimeter constant should be done under comparable conditions as measurements itself. Calibration constant is determined by using a suitable reference material whose heat capacity is known (e.g. Ag, Sn, Cu, Zn, Hg, Au and Al_2O_3) along with the sample.

2.2.2. Classification of calorimeters

In a broad way calorimeters can be classified in to two categories. They are: (i) reaction

thermochemical calorimeter, wherein the change in the chemical state of the sample is being monitored and (ii) non-reaction calorimeters where change in the physical state of the sample such as temperature, phase transformation etc are monitored. Measurement of the enthalpy of phase transformation, enthalpy increment, heat capacity data comes under non-reaction calorimetry, whereas determination of partial or integral enthalpy of mixing, enthalpy of formation of the compounds fall under reaction calorimetry methods.

According to Kubaschewski and Alcock [8-10] calorimeters can be classified in to three categories based on three variables that are namely T_C -temperature of calorimeter, T_S -temperature of the surrounding and Q -heat produced per unit time.

- *Isothermal Calorimeter*: $T_S = T_C = \text{constant}$ and Q varies, example is Bunsen Ice calorimeter.
- *Adiabatic Calorimeter*: $T_S = T_C \neq \text{constant}$, T_S and T_C varies with Q , example is Adiabatic scanning calorimeter.
- *Isoperibol Calorimeter*: $T_S = \text{constant}$, T_C is measured before, during and after the reaction (sometimes referred as isothermal calorimeter but not correct.), example is Drop Calorimeter.

According to Hemminger and Hohne [8] calorimeters can be also classified based on the working principles, mode of operation and construction.

Based on the working principle there are three type of calorimeters

- *Heat Compensation Calorimeters*: In this type of calorimeters any change in the sample is compensated by an external source of energy that could be either by phase transformation or by electrical heating/cooling or by chemical reaction. Examples are the ice calorimeter where compensation is done by latent heat of ice melting, power compensated DSC etc.

Heat Accumulating Calorimeters: In this type of calorimeter the effect of heat to be

measured is not compensated unlike power compensating type; but it causes a change in the temperature of calorimeter and sample and this change in temperature is measured. This change in temperature is basically proportional to the amount of heat exchanged between sample and calorimeter. An example is the drop calorimeter.

➤ *Heat Exchanging Calorimeters:* In this type, one measures the heat flow rate between sample and surroundings due to thermal gradient which has to reach a steady state, in ideal conditions. An example would be the heat flux type DSC, which is employed in this study.

Further based on the mode of operation and construction calorimeters can be classified as follows.

Static Mode – (i) Isothermal (ii) Isoperibol (iii) Adiabatic

Dynamic Mode – (i) Scanning of surrounding; example is heat flux DSC (ii) Isoperibol scanning; example is power compensating DSC (iii) Adiabatic scanning; example is adiabatic scanning calorimeter

Construction principle – (i) Single calorimeter; an example is ice calorimeter (ii) Twin calorimeter; an example is DSC

For the sake of brevity it is not possible to discuss in detail all types of calorimeters. In the present thesis, the description is confined to heat flux differential scanning calorimeter and inverse drop calorimeter, as these are the techniques employed.

2.3. Differential scanning calorimetry (DSC)

2.3.1. General principle

A differential scanning calorimetry is a twin type calorimeter and work on the principle of differential thermal analysis. Differential scanning calorimetry (DSC) is an experimental technique for measuring the energy necessary to establish a nearly-zero temperature difference between a test substance S (and its reaction products) and an inert

reference material R, while the two samples are subjected to an identical (heating, cooling or constant) temperature programme. Two types of DSC systems are commonly in use and these are power compensating type and heat flux type.

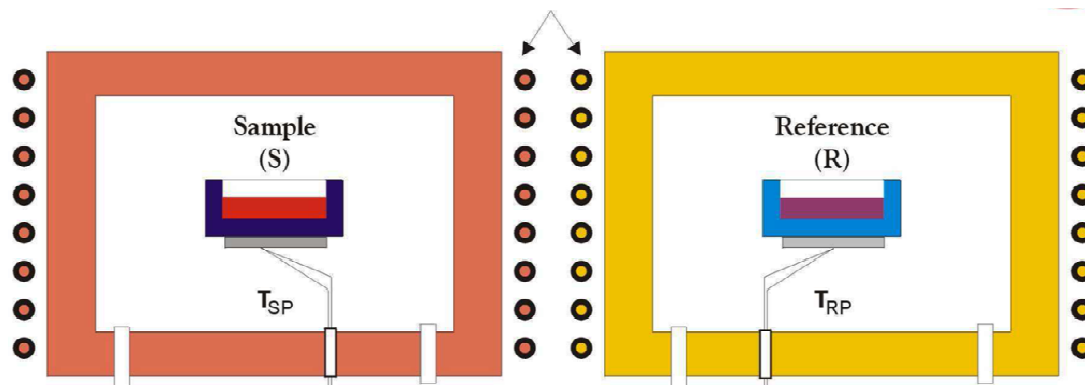


Fig. 2.1. Schematic representation of power compensated DSC

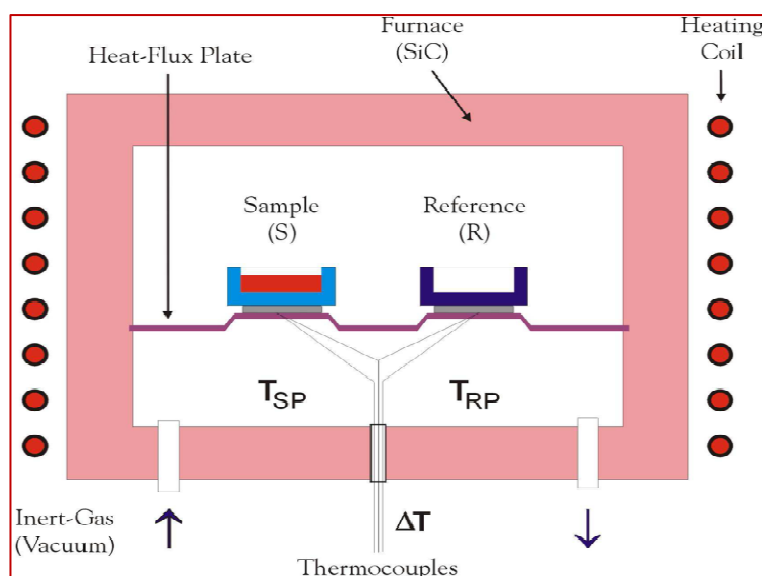


Fig. 2.2. Schematic representation of heat flux DSC

2.3.2 Power compensating DSC

In the power compensating DSC any change in the sample or reference temperature is being compensated by means of an electric power from external source to maintain the temperature difference between sample and reference material either zero or constant. In addition, in power compensated DSC both sample and reference materials are heated by

two separate identical furnaces at equal heating rate. The schematic diagram of power compensated DSC is given in **figure 2.1**. The temperature difference between the sample (T_S) and reference (T_R) is maintained to zero by varying the power input to the two furnaces. Since the compensation is being done by a known electrical power from an

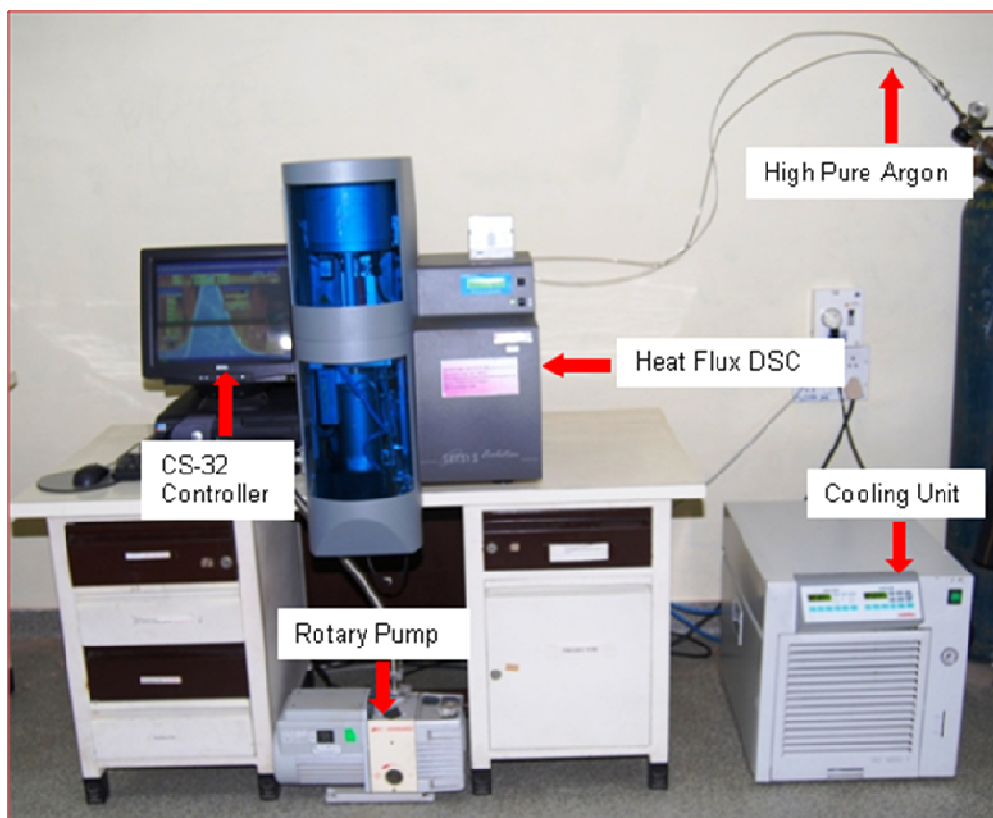


Fig. 2.3. Experimental setup of heat flux DSC used in the present study

external source, the output of this type DSC is in mW. The compensating heating power is linearly proportional to the temperature difference ΔT between sample and reference. The use of this type DSC at high temperatures above 700°C is limited because the heat loss due to radiation is more prominent and cannot be exactly compensated.

2.3.3. Heat flux DSC

In this type of DSC the test specimen S and reference material R (usually an empty sample pan + lid) are enclosed in the same furnace together with a metallic block of high thermal conductivity that ensures a good heat-flow path between S and R. The schematic

diagram of heat flux DSC is portrayed in **figure 2.2**. Further, the enthalpy or heat capacity changes in the specimen S leads to a temperature difference between S and R pans. This result in a certain heat-flow between S and R, however small compared to those in DTA, because of the good thermal contact between S and R. The temperature difference ΔT between S and R is recorded and this is related to the differential heat flux. The heat-flux DSC system is thus a carefully modified DTA system. The important difference is the good heat-flow path between the specimen and reference crucibles. Because of the specific design like DTA, the radiation loss at high temperature is same for both sample and reference materials and hence the outgoing heat flow does not get affected much. The accuracy of results obtained with this type DSC is slightly inferior at high temperature, notwithstanding the possibility of ensuring adequate experimental precaution [11]. The DSC instrument used in the present experiment is a heat-flux type, namely Setaram[®] Setsys 1600, which is portrayed in **figure 2.3** [12]. The detail of this equipment is given in next section.

2.4 Basic components of Setaram Setsys 1600 DSC

The Setaram[®] Setsys 1600 heat flux differential scanning calorimeter is comprises of basically a furnace, measurement head, mass flow controller, gas circuits and the controllers that are housed on a single mount. A separate chiller (Julabo[®] FC 1600 T) for water circulation is connected to cool the instrument furnace. The control of equipment is made through the proprietary software that is interfaced with the equipment. The essential components of this DSC are as follows [12]:

2.4.1. High temperature furnace

In **figure 2.4 (a)** cross sectional view of internal chamber of Setaram[®] Setsys 1600 flux DSC is presented. The furnace is of cylindrical shape and its heating element is made up of a graphite element. The heating principle employed in this type of furnace is resistance

heating. Being graphite used as heating element, an inert gas atmosphere (high pure argon) is always maintained at the furnace chamber to avoid carbon evaporation at higher temperature. A thermocouple of B-type (Pt-Rh with Pt-6% and Rh- 30%) is placed in the analysis chamber and furnace chamber for respective temperature measurement.

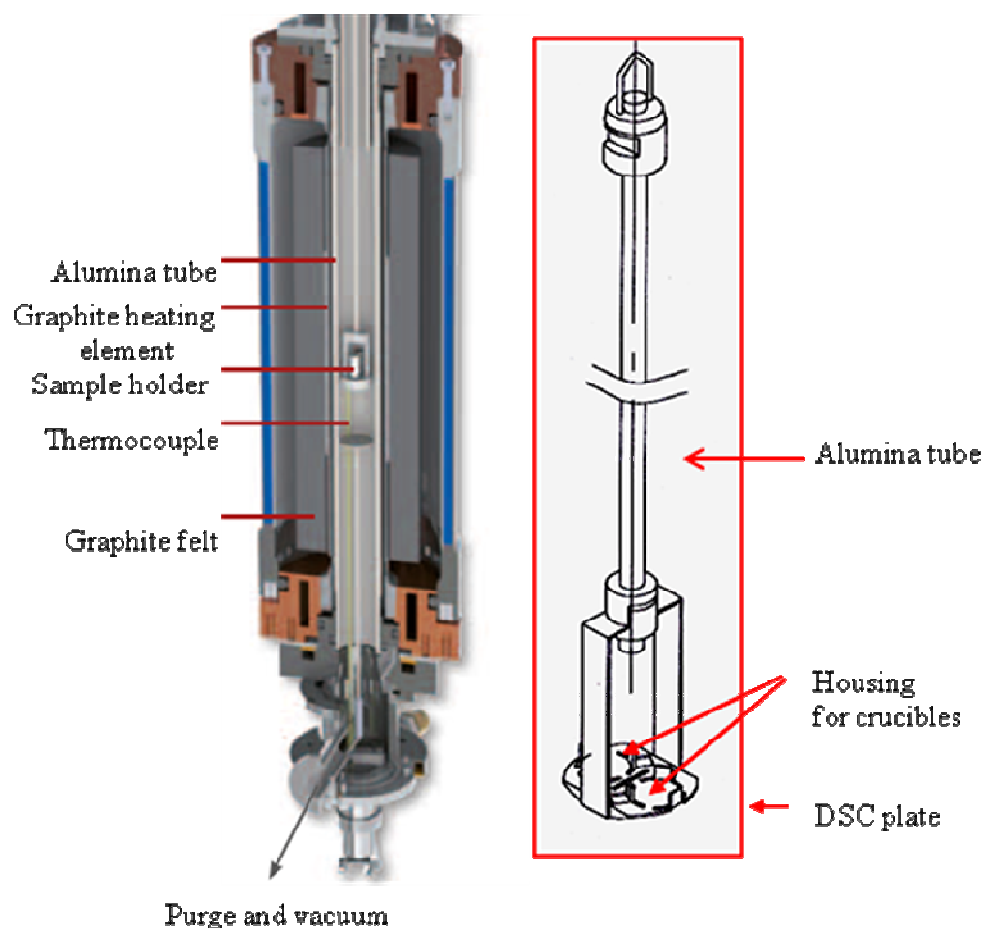


Fig. 2.4 (a). Setaram high temperature DSC furnace, **(b).** Heat flux DSC plate-rod

2.4.2. Measurement head – DSC probe

The DSC measurement head used in the present DSC is of hanging type and it is displayed in **figure 2.4 (b)**. The DSC probe or measurement head consists of the DSC plate, sample and reference crucibles, thermocouples and guiding alumina tube. The sample and reference crucibles are made of recrystallized alumina having nearly identical mass of about 240–250 mg and a volume of about 100 μL on either side. Both reference

and sample housing base are connected to each other via a metallic plate consists of an embedded thin wire of highly conductive platinum that serves the purpose of heat resistor between sample and the reference. Through this conducting platinum wire any kind of gain or loss of heat that happens either on sample or reference side is being immediately to maintain constant temperature difference between both reference and sample pan. The differential thermocouple of B-type (Pt/Rh 6%/Pt/Rh 30%) is positioned exactly below the DSC plate and the gap between them is less than 2 mm [12]. In addition, the central section of the DSC plate sensor contains a thermocouple of B-type that measures the sample temperature directly. The whole set up comprising DSC plate, sample, reference crucibles, thermocouples and guiding alumina tube together make up the heat flux DSC probe which is hung from the top balancing plate. The DSC probe is always kept within the uniform temperature zone of the water cooled graphite furnace. During the experiment, one of these crucibles is kept empty (reference crucible), while the sample is placed on the other crucible during the experiment.

2.4.3. Vacuum pump, gas circuit, chill water cooling circuit

After loading the sample both analysis and furnace chambers are purged with flowing argon gas and subsequently evacuated to a vacuum level of 10^{-3} torr using Edwards[®] rotary pump to avoid any contamination. Thereafter, both the chambers are filled with high pure argon gas. The pressure in the analysis chamber is maintained between 1.2 to 1.3 bars. There are separate ports to carry protective gas and carrier gas. During the experiment the flow rate for carrier gas is maintained at 50 ml/min. For controlled heating and cooling an external air cooled water circulator of model Julabo FC 1600 from Julabo[®] is used. The gas filling, vacuum and the water supply operations are controlled through an electronic valve command with the help of CS-32 interface.

2.4.4. Mass flow controller (MFC)

An automatic mass flow controller is attached along with DSC for controlling the gas flow inside the analysis and furnace chambers. The functioning of MFC depends on various parameters such as purity of the gas, humidity of the external atmosphere, temperature maintained in the atmosphere etc. MFC can maintain the gas flow in the range of 0-200 ml/min. The improper functioning of MFC can disturb the DSC output.

2.5. Experimental procedure

The samples for DSC studies are obtained in the form of small cubes of about 2.5 *mm* in length and of mass that varied generally between 80–100 ± 0.01 *mg*. The specimen is housed in a well cleaned 100 μ L cylindrical recrystallized alumina crucible inside the DSC cradle, which is alternately evacuated and purged with high purity argon (Iolar grade I; Oxygen \approx 0, moisture < 2ppm, nitrogen < 2ppm) a few times, before the commencement of an experimental run. A steady flow of argon of about 50 *ml* per minute is maintained throughout the experiment. Although argon being a poor conductor of heat, as compared to say, helium, the constant and steady trickle of argon served to minimize the thermal turbulence throughout the experiment and this is necessary in ensuring wiggle free base line runs, as argon in this case is a sink for heat. Since the mass of our samples including pure metal references are in milligram range, it is believed that the use of argon in place of a better heat conductor like helium will not seriously skew the caloric calibration of the signal [13]. An argon pressure of about 1300 *mbar* is maintained in the graphite furnace chamber.

It is found in case of pure iron, which is used as a secondary calibrant that for slow heating and cooling rate scans (1 K min⁻¹), there will not be any appreciable temperature gradient across the section thickness of the DSC sample. This is judged by the sharpness of the transformation peak and also from the absence of multiple serrations

arising from discrete melting events. The issues involved in DSC calibration is discussed by Richardson [13] and in deference to brevity, these aspects are not dealt with in detail here. A typical isochronal DSC run employed in the present study consists of following heating and cooling schedules:

To begin with, the furnace temperature is gradually raised to 473 K (200°C) and is allowed to stabilize at this temperature for about 15 minutes. This is required for the attainment of thermal equilibrium of the system before starting any measurement. Such preconditioning also facilitates the attainment of a smooth non-wavy baseline. This step is followed by actual heating ramps and holding isotherms that are characteristic of present DSC experiments. In an actual experimental run, the sample is heated at a pre determined rate from 473 K (200°C) to a desired temperature in the range of 1273-1773 K (1000-1500°C) depending on the alloy used and is equilibrated at this temperature for about 15 minutes, and then cooled at the same scan rate to 473 K, again kept at this temperature for a period of about 15 minutes, before cooling to room temperature. The scanning rate employed is varied between 0.1 to 100 K min⁻¹ in order to study the transformation kinetics. The very low scan rate of 0.1 K min⁻¹ is employed for special experiments only (see chapter # 5). Fresh samples are employed for each individual run and a few repeat runs are also performed for select heating rates (10 and 100 K min⁻¹) in order to assess the reproducibility at either end of the scan rate spectrum. In general DSC is employed for following studies:

- (i) Accurate determination of solidus, liquidus and other solid phase transformation temperatures
- (ii) Determination of enthalpy of transformation
- (iii) Studying of phase transformation kinetics
- (iv) Measurement of heat capacity

Before giving details about measurement of any quantities mentioned above, a brief description about calibration of DSC is presented in the following section.

2.5.1. Determination of phase transformation temperatures

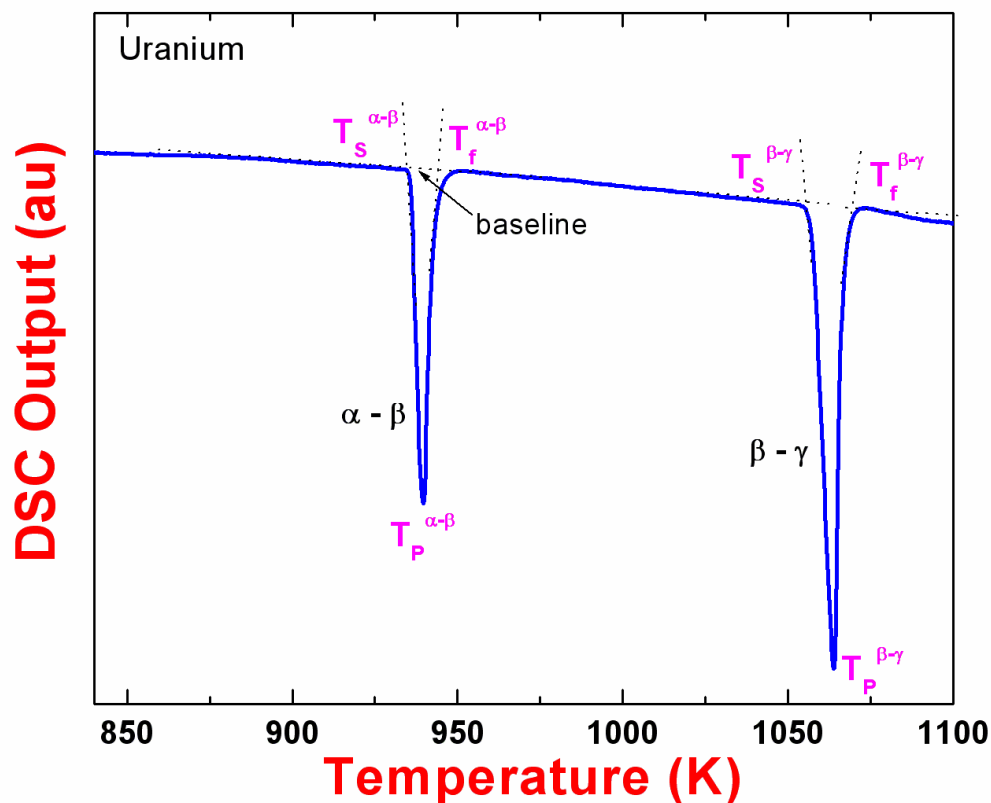


Fig. 2.5. DSC thermogram obtained during heating cycle for uranium

A typical DSC thermogram obtained during heating cycle for uranium is shown in **figure 2.5**. The difference in heat flow between the sample and reference is plotted along y-axis and the temperature or time along x-axis. When the sample experiences no phase change, the basic DSC signal is a smooth baseline without any characteristic features; in the ideal case the heat flow is parallel to the x-axis, a straight line should be obtained [8-9]. This can be witnessed even in the case of uranium where the baseline is nearly parallel to X-axis. However, in a heat flux DSC the heat flux compensation between sample and reference is far from being exact, especially at high temperatures; due to the non identical thermal character of sample as well the crucible pans. A mild

deviation from horizontal base line is what often obtained, which constitutes the base response of the equipment + sample under no phase change conditions. However, when there occurs a phase transformation in the sample, the differential heat flow due to the latent heat of transformation which is transported across the heat flux resistor results in the production of a distinct thermal arrest, often evident as a peak in the otherwise featureless baseline plot. This is illustrated in **figure 2.5**. The phase transformation onset (start) and finish temperatures are determined by drawing a tangent to the baseline from the point of maximum inclination (inflection point of the peak); - their intersection is taken as the transformation temperature [8-9]. This is illustrated in **figure 2.5**. Throughout this study, T_s is taken to represent the start of the phase transformation, T_p the peak and T_f the finish of the phase transformation. In **figure 2.5** determination of phase transformation temperature for two phase changes i.e. $\alpha \rightarrow \beta$ and $\beta \rightarrow \gamma$ respectively occur in the case of pure uranium is demonstrated.

2.5.2. Determination of transformation enthalpy

The enthalpy of transformation of a phase change is found to be proportional to measured area of the peak observed during phase change. Thus,

$$\Delta H_{tr} = k(T) \times Peak Area \quad (2.2)$$

where, ΔH_{tr} is the enthalpy change accompanying phase transformation, $k(T)$ is the temperature dependent calibration constant. Peak area is the total area under the phase transformation peak and it can be readily obtained by integrating the area by using the software provided by SETARAM with proper baseline construction [12]. The determination of calibration constant is described in the next section.

2.5.3. Calibration of DSC

Calibration is at the heart of quantitative measurements by differential scanning calorimetry [11, 14]. There is an inherent potential for inaccuracy of measurements in all

DSC analysis. Therefore in order to ensure optimum accuracy and repeatability of any data calibration is needed. There are basically two types of calibration done before commencing any experiment; (i) temperature calibration (ii) Enthalpy calibration.

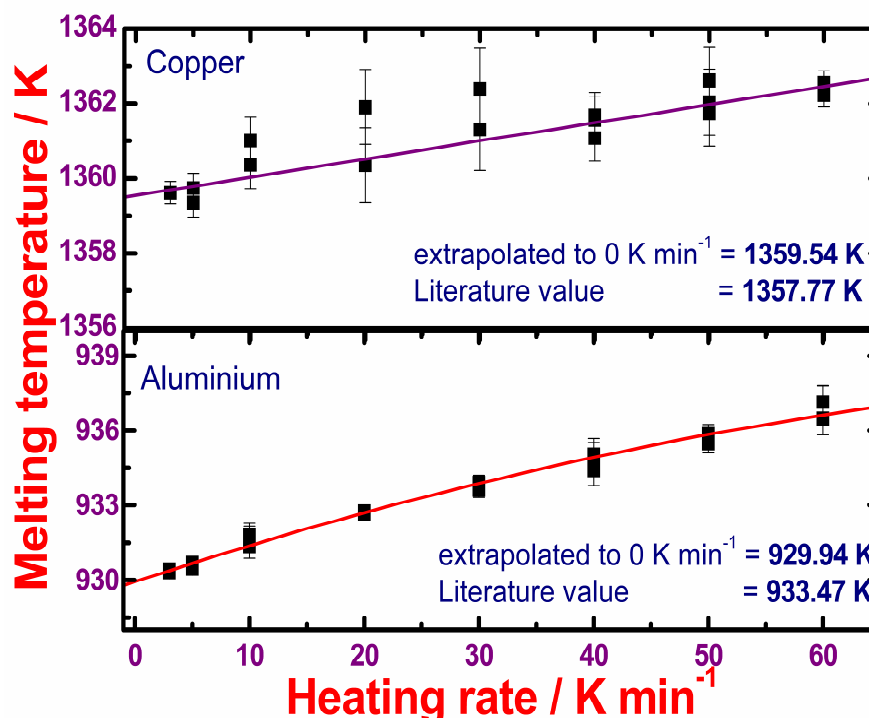


Fig. 2.6. Temperature calibrations with Al and Cu

2.5.4. Temperature calibration

The temperature calibration is carried out by measuring the onset temperature of melting of given standards e.g. aluminium, zinc, tin, copper, silver, gold, and iron standards depending on the temperature range [11]. The start temperature (T_s) of the melting has been determined, based on the procedure explained in figure 2.5. These start temperatures are determined for various heating rates such as 1, 3, 5, 7, 10, 15, 20, 30 K min⁻¹ etc., and is extrapolated to hypothetical 0 K min⁻¹ limit which represents the equilibrium onset temperature [15, 16]. These values are compared with the literature values in order to estimate the correction to be employed for obtaining the true transformation temperature. The temperature calibration procedure for aluminum and

copper is illustrated in **figure 2.6**. The extrapolated melting temperature of Cu and Al is compared with literature values and the deviation is found to be within ± 4 K. The temperature accuracy in case of low heating rate experiments ($1\text{--}30\text{ K min}^{-1}$) is found to be ± 2 K for samples of mass up to 50–100 mg; while, it is ± 4 K for high heating rates (99 K min^{-1}). The temperature calibration of DSC for the cooling cycle is comparatively difficult because of varying degree of undercooling associated with the solidification. Hence, the temperature calibration is only performed for heating cycle of DSC experiments.

2.5.5. Peak area calibration

The calibration constant $k(T)$ is obtained by measuring the peak area for either melting or fusion reactions or structural phase change of primary or secondary standards like pure aluminium, zinc, tin, copper and iron of known enthalpy [16-19]. The sensitivity of calibration constant $k(T)$ is influenced by many factors like heating or cooling rate, the hydrodynamic nature of the ambience and the nature of calibrant which introduces additional error in the measurement. Most preferably, the melting or solidification reactions of pure metals are employed for calibrating the heat effects of unknown transformation events. In case of metals which solidify with large undercooling, the actually measured enthalpy will exhibit a deviation from the literature value which pertains to equilibrium solidification. It is for this reason the calibration constants are quite reliably estimated for low heating rates. In addition, it is also desirable to employ a calibrant that has similar thermophysical characteristics to the alloy under investigation so that spurious effects arising from the disparate conduction characteristics are generally avoided. It is even preferable to employ a known member derived from the same family as that of the alloy under investigation as a secondary calibrant. For example in the present study pure uranium and Fe has been used as calibrants for enthalpy

calibration for determining the enthalpy of transformation in the case of U-Zr and Fe-U alloys respectively. Another source of error in the estimation of the enthalpy arises from the uncertainty associated with the measured peak area, in cases where there is difficulty in unambiguously fixing the transformation start and finish temperatures. In such cases, the measured area might not correspond to 100% of phase change or else, it could be an overestimate as well by the selection of wrong baseline. Hence, in the present study this pertinent source of error has been minimized by going in for accurate baseline calibration by subtracting a nil sample empty run signal from the actual run recorded with the sample in position. Also, identical pair of crucibles, gas flow rate and scanning rate conditions etc., are employed to minimize the effect of spurious factors from affecting the accuracy. The accuracy of the reported enthalpy of transformation data is $\pm 5\%$.

2.6. Inverse drop calorimeter

In the present study, for measuring the enthalpy increment $\Delta^{\circ}H(T)=(H_T-H_{298.15})$ and heat capacity as a function of temperature, high resolution *Setaram*® multi HTC inverse drop calorimeter has been used [20]. The general principle of drop calorimeter is discussed as follow.

This calorimeter is isoperibol type and it involves the isothermal measurement of heat content of material under quasi adiabatic condition [20]. Conventionally the enthalpy content is used to be measured by heating a sample to the desired temperature and after equilibration at this temperature for some fixed time the sample is dropped in to a well-equilibrated calorimeter block or bed that is maintained at fixed reference temperature. This type of calorimeter is called as direct drop calorimeter. In this type of calorimeter the differential rise in the temperature of the calorimeter with respect to the sample is being measured. The temperature difference between calorimeter and sample causes the heat transfer under externally insulated conditions and this can be converted

into enthalpy with proper calibration. The measured rise in the temperature can be correlated to heat flow (Q_S) the following standard relation.

$$Q_S = m_S \times C_P^S \times \Delta T. \quad (2.3)$$

Where m_S the mass and C_P^S are the heat capacity of the sample. The calibration is usually done by dropping the reference or calibrating sample of known mass and known enthalpy under identical experimental conditions and for reference.

$$Q^R = m_R \times C_P^R \times \Delta T. \quad (2.4)$$

Where m_R the mass and C_P^R are the heat capacity of reference material. With the help of *Eqs.*(2.3 & 2.4) heat flow for unknown sample can be obtained. Further the output of the drop calorimetry experiment, heat flow (Q) is related to enthalpy by the following equation.

$$Q = m \times C(T) \times (H_T - H_{298.15}) \quad (2.5)$$

where $C(T)$ is the calibration constant which is determined by calibration with a reference material like α - Al_2O_3 . By determining $Q(T)$ as a function of temperature T , the enthalpy of the sample at various temperatures can be obtained. In an actual schedule of drop calorimetry measurements, temperature of sample is varied in discrete closely spaced steps and the experiments are repeated afresh at each new temperature with new sample. Despite the possibility that the successive drops can be performed at fairly closely spaced temperature intervals; the drop calorimetry offers only a set of closely spaced discrete data points rather continuous. *The enthalpy increment ($H_T - H_{298.15}$) as a function of temperature is nonlinear in nature and it suffers a distinct change at phase transformation point.* A schematic variation of enthalpy increment as function of temperature is shown in **figure 2.7**.

In the present study inverse drop calorimeter has been employed and measurements are made in the inverse manner, namely the sample is dropped onto the

hot calorimeter bed from the ambient temperature. The principal advantage of this inverse drop mode over the normal one is that the heat losses that are accrued in the normal mode of dropping the hot sample are minimized by resorting to dropping of cold samples. In accordance with this change, the instrument is also tailored in its design in the appropriate manner [21]. Inverse drop calorimetry has some advantages; namely it can easily adopt small sample size, avoid any metastable phase retention from high temperature excursion and ability to study many different types of chemical reactions etc

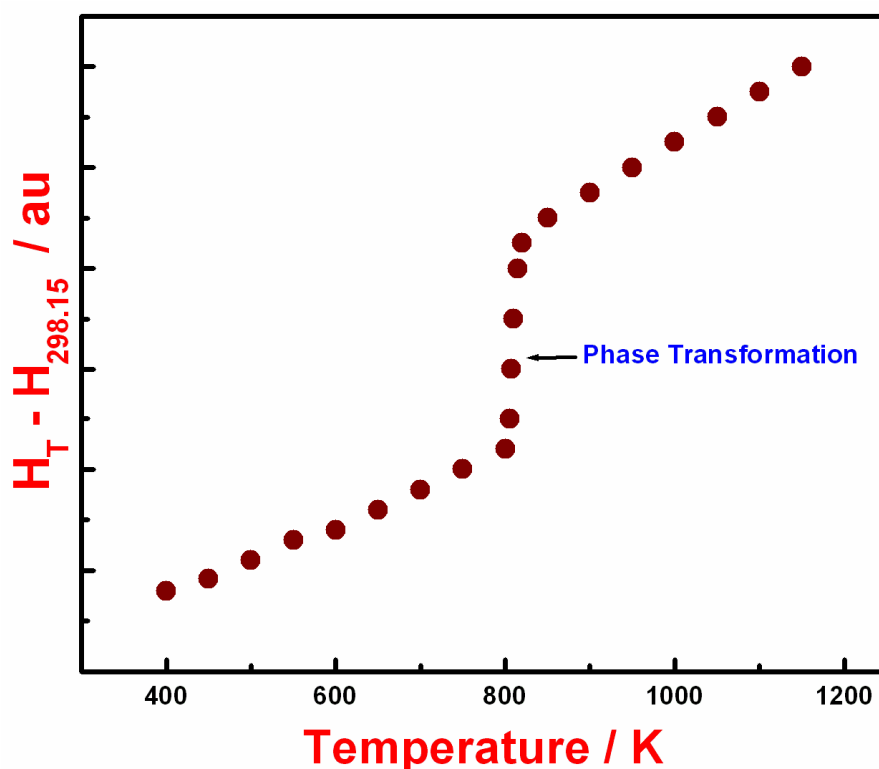


Fig 2.7. Schematic of enthalpy increment variation with temperature

[22]. The experimental set up of *Setaram*[®] multi HTC 96 inverse drop calorimeter used in the present study is shown **in figure 2.8**. The essentials parts of drop calorimeter are described below very briefly [21].

2.6.1. High temperature furnace

The high temperature furnace is suspended from the calorimeter cabinet's top plate. The

heating element of the furnace is made of graphite tube which surrounds the experimental chamber of the calorimeter and is heated by resistance heating element up to a maximum temperature of 1773 K. A sealed alumina tube crosses the furnace through the centre of the heating element and insulates the experimental chamber from the furnace atmosphere. The line diagram of the high temperature furnace is shown in **figure 2.9**.



Fig. 2.8. The experimental setup of inverse drop calorimeter used in the present study

2.6.2. Measurement head – drop Transducer

The measurement head itself is an integrated structure made of a cylindrical re-crystallized alumina tube in which two grooves are cut at its bottom to introduce the sample crucible. The crucible has a working volume of 62.5 mm^3 with dimensions 16.20 mm in diameter and 44.50 mm in height. The measuring crucible's temperature is monitored by a thermopile made up of 28 B-type thermocouples distributed over the bottom and all over the side surface of the crucibles and it can be seen in **figure 2.9** [21]. In addition, another dummy reference crucible having an identical thermopile

arrangement is kept underneath the sample crucible. This vertically aligned arrangement of both the sample and reference crucible is placed in the uniform temperature zone of the graphite furnace. Measurement of the sample and furnace temperatures is undertaken by two thermocouples of B type (PtRh-6% / PtRh-20%) [21].

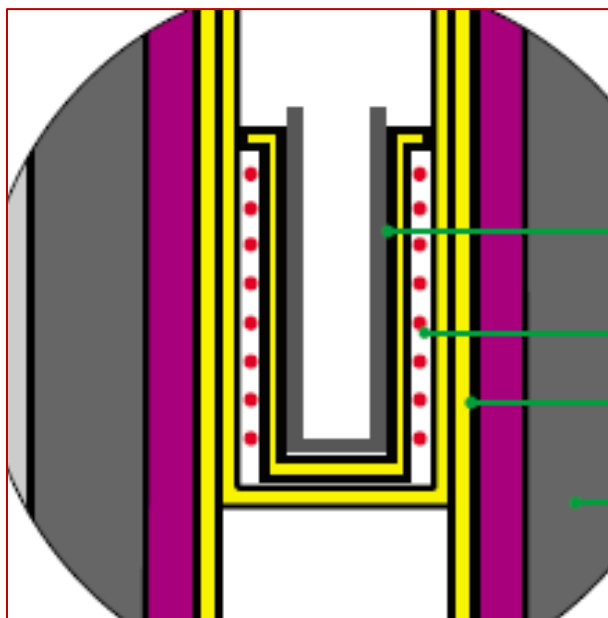


Fig. 2.9. Schematic representation of inverse drop calorimeter

2.6.3. Multi-sample introducer and the drop tube

The multi sample introducer is equipped at the top portion of the experimental chamber and provides 23 slots to load samples in to it. The samples are being dropped manually from this introducer. Normally four to six samples are loaded for each measurement. For each sample, a reference sample is also loaded in to the adjacent slot. The sample from introducer are dropped to the alumina bed via guiding tube made of alumina known as drop tube.

2.6.4. Gas, vacuum, chill-water circuit and controller

The equipment contains two separate gas circuits, one for the furnace and another for the analysis chamber to maintain the required inert gas atmosphere. An external

rotary vacuum pump (EDWARDS®) supplied by *Setaram* is used for evacuating both the experimental and furnace chambers before starting the experiment. An external chill water supply with controlled flow (Julabo FC 1600 T) is provided for the furnace cooling. The heating schedule programming, the data acquisition and storage are performed through the CS 32 controller interfaced with the personal computer. In the following section, the procedure for performing inverse drop calorimetry experiment is discussed.

2.6.5. *Experimental procedure*

The samples for drop calorimetry measurements were loaded in to the specimen slots of the multi sample introducer of *Setaram* multi HTC 96 inverse drop calorimeter. The standard or reference α -Al₂O₃ samples, supplied by *Setaram* drop were also loaded adjacent to the sample used for the experiment. The sample crucible was filled with high pure alumina powder to 3/4th of its capacity and loaded in to the measurement head. After loading the samples and placing the working crucible in its position, both furnace and experimental chambers were evacuated using rotary pump. This was followed by purging both the experimental chamber and furnace with high purity argon gas (Iolar grade II) for few times and continuing with further evacuation. Once the evacuation process was completed both the chambers were allowed to fill with argon gas until the gas pressure level reaches one atmosphere pressure. An inert atmosphere was maintained throughout the experiment in order to prevent the evaporation of carbon from the graphite furnace at high temperature and also to avoid the oxidation of sample. The chill water supply was switched on before the furnace is started to heat. The furnace was gradually heated from 298.15 K to a desired temperature at the rate of 10 K min⁻¹. The surrounding graphite furnace heats the alumina bed. Once the pre-set value of the alumina bed temperature was reached within the accuracy of ± 0.1 K, the samples were dropped from the

respective slot to the hot alumina bed through drop tube. The heat absorbed by the sample upon its drop from the ambient temperature into the hot alumina bed can be quantified by monitoring the change in temperature as a function of time t . The

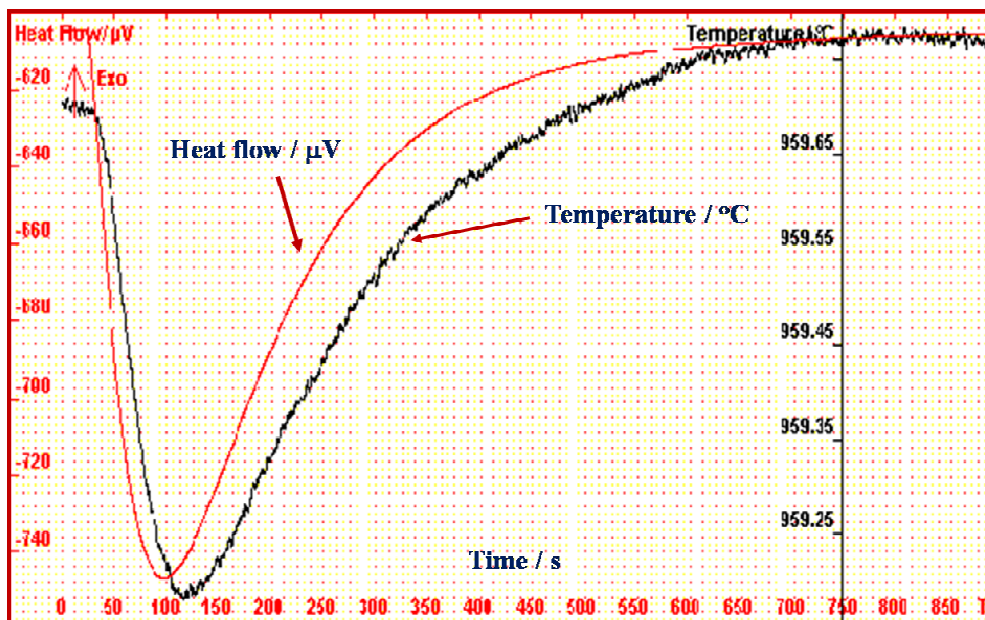


Fig. 2.10. Snapshot of the drop experiment output ΔV vs t

integrated output of the drop experiment ΔV vs time for one experimental run is shown in **figure 2.10**. The net heat flow Q from the hot alumina bed to the cold sample was measured as area under ΔV vs time t curve [23] and can be represented by the following expression.

$$Q = C(T) \times \Delta V \times \Delta t. \quad (2.6)$$

The dropping of the sample at a particular temperature was followed by the dropping of a standard or reference sample like $\alpha\text{-Al}_2\text{O}_3$ with known enthalpy and mass at the same temperature in order to determine the calibration constant $C(T)$. Both dropping of the sample and reference were performed under identical conditions. The whole experiment other than the dropping of sample was controlled through a computer that is connected to

the calorimeter by a proprietary interface module. The signals from the calorimeter are digitalized and transferred to a computer *via* a CS 232 series interface. The data acquisition period for each drop was maintained for about 20-25 minutes in the present study. Once the data acquisition was completed for one experiment, a gap of about 20 minutes was kept before dropping the next sample so that the alumina bed regain its thermal equilibrium. Fresh samples were used for each drop experiment. In the present study, the drop experiments for UFe₂ and URh₃ alloys were performed in the temperature range of 463-1500 K. After the experiment, the samples were weighed to check any loss or gain due to reaction or due to oxidation. The weight change was found to be less than 1 mg. The isothermal drop experiment is performed at successively higher temperatures with approximate temperature step of 25 K

2.6.6. Temperature and heat calibration of drop calorimeter

Prior to the experiment the calorimeter has been calibrated for temperature and the peak area which is referred as heat flow (Q) [24]. The temperature calibration has been carried out with melting points of pure element such as In, Sn, Al, Ag, Au and Cu. The resulting error in the measured temperature was found to be ± 2 K. The heat flow (Q) has been calibrated by dropping α -Al₂O₃, the reference material into the hot alumina bed set at different temperatures during enthalpy measurement of unknown samples. The temperature variation of heat flow Q is shown in **figure 2.11**. The individual data points of Q shown in figure 2.10 were taken from different experimental runs (more than 5 experiments) and were compared in the temperature range of 460 to 1373 K. It is observed that the standard deviation of Q is less than 5 up to 910K and is less than 15 for higher temperature. A typical sensitivity calibration curve used for enthalpy evaluation is shown as an inset in **figure 2.11**. The calibration constant data obtained as a function of temperature was fitted to fourth order polynomial expression $a+bT+cT^2+dT^3$ and the fit

coefficients obtained were: $a=0.248\pm0.078$, $b=7.84\pm2\times10^{-4}$, $c=8.795\pm3\times10^{-8}$, $d=-2.5\pm1\times10^{-10}$. The high scatter above 910 K is due to the radiation heat loss.

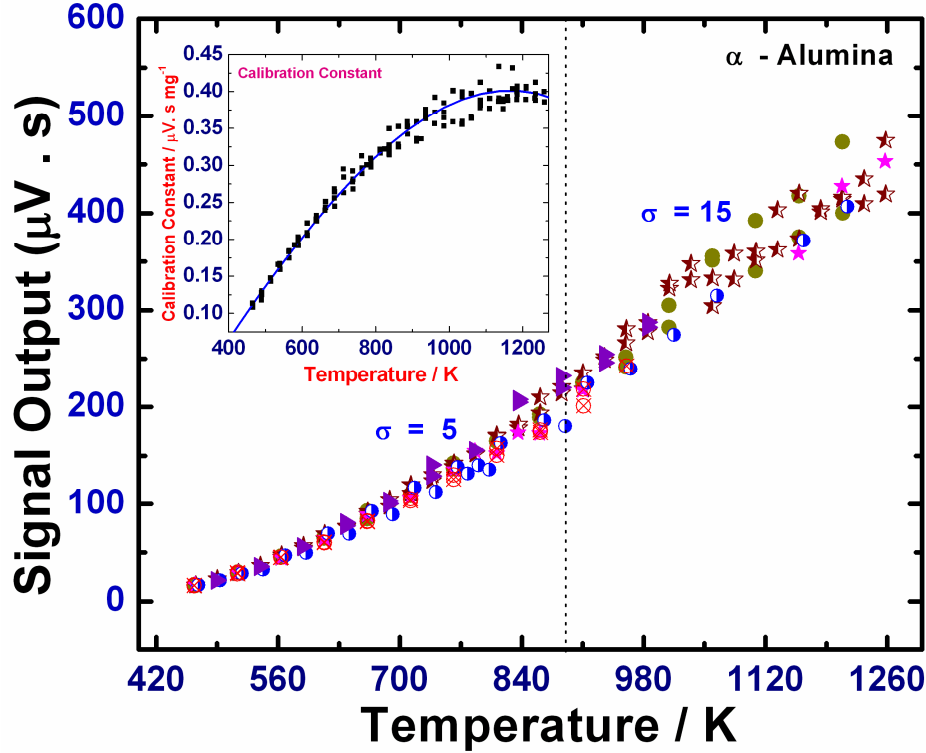


Fig. 2.11. Illustration of the temperature variation of Q for a typical experimental schedule and calibration constant (inset)

2.6.7. Estimation of enthalpy

The raw data which obtained from the output of experiment is basically the heat flow Q ($\mu\text{V.s}$) for both sample and reference. Assuming negligible heat loss due to radiation and quasi adiabatic condition in the experimental chamber, $Q_s(T)$, the heat energy transported from the bed to the sample may be written as follows [25-27].

$$Q_s(T) = C(T) \times (m_s/M_s) \times (H_T - H_{298.15}). \quad (2.7)$$

In the above expression, m_s is the mass of the sample, M_s its molecular weight and $H_T - H_{298.15}$ is the measured enthalpy increment with respect to reference temperature 298.15 K (25 °C) and $C(T)$ is a temperature dependent calibration constant. The calibration

constant can be obtained from the heat change measured for the standard alumina reference (Q_R) and from the knowledge of its assessed enthalpy increment data [28].

Thus

$$Q_R(T) = C(T) \times (m_R/M_R) \times (H_T - H_{298.15})_R \quad (2.8)$$

In the above equation m_R is the mass of the reference sample and M_R is its molecular weight which is taken to be 101.96 kg m^{-3} [28]. Once the calibration constant $C(T)$ is obtained as a function of temperature from Eq. (2.8), the enthalpy for the unknown sample can be calculated using Eq. (2.7) as a function of temperature.

2.6.8. General observation of result of drop calorimeter

It is generally assumed that the drop calorimetry measurements are carried out at thermally equilibrium conditions. As a result, a reliable and consistent thermodynamic data are obtained with static calorimetric measurements. The enthalpy variation with temperature measured at discrete temperature increments is used to derive heat capacity by fitting the temperature variation of enthalpy to a suitable analytical representation. In principle, it is desirable to have as large a number of data points as is possible for obtaining reliable conversion of enthalpy into specific heat [28]. This is especially true for characterizing the thermal property variation in the phase transformation domain. In drop calorimetry, when adequate precautions are ensured such as temperature stability high purity argon atmosphere etc., it is possible to achieve reproducible experimental data points, especially since a high level of accuracy in measuring and maintaining temperature stability is possible. In the present study, we have allowed enough equilibration time so as to achieve a temperature stability of $\pm 0.1 \text{ K}$. The accuracy of temperature measurement is $\pm 2 \text{ K}$. In order to avoid the effect of thermal gradients in the sample affecting the attainment of true equilibrium, a slow heating rate of 5 K min^{-1} and a reasonable sample mass of 50 to 75 mg are adopted in this study. Too large a sample

mass, while contributing to signal strength also add up to data scatter as the noise level is also raised in general. In view of such careful measures adopted in the present study, it is assured that drop calorimetry technique has yielded reliable estimates for basic thermodynamic quantities. However, drop calorimetry has certain limitations and these are described in the following section.

2.6.9. *Limitation of drop calorimeter*

The discrete nature of measurement is the major limitation of drop calorimetry results. If one needs to access the phase transformation point then fixing the transformation temperature is quite tedious with drop calorimetry results (alone) because of discrete nature of data points. To minimize the error associated with fixing the transformation temperature one needs to perform the experiments at very closely spaced temperature interval say about 1 K. Each experimental run at a given temperature takes about an hour. Hence conducting the drop experiment at every 1 K interval is practically difficult. However, the accumulating drop data points at 20 to 25 K interval is practically possible. In addition, even if a close temperature step is taken to generate the enthalpy vs temperature curve, a continuous curve cannot be generated using drop calorimetry unlike differential scanning calorimetry. Hence, a precise measurement of transformation temperatures is not generally realized in the drop calorimetry. Also, as drop calorimetry technique involves the measurements under equilibrium conditions, the energetics of metastable phases like martensites cannot be studied by this technique, which forms under non-equilibrium conditions during rapid cooling. However, a precise transformation temperature can be fixed with the help of DSC which has been already described in the previous section of this chapter. In next section the other supplementary techniques which have been employed in the present study are discussed.

2.7. *Optical metallography studies*

The optical microscopy studies are carried out with the *Leica*[®] *MeF4A*[®] optical microscope fitted with a *Leica*[®] digital camera and associated proprietary software for image acquisition and treatment. The sample for optical metallography has been prepared using established procedures [29]. Due care has been taken to ensure that it contains all the representative features present in the investigated material. Low speed diamond wire saw has been used for sample cutting to minimize the damage. Mounting of sample is usually done using cold setting resin (epoxy resin) and some samples through hot mounting press (thermosetting plastic – phenolic resin). Mounted specimens are ground with rotating discs of abrasive papers such as wet silicon carbide paper. Samples are systematically ground from coarser to finer emery grades. The final grinding is done with 4000 mesh, after which the samples are alumina and diamond polished. Since uranium is being as soft metal alumina polishing is preferred over diamond. After polishing each samples were ultrasonically cleaned in soap solution. Finally electro-etching has been carried out for different samples with appropriate etchant. Etched samples are immediately washed with distilled water and methanol to protect from any further chemical attack. U-Zr alloys have been etched electrochemically by using 50 % H₃PO₄ aqueous solution as the electrolyte and 304 SS as cathode at a constant voltage of 2V. However Fe-U based samples were etched manually by using solution having 50% HNO₃:50% H₂O.

2.7.1 Grain size measurement

The average linear intercept method is used to measure the grain size. It is obtained by drawing a set of line segments on the microstructure and counting the number of times the line segments are intersected by grain boundary and finding the ratio of the intercepts to line length. Thus it is written as

$$\text{Average grain size} = \text{line length} / N \times M \quad (2.9)$$

where N = number of intercepts and M = magnification. The statistical scatter in grain size quantification from 50 measurements is of the order of $\pm 10\%$.

2.7.2. Microhardness measurement

The hardness measurements have been carried out with *Leitz*[®] Vickers micro hardness tester. All the measurements are taken with 50 g load which lies in the load independent region of the load vs. diagonal length plot made for uranium alloys. About eight to ten measurements are taken for each sample and the average value is reported here. A standard test block of known hardness with prescribed load of 50 g is used for calibration. The probable error calculated by taking 15 indentation measurements on the standard sample is found to be within $\pm 2\%$. The Vickers hardness number (VHN) is calculated using the following formula

$$VHN = 1.854 \times (F/D^2). \quad (2.8)$$

with F being the applied load (measured in kilograms-force) and D^2 , the area of the indentation (measured in square millimeters). The applied load is also specified when VHN is cited.

2.8. Scanning electron microscopy (SEM) study

The scanning electron microscopy studies are carried out with *Philips*[®] *XL30 ESEM* attached with *EDAX* facility. Secondary electron and back scattered electron modes are used for the microstructural observations. The sample preparation procedure for SEM studies is similar to the one employed for optical microscopy studies. In order to prevent the electrostatic charge formation, samples are gold coated and when required, conducting carbon tapes are also used for the purpose of charge grounding. The magnification calibration is made with standard cross grating samples of 20 lines / mm and 2160 lines/mm. The high resolution calibration test is performed on a carbon film embedded with gold nanoparticles, whose spacing is of the order of 20 Å. Energy

dispersive X-ray analysis is carried out using energy dispersive spectrometer for qualitative identification of elements with atomic number greater than 10. Energy calibration is carried out with a detector resolution of 132 eV at Mn-K_α.

2.9. X-ray diffraction (XRD) study

The X-ray characterization is performed with *Inel*[®] XRG 3000 -X-Ray Diffractometer which makes use of a curved position sensitive X-ray detector for detecting diffracted X-ray intensity. Such type of detectors can measure up to 120 degrees of 2θ simultaneously and have high speed of data acquisition, especially during high temperature measurements. Thin slices of samples have been cut from respective uranium alloys with a disc shape of diameter 10mm and thickness of about 2 mm using diamond saw. The sample is cut in such a way that it is easily leveled flat in a sample stage to avoid the height problem. Before loading, the samples have been ground well with 2000 grit paper to remove any unwanted particles sticking in to it. The voltage and the current level in X-ray tube are set as 40 kV and 30 mA. The wavelength used is of 1.5406 Å (Cu-K_α) fitted with nickel filter. The diffraction pattern for each sample is recorded for 1h duration. The diffractometer has been calibrated with annealed silicon powder supplied by NPL, India. The particle size of the silicon powder is about 5000 Å. The peak positions, the full width at half maximum, and the d-spacing recorded with this machine are compared with the standard values suggested by NPL. The accuracy of lattice parameter reported for different materials in the present study is of the order of ±5%

2.10. References

1. Arun Kumar Rai, S. Raju, Haraprasanna Tripathy, R. N. Hajra and M. Vijayalakshmi, *Trans. Ind. Inst. Met.*, 66 (2013) 387.
2. C. B. Basak, R. Keswani, G. J. Prasad, H. S. Kamath and N. Prabhu, *J. Alloys Compd.*, 471 (2009) 544.
3. S. Kaity, J. Banerjee, M. R. Nair, K. Ravi, S. Das, T. R. G. Kutty, Arun Kumar and R. P. Singh, *J. Nucl. Mater.*, 427 (2012) 1.
4. Arun Kumar Rai, S. Raju, B. Jeyaganesh, E. Mohandas, R. Sudha, and V. Ganesan, *J. Nucl. Mater.*, 383 (2009) 215.
5. Arun Kumar Rai, S. Raju, and M. Vijayalakshmi, *J. Nucl. Mater.*, 432 (2013) 520.
6. Arun Kumar Rai and S. Raju, *J. Therm. Anal. Calorim.*, 112 (2013) 73.
7. Arun Kumar Rai, Haraprasanna Tripathy, B. Jeya Ganesh and S. Raju, *J. Nucl. Mater.*, 427 (2012) 378.
8. W. Hemminger and G.W.H. Höhne, *Calorimetry — Fundamentals and Practice*, Weinheim, Verlag Chemie, 1984.
9. Michael E. Brown, *Introduction to Thermal Analysis, Techniques and Applications*, second edition, 2001, Kluwer Academic Publishers, The Netherlands.
10. P. K. Gallagher, *Handbook of Thermal Analysis and Calorimetry*, 1, (Ed. M.E. Brown), Elsevier, Amsterdam, 1998.
11. S. M. Sarge, E. Gmelin, G. W. H. Hohne, H. K. Cammenga, W. Hemminger and W. Eysel, *Thermochim. Acta*, 247 (1994) 129.
12. <http://www.setaram.com/SETSYS-Evolution-DTA-DSC.htm>.

13. M. J. Richardson, in : K. D. Maglic, A. Cezairliyan, V. E. Peletsky (Eds.), *Compendium of Thermophysical Property Measurement Techniques*, Plenum Press, New York. 2 (1992) 519.
14. R. Sabbah, An Xu-wu, J.S. Chickos, M.L. Planas Leitão, M.V. Roux and L.A. Torres, *Thermochim. Acta*, 331 (1999) 93.
15. L. Richardson, E. L. Charsley; "Calibration and Standardisation in DSC", in *Handbook of Thermal Analysis and Calorimetry. Vol. 1: Principles and Practice*, M. E. Brown (editor), Elsevier Science B.V. (1998).
16. E. Gmelin and St. M. Sarge, *Pure Appl. Chem.*, 67 (1995) 1789.
17. B. Wunderlich, *Thermal Analysis*, San Diego, CA, Academic Press, 1990.
18. M. Brown, *Introduction to Thermal Analysis*, London, Chapman and Hall, 1988.
19. G.W.H. Höhne, W. Hemminger, and H.-J. Flammersheim, *Differential Scanning Calorimetry: An Introduction for Practitioners*, Berlin, Springer-Verlag, 1996.
20. <http://www.setaram.com/MHTC-96-Accessories.htm>.
21. Multi HTC-96, Setaram Installation Guide and Manual (1997).
22. K. D. Maglic, A. Cezairliyan, V. E. Peletsky (Eds.), *Compendium of Thermophysical Property Measurement Techniques*, vol. 2, Plenum Press, New York, (1992).
23. Yoichi Takahashi and Yuji Kohsaka, *J. Nucl. Mater.*, 130 (1985) 109.
24. B. Jeya Ganesh, "Calorimetric investigation of phase stability, energetics and kinetics of phase transformations in 9Cr based ferritic steels", A Ph. D thesis submitted to University of Madras, 2011.
25. J. Leitner, A. Strejc, D. Sedimidubsky, and K. Ruzicka, *Thermochim. Acta.*, 401 (2003) 169.

26. S. Raju, B. Jeya Ganesh, Aritra Banerjee and E. Mohandas, *Mater. Sci. Engg. A*, 465 (2007) 29.
27. D. G. Archer, Thermodynamic Properties of Synthetic Sapphire (α -Al₂O₃), Standard Reference Material 720 and the Effect of Temperature Scale Differences on Thermodynamic Properties, *J. Phys. Chem. Ref. Data*, 22 (1993) 1441.
28. M. Nevriva, D. Sedimidubsky and J. Leitner, *Thermochim. Acta.*, 347 (2000) 123-128.
29. L.E. Samules, *Metallographic Polishing by Mechanical Methods*, IVth edition, ASM International, Materials Park, USA (2003).

Chapter 3

Theoretical Aspects of Phase Transformation Kinetics and Evaluation of Thermo-Physical Properties

In this chapter the salient features of modelling of phase transformation kinetics in the purview of dynamic calorimetry measurements and a brief description of quasi harmonic Debye-Gruneisen formalism are presented. The theory of phase transformation kinetics is in fact very broad. But in the current chapter attention is focused on modelling aspects of kinetic issues of diffusion mediated and displacive (martensitic) phase changes in the physical metallurgical context. In precise terms, the non isothermal version of the Kolmogorov-Johnson-Mehl and Avrami (KJMA) model of diffusional phase changes is taken up for detailed discussion. This incorporates different nucleation and growth modes for the overall progress of transformation extent with time under linear heating or cooling rate conditions. For modeling the kinetics of martensitic transformation, the empirical relation given by Koistinen and Marburger is used. Further, the second part of this chapter deals with an analytical description of a particular version of thermophysical equation of state that is known as Debye-Gruneisen formalism. Before proceeding further, the general aspect of kinetics of phase transformation is discussed in the next section.

3.1. Basic glimpse of kinetics of phase transformation

A study of phase transformations that occur in solid state is of interest on both basic and applied grounds. Since phase transformations represent the explicit manifestation of thermodynamic instability, a comprehensive mapping of the evolutionary character of different phase fields in terms of appropriate intensive thermodynamic variables such as volume, pressure; temperature is extremely useful in constructing phase diagrams, the use of which in the design of materials is only too obvious [1-5]. If any of the thermodynamic variables suffer a change, correspondingly the Gibb's free energy of the system also changes continuously or discontinuously. Finally if the variation in free energy leads to change in structural details of a phase, then

"Phase transformation" is said to occur. Hence the system undergoes a phase transformation to that new structure [1-5]. The free energy may vary continuously if the thermodynamic variables like temperature or pressure is varied and the rate of variation is actually structure and system dependent. On alteration of the external conditions such as pressure and temperature, the initial state of the system is no more in the equilibrium state.

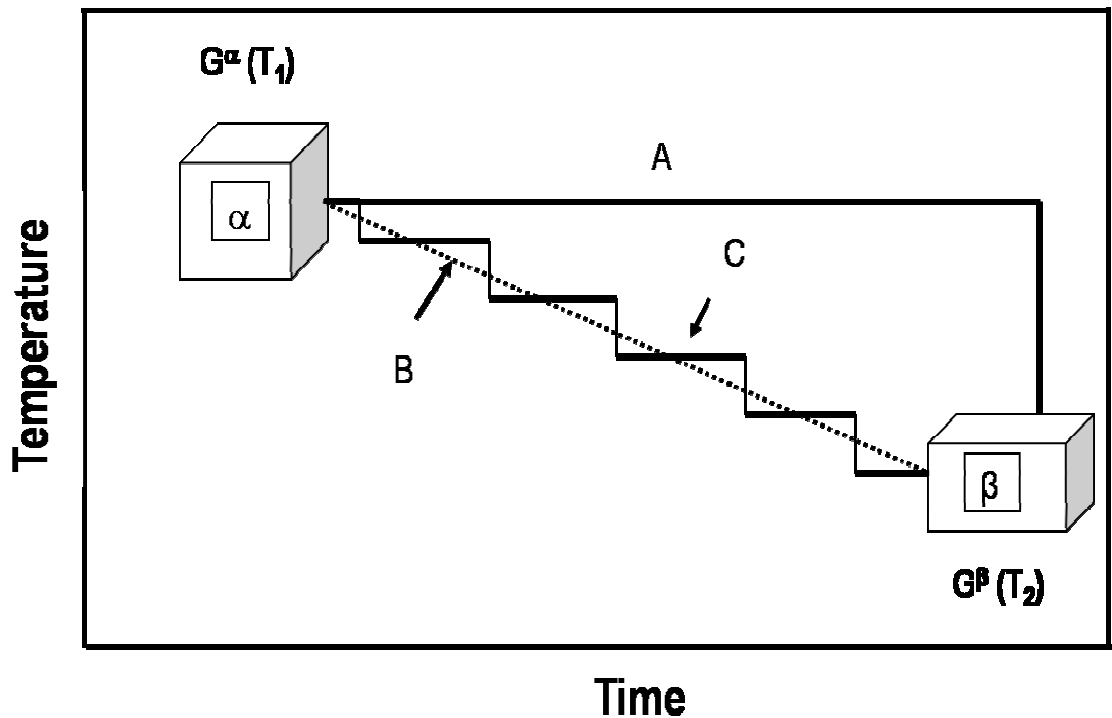


Fig.3.1 A schematic of different kinetic path ways offered by three different cooling histories is shown. Paths A and B stand for transformations occurring under isothermal and linear cooling conditions, where as the path C represents a step wise cooling with small incremental isothermal holds. Note that in all the three paths A, B and C the net reduction in Gibbs energy $\Delta^0 G$ is the same.

While thermodynamic considerations decide the ultimate stability of condensed systems, it is the time scale that marks the rate of attainment of this true thermodynamic equilibrium, which decides the effective usefulness of a solid as a practically useful engineering material. While thermodynamics classifies phase changes in terms of the nature of discontinuity in appropriate susceptibility functions, the kinetic considerations serve to broaden this classification further [1-5]. The number of *kinetic paths* available in

general for solid state phase transformations are many and these can be realized by selecting appropriate *kinetic path* variable [1-5]. Let us consider a system undergoing phase transformation from one state α to other state β during cooling from the high temperature. In **figure 3.1** the schematic illustration of path variable respect to one kinetic variable, namely cooling rate (β) is presented. From **figure 3.1**, it is clear that system can choose three independent paths which are A, B and C which involve different time durations for the same transformation [1-5]. There are other possible kinetic path variables which includes starting grain size (d) or morphology of the material, stress state (σ) and irradiation level *etc.* These could act either singly or in combination to decide the overall kinetics of transformation. In the present case, an attempt is made to highlight the role of one important kinetic variable, namely the heating or cooling rate in decisively altering the kinetics of simple structural transformations that occur in metals and alloys. The choice of this variable is based on the fact that it plays a vital role in dictating the final microstructure of many engineering alloys used in strategic applications. The other reason is that relevant experimental kinetic data with sufficient degree of accuracy are easily generated by carrying out the high resolution thermal analysis experiments and the results of which are rather easily processed to obtain information on transformation temperatures, the transformation velocity, especially their dependence on thermal history. In the present study in order to study the phase transformation kinetics heat flux differential scanning calorimeter has been used.

3.2. Isothermal and non-isothermal transformations

As illustrated in **figure 3.1**, a phase transformation between two phases α and β can be realized under varying time (t) – temperature (T) combinations, known under the generic name of thermal history. In the purely isothermal case, the sample is held at a fixed temperature (*path A*) the magnitude of which decides effectively the available

chemical driving force ($\Delta^{\circ}G$) and diffusional mobility of atoms. Apart from temperature, the time duration of isothermal holds decides the extent of transformation.

The isochronal process involves continuous heating or cooling as a function of time (*path B* shown in **figure 3.1**) or with interrupted isothermal holds (*path C* shown in **figure 3.1**). The kinetics of such non-isothermal transformations is basically decided by the cooling rate adopted. There is enormous evidence in metallurgical literature, which suggests that on rapid heating or cooling conditions, there is strong possibility that classical nucleation and growth mediated phase changes are inhibited and yield way to *martensitic* or *displacive* types of transformation [1-5]. This situation arises because under rapid heating or cooling conditions the diffusion of species become difficult due less available time.

It is generally the case that non-isothermal experiments are easily performed with minimal expenditure of time; but their results are the difficult ones to understand and interpret in concrete terms. From an applied context, most of the industrial heat treatments are done under complex thermal history, thereby necessitating a holistic understanding of both isothermal and non-isothermal phase transformation kinetics. In literature, there are very few rigorous treatments aimed primarily at tackling the problem of phase evolution under varying time-temperature history [6-16] and generally their mathematical complexity comes in the way of their widespread practical appeal. In the next section the theoretical aspect of transformation kinetics of diffusional based transformation under both isothermal and non-isothermal case is discussed in detail.

3.3 Kinetics model for nucleation & growth type transformation

There have been immense efforts from different research groups to develop suitable kinetics models for solid state transformations [8-35]. In past, especially the contributions from Johnson and Mehl [9], Avrami [10-12] and Kolmogorov [13] known jointly as the Johnson-Mehl-Avrami-Kolmogorov model (JMAK) are found to be

significant. The derivation of the KJMA model is based on the combination of three specific independent processes that are nucleation, growth and impingement of growing particles. It has been observed that mode of nucleation and growth can be different depending on the transformation. The nucleation processes considered are either continuous nucleation, when the nucleation rate is changing with temperature or as site saturation if all nuclei are present before the growth starts. Further, the growth processes can be either diffusion controlled, or interface controlled depending on whether overall kinetics is being decided by diffusion or interface mobility [6-16]. In the following sections the derivation of KJMA equation is discussed in detail.

3.4 Rate of transformation

For the analysis of kinetics of solids state transformation experimentally, one needs to measure the variation of a physical property (enthalpy, electrical resistivity, length, hardness, specific volume and magnetization etc.) as a function of time or temperature during the course of a phase change. From such data the degree of transformation X ($0 \leq X \leq 1$) can be calculated as follow.

$$X = \frac{(P_T - P_0)}{(P_f - P_0)} \quad (3.1)$$

Where, P_T is the instantaneous physical property measured during the transformation at any temperature T , P_0 and P_f are the value of P at the start and finish of the transformation, respectively. The transformed fraction does not depend on t or $T(t)$ in a direct way, although the thermal history of the material decides the extent of transformation. In order to correlate the extent of transformation and thermal history, let us now define a path variable Ω which determines the extent of transformation and depends on thermal history. Therefore one can express the fraction of transformation as follows [14].

$$X = F(\Omega) \quad (3.2)$$

The above Eq. (3.2) does not impose any constraint on the type of transformation considered. If the transformation mechanism is not changing for a given time-temperature path (t-T), then Ω can be assumed to be proportional to number of atomic jumps because temperature decides the atomic mobility and time defines the duration of transformation process. Under these circumstances, the thermal history dependence of Ω can be described in the following way depending on whether process is isothermal or non-isothermal [14].

$$\Omega = k(T(t)). \quad (3.3)$$

$$\Omega = \int k(T(t))dt. \quad (3.4)$$

In above Eqs $k(T)$ is rate constant and assumed to be of the Arrhenius form.

$$k(T(t)) = k_0 \exp\left(-Q_{eff}/RT(t)\right). \quad (3.5)$$

With k_0 as the pre-exponential or frequency factor, Q_{eff} is the *apparent* or *effective* activation energy for the overall transformation process and R is gas constant. In general terms, Q_{eff} must be treated as dependent on the transformation extent $X(T(t))$ as well, but for reasons of convenience and simplicity, is often taken to be a constant. In the reported literature, the kinetic theories for non-isothermal phase transformations have been derived from the theory of isothermal transformations in conjunction with additivity rule [14] given below.

$$\int_0^\tau \left(dt/\tau^{iso}\right) = 1. \quad (3.6)$$

Where, τ^{iso} is the time required during one isothermal step. In words, it can be stated that if a non isothermal transformation is composed of a series of isothermal processes then the total time required follows by adding relative durations of time spent at each temperature and equating this sum to one. But it must be remembered that this will only hold when process is isokinetic [6]. If a non-isothermal experiment is described as a

series of isothermal anneals, each of infinitesimal length of time, and Eq. (3.3) is applied to each time step [14-15] for overall isochronal (i.e. constant heating rate) experiments. Then only the outcome will be in accordance with the Eq. (3.4). In the classical methodology adopted for analysing the kinetics of a nucleation and growth type of transformation as studied by thermal analysis methods, the following separable functional representation is often invoked to represent the instantaneous reaction rate from Eq. (3.2) [14-17].

$$dX/dt = \left(dF(\Omega)/d\Omega \right) (d\Omega/dt). \quad (3.7)$$

If we assume that the time gap between two isothermal processes under isothermal transformation is infinitesimal then $d\Omega = k(T(t))dt$, this leads to Eq. (3.4), therefore with the help of Eq. (3.3) and Eq. (3.4), we can write [25].

$$dX/dt = k(T(t)) dF(\Omega)/d\Omega. \quad (3.8)$$

From the above equation it is clear that the rate of transformation can be described if both the terms are clearly defined in Eq. (3.8). The first term is standard Arrhenius term and therefore one need to have a clear idea about the second term alone.

3.5. Transformation mechanism: nucleation and growth

The overall kinetics of phase transformation can be described in terms of fraction transformed as function of time/temperature. The overall fraction transformed is function of nucleation and growth. In the next section the detailed descriptions of nucleation and growth modes are discussed.

3.5.1. Nucleation modes

There are four different categories of nucleation modes; (1) continuous nucleation (2) site saturation nucleation, (3) mixture of continuous and site saturation nucleation, (4) Avrami nucleation.

The continuous nucleation means the rate of nucleation is monotonically increasing with time. The rate of nucleation is decided by the number of critical nuclei present and the rate of jump of atoms across the interface from parent to the critical nuclei of the product phase. The jump frequency through the interface can be described in the form of Arrhenius form $\exp(-Q_N/RT)$ [6] where Q_N stands for activation energy for nucleation. The number of critical nuclei depends on an activation energy ΔG^* and it can be approximated in the following form [7].

$$\Delta G^* \approx C/\Delta T^2. \quad (3.9)$$

Where C , is constant relatively intensive to temperature and ΔT is under cooling or overheating. Hence the nucleation rate per unit volume can be written as [7].

$$\dot{N}(T) = N_0 \exp\left(-Q_N/RT\right) \exp\left(-\Delta G^*/RT\right). \quad (3.10)$$

If ΔT is very high then ΔG^* will be very small and in this case nucleation rate will only depends on the mobility of the atoms across the interface and the Eq. (3.10) can be written as follow [6-7].

$$\dot{N}(T) = N_0 \exp\left(-Q_N/RT\right). \quad (3.11)$$

The main features of continuous nucleation is that at $t=0$ the number of nuclei of supercritical size will be zero.

In the case of site saturation nucleation the nucleation rate does not change during transformation and it remains constant throughout the transformation, in this case the rate of nucleation can be defined as follows [6-7].

$$\dot{N}(T) = N' \delta(t - 0). \quad (3.12)$$

Where δ denotes Dirac function and N' is number of nuclei presents at $t=0$.

It has often been observed that mixed mode of nucleation are present during phase transformation in real system. Under this category there are some nuclei already

present at $t=0$ and other formed during the course of transformation. The rate of nucleation for mixed mode is just the weighted average of the rate of continuous and site saturation nucleation. The rate of nucleation for mixed mode can be written in the following way [6-7].

$$\dot{N}(T) = N' \delta(t - 0) + N_0 \exp\left(-Q_N/RT\right). \quad (3.13)$$

In Eq. (3.12) N' and N_0 represents the relative contribution from two different modes.

In the case of Avrami nucleation mode the nuclei of supercritical size formed from the nuclei of subcritical size, such that the total number of nuclei of supercritical and subcritical remains constant. Therefore the rate change of supercritical nuclei number can be expressed as follow [10-12].

$$\dot{N} = \dot{\eta} N_{sub}. \quad (3.14)$$

Where $\dot{\eta}$ is the rate at which subcritical nuclei change to supercritical nuclei and it can be expressed in the following form

$$\dot{\eta} = \eta_0 \exp\left(-Q_N/RT\right). \quad (3.15)$$

with η_0 pre-exponential factor. Upon integration of Eq. (3.14), after separation of variables, using Eq. (3.15) and the boundary condition that the number of subcritical nuclei equals N' at $t=0$, it is obtained for the rate of formation of supercritical nuclei at $t=t^*$.

$$\dot{N}(T) = \eta_0 N' \exp\left(-\int_0^{t^*} \dot{\eta} dt\right). \quad (3.16)$$

By variation of η_0 the mode of nucleation can be varied from site saturation (η_0 infinitely large) to continuous nucleation (η_0 infinitely small).

3.5.2. Growth modes

In a more general way two types of growth modes are identified, one of which is

diffusion controlled growth where long range diffusion is involved. Under diffusion controlled growth mode the product phase has different composition than parent phase. The second category of growth mode is interface controlled. The interface controlled growth mode involves short range diffusion and overall composition of the product phase is same as the parent phase.

In the case of diffusion controlled growth, long range diffusion in the matrix governs the growth of the new phase particles. The diffusion length, R is proportional to square root of time and it can be expressed in the following form [6-7].

$$R = (Dt)^{1/2}. \quad (3.17)$$

Where D is diffusion coefficients, *Eq.* (3.17) is valid under isothermal condition only and it is also known as parabolic growth. Under non-isothermal condition the diffusion length can be approximated as follow [6-7].

$$R = [\int DT(t)dt]^{1/2}. \quad (3.18)$$

Further the temperature dependence of diffusion coefficient can be described according to following equation

$$D(T(t)) = D_0 \exp\left(-Q_D/RT\right). \quad (3.19)$$

with D_0 as the pre-exponential factor and Q_D as the activation energy for diffusion. The growth laws given in *Eq.* (3.17 & 3.18) are only valid in very large matrix of parent phase and holds only in the initial stages of transformation until there is no impingement. [18]. If *Eq.* (3.17 & 3.18) holds together then the volume of growing particle will be

$$V = gR^d. \quad (3.20)$$

Where g is particle geometry factor and d is the dimensionality of the growth.

In the case of interface controlled growth model the particle growth is governed by the mobility (driving force normalized velocity) of interface between product and parent. The velocity of the interface is decided by the net jump of atoms from the parent

phase to the new growing phase per unit of time. The jump of atoms is determined by the difference in the Gibb's free energy for an atom between parent and product phase. However, the transfer of the atom is inhibited due to formation of new interface which in turn create an energy barrier for the jump of atoms across the interface. If ΔG^a is the net free energy difference between parent and product phase, then the net flux of atoms jumping from the parent to the product phase across the interface can be approximated as follow [6-7].

$$J = J_0 \exp\left(-\Delta G^a/RT\right). \quad (3.21)$$

In Eq. (3.21) J_0 is the pre exponential factor. Further in the case of interface controlled growth the volume of growing particle can be written as follows [15-17].

$$V = g(\int J dt)^d. \quad (3.22)$$

The Eqs. (3.20 & 3.21) for both diffusion and interface controlled growth model can be combined and given in compact form. At any time t the volume V of growing particle that nucleated at time t_0 is given by [15-17]

$$V = g(\int \vartheta dt)^{d/m}, \quad (3.23)$$

$$\vartheta = \vartheta_0 \exp\left(-Q_g/RT\right). \quad (3.24)$$

with ϑ_0 as the pre-exponential factor for growth, Q_g the activation energy for growth, and m as the growth mode parameter. For the case of diffusion controlled growth, $m=2$, Q_g equals Q_D (activation energy for diffusion) and ϑ_0 equals D_0 . For the case of interface controlled growth $m=1$, Q_g equals ΔG^a (interface energy barrier) and ϑ_0 equals J_0 .

3.5.3. Effect of impingement on growth

The volume of the growing particle given by Eq. (3.23) is referred to as the extended volume, which counts for the entire transformed volume without considering impingement of transformed domains, is a virtual concept [14-17]. Thus the overlapped

domains should be counted twice or even multiple-times in order to obtain the virtually defined extended volume. In reality, the particles are not growing into an infinitely large parent phase and the extended volume does not account for the overlap of particles (hard impingement) and their possibly surrounding diffusion fields (soft impingement). Therefore, the relationship between the extended volume V_{ext} and the actual volume V^t of transformed phase is needed. If it is assumed that the nuclei are randomly dispersed throughout the space and suppose that at a given time t the actually transformed volume is V^t and during the course of transformation after an infinitesimal time laps of dt , if the extended and the actual transformed volumes are increase by dV_{ext} and dV^t . Then from the change of the extended volume dV_{ext} , only a part will contribute to the change of the actually transformed volume dV^t , namely a part as large as the untransformed volume fraction $(V-V^t)/V$. where V is the total volume of the system. Therefore the change in the real volume can be expressed as follow [14-17].

$$dV^t = \left(V - V^t/V \right) dV_{ext}. \quad (3.25)$$

Further the degree of transformation can be defined as.

$$X = V^t/V. \quad (3.26)$$

After integrating Eq. (3.25), one can get the following expression for extent of transformation [14-17].

$$X = V^t/V = 1 - \exp\left(-V_{ext}/V\right). \quad (3.27)$$

3.5.4. Overall transformation kinetics

The overall transformation kinetics describes the relationship between fraction transformed and time for different reaction temperature. Actually it is function of both nucleation and growth rate. The empirical expression describing the overall

transformation kinetics can be obtained by substituting the expression for extended volume in Eq. (3.26)

$$X = V^t/V = 1 - \exp[-\{k(T)t\}^n]. \quad (3.28)$$

Where $k(T)$ is rate constant and is function of T and n is time exponent. Note that this equation cannot be derived for a mixture of the nucleation models. Eq. (3.28) has first been derived by Johnson and Mehl (for the case of isothermal transformations with continuous nucleation [9] and by Kolmogrov and Avrami (for isothermal transformations with continuous nucleation and site saturation) and therefore it is referred as the KJMA equation with Avrami exponent n [10-12].

3.5.5. Formulation of Kolmogrov-Johnson-Mehl and Avrami model for isothermal and non-isothermal transformations

By combining Eq. (3.3) & Eq. (3.28), the expression for fraction transformed under isothermal case can be rewritten as follow.

$$X = F(\Omega) = 1 - \exp[-\Omega^n]. \quad (3.29)$$

However, for the case of non-isothermal annealing, on the basis of nucleation and growth models, an equation for V_{ext} can be derived and after substitution into Eq. (3.28) leads to a KJMA-like equation and also fulfill the prescription of Eq. (3.2) with Ω defined according to Eq. (3.3). Additionally, if a KJMA-like equation can be obtained then the associated kinetic parameters n , Q and k_0 can be given in terms of appropriate nucleation and growth models even in the case of non-isothermal transformation. In the following, it will be shown that this is possible for at least in the case of isochronal annealing as long as the nucleation process involved is either site saturation or continuous nucleation.

Considering the case of isochronal annealing, the phase transformation temperature under dynamic heating condition can be expressed as follows.

$$T(t) = T_o + \beta t. \quad (3.30)$$

Where T_o is the start temperature (at $t=0$) of the experiment and β is the constant heating rate. The above formulation can be analogous to that for isothermal transformations with certain mathematical intricacy. The integral in Eq. (3.22) cannot be evaluated analytically in general. An Arrhenius term can be obtained by substitution of Eqs. (3.5) and (3.30) into Eq. (3.20) and integrated over time as follows [17].

$$\Omega = k_o \int_0^t \exp \left(- \frac{Q_{eff}}{R(T_o + \beta t)} \right) dt. \quad (3.31)$$

The above equation can be also be integrated over temperature by replacing time with temperature by using of Eq. (3.30).The integration in Eq. (3.31) is performed over a new time parameter $t'=t + T_o / \beta$ by invoking $dt=dt'$ and $T_o+\beta t=\beta t'=T(t')$. The boundaries for the integration then become T_o/β and t' . If on heating T_o is chosen small, such that $\beta (T - T_o) \approx 0$, the start of the new time scale (i.e. $t'=T_o/\beta$) can be shifted to $t'=0$ without changing the value of the integral [19]

$$\Omega = k_o \int_{T_o/\beta}^{t'} \exp \left(- \frac{Q_{eff}}{R\beta t'} \right) dt' = k_o \int_0^{t'} \exp \left(- \frac{Q_{eff}}{R\beta t'} \right) dt'. \quad (3.32)$$

With this it become possible to obtain an analytical integration by using a series expansion of type [15-17]

$$\int_0^\infty \frac{e^{-xt}}{t^n} dt = \frac{e^{-x}}{x} \left[1 - \frac{n}{x} + \frac{n(n+1)}{x^2} + \dots \right]. \quad (3.33)$$

With the help Eq. (3.33), Ω can be approximated as follow

$$\Omega = \left(k_o R \beta t'^2 / Q_{eff} \right) \exp \left(- \frac{Q_{eff}}{R\beta t'} \right) \left[1 - 2 \frac{R\beta t'}{Q_{eff}} + 6 \left(\frac{R\beta t'}{Q_{eff}} \right)^2 \right]. \quad (3.34)$$

Further the back substitution $t'=T(t')/\beta$ can be made so that there is no time parameters (t or t') is involved anymore. On basis of Eq. (3.34), explicit analytical equations can be

derived for the degree of transformation in the case of isochronal annealing, and for specific nucleation and growth models following the recipe indicated at the beginning.

For pure site saturation and for pure continuous nucleation or both in combinations with growth according to Eq. (3.24), KJMA like equations can be obtained that will be compatible with Eq. (3.1) with Ω as given by Eq. (3.2) and k given by Eq. (3.5). In this

Table 3.1		
Listing of different kinetics parameters under isothermal and isochronal condition		
Continuous Nucleation	Isothermal	Isochronal
n	$d/m+1$	$d/m+1$ (with d/m as integer value)
Q	$(n-1)Q_g+Q_N/n$	$(n-1)Q_g+Q_N/n$
k_o	$\sqrt[n]{\frac{gN_o\vartheta_o^{n-1}}{n}}$	$\sqrt[n]{\frac{gN_o\vartheta_o^{n-1}}{n}} s$
Site saturation		
n	d/m	d/m
Q	Q_g	Q_g
k_o	$\sqrt[n]{gN^*\vartheta_o^n}$	$\sqrt[n]{gN^*\vartheta_o^n}$

way explicit expression for n , Q and k_o can be obtained in terms of the operating nucleation and growth mechanisms and corresponding expressions are listed in **table 3.1**

From **table 3.1** it can be seen that for the nucleation and growth cases the KJMA parameters pertaining to isothermal annealing and to isochronal annealing are equal (except for the correction factor s given below as in Eq. (3.35) [17].

$$s = (n-1)! / n^{n-1} \left(\frac{(Q_N + (n-1)Q_g)^n}{\prod_{j=0}^{j=n-1} (Q_N + jQ_g)} \right). \quad (3.35)$$

In above table m decides the mechanism of transformation and for interface controlled $m = 1$ and for diffusion controlled process $m=2$. The second term d is the dimensionality of growth. Further, the expressions for the overall, effective activation energy, Q , given in **table 3.1** can be represented by a single equation, incorporating the exponent n , the ratio of the number of growth dimensions and the growth mode, d/m , and the separate activation energies for nucleation, Q_N , and for growth, Q_g , as follows [17].

$$Q_{eff} = \left\{ \left[\left(\frac{d}{m} \right) Q_g + \left(n - \frac{d}{m} \right) Q_N \right] / n \right\}. \quad (3.36)$$

The above equation holds for both isothermal and isochronal annealing.

3.6. Determination of kinetics parameter from DSC results

From the experimental DSC peak profile as shown in **figure 3.2** as a model, the fractional extent of transformation as a function of temperature $X(T)$, is estimated using the following expression.

$$X(T) = \frac{\int_{T_s}^T \varphi(T) dT}{\int_{T_s}^{T_f} \varphi(T) dT}. \quad (3.37)$$

Here, the integral in the numerator, namely, $\int_{T_s}^T \varphi(T) dT$, stands for the partial area under the peak in the temperature domain T_s-T as shown in **figure 3.2** by crossed lines. The

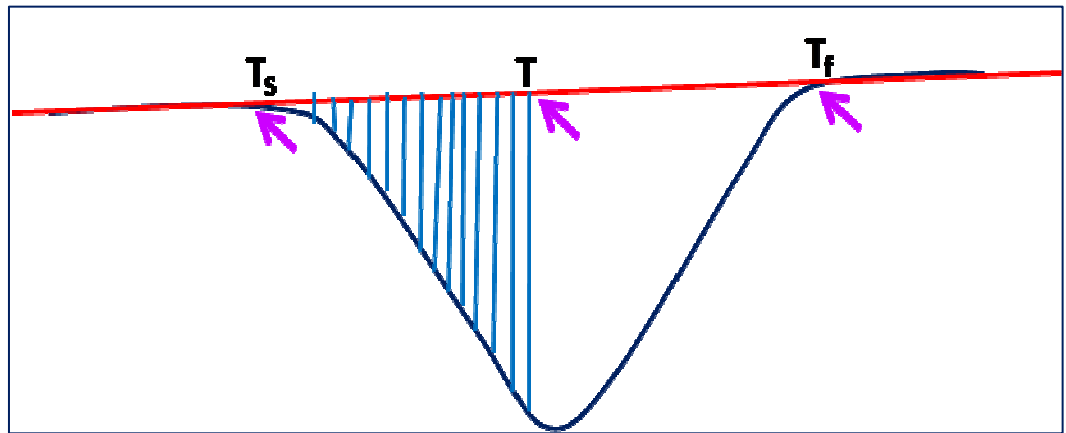


Fig. 3.2. Schematic of DSC peak profile used for calculating phase fraction

denominator $\int_{T_s}^{T_f} \varphi(T) dT$ stands for the total peak area covering the entire transformation temperature range (T_s-T_f) . *Eq. (3.37)* assumes that transformation is complete upon reaching T_f , although this is certainly not true for higher heating rates. The transformation plots obtained using *Eq. (3.37)* is displayed in **figure 3.3**. In the

present study the transformation plots are fitted with the following non-isothermal version of the Kolmogorov-Johnson-Mehl-Avrami (KJMA) formalism for the fraction transformed $X(T)$ as a function of temperature at constant heating rate (β) [17]

$$X(T) = 1 - \exp \left[-k^n \left\{ \frac{R(T - T_S)^2}{\beta Q_{eff}} \right\}^n \right]. \quad (3.38)$$

The above expression assumes site saturation type of nucleation. It may be noted that in the above model, we have chosen $T - T_S$, the temperature increment with respect to the experimentally observed threshold or onset temperature (T_S) as the independent variable, since this corrects in an apparent manner for the error incurred in not accounting precisely for the true start of the transformation corresponding to near zero transformed fraction ($X = 0$). In above equation k is Arrhenius rate constant and n is the so-called Avrami or transformation exponent.

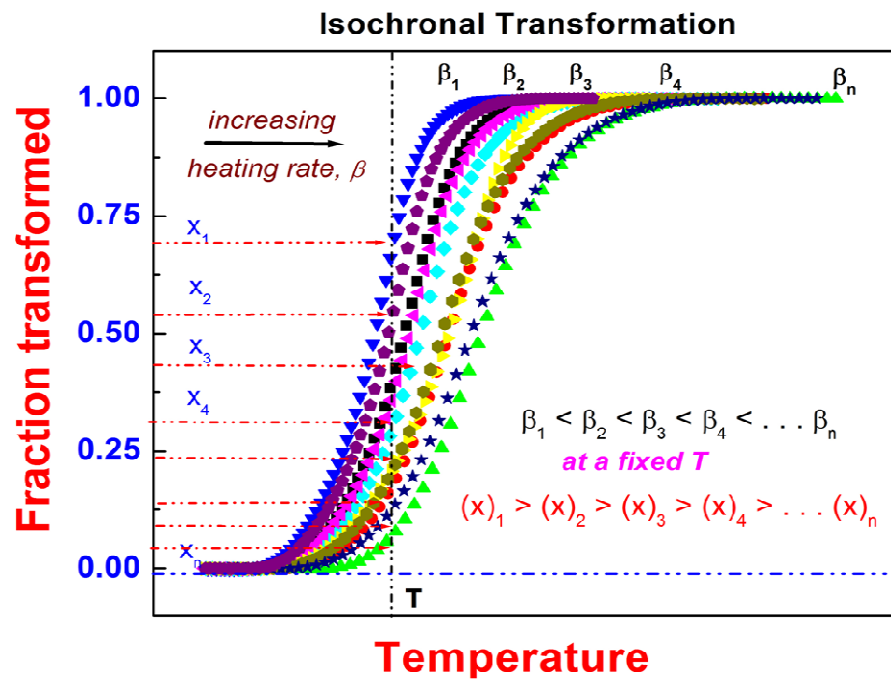


Fig. 3.3. Phase fraction curve obtained using Eq. (3.38)

3.7. Martensitic Transformation: Koistinen- Marburger Relation

The kinetics of martensitic transformation is modelled after the popular relation

proposed by Koistinen and Marburger on empirical grounds [32]. In what follows, we use this relation in a slightly modified form, in order to incorporate explicitly the cooling rate in it.

$$X(T) = \exp \left\{ - \left[\left(\frac{b'}{\beta} \right) (M_s - T) \right]^n \right\} \quad (3.39)$$

Here $X(T)$ is fraction of martensite formed at temperature T . In the above expression, β is the cooling rate in K sec^{-1} , M_s is the onset temperature in Kelvin and n is a constant. By setting $(b'/\beta)^n = b$, a simple two parameter description of *martensitic* transformation after the well-known empirical framework of Koistinen and Marburger (K-M) can be readily obtained [32]. It must be added that in the original K-M prescription, n is taken to be unity [32]; but we allowed it to vary here in order to get better numerical agreement. The results of fitting of the experimental data obtained on uranium using Eq. (3.39) will be discussed later. However, it is useful to note that, since Eq. (3.39) is empirical in origin, it is not possible to provide a physicochemical basis for the cooling rate variation of parameter b . The negative value of n arises from the fact that with positive values for the argument $(T_s - T)$, the transformation extent $X(T)$ increases with decreasing temperature. The K-M equation was justified by Magee on phenomenological grounds in the following manner [33]. Magee assumed that in a finite temperature drop dT , the number of new martensitic plates per unit volume of austenite dN , is proportional to the increase in chemical driving force, ΔG_V . That is,

$$dN = k_m d(\Delta G_V) \quad (3.40)$$

k_m is the proportionality constant for martensite transformation. If dy is the corresponding change in volume fraction of martensite in this temperature interval dT , then,

$$dy = V dN_V \quad (3.41)$$

V , is the average volume of the newly formed plates, and dN_V is the change in the number of plates per unit volume. Setting $dN_V/dN = 1-y$, we get,

$$V(1 - y)k_m \Delta S_V(\Delta T). \quad (3.42)$$

In Eq. (3.42), we have used, $d(\Delta G_V)/dT = \Delta S_V$ the entropy of transformation. Thus, in final analysis

$$\int \frac{dy}{1 - y} = \int V k_m \Delta S_V \Delta T \quad (3.43)$$

Integration by variable separable, yields with the assumption that $V k_m \Delta S_V$ is a constant and that $dT = \Delta T = M_s - M_f$. the temperature interval between martensite start and finish temperatures. Thus,

$$\ln(1 - y) = V k_m \Delta S_V [M_s - M_f]. \quad (3.44)$$

Thus, we get the K-M relation, with the tacit identification that $V k_m \Delta S_V = b$, the K-M constant in the empirical equation. The effect of altering β , the cooling rate has to do with the constant k_m , since ΔS_V and V are independent of thermal history. But this aspect is not probed in this study any further.

3.8. Quasi harmonic theory

In recent years many first principles and semi-empirical modelling methodologies have been developed alongside with advances in experimental techniques and these have been successfully applied for many metallic alloys to derive basic thermodynamic properties in a self-consistent manner [36-46]. Harmonic approximation given by Debye model has been widely used to calculate the vibrational free energy. But under harmonic approximation it has been assumed that the frequency of vibration is independent of volume as well the temperature and there is no inter-phonon interaction. The vibrational free energy can be expressed analytically by the phonon frequency alone. However, the harmonic approximation failed to explain thermal expansion. In order to explain anharmonicity, quasi-harmonic Debye-Grüneisen formalism has been developed. This considers the volume dependence of frequencies but ignored the temperature effect on frequencies. Based on the knowing of the vibrational spectrum obtained by experiment or

calculated precisely with numerical methods such as density functional perturbation theory or frozen phonon method, quasi harmonic formalism has been found to reproduce thermodynamic properties quite consistently with experimental results. However, many investigations also discover that the quasi harmonic formalism is inadequate in the region of high pressure and high temperatures [36-50]. At high temperatures, the intrinsic phonon interaction (anharmonicity) neglected by quasi harmonic formalism becomes prominent in many materials. But as of today invoking the intrinsic anharmonicity in a rigorous way is quite difficult; however there is significant improvement in this field [36-50].

Accordingly, in the present study, we have adopted this method for obtaining reliable first-order estimates of thermal quantities, including heat capacity and thermal expansion in an integrated and self-consistent manner. In the following section, a brief familiarizing account of this formalism is provided.

The Debye-Grüneisen quasiharmonic formalism is quite a robust method for modelling the vibrational contribution to thermal properties and requires only standard input data [36-50]. The details of this model are adequately described by the monograph of Anderson, for example [45]; only a brief familiarizing account is given here. In essence, the quasi-harmonic approximation involves the treatment of the volume dependence of the vibrational frequencies through the Mie Grüneisen parameter ‘ γ_G ’ which has been brought into play for explaining the thermal expansion effects arising out of lattice anharmonicity. The Grüneisen parameter (γ_G) may be defined as [45].

$$\gamma_G = - \frac{d \ln \omega}{d \ln V} \approx - \frac{d \ln \theta_D}{d \ln V}. \quad (3.45)$$

In the above expression ω is frequency of lattice vibration, θ_D is Debye temperature and V is (molar) volume of solid. *Eq.* (3.45) is an approximation to γ_G under the validity of Debye model [45]. Basically γ_G has been introduced to relate thermal properties with

elastic properties of materials [45]. In more basic way γ_G can be defined as change in pressure of a material resulting from increase in energy density at constant volume.

$$\gamma_G = V \left(\frac{\partial P}{\partial E} \right)_V. \quad (3.46)$$

Where E stands for energy density, V is molar volume and P is pressure. If the change in pressure is exactly proportional to the change in energy density then γ_G will be independent of both P and T , and experiments show this to be nearly correct if one considers the case for the variation of γ_G with T at constant V . In fact, the proportionality constant usually lies between 1 and 2. Further, γ_G can be expressed in terms of measured physical properties as follows.

$$\gamma_G = \left(\frac{\partial P}{\partial E} \right)_V = \left(\frac{\left(\frac{\partial P}{\partial T} \right)_V}{\left(\frac{\partial E}{\partial T} \right)_V} \right). \quad (3.47)$$

Further, the numerator and denominator in *Eq.* (3.47) can be defined in the following forms.

$$\left(\frac{\partial P}{\partial T} \right)_V = \alpha_V B_T. \quad (3.48)$$

$$\left(\frac{\partial E}{\partial T} \right)_V = C_V. \quad (3.49)$$

With the help of *Eqs.*(3.46, 3.47, 3.48 & 3.49) we can get γ_G in the following form.

$$\gamma_G = \alpha_V B_T V / C_V. \quad (3.50)$$

In the above expression, α_V is the volume thermal expansivity, B_T is the isothermal bulk modulus and C_V is the isochoric or constant volume specific heat. Thus γ_G given by *Eq.* (3.50) is composed of individual measurable physical properties, each of which varies significantly with temperature, but the ratio of these properties as given by *Eq.* (3.50) does not vary greatly with temperature, and sometimes not at all.

The starting point of Debye-Grüneisen quasiharmonic formalism is that for a condensed system at equilibrium, the total pressure acting on the system P is assumed to be composed of two components. Of these, the cold or potential pressure, corresponding to zero Kelvin temperature is a function of only volume. The other thermal pressure component (at fixed volume) is a function of only temperature. Thus,

$$P_{total} = P_o(V) + P_{th}(T, V). \quad (3.51)$$

Where P_o is the zero Kelvin cold pressure arising due to cohesive forces of the solid, which can be expressed in terms of the Helmholtz free energy F as follow.

$$P_o = -\left(\frac{\partial F}{\partial V}\right)_T. \quad (3.52)$$

It is clear from above equation that a complete description of P_o could be obtained by calculating Helmholtz free energy as a function of volume at 0 K using a suitable *ab-initio* method or through semi-empirical inter atomic potential schemes or from suitable empirical P-V equations of state [44-46]. Irrespective of the methodology employed, it is clear that at equilibrium conditions.

$$dP = 0 \text{ and hence } P_o = P_{th}. \quad (3.53)$$

The thermal pressure can be estimated from the following fundamental thermodynamic identity given in Eq. (3.48) [42].

$$\left(\frac{\partial P_{th}}{\partial T}\right)_V = \alpha_V B_T = \gamma_G C_V / V. \quad (3.54)$$

It is true that in the real case γ_G is temperature dependent [45-47], which can be treated accurately if details of experimental phonon spectrum data are available [45]. On the contrary, with little or no details of phonon dispersion, it is customary to neglect this temperature dependence of γ_G in many first order calculations of thermal effects at moderate pressures [45]. Sometimes, $\gamma_G(V)$ dependence is also empirically approximated in terms of a simple power law, namely

$$(\gamma_G/\gamma_o) = \left(V_T/V_o \right)^q \quad (3.55)$$

In the above expression, γ_o is the reference volume Grüneisen parameter and q is the power law exponent [45]. In many simulations that $q = 1$, is often assumed. However, in the present study, the thermal pressure component is treated in the following manner.

Integrating Eq. (3.54) along the isotherm, one can write

$$\int dP = - \int \left(\alpha_V B_T / V \right) dT = - \int \left(\gamma_G C_V / V \right) dT. \quad (3.56)$$

By taking $(\gamma_G/V) = (\gamma_o/V_o)$, the value at the reference temperature of 298.15 K, it is easy to simplify the above approximation as follows.

$$P_o - P_{th} = (\gamma_o/V_o) \int C_V dT = (\gamma_o/V_o) E_{vib} \quad (3.57)$$

In above expression E_{vib} is the internal energy, which is a function of volume and hence temperature. P_o can be expressed by adopting for example, the popular Murnaghan equation of state [45, 46], which considers the linear variation of the bulk modulus B_T with pressure with proportionality constant being the isothermal pressure derivative of bulk modulus B'_T [45]. It may be added that Murnaghan equation of state holds good only for small excursions from equilibrium volume. Finally at thermodynamic equilibrium the condition that $P_o = P_{th}$, must hold good. Accordingly, the basic Mie-Grüneisen thermal equation of state can be re-expressed in the following manner [45].

$$V_T = V_o \left\{ \left[E^{vib} / (Q_o - r E_{vib}) \right] + 1 \right\}. \quad (3.58)$$

More details on Mie-Grüneisen quasi-harmonic formalism can be obtained from the recent monograph of Anderson [45]. Where $Q_o = B_o V_o / \gamma_o$ and $r = (B'_T - 1)/2$; V_o is the volume, B_o is isothermal bulk modulus and B'_T is the pressure derivative of bulk modulus at 298.15 K. In order to evaluate the consistent temperature dependence of volume using

Eq. (3.58), one need to have accurate estimation of E_{vib} , B_T , B'_T and γ_G . and these discussed in ensuing sections

3.8.1. Evaluation of vibrational energy

The internal energy and specific heat at constant volume can be described in terms of either Debye or Einstein model with a constant Θ_D or Θ_E . Alternately one can incorporate the temperature dependence of Θ_D via Grüneisen parameter defined in Eq. (3.45) [45]. In the current study, we however adopted a constant value of Θ_D as this gives satisfactory results. The temperature dependence of E_{vib} as well as C_v have been estimated using the Debye formula [45]. The choice of this formula is that it satisfactorily approximates the integral especially at the low temperature. In terms of Debye model, the vibrational free energy can be written as [44-46]

$$E_{vib} = 9NK_B T \left(T/\theta_D \right)^3 \int_0^{x_D} D \left(x^3 dx / (e^x - 1) \right) \quad (3.59)$$

In above expression $x_D = \theta_D/T$ and θ_D is Debye temperature. The Debye temperature in the present study has been taken from the literature and preference is given for calorimetric based data. On the other hand, the estimation of other parameters namely, isothermal bulk modulus B_T , its pressure derivative B'_T and Grüneisen parameter γ_G are discussed in the following sections.

3.8.2. Estimation of isothermal bulk modulus and its pressure derivative

In order to obtain a reliable estimate of isothermal bulk modulus and its partial derivative first we have scrutinized the literature and given the priority to P - V based data. The available P - V data has been re-analyzed in the present study using linearized form of Murnaghan equation of state given by Smith [49]. Therefore, the advantage of this linear transformation of raw P - V data is that appropriate choice of the empirical equation of state can be made for proper treatment of the experimental data. The equation which relates the scaled P - V quantities is given below [48].

$$P/\mu = (B_T)^{1/2} + s[P\mu]^{1/2}. \quad (3.60)$$

In the above equation, $\mu = 1-V/V_o$ and $s = (B'_T+1)/4$; V_o is the volume at atmospheric pressure, V is volume at any pressure P .

In the second scheme we have collected the data on isothermal bulk modulus and corresponding lattice parameter for different homologous compounds. Based on previous systematic studies carried out on minerals [45], it is well known that bulk modulus and corresponding molar volume for homologous compounds or elements obey the following relation.

$$B_T V^n \cong \text{constant} \quad (3.61)$$

The above equation holds good for many isostructural elementals and compounds.

3.8.3. Estimation of Grüneisen parameter

The other important quantity required for calculating the temperature dependence of volume under Debye-Grüneisen formalism is the Grüneisen parameter (γ_G). There are various methods which have been adopted to calculate γ_G in terms of experimentally measured thermo physical properties or based on lattice dynamics [45]. There are two types of Grüneisen parameters one of which is known as macroscopic or thermal Grüneisen parameter and other is referred as microscopic Grüneisen parameter. Thermal Grüneisen parameter can be evaluated either in terms of macroscopic first order properties that includes heat capacity, thermal expansivity, bulk modulus and molar volume or in terms of equation of state properties such as pressure derivative of bulk modulus [45]. Thus, Grüneisen parameter in terms of macroscopic physical properties can be written as follows [43].

$$\gamma_G = \alpha_V B_T V / C_V = \alpha_V B_S V / C_P. \quad (3.62)$$

On the other hand if one considers the theory of lattice dynamics then the Grüneisen parameter can be evaluated in terms of intrinsic elastic constants. In the

present case for evaluating γ_G , the famous equation of state known as Slater formula which has been employed and the respective formula can be written as follow.

$$\gamma_G = 1/2 \left(dB_T/dP \right) - 1/6 \quad (3.63)$$

If for a given material B'_T is known then γ_G can be calculated using above equation.

3.8.4. Calculation of thermal expansivity and heat capacity

Having thus estimated all the required quantities, the temperature dependence of volume can be calculated using Eq. (3.58). Further from the derivative of Eq. (3.58) gives thermal expansivity data and it is expressed in Eq. (3.64).

$$\alpha_V = \left[\frac{(Q_o C_V)}{\{r(r-1)E_{vib}^2 - Q_o E_{vib}(2r-1) + Q_o^2\}} \right] \quad (3.64)$$

Subsequent to the estimation of thermal expansion, the harmonic contribution to isochoric heat capacity C^h_v has been estimated from the temperature derivative of Eq. (3.59). The dilatational and the electronic contributions to heat capacity have been estimated from the following relation [45].

$$C_p = C^h_v (1 + \alpha_V \gamma_G T) + I_e T. \quad (3.65)$$

The last term, $(I_e T)$ accounts for the small, linear electronic contribution to the heat capacity. The details regarding the actual implementation of Debye-Gruneisen model for obtaining self consistent estimates of thermal expansion and heat capacity for UFe_2 and URh_3 intermetallic compounds are presented in **Chapter 7**.

3.9. References

1. P. R. Roy, "Phase Transitions", Pergamon Press, New York (1973).
2. A. K. Jena and M. C. Chaturvedi "Phase Transformations in Materials", Prentice Hall, New Jersey (1991).
3. C. N. R. Rao and K.J. Rao, "Phase Transitions in Solids", McGraw-Hill, New York (1978).
4. V. Raghavan, "Solid State Phase Transformations", Prentice-Hall of India, New Delhi (1992).
5. J. E. Ricci, "The Phase Rule and Heterogeneous Equilibria", Van Nostrand, New York (1951).
6. J. W. Christian, "The Theory of Transformations in Metals and Alloys". Pergamon Press, Oxford (1965).
7. D. A. Porter, K.E. Easterling and M. Y. Sherif, "Phase Transformations in Metals and Alloys", CRC Press Taylor and Francis Group, New York. (1981).
8. D. Turnbull, Solid state physics: Advances in research and applications, Vol. 3, Academic Press, New York (1956).
9. W. A. Johnson and R.F. Mehl, Trans. Am. Inst. Min. (Metall.) Eng., 135 (1939) 416.
10. M. Avrami, J. Chem. Phys., 7 (1939) 1103.
11. M. Avrami, J. Chem. Phys., 8 (1940) 212.
12. M. Avrami, J. Chem. Phys., 9 (1941) 177.
13. A. N. Kolmogorov: Izv. Akad. Nauk SSSR Ser. Mat., 3(1937) 355.
14. E. J. Mittemeijer, J. Mat. Sci., 27 (1992) 3977.
15. Y. C. Liu, F. Sommer and E. J. Mittemeijer, Acta Mater., 54 (2006) 3383.
16. P. Kruger, J. Phys. Chem. Solids, 54 (1993) 1549.
17. F. Liu, F. Sommer and E. J. Mittemeijer, Int. Mater. Rev., 52 (2007) 193.

18. F. S. Ham, *J. Phys. Chem. Solids*, 6 (1958) 355.
19. R. Benedictus, A. Böttger and E.J. Mittemeijer, *Zeitschrift für Metallkunde*, 89 (1998) 168.
20. J. Sietsma and S. van der Zwaag, *Acta Mater.*, 52 (2004) 4143.
21. R. G. Thiessen, I. M. Richardson and J. Sietsma, *Mater. Sci. Engg.*, 247 A (2006) 223.
22. J. A. Martins and J. J. C. Cruz-Pinta, *Thermochim. Acta*, 332 (1995) 179.
23. E. Gmelin and S. M. Sarge, *Thermochim. Acta*, 347 (2000) 9.
24. A. T. W. Kempen, F. Sommer and E. J. Mittemeijer, *Thermochim. Acta*, 383 (2002) 23.
25. M. J. Starink, *Thermochim. Acta*, 404 (2003) 163.
26. M. T. Todinov, *Acta Mater.*, 44 (1996) 4697.
27. I. I. Boyadjiev, P. F. Thompson, and Y. C. Lam, *ISIJ Int.*, 36 (1996) 1413.
28. Y. Zhu and J. Devletian, *J. Mat. Sci.*, 26 (1991) 6218.
29. C. A. Apple and G. Krauss, *Acta Metall.*, 20 (1972) 849.
30. W. J. Kaluba, R. Taillard and J. Foct, *Acta Mater.*, 46 (1998) 5917.
31. H. Mehrer, "Diffusion in solid metals and alloys", *Landolt-Bornstein New Series*, III/26, (Series Eds. K.-H. Hellwege and A. M. Hellwege), Springer, Heidelberg (1990).
32. D. P. Koistinen and R. E. Marburger, *Acta Metall.*, 7 (1959) 59.
33. C. L. Magee, in: *Phase Transformations*, ASM Metals Park, OH, (1968), p.118.
34. I. Sinha, R.K. Mandal, *J. Non-Cryst. Solids* 355 (2009) 361.
35. I. Sinha, R.K. Mandal, *J. Non-Cryst. Solids* 357 (2011) 919.
36. A. R. Oganov, J. P. Brodholt, and G. D. Price, *Phys. Earth Planet. Inter.*, 122 (2000) 277.
37. A. Chopelas, *Phys. Earth Planet. Inter.*, 98 (1996) 3.

38. O. L. Anderson and K. Masuda, *Phys. Earth Planet. Inter.*, 85, (1994) 227.
39. B. B. Karki, R. M. Wentzcovitch, S. De Gironcoli, and S. Baroni, *Phys. Rev.*, 61 B, (1999) 8793.
40. M. Matsui, G. D. Price and A. Patel, *Geophys. Rev. Lett.*, 21 (1994) 1659.
41. I. Inbar and R. E. Cohen, *Geophys. Rev. Lett.*, 22 (1995) 1533.
42. B. Bertheville, H. Bill, and H. Hagemann, *J. Phys.: Condens. Matter.*, 10 (1998) 2155.
43. G. Kern, G. Kresse and J. Hafner, *Phys. Rev.*, 59B (1999) 8551.
44. D. C. Wallace, *Thermodynamics of Crystals*, Wiley, New York (1972).
45. O. L. Anderson, *Equation of state of solid for Geophysics and Ceramic Science*, Oxford University press, New York (1995).
46. T. H. K. Barron, J. G. Collins and G. K. White, *Thermal expansion of solids at low temperature*, *Adv. Phys.*, 29 (4) (1980) 609.
47. R. Jose, S. Raju, R. Divakar, E. Mohandas, G. Panneerselvam, M. P. Antony and K. Sivasubramanian, *J. Nucl. Mater.* 317 (2003) 54.
48. Arun Kumar Rai, Haraprasanna Tripathy, B. Jeyaganesh and S. Raju, *J. Nucl. Mater.*, 427 (2012) 378.
49. G. S. Smith, *A. Phys. Lett.*, 140 A (1989) 431.
50. Arun Kumar Rai and S. Raju, *J. Therm. Anal. Calorim.*, 112 (2013) 73.

Chapter 4

Investigation of Effect of Heating/Cooling Rates on Phase Transformation in Uranium using Calorimetry

4.1. Introduction

In **chapter 1**, the relevance of study of the phase stability and phase transformation kinetics in U-Zr, U-Fe and U-Rh alloys in context to the fast reactor program has already been discussed. Before starting study on these alloy systems, it is decided to investigate the role of heating and cooling rates on the structural phase changes in uranium. This is because a clear enunciation of relevant issues in a relatively simple and relevant system as pure uranium is vital to evolving a proper appreciation of composition mediated effects in Uranium based alloys. Hence, before proceeding further, brief information related to phase transformation kinetics on uranium are presented here.

It has already been discussed that uranium exists in three allotropic modifications namely α -orthorhombic, β -tetragonal and γ -bcc, in the order of increasing temperature [1]. Owing to the fact that uranium being a reactive metal and is prone to easy oxidation and picking up of impurities, a certain scatter is found among the reported values for the transformation temperatures in literature [1-6]. According to the recent assessment of U-Zr phase diagram by Okamoto uranium undergoes two polymorphic transformations $\alpha \rightarrow \beta$ and $\beta \rightarrow \gamma$ at temperature of about 941 K (668°C) and 1049 K (776°C) respectively [7]. The allotropic phase changes in pure uranium have attracted a great deal of interest right from the early days of research on actinide metallurgy [8–18]. Thus for example, it has been established that both $\gamma \rightarrow \beta$ and $\beta \rightarrow \alpha$ transformation temperatures are very sensitive to the cooling rate from the high temperature γ -bcc phase [15]. A highly non-linear decrease in the transformation temperatures with increasing rate of cooling in the range, 10^0 to 10^4 K sec⁻¹ has been found [15]. A similar scenario is witnessed during heating for the $\alpha \rightarrow \beta$ transformation as well for a smaller range of heating rate variation [2]. These early studies clearly revealed that it is rather difficult to quench and retain the intermediate β phase in pure uranium at room temperature, since the $\beta \rightarrow \alpha$

transformation kinetics is very rapid and it becomes necessary to alloy uranium with small amounts of transition element to stabilise the β phase at room temperature [8]. It has been convincingly argued by Burke [16] following a critical appraisal of the experimental findings available then [8-15], that the $\beta \rightarrow \alpha$ structural change can assume different mechanisms under different cooling rate regimes. In fact a TTT curve with two noses that are separated by a plateau has been established for the formation of α phase from β phase [9, 16]. It must be added that there exists an extensive literature on the physical metallurgy of uranium alloys covering thermodynamic, structural and phase transformation aspects [1, 8]. Nevertheless, many issues related to the fundamental kinetic aspects of these phase changes still remain unclear [8, 17, 18]. A comprehensive account of the intricacies of the $\alpha \leftrightarrow \beta$ phase transformation in uranium is provided by Vandermeer, who used dilatometry and metallography to monitor the β formation kinetics [18]. This study supported that kinetics of $\beta \rightarrow \alpha$ transformation is massive in nature based on the light microscopy characterisation and Turnbull's theory of interface controlled phase transformation [19]. Subsequent to Vandermeer's study not much progress has been made in explaining the basic issues of various phase transformations in uranium and its alloys. Subsequent to this study, to the best of our knowledge, we are not aware of any controlled thermal analysis investigation of the transformation kinetics at the lower end of the heating and cooling rate spectrum in the recent past.

In this context, in the present study, characterisation of phase transformations in reactor grade uranium using differential scanning calorimetry (DSC) has been taken up. The kinetic aspects of allotropic phase changes in uranium are studied as a function of heating/cooling rate in the range 10^0 to 10^2 K min⁻¹ by DSC. Further, the results obtained for the $\alpha \rightarrow \beta$ and $\beta \rightarrow \gamma$ transformations during heating confirm to the standard Kolmogorov-Johnson-Mehl-Avrami (KJMA) model for a nucleation and growth

mediated process. The kinetics of $\gamma \rightarrow \beta$ phase change on the other hand is best described by the two-parameter Koistinen-Marburger empirical relation for the martensitic transformation. However the kinetics of $\beta \rightarrow \alpha$ transformation is modelled using another empirical relation given by Kamamoto.

4.2. Experimental Details

The detail about the uranium melting, its composition (**table 2.1**) is already presented in **chapter 2** along with the experimental detail about differential scanning calorimetry (DSC). Therefore in this present chapter only the results part will be discussed in the ensuing sections.

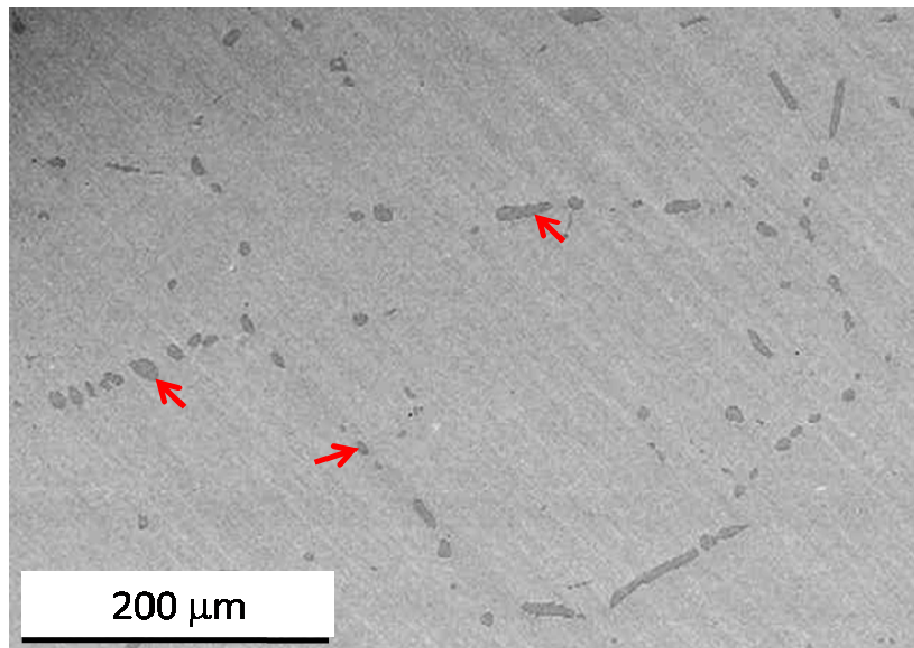


Fig. 4.1. SEM micrograph obtained for uranium annealed at 800°C for 10h

4.3. Results

4.3.1 Preliminary Characterization

The SEM micrograph of reactor grade uranium annealed at 1273 K (800°C) for 10h is shown in **figure 4.1**. As can be seen, the grain size of the starting microstructure is rather large and is estimated to be in the range 350 to 400 μm . The necklace like

decoration of the α -phase grain boundary marked by arrows in **figure 4.1** is due to coarse uranium silicide particles which are also identified using EDX spectra shown in **figure 4.2**. Further XRD pattern obtained for uranium given the same annealing treatment is

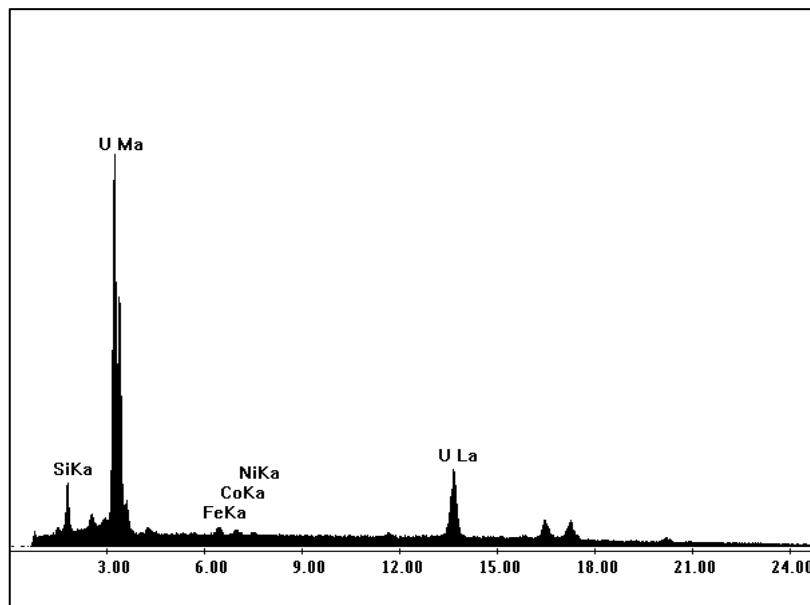


Fig. 4.2. EDX spectrum from the particle shown by arrow in **figure 4.1**

presented in **figure 4.3**. From the XRD pattern it is clear that the annealed microstructure of uranium contain only the orthorhombic α -phase. No extra peak related to uranium silicide is noticed in the present XRD results. With all these results it can be stated that the uranium used in the present study is fairly pure besides the presence of some impurities of C, O and Si (see **table 2.1**).

4.3.2. Transformation peak profiles and transformation temperatures

In **figure 4.4**, a typical DSC profile obtained during a 3 K min^{-1} heating and cooling schedule is displayed. Very sharp transformation peaks associated with the heat effects of $\alpha \leftrightarrow \beta$ and $\beta \leftrightarrow \gamma$ transformations are clearly revealed. A considerable degree of undercooling is also noticed for both $\gamma \rightarrow \beta$ and $\beta \rightarrow \alpha$ transformations. Further, a careful inspection of the $\alpha \rightarrow \beta$ endothermic transformation peak indicates the presence of a very

weakly discernible shoulder like feature. This is more clearly brought out in **figure 4.5(a)**, wherein the $\alpha \rightarrow \beta$ peak profiles observed for smaller heating rates ($1-30 \text{ K min}^{-1}$)

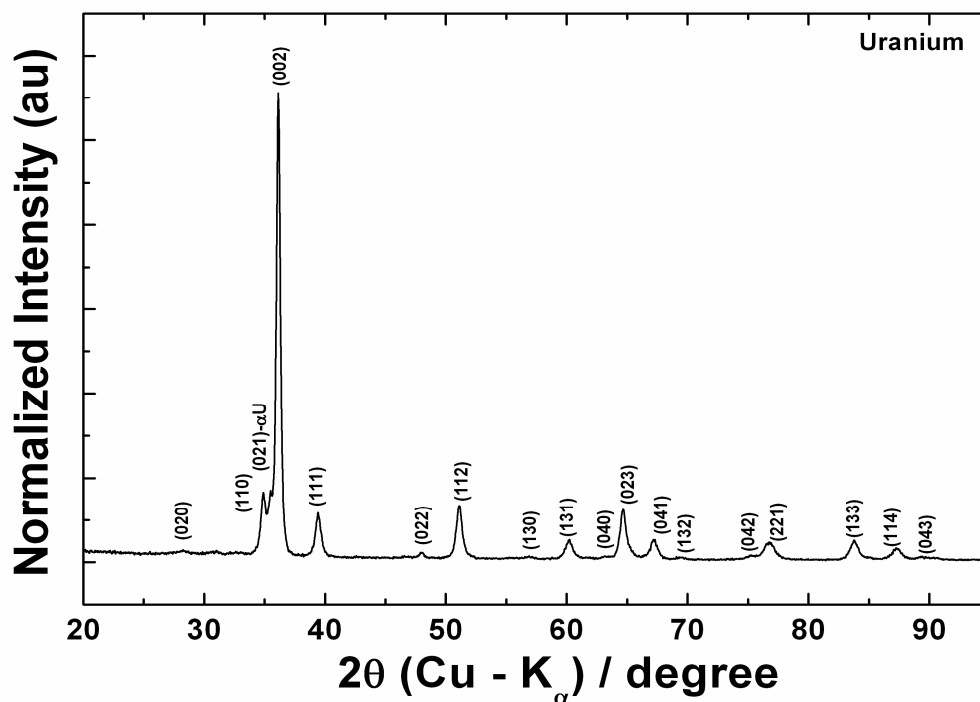


Fig. 4.3. XRD pattern obtained for uranium annealed at 800°C for 10h

are collated together. Further, the peak profiles for $\alpha \rightarrow \beta$ transformation for higher heating rates ($40-99 \text{ k min}^{-1}$) are portrayed in **figure 4.5 (b)**. In order to enhance clarity, we have sketched only the transformation profile zone using the no-sample base-line subtracted DSC profiles and this base line compensation is done for each scan rate independently.

Since the present study focuses on the transformation kinetics, the mapping of the ordinate of DSC plot in terms of heat flow rate is not done here. Further the DSC peak profiles obtained at different heating/cooling rates are normalized with the mass of samples. A clear shoulder like feature is noticed for $1, 3,$ and 5 K min^{-1} heating rate scans. In fact, this shoulder is fairly resolved only for very low heating rate scans, and is found to gradually merge with the main part of the peak profile as the heating rate is increased (compare, **figure 4.5 (a)&(b)**). A similar set of transformation peak

profiles are obtained for the $\beta \rightarrow \gamma$ phase change as well; but with the difference that no specific shoulder like splitting is seen in this case for low heating rate scans. The

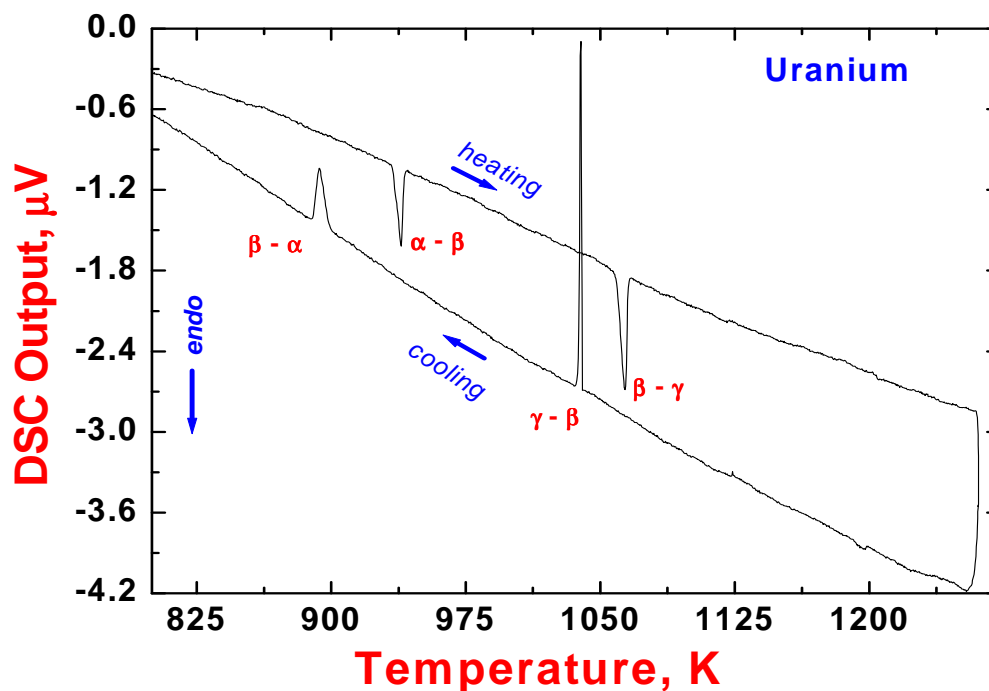


Fig.4.4. A typical DSC profile obtained for uranium at the scan rate of 3 K min^{-1}

individual peak profiles are not presented here in order to avoid unnecessary proliferation of graphical information. In **figure 4.6**, the heating or cooling rate (β) induced variations of transformation start (T_s), peak (T_p) and finish temperatures (T_f) for both $\alpha \leftrightarrow \beta$ and $\beta \leftrightarrow \gamma$ transformations are graphically illustrated. Although a general increase (decrease) of the transformation temperatures to varying extents with heating (cooling) rate is clearly revealed in **figure 4.6**, it is nevertheless interesting to note that this increase is highly non-linear in nature. This non-linear behaviour is quite remarkably revealed in the heating rate variation of T_f , the transformation finish temperature. On the contrary, the T_s temperature after a clear initial increase at the slow heating rate regime ($2\text{-}7 \text{ K min}^{-1}$) evinces a sort of plateau for higher values of β . As a result, the width of the transformation domain given by the temperature interval $T_f - T_s$, increases effectively with increasing heating rate, implying thereby a kinetics induced expansion of $(\alpha + \beta)$ and

($\beta+\gamma$) two phase fields at higher heating rates. The transformation temperatures for both $\alpha\rightarrow\beta$ and $\beta\rightarrow\gamma$ structural changes measured for the slowest heating rate of 1 K min^{-1} recorded in the present work are 936 K (663°C) and 1056 K (783°C) respectively.

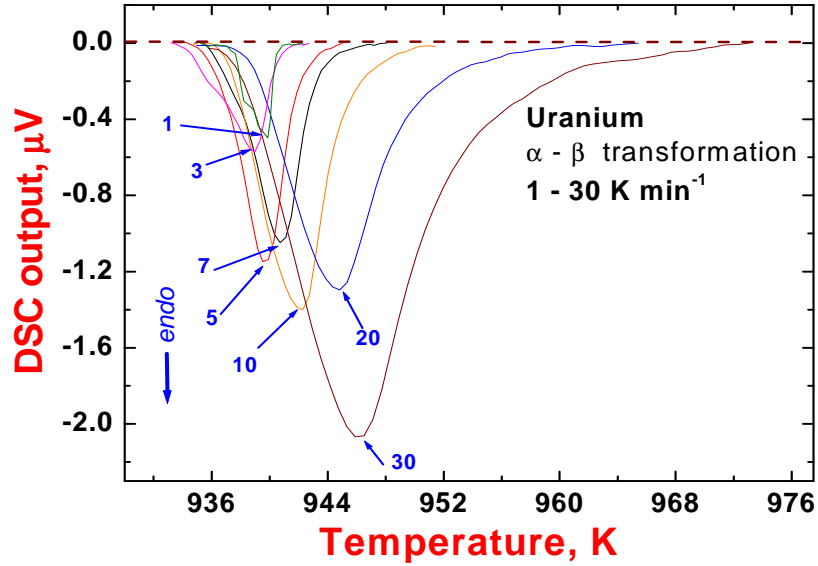


Fig.4.5(a). The DSC profiles for the $\alpha\rightarrow\beta$ transformation obtained at lower heating rates are stacked together ($1\text{-}30\text{ K min}^{-1}$).

Notwithstanding the presence of impurities in our starting material and the invariable

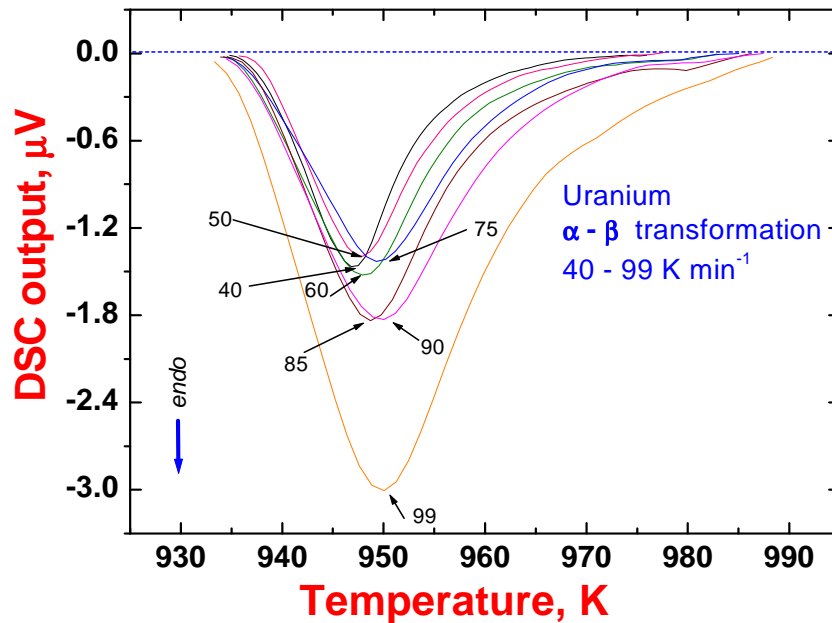


Fig.4.5(b). The DSC profiles for the $\alpha\rightarrow\beta$ transformation obtained at higher heating rates are stacked together ($40\text{-}99\text{ K min}^{-1}$).

presence of thermal lag in the DSC equipment (the influence of this factor has been minimised by proper temperature calibration; but not altogether eliminated), these values are fairly in agreement with the ones quoted in the literature for the equilibrium transformation temperature [1, 2]. One final point to note in **figure 4.6**, is that for the $\beta \rightarrow \alpha$ phase change, the observed T_s value for 99 K min^{-1} seems to be somewhat higher,

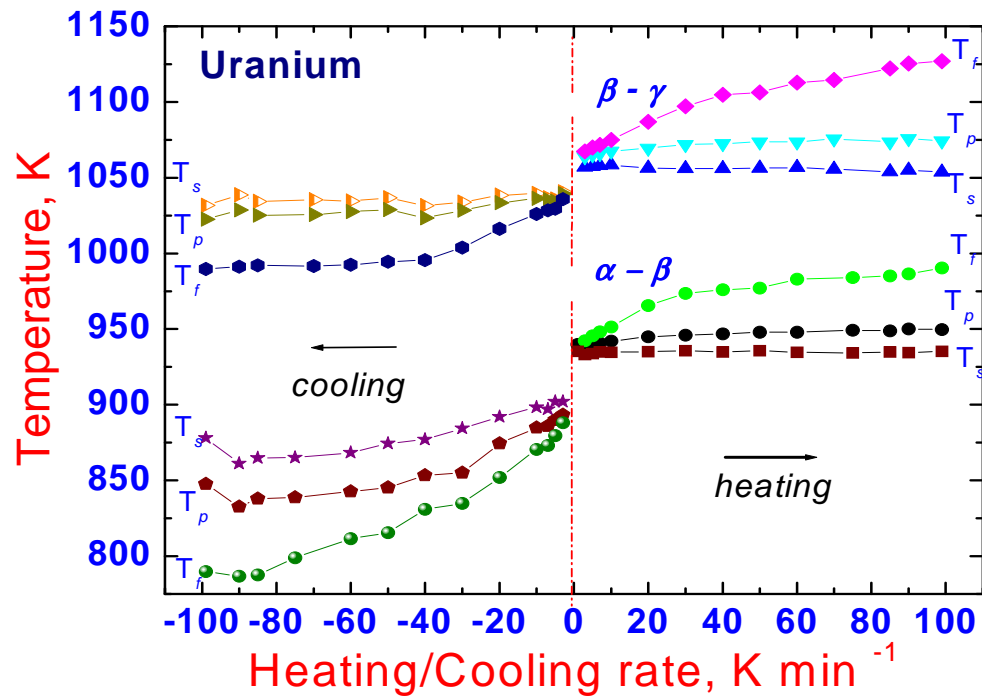


Fig.4.6. The non-linear variation of the transformation start (T_s), peak (T_p) and finish (T_f) temperatures with heating / cooling rate for $\alpha \leftrightarrow \beta$ and $\beta \leftrightarrow \gamma$ transformations

which is contrary to the expected decreasing trend. Since in the present study, higher than 100 K min^{-1} cooling could not be achieved, it could not be ascertained by higher cooling rate experiments as to whether this upheaval represents a genuine physical effect like the onset of a new plateau, or is it arising from the unavoidable experimental scatter.

In **figures 4.7(a) and 4.7(b)** the DSC peak profiles of $\gamma \rightarrow \beta$ and $\beta \rightarrow \alpha$ transformations that occur during the cooling part of thermal cycle are illustrated. Again, for the sake of brevity, only the low heating rate traces are presented. As a general remark, it may be

added that the $\gamma \rightarrow \beta$ peak profiles are fairly sharp and smooth for the entire range of cooling rate adopted in this study; on the contrary, the $\beta \rightarrow \alpha$ profiles contained some undulations for slow heating rates (*see*, the circled region in 1 K min^{-1} scan in **figure 4.7(b)**). The cooling rate dependencies of respective transformation temperatures are illustrated in the left half of the composite **figure 4.6**. Again the non-linear variation of the transformation temperatures with respect to cooling rate is readily apparent. For a given cooling rate say 1 K min^{-1} , the observed transformation start (T_s) temperatures for

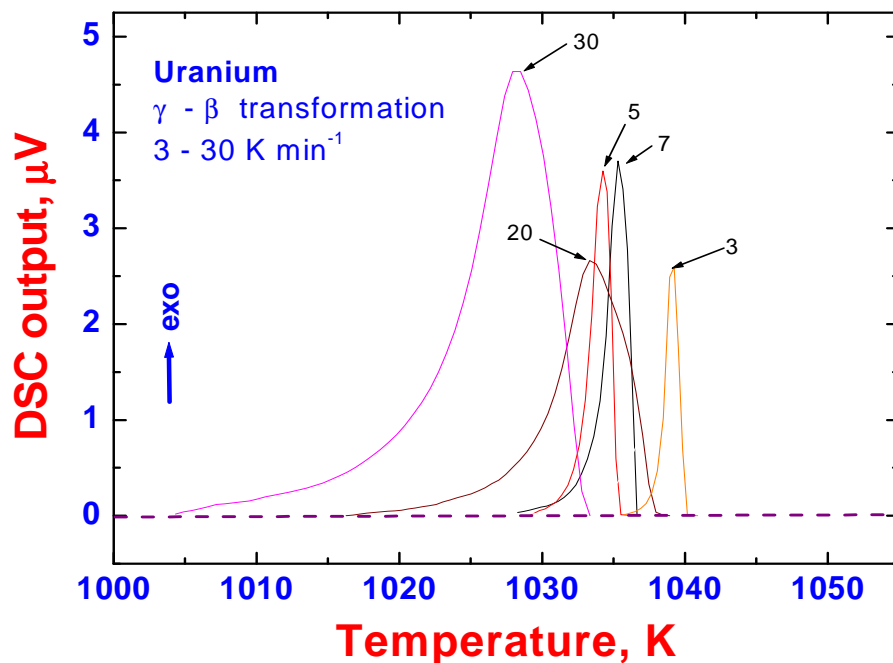


Fig.4.7(a). DSC profiles for the $\gamma \rightarrow \beta$ transformation during cooling

$\gamma \rightarrow \beta$ and $\beta \rightarrow \alpha$ transformations are 1038 K (765°C) and 913 K (640°C) respectively.

4.3.3. Transformation plots

From the experimental DSC peak profile, the fractional extent of transformation as a function of temperature $X(T)$ can be calculated by recalling the expression given in Eq. (3.37) of **chapter 3** as follow.

$$X(T) = \frac{\int_{T_s}^T \varphi(T) dT}{\int_{T_s}^{T_f} \varphi(T) dT} \quad (4.1)$$

In above equation, the integral in the numerator, namely, $\int_{T_s}^T \varphi(T) dT$, stands for the partial area under the peak in the temperature domain T_s-T . The denominator $\int_{T_s}^{T_f} \varphi(T)$

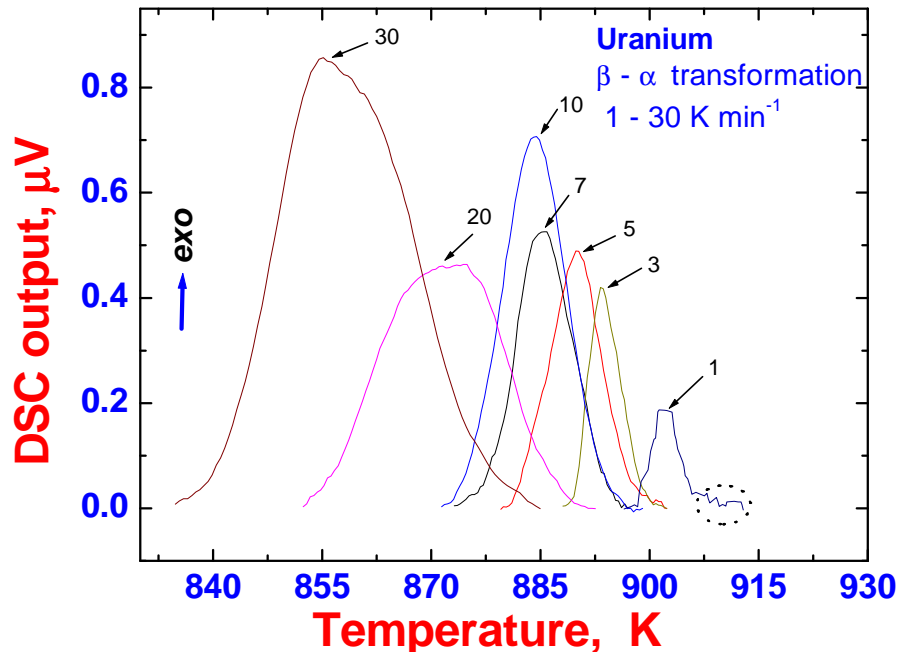


Fig.4.7 (b). DSC profiles for the $\beta \rightarrow \alpha$ transformation during cooling

dT stands for the total peak area covering the entire transformation temperature range (T_s-T_f). *Eq.* (4.1) assumes that transformation is complete upon reaching T_f , although this is certainly not true for higher heating rates. The transformation plots obtained using *Eq.* (4.1) are shown in **figure 4.8(a)** for $\alpha \rightarrow \beta$, and in **4.8(b)** for $\beta \rightarrow \gamma$ respectively. In **figures 4.9(a)** and **4.9(b)**, these are presented for $\gamma \rightarrow \beta$ and $\beta \rightarrow \alpha$ transformations respectively.

4.3.4. Empirical description of transformation kinetics

As had been briefly sketched in the introduction, both nucleation and growth and martensitic modes of transformations are found in uranium. In the classical methodology adopted for analysing the kinetics of a nucleation and growth type of transformation as

studied by thermal analysis methods [20-24], the following separable functional representation is often invoked to represent the instantaneous reaction rate, $(\partial X/\partial t)_\beta$ [25].

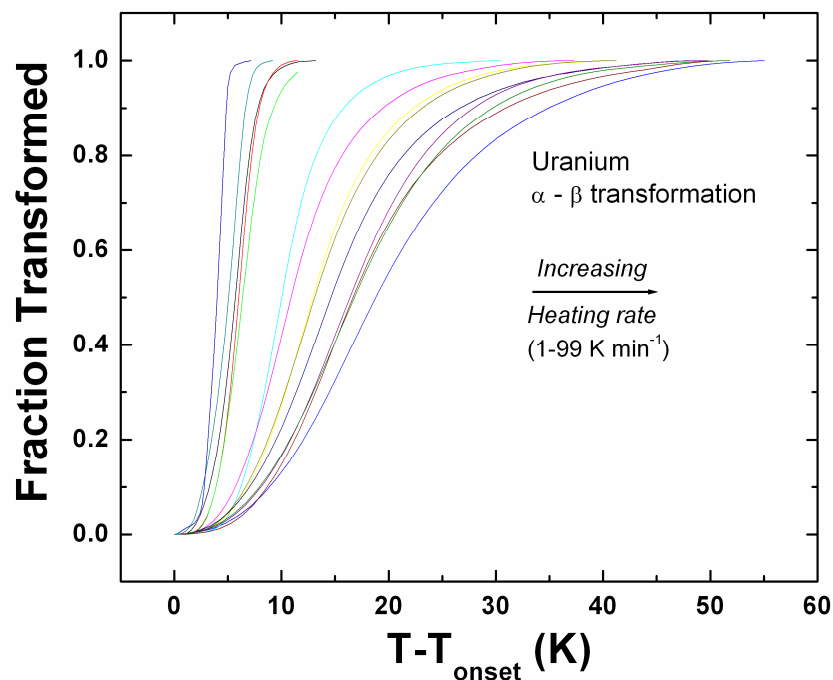


Fig.4.8(a). The transformation plot for $\alpha \rightarrow \beta$ transformation

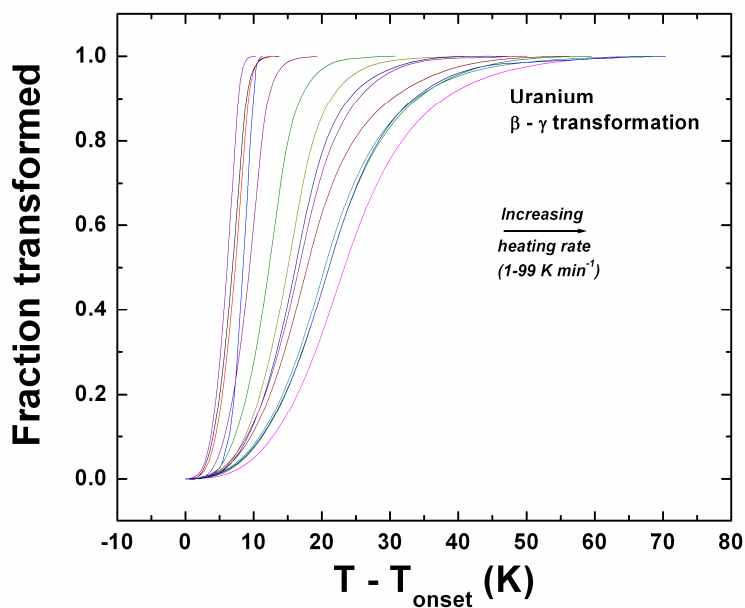


Fig.4.8(b). The transformation plot for $\beta \rightarrow \gamma$ transformation

$$(\partial X/\partial t)_\beta = (\partial X/\partial T)_\beta \times \beta = f(X) k(T). \tag{4.2}$$

In the above expression, $f(X)$ is often taken to be an empirical, but suitable reaction model that is consistent with the established kinetic features of the transformation under consideration. The empirical rate constant $k(T)$ is normally assumed to be of the

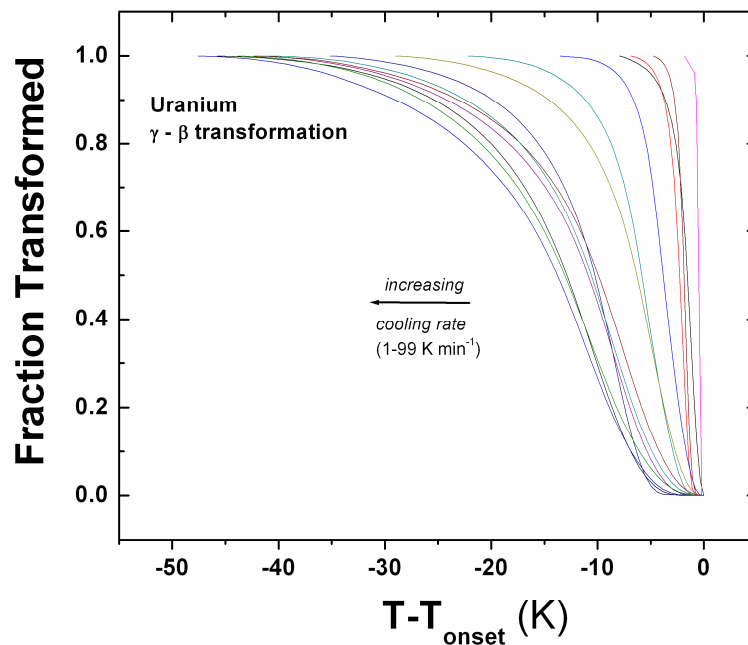


Fig.4.9(a). The transformation plot for $\gamma \rightarrow \beta$ transformation

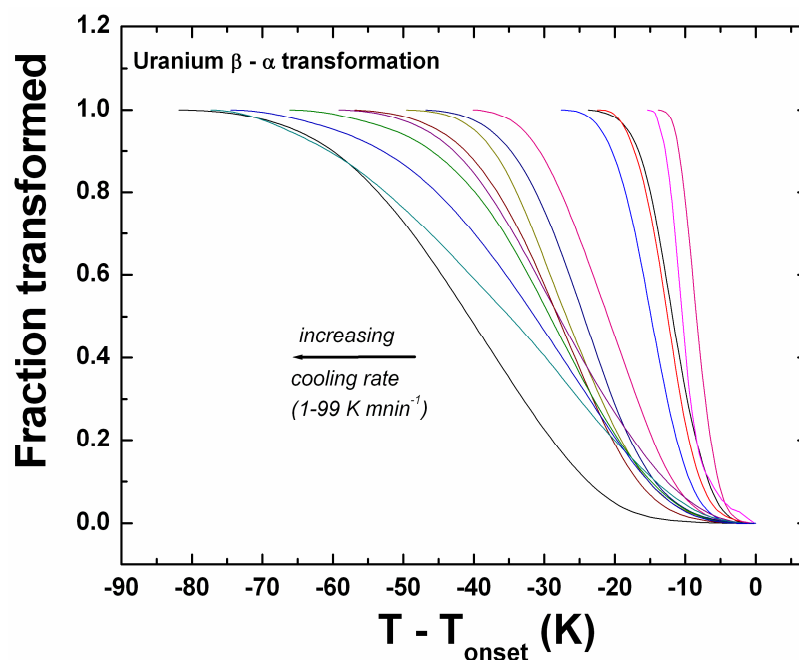


Fig.4.9(b). The transformation plot for $\beta \rightarrow \alpha$ transformation

Arrhenius form as already discussed in **chapter 3**.

$$k = k_0 \exp(-Q_{eff}/RT), \quad (4.3)$$

with Q_{eff} being the *effective or apparent* activation energy for the *overall transformation process*. In general terms, Q_{eff} must be treated as dependent on the transformation extent $X(T)$ as well, but for reasons of convenience and simplicity, it is often taken to be a constant. A few technical points need be elaborated with regard to the application of *Eq. (4.2)* in explaining the non-isothermal reaction kinetics. It is a standard practice to use *Eq. (4.2)* in conjunction with the additivity rule for explaining the transformation kinetics occurring during continuous heating or cooling [26]. It must be admitted however, that in a rigorous sense *Eq. (4.2)* is incorrect for representing the continuous transformation kinetics, when the law of additivity itself is violated due to the possible non-isokinetic character of the transformation concerned [27]. Such a situation could arise due to changing nucleation, growth or impingement conditions as the transformation gradually progresses towards completion. As an alternative to the combination of isothermal KJMA plus additivity rule, one may adopt the approach followed by Mittemeijer and his group in their study of solid state transformation kinetics by thermal analysis methods [21]. Here, the reaction rate is taken to be a function solely of a path variable that implicitly expresses the thermal history of the sample during the course of transformation. It has been shown that a formal Kolmogorov-Johnson-Mehl-Avrami (KJMA) type integral expression for the fraction transformed $X(T)$, can be derived for practical applications under certain restrictions placed on the type of nucleation, growth and impingement process (*see chapter 3*) [21, 28]. Under such simplified conditions, Q_{eff} can be identified with a physically based model of nucleation and growth [28]; in fact, it can be shown that Q_{eff} is actually a weighted sum of individual activation energies involved in nucleation and growth processes [28]. In any case, the kinetic parameters of a true rate equation are a function of both X and T and the adoption of a separable rate expression like *Eq. (4.2)* is essentially a crude approximation to the real non-linear state

of affairs [29]. With this understanding, we adopt in this thesis a relatively simple non-isothermal form of KJMA expression for fitting the transformation data of nucleation and growth phenomenon.

Table 4.1						
Listing of the kinetics parameters estimated for the $\alpha \rightarrow \beta$ transformation using Eq. (4.4).						
Heating rate (β) (K min ⁻¹)	Q_{eff} (kJ mol ⁻¹)	$k_o \times 10^{11}$ (s ⁻¹)	n	k (s ⁻¹)	k/β (K ⁻¹)	R ² value for the fit
1	180±1	2.1±0.2	3.6±0.01	21	1231	0.99
3	176±1	2.2±0.1	3.1±0.02	40	718	0.99
5	174±2	3.0±0.4	2.9±0.01	61	724	0.99
7	176±2	4.0±0.1	2.7±0.03	63	541	0.99
10	182±1	7.3±0.1	2.6±0.01	57	344	0.99
20	186±3	10.9±0.2	2.4±0.04	55	164	0.99
30	188±1	14.8±0.3	2.3±0.01	61	123	0.99
40	190±1	18.6±0.2	2.2±0.02	58	89	0.99
50	191±1	24.8±0.4	2.1±0.07	71	85	0.99
60	193±2	30.6±0.8	2.1±0.08	67	67	0.99
75	194±2	33.3±1.2	1.9±0.01	72	58	0.99
85	195±2	43.0±1.5	1.9±0.02	75	53	0.99
90	197±1	50.6±2.2	1.9±0.02	77	52	0.99
99	199±3	56.3±3.2	1.8±0.01	63	38	0.99

In the present study, for the $\alpha \rightarrow \beta$ and $\beta \rightarrow \gamma$ transformations, the following non-isothermal version of the Kolmogorov-Johnson-Mehl-Avrami (KJMA) formalism for the fraction transformed X(T) as a function of temperature at constant heating rate (β) (see **chapter 3**) is adopted [21].

$$X(T) = 1 - \exp\{-k^n [R(T-T_s)^2/\beta Q_{\text{eff}}]^n\}. \quad (4.4)$$

The above expression assumes site saturation type of nucleation. It may be noted that in the above model, we have chosen T-T_s, the temperature increment with respect to the

experimentally observed threshold or onset temperature (T_s) as the independent variable, since this corrects in an apparent manner for the error incurred in not accounting precisely for the true start of the transformation corresponding to near zero transformed fraction ($X = 0$). The Arrhenius rate constant k is given by Eq. (4.3). n is the so-called Avrami or transformation exponent, whose theoretical value (ranging from 0.5 to 4) depends on whether the transformation is bulk diffusion or interface controlled, besides

Heating rate (β) (K min ⁻¹)	Q_{eff} (kJ mol ⁻¹)	$k_o \times 10^{11}$ (s ⁻¹)	n	k (s ⁻¹)	k/β (K ⁻¹)	R ² value for the fit
1	159±2	2.5±0.3	3.17±0.01	4	242	0.99
3	147±1	3.5±0.5	3.12±0.01	20	407	0.99
5	143±2	2.5±0.1	2.98±0.01	24	283	0.99
7	143±1	3.7±0.1	2.76±0.03	37	312	0.99
10	144±3	3.2±0.2	2.68±0.02	29	171	0.99
20	151±1	7.6±0.4	2.48±0.05	33	100	0.99
30	154±1	10.3±1.1	2.31±0.01	33	66	0.99
40	155±2	12.4±1.2	2.25±0.04	37	55	0.99
50	155±1	14.3±2.1	2.18±0.01	43	51	0.99
60	157±3	18.2±2.2	2.08±0.02	40	40	0.99
75	164±2	34.7±3.1	1.99±0.05	39	30	0.99
85	165±2	48.1±3.5	1.93±0.08	45	32	0.99
90	166±1	52.9±4.1	1.88±0.02	48	32	0.99
99	175±1	128.7±8.1	1.85±0.01	41	25	0.99

the dimensionality of growth. Since, only allotropic transformations are being dealt with here, the transformation kinetics is taken to be interface controlled. The dimensionality of growth may take various values. The experimental $X(T)$ data for both the on-heating

transformations, namely the $\alpha \rightarrow \beta$ and $\beta \rightarrow \gamma$ are fitted using Eq. (4.4) by means of a standard non-linear optimisation routine and the resulting values for the kinetic quantities namely Q_{eff} , k_0 , and n are listed in **table 4.1** for the $\alpha \rightarrow \beta$ phase change. **Table 4.2** presents the same information for $\beta \rightarrow \gamma$ phase change. As may be judged from these tables, the value of n for the overall transformation kinetics exhibits a gradual decrease with increasing heating rate, suggesting thereby the changing role of nucleation and growth characteristics with the extent of transformation. The value of n for both $\alpha \rightarrow \beta$ and $\beta \rightarrow \gamma$ transformations is found to be varying in the range of 1.8-3.6; which suggest that kinetics is of interface controlled. The apparent overall activation energy Q_{eff} shows a mild increase with respect to β . Putting it more candidly, the ratio k/β , representing the heating rate normalised value of the rate constant, exhibits a remarkable decrease with increasing heating rate. While the physical implication of this point will be addressed in the discussion section, it is sufficient to note here that notwithstanding the theoretical restrictions placed on its applicability, a simplified KJMA model is able to provide a good analytical fit for both $\alpha \rightarrow \beta$ and $\beta \rightarrow \gamma$ transformation kinetics.

4.3.5. Transformation kinetics upon cooling

An attempt to fit the $X(T)$ data for the $\gamma \rightarrow \beta$ transformation on cooling by means of Eq. (4.4) turned out to be unsuccessful. This is in a sense expected, since this reverse transformation on cooling is known to be non-diffusional in character [8]. Further, the transformation plots obtained in the present study are also non-sigmoidal in character (*see, figure 4.9 (a)*) suggesting thereby the inapplicability of the standard KJMA formalism for modelling the displacive transformation kinetics. In view of this, we have invoked the following empirical expression given in Eq. (4.5) for fitting the temperature dependent progression of the $\gamma \rightarrow \beta$ martensitic transformation.

$$X(T) = \exp \{ -[(b'/\beta) (T_s - T)]^n \}. \quad (4.5)$$

In the above expression, β is the cooling rate in K sec^{-1} , T_s is the onset temperature in Kelvin and n is a constant. By setting $(b'/\beta)^n = b$, a simple two parameter description of $\gamma \rightarrow \beta$ transformation after the well-known empirical framework of Koistinen and

$\gamma \rightarrow \beta$				$\beta \rightarrow \alpha$		
Cooling rate (β) (K min^{-1})	b' (s^{-1})	n	R^2 Value for the fit	b (K s^{-1})	n	R^2 value for the fit
1	0.05±0.001	-3.2±0.01	0.99	0.03±0.001	5.3±0.03	0.99
3	0.03±0.002	-4.1±0.01	0.99	0.08±0.001	4.3±0.02	0.99
5	0.04±0.001	-3.4±0.02	0.99	0.14±0.001	3.8±0.01	0.99
7	0.09±0.001	-1.9±0.01	0.99	0.22±0.001	3.4±0.01	0.99
10	0.05±0.003	-2.6±0.01	0.98	0.29±0.001	3.8±0.01	0.99
20	0.07±0.001	-2.5±0.02	0.99	0.58±0.001	3.1±0.02	0.99
30	0.09±0.001	-2.0±0.01	0.99	0.85±0.001	3.4±0.01	0.99
40	0.08±0.001	-2.8±0.10	0.99	1.16±0.002	3.4±0.02	0.99
50	0.09±0.002	-2.2±0.01	0.99	1.57±0.001	2.6±0.01	0.99
60	0.12±0.003	-2.0±0.02	0.99	1.82±0.003	3.2±0.02	0.99
75	0.12±0.001	-2.3±0.01	0.99	2.49±0.002	2.7±0.01	0.99
85	0.16±0.001	-2.2±0.03	0.993	2.66±0.003	2.1±0.02	0.99
90	0.13±0.002	-2.3±0.01	0.99	3.05±0.001	2.3±0.03	0.99
99	0.15±0.001	-2.5±0.02	0.99	2.96±0.004	3.2±0.01	0.99

Marburger (K-M) is readily obtained [30]. It must be added that in the original K-M prescription, n is taken to be unity [30]; but we allowed it to vary here in order to get better numerical agreement. The results of fitting of the present experimental data using Eq. (4.5) are tabulated in **table 4.3**. It is useful to note that just as in the case of $\alpha \rightarrow \beta$ and

$\beta \rightarrow \gamma$ transformations wherein, the value of k/β changed with β , the values for b' also exhibited an increase with increasing cooling rate (**table 4.3**). Since *Eq. (4.5)* is empirical in origin, it is not possible to provide a physicochemical basis for the cooling rate variation of parameter b' . The negative value of n arises from the fact that with positive values for the argument $(T_s - T)$, the transformation extent $X(T)$ increases with decreasing temperature.

In a similar manner, the transformation data $X(T)$ for the $\beta \rightarrow \alpha$ transformation during cooling have also been modelled by the following empirical expression proposed by Kamamoto [31],

$$X(T) = 1 - \exp\{-[b'/\beta \times \tau]^n\}. \quad (4.6)$$

Where, $\tau = (T_s - T)/(T_s - T_f)$, is a dimensionless quantity defined in terms of T_s and T_f . b and n are empirical fit-constants. Again by setting $(b'/\beta)^n = b$, we obtain a simple two parameter model for the variation of transformation extent with temperature. As a passing remark, we may also add that the empirical expression of Kamamoto is not known to have been used for describing displacive transformation kinetics, since it is basically a recasting of a KJMA nucleation and growth type kinetics [32]; but with the major advantage that it provides a better numerical description of certain complicated nucleation and growth kinetics, but with poor interpretability of the fit parameters in terms of a rigorous physical model. Kamamoto's expression is more generic of diffusional transformation kinetics. It should be mentioned here that neither the simplified KJMA (*Eq. (4.4)*) nor the K-M expression (*Eq. (4.5)*) were able to fit satisfactorily the observed $X(T)$ data of $\beta \rightarrow \alpha$ transformation, partly because, this transformation is known to adopt a mixed mode depending upon the cooling rate, as Burke and Dixon have argued long ago [16]. In **table 4.3**, the parameters, b and n obtained by fitting the experimental results to *Eq. (4.6)* are listed.

4.4. Discussion

4.4.1 Nucleation modes and the role of heating rate

The present study clearly brought out the fact that the transformation arrest temperatures for all the allotropic phase changes are found to be strongly dependent on the heating or cooling rate, intact, which is inherent to many nucleation and growth processes and for which quite a few explanations have also been proposed based on established viewpoints on nucleation and growth processes [33]. In the case of uranium, such a finding had been recorded earlier as well; however, to the best of our knowledge a careful reasoning of the underlying physical phenomenon in terms of appropriate metallurgical factors has not been undertaken so far. The present investigation conducted with nearly thermal gradient free small samples, although in a restricted range of (10^0 to 10^2 K min⁻¹) heating and cooling rates, clearly suggests that in case of the $\alpha \rightarrow \beta$ transformation, a split DSC peak profile or a peak with shoulder is observed for slower heating rates, while a standard, single peak is observed for faster rates of heating.

At this point it is rather instructive to recall the fact that very similar observations have recently been recorded by Liu *et al* in their thermal analysis characterisation of the kinetics of $\gamma(\text{fcc}) \rightarrow \alpha(\text{bcc})$ phase change during cooling in fairly large grained pure iron samples [34]. A direct comparison of our result with the findings of Liu *et al* [34] suggests that there could be a possible change in the transformation nucleation mechanism, when the starting grain size exceeds a threshold limit. A so-called abnormal mode of allotropic phase change is advocated for fairly large starting grain size samples. Stated briefly, the explanation given by Liu, Sommer and Mittemeijer [34] rests on the fact that repeated autocatalytic nucleation of the product phase ahead of the moving transformation front is what is responsible for the occurrence of a split or multiple peak phenomena in DTA peak profiles. But what is important to note is that such “ahead of the interface bulk nucleation events”, must occur in discrete pulses with passage of time to

account for the multi-peaked nature of the variation of the transformation rate with time. In what follows, we seek a logical exploration of such a possibility for a simple nucleation growth mediated phase transformation phenomenon.

Taking the general case of a phase transformation involving no change in composition and occurring upon heating for example, it can be argued, that for a given initial microstructure and heating rate, owing to the ubiquitous presence of energy barriers associated with diverse modes of nucleation, appreciable overheating of the sample results before product phase nucleation can be effected. This extent of superheating, or more appropriately the degree to which the transformation onset temperature is made to exceed its equilibrium value is a function of the heating rate. If τ is the typical incubation time for steady state nucleation of β -phase at temperatures that are not too away from the equilibrium transformation point (T_o). Then for a sample that is heated at a rate of β , the first instances of nucleation would be registered at a temperature $T(\beta)$ and it can be approximated as follow,

$$T_s(\beta) = T_o + \beta \tau. \quad (4.7)$$

In the present study, the variation of $T(\beta)$ with β is rather non linear (**figure. 4.6**), which in essence suggests *Eq. (4.7)* is technically correct but not able to explain the non linear behaviour of $T(\beta)$ with β observed in the present study. This is because, when more than one type of nucleation modes with different characteristic time scales, τ_1 and τ_2 are under operation, then the linear approximation given in *Eq. (4.7)* needs to be modified accordingly. In the present case, we chose the following form.

$$T_n(\beta) = T_o + \beta (f_1 \tau_1 + f_2 \tau_2 + \dots). \quad (4.8)$$

In the above relation, we have further included two additional weighting factors, f_1 and f_2 that reflect the relative contributions from the two different nucleation modes to overall number density of nuclei. Further, if we make these weighting factors sensitive to the

variations in heating rate (β), that is $f_1 = f_1(\beta)$ and $f_2 = f_2(\beta)$, then a non linear variation of the transformation arrest temperatures with β is readily obtained.

Recasting this model in terms of the standard output of a DSC experiment, namely the total rate of transformation, $(dX/dt)_\beta = (dX/dT)_\beta \times \beta$, we obtain

$$(dX/dT)_\beta = (1/\beta) \{f(X_1) \times k_1(T) + f(X_2) \times k_2(T)\}. \quad (4.9)$$

The above relation is written using the simple separable representation of $(dX/dT)_\beta$ invoked in Eq. (4.2) with $k_1(T)$ and $k_2(T)$ are respective Arrhenius rate constants. Thus it emerges from this reasoning that the occurrence of a composite peak structure with split or multiple shoulders is due to the operation of concurrent but differently weighted contributions from two different reaction mechanisms, which could in principle be multiple and concurrent nucleation modes, or growth mechanisms or a combination of these two. For a sample with a fairly large starting α -phase grain size, the choice of small heating rates (1 to 10 K min⁻¹ in our experiment) with resulting small overheating ($T_s - T_o$), would first enable the heterogeneous nucleation of the β phase from triple junctions, that is grain corners, then grain edges and finally in the grain interior. The incidence of a large starting grain size results in a net reduction in the number of potential low energy nucleation sites (grain edges and corners) to start with. Hence, after the quick initial exhaustion of such low activation energy nucleation sites, there is a drop in the nucleation rate from this mode. In addition, the formation of β phase with a larger specific volume and elastic stiffness than the parent α -grain will result in the development of stresses at the transformation interface and this would also effectively reduce the driving force available for further propagation of the transformation. This then results in a slowing down of the reaction rate that would reflect as a dip or a kink in the corresponding DSC profile. This kinetic retardation of nucleation is only temporary in that it will be followed by fresh nucleation events at more difficult to nucleate sites such

as grain interior, which will now become accessible upon reaching to higher temperatures with further passage of time. Thus repeated nucleation events at successively higher time or temperatures in case of continuous heating can in principle lead to multiple peaked DSC profiles. Now, if we chose to heat the sample at a faster rate ensuring thereby the attainment of a higher transformation start temperature, then both homogeneous and heterogeneous types of nucleation events are triggered simultaneously and with the predominant contribution coming from homogeneous nucleation mode for larger grain sized samples and this leads to a normal DSC profile with single peak. If the starting α -phase grain size is very small then at all points of time, there will be present enough catalytic nucleation sites to ensure the continuous propagation of the transformation front for practically all the heating rates. Thus, there exists a threshold grain size above which only, the anomalous transformation mode is triggered in simple interface controlled nucleation and growth transformations [38].

To complete the explanation, we may also add that at very high rates of cooling (10^6 K sec^{-1}), as for example adopted by Duwez [15], it emerges from *Eq. (4.7)*, that a very large under cooling and hence a significant pile up of the thermodynamic driving force is made available at T_s , for both initiation and progress of the transformation. This higher driving force can facilitate the rapid propagation of the transformation front. Thus, the small number of β -phase nuclei that are the first ones to form, say in the matrix α -phase triple junctions for reasons of energetic can now transform by rapid advancement of the α/β interface. Although, the present study is not concerned with such very high heating or cooling rates, there are adequate precedence in literature to support the fact that massive and martensitic modes of allotropic transformation do in fact occur for faster rates of heating and cooling [35-37].

4.4.2. Kinetics parameters: heating rate dependence of Q_{eff}

At the outset, it must be admitted that following the reasoning advocated by Berkenpas *et al* with regard to a model based analysis of transformation kinetics [38], and by Sewry and Brown with regard to the intricacies involved in a so-called model-free reaction kinetics [39], it is not clear as to how far the values extracted for the kinetic quantities by fitting the transformation data to empirical rate expressions are meaningful in a fundamental sense. Nevertheless, we indulge in such an exercise in the present study only to offer a plausible estimate of Q_{eff} involved in the structural phase changes in pure uranium. A straight forward application of Kissinger or Ozawa formalism [40] for effective linearization of the data on shift in the peak transformation temperature with heating rate yielded non-linear plots that in spirit obviates the applicability of these methods for extracting the kinetics quantities. In fact, a similar observation had earlier been recorded in case of a DTA study on the allotropic transformation of plutonium [41]. In deference to the limited scope of this study, we do not present a detailed discussion on this issue, but it is suffice to say that the application of Kissinger like method for extracting the apparent activation energy of transformations involving multiple and concurrent steps is strictly not correct. In the present study, this difficulty is however overcome by directly fitting the transformation data to suitable empirical reaction models by means of a robust non-linear optimisation routine.

The values for Q_{eff} thus obtained for the $\alpha \rightarrow \beta$ phase change varies from 174 to 199 kJ mol^{-1} , and for the $\beta \rightarrow \gamma$ transformation, it ranges from 143 to 175 kJ mol^{-1} (**Tables 4.1&4.2**). The activation energy reported for self-diffusion in the three structural modifications of uranium are about: α -U:167.5, β -U : 175.8 and γ -U : 115.1 kJ mol^{-1} [42]. It must be remarked that we have adopted a simplified version of KJMA model, which do not really incorporate the role of changing nucleation and growth rates with the

extent of transformation. Notwithstanding this serious limitation, and taking cognisance of the fact that Q_{eff} is actually a weighted sum of individual contributions from nucleation (Q_N) and growth (Q_G), we may write, $Q_{eff} = pQ_N + qQ_G$, with p and q being arbitrary constants. It is normally the case that Q_N , which is of the order of a few kilo joules per mole is much less than Q_G . Under this condition, we may note that the measured

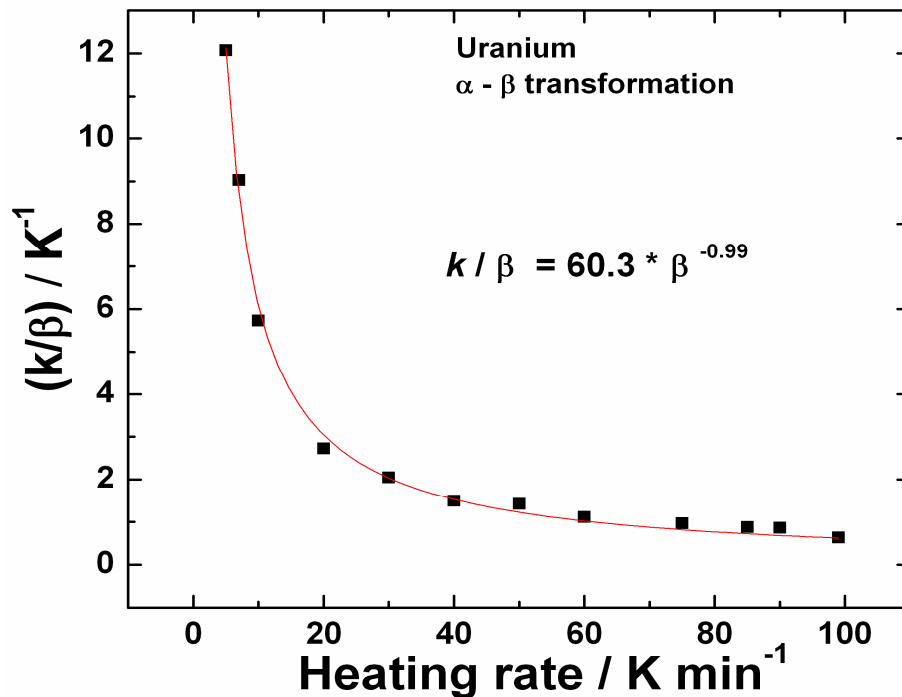


Fig.4.10 The variation of heating rate normalised Arrhenius rate constant (k/β) with β for $\alpha \rightarrow \beta$ transformation

activation energies are primarily reflective of the growth component and going by the fact that Q_{eff} is in the same range as the self-diffusion activation energies. Finally we may conclude that $\alpha \rightarrow \beta$ and $\beta \rightarrow \gamma$ transformation mechanism is one of involving atomic jumps across the phase interface. As for the n values are concerned, we refrain from attributing a definite physical meaning, as we primarily treat it as a fit parameter in this study. Besides, it must also be added that the kinetic quantities, k_o , Q_{eff} and n form a

unique kinetic triplet in the sense that a change in one parameter totally off-sets the overall goodness of fit.

In the present study, we also note a small but steady increase in Q_{eff} with heating rate. This reflects probably the increasing degree of difficulty associated with nucleation at high rates of heating, as growth rates at these temperatures are expected to be high and remain constant. The dramatic role of heating rate on k/β , the *overall* heating rate

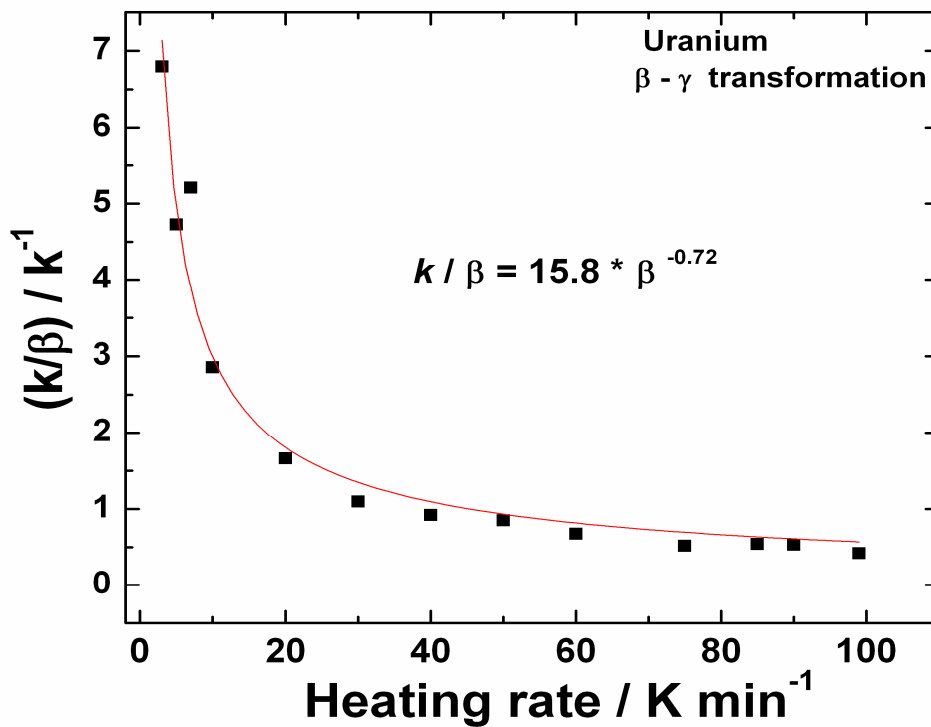


Fig.4.11. The variation of heating rate normalised Arrhenius rate constant (k/β) with β for $\beta \rightarrow \gamma$ transformation

normalised rate constant is nicely brought out in **figure 4.10** and **figure 4.11**. Quite interestingly, the observed behaviour for both $\alpha \rightarrow \beta$ and $\beta \rightarrow \gamma$ transformations can be fitted to a simple power law of the following form

$$k/\beta = C(\beta)^{-m}. \quad (4.10)$$

From, Eq. (4.10) it is possible to define a dimensionless quantity, ξ characterising the bi-logarithmic variation of k with β . Thus, it emerges from Eq. (4.10)

$$\xi = d \ln k / d \ln \beta = (1-m). \quad (4.11)$$

The value of m obtained in the present study is 0.99 for $\alpha \rightarrow \beta$ and 0.72 for $\beta \rightarrow \gamma$ transformation. The physical import of this finding is that there is present an intrinsic scaling behaviour in the heating rate dependence of $(dX/dT)_\beta$ for both the on-heating transformations. If we were to assume the validity of standard iso-conversional rate equation formalism, namely that given by equations (4.2) and (4.3), it may be deduced from the scaling law presented in *Eq.* (4.11) that for fixed X , the fraction transformed, the pseudo reaction rate $(dX/dT)_\beta$ varies with respect to heating /cooling rate as $(\beta)^{-m}$. Thus, the knowledge of $(dX/dT)_\beta$ for one standard heating rate with attending information on

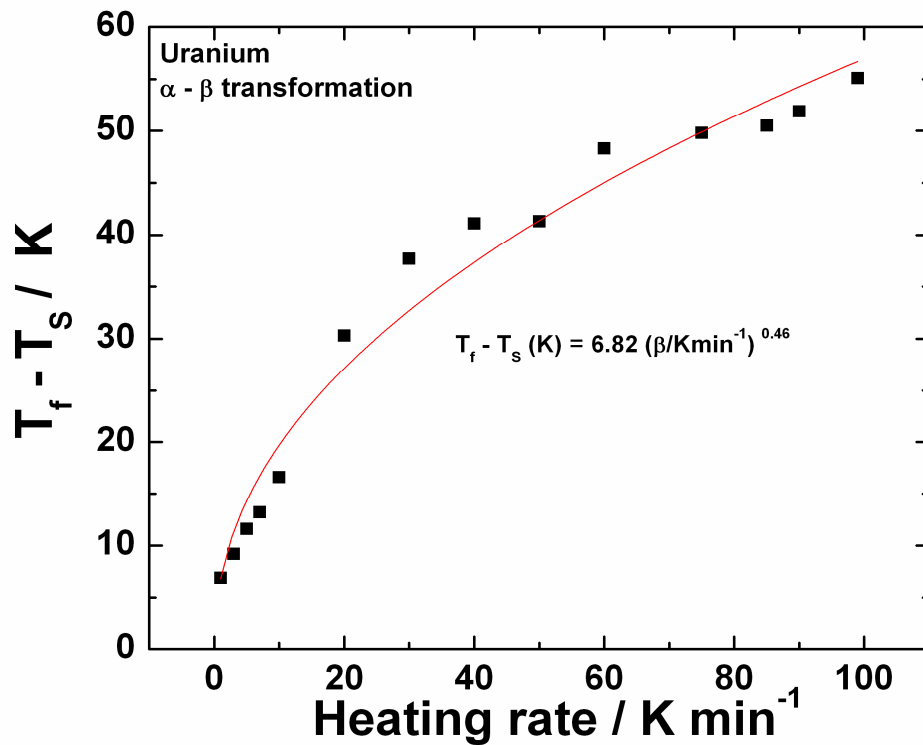


Fig.4.12 The heating rate dependence of the width of the transformation zone ($T_f - T_s$) for the $\alpha \rightarrow \beta$ transformation

the Arrhenius rate constant can be used to generate the transformation plot for other heating rates. This predictive capability is rather inbuilt in our transformation plots (**figure 4.8(a) & 4.8(b)**) in the sense that the gradually changing nature of the slope of

transformation plots with increasing heating rate is readily apparent. If on the other hand, the heating rate has no influence on the transformation kinetics, then the transformation curves for different heating rates, when plotted on a normalised temperature ($T-T_s$) basis, should all merge to give a single master curve. However, such is not the case witnessed in the present study. Before closing this point, we may also add that this simplified interpretation of scaling law rests on the validity of iso-conversional rate equation hypothesis; but in reality this is rather questionable [21].

4.4.3. Other general aspects

The other useful point to emerge from this study is that for both $\alpha \rightarrow \beta$ and $\beta \rightarrow \gamma$

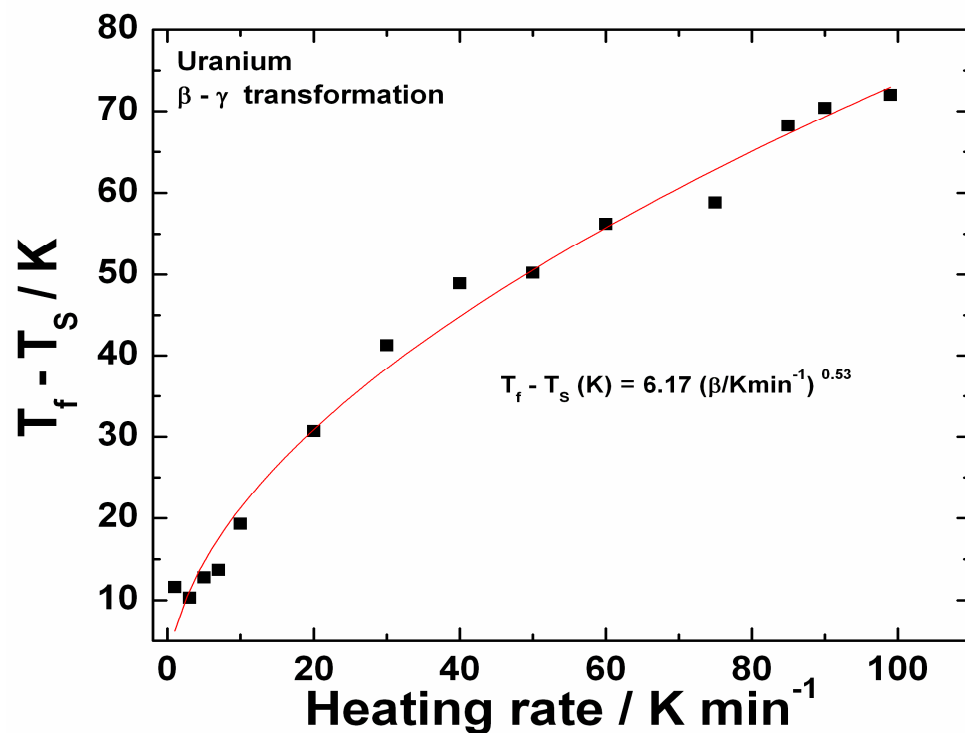


Fig.4.13 The heating rate dependence of the width of the transformation zone ($T_f - T_s$) for the $\beta \rightarrow \gamma$ transformation

phase changes, the effective width of the transformation domain represented by the differential temperature, $T_f - T_s$, varies approximately as the square root of the heating rate. This is illustrated in **figure 4.12** and **figure 4.13** for $\alpha \rightarrow \beta$ and $\beta \rightarrow \gamma$ phase

transformations respectively. It can be seen that very similar exponent values are noticed for both phase changes. At present this aspect has not been fully analysed and understood, but an attempt to arrive at a comparative interpretation of this finding in terms of a similar finding in massive phase transformations suggests that the heating rate dependence of the nucleation event could be one of the reasons [49, 50]. Considering the experimental uncertainties involved, the values of the power law exponents obtained from the fits shown **figure 4.12** and **figure 4.13** may be taken as close to 0.5, a fact supported by the findings of Bhattacharya et al [43] and also by Caretti and Bettorello [44] regarding nucleation controlled massive mode of phase change. Admittedly, a mathematical treatment on this line is not carried out in this study, as reliable values for many parameters like interface energy, mobility *etc.*, are currently lacking for uranium.

4.5 Conclusions

- (i). A comprehensive thermal analysis investigation of the kinetics of allotropic phase changes in uranium metal has been carried out in the present chapter which include measurement of transformation temperature as function of heating and cooling rate for different phase changes occur during heating and cooling cycle.
- (ii). The transformation temperatures exhibit a strong non-linear variation with the heating or cooling rate. For small heating rates, the DSC profile for the $\alpha \rightarrow \beta$ transformation contains a shoulder, which feature is however absent for larger heating rates. For small heating rates, the relative competition between heterogeneous and homogeneous grain interior nucleation events controls the structure development.
- (iii) The considerable hysteresis have observed between on-heating and cooling transformation.
- (iv). The kinetics of both the on-heating phase changes, namely, $\alpha \rightarrow \beta$ and $\beta \rightarrow \gamma$ are described well by a standard KJMA formalism for the nucleation and growth process. This however is not true for the $\beta \rightarrow \alpha$ and $\gamma \rightarrow \beta$ phase changes that occur during cooling.

(v). The effective activation energies estimated for the on-heating phase transformations are of the same order of the activation energies involved in the self-diffusion process in α and β uranium lattices.

(vi). The kinetics of $\gamma \rightarrow \beta$ phase change is found to be non-sigmoidal in character and is well described by the empirical Koistinen and Marburger expression for the martensitic transformations. The $\beta \rightarrow \alpha$ phase change on the other hand is sensitive to cooling rate and is accounted for by the empirical Kamamoto's relation for the fraction transformed.

(vii). The heating or cooling rate normalised empirical rate constant, namely k/β exhibits a power law relationship with β .

4.6. References

1. A. N. Holden, *Physical Metallurgy of Uranium*, Addison-Wesley Pub. Co., Reading, Mass. (1958).
2. B. Blumenthal, *J. Nucl. Mater.*, 2 (1960) 23.
3. S. E. Moore and K. K. Kelley, *J. Am. Chem. Soc.*, 69 (1947) 2105.
4. D. C. Ginnings and R. J. Corruccini, *J. Res. Natl. Bur. Std.*, 39 (1947) 309.
5. A. I. Dahl and M. S. Van Dusen, *J. Res. Natl. Bur. Std.*, 39 (1947) 53.
6. P. Gordon, A. R. Kaufman, *Trans. A.I.M.E.*, 188 (1950) 182.
7. H. Okamoto, *J. Phase Eq.*, 13 (1992) 109.
8. D. Blake and R. F. Hehemann, *Transformations in uranium base alloys*, In: *Physical Metallurgy of Uranium alloys*, Eds. J. J. Burke, D. A. Colling, A. E. Gorum and Jacob Greenspan, Brook Hill Pub.Co., (1976), Mass., pp. 189.
9. K. M. Pickwick and W. J. Kitchingman, *J. Nucl. Mater.*, 19 (1966) 109.
10. R. D. Townsend and J. Burke, *J. Nucl. Mater.*, 17 (1965) 279.
11. I. F. Barwood and B. R. Butcher, *J. Nucl. Mater.*, 8 (1963) 232.
12. W. J. Kitchingman, K. M. Pickwick, I. G. Brown and R. J. Edwards, *J. Nucl. Mater.*, 18 (1966) 219.
13. G. Donze, *J. Nucl. Mater.*, 5 (1962) 150.
14. J. J. Rechtein and R. D. Nelson, *Metall. Trans.*, 4B (1973) 2755.
15. P. Duwez, *J. Appl. Phys.*, 24 (1953) 152.
16. J. Burke and P. H. Dixon, *J. Nucl. Mater.*, 7 (1962) 38.
17. H. Yakel, A review of x-ray diffraction studies in uranium alloys, In :*Physical Metallurgy of Uranium alloys*, Eds. J. J. Burke, D. A. Colling, A. E. Gorum and Jacob Greenspan, Brook Hill Pub.Co., (1976), Mass., pp. 259.
18. R. A. Vandermeer, *Metall. Trans.*, 17A (1986) 1717.
19. D. Turnbull, *Trans. AMIE*, 191 (1951) 661.

20. Y. C. Liu, F. Sommer and E. J. Mittemeijer, *Acta Mater.*, 54 (2006) 3383.
21. F. Liu, F. Sommer and E. J. Mittemeijer, *Int. Mater. Rev.*, 52 (2007) 193.
22. J. Sietsma and S. van der Zwaag, *Acta Mater.*, 52 (2004) 4143.
23. R. G. Thiessen, I. M. Richardson and J. Sietsma, *Mater. Sci. Engg.*, 247 A (2006) 223.
24. P. R. Rios, *Acta mater.*, 53 (2005) 4893.
25. M. J. Starink, *Thermochim. Acta*, 404 (2003) 163.
26. P. Kruger, *J. Phys. Chem. Solids*, 54 (1993) 1549.
27. C. Verdi and A. Visintin, *Acta Metall.*, 35 (1982) 2711.
28. G. Ruitenbergh, E. Woldt and A. K. Petford-Long, *Thermochim. Acta*, 378 (2001) 97.
29. M. T. Todinov, *Acta mater.*, 44 (1996) 4697.
30. D. P. Koistinen and R. E. Marburger, *Acta Metall.*, 7 (1959) 59.
31. S. Kamamoto, T. Nishimori and S. Kinoshita, *Mater. Sci. Tech.*, 1 (1985) 798.
32. I. I. Boyadjiev, P. F. Thompson, and Y. C. Lam, *ISIJ Int.*, 36 (1996) 1413.
33. Y. Zhu and J. Devletian, *J. Mat. Sci.*, 26 (1991) 6218.
34. Y. C. Liu, F. Sommer and E. J. Mittemeijer, *Philos. Mag.*, 18 (2004) 1853.
35. C. A. Apple and G. Krauss, *Acta Metall.*, 20 (1972) 849.
36. W. J. Kaluba, R. Taillard and J. Foct, *Acta Mater.*, (1998) 5917.
37. E. A. Wilson, *ISIJ Int.*, 34 (1994) 615..
38. M. B. Berkenpas, J. A. Barnard, R. V. Ramanujan and H. I. Aaronson, *Scripta Metall.*, 20 (1986) 323.
39. J. D. Sewry and M. E. Brown, *Thermochim. Acta*, 390 (2002) 217.
40. M. J. Starink, *Int. Mater. Rev.*, 40 (2004) 191.
41. R. D. Nelson and J. C. Shyne, *J. Nucl. Mater.*, 19 (1966) 345.

42. H. Mehrer,; *Diffusion in solid metals and alloys*, Landolt-Bornstein New Series, III/26, (Series Eds. K.-H. Hellwege and A. M. Hellwege), Springer, Heidelberg (1990).
43. S. K. Bhattacharyya, J. H. Perepezko and T. B. Massalski, *Acta Metall.*, 22 (1974) 879.
44. J. C. Caretti and H. R. Bettorello, *Acta Metall.*, 31 (1983) 325.

Chapter 5

Calorimetric Investigation of Phase stability and kinetics in U-x wt.% Zr (x=0, 2, 5 & 10 wt.%) Alloys

5.1. Introduction: genesis of the present study

This chapter presents and discusses the results of calorimetric characterization of phase stability and phase transformation in U-0, 2, 5 & 10 wt.% Zr alloys. The literature information related to the phase equilibria and phase transformations in U-Zr alloy has already been presented in **chapter 1**. From this survey, it emerges that reliable experimental data on basic thermodynamic and kinetic quantities of different phases as a function of temperature and composition in U-Zr, alloys are still lacking. In addition it has been observed that the temperature and composition of all the invariant reactions are not confirmed beyond doubt. Further, the nature of formation of metastable displacive α' -martensite either separately or in conjunction with δ -UZr₂ intermetallic phase upon cooling from high temperature γ -bcc is yet to be clarified beyond doubt. It also appears that the kinetic aspects of various solid state transformations have also not been investigated clearly thus far. Rigorous computational modelling of phase equilibria and phase transformation kinetics is also hampered, partly due to the lack of reliable (recent) data on various mobility values for Zr and U in different allotropes of uranium. In order to fill this gap to certain extent, comprehensive calorimetric study of high temperature phase equilibria and phase transformation characteristics in U-xZr ($x = 2, 5, 10$ wt.%) alloys has been undertaken, as a function of several heating/cooling rates.

5.2. Experimental details

The experimental information related to alloy synthesis, composition analysis and annealing treatment given to different alloys of U-Zr (U-0, 2, 5 & 10 wt.& Zr) used in the present study are presented in **chapter 2**. In addition the experimental methodology adopted for differential scanning calorimetry metallography and X-ray diffraction are also presented in **chapter 2**. In the present chapter the results and discussion parts are presented in detail.

5.3. Results

5.3.1. X-ray diffraction and microstructure

The X-ray diffraction (XRD) patterns of U-0, 2, 5 & 10 wt.% Zr alloys annealed at 1073 K (800°C) for 2 h in high pure argon atmosphere followed by furnace cooling to room temperature, is shown in **figure 5.1**. The XRD profiles clearly showed that all the three alloys consist of only supersaturated α (orthorhombic) solid solution phase. At this stage, it cannot be said in definite terms as to whether the formation of α in the present samples occurred *via*, martensitic mode, or through diffusional mode of decomposition

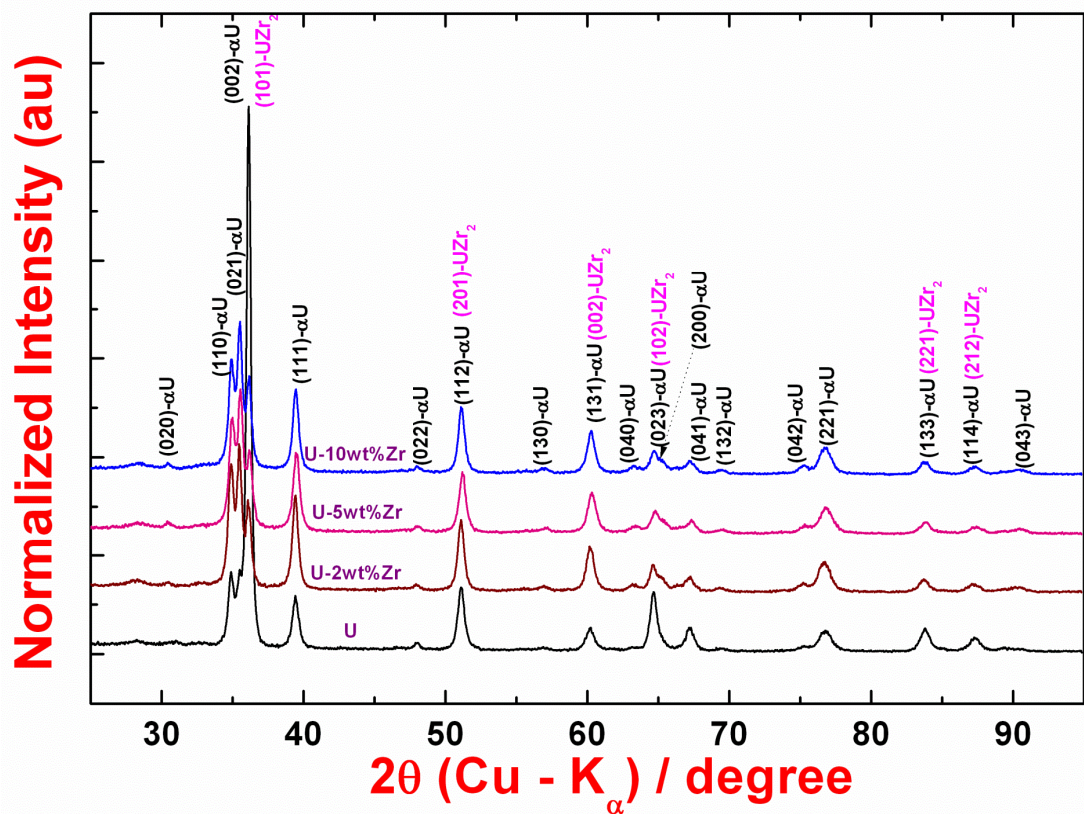


Fig.5.1. X-ray diffraction patterns obtained on U-0, 2, 5 & 10 wt.% Zr alloys.

of high temperature γ -bcc (refer the equilibrium phase diagram of U-Zr system given in **figure 5.2**), since the structure of α' -martensite is basically the same as that of diffusively formed α , with little difference in lattice parameters [1]. It is only the co-presence of accompanying δ -UZr₂ phase that might probably indicate the diffusive mode

of α -phase formation, since in this case, the formation of δ -UZr₂ along with α_{eq} requires appreciable long range diffusion [1-4]. According to the equilibrium diagram shown in **figure 5.2** the alloys of U-2, 5 and 10 wt.% Zr must at room temperature have some amount of δ -UZr₂ phase [5]. However, it is very difficult to confirm the definite presence of δ -UZr₂ from powder XRD profiles shown in **figure 5.1**, since most of the prominent peaks of δ phase match closely with that of orthorhombic α phase [1]. In addition, the phase fraction of δ -UZr₂ is also rather small in alloys of lean Zr content, making its weak

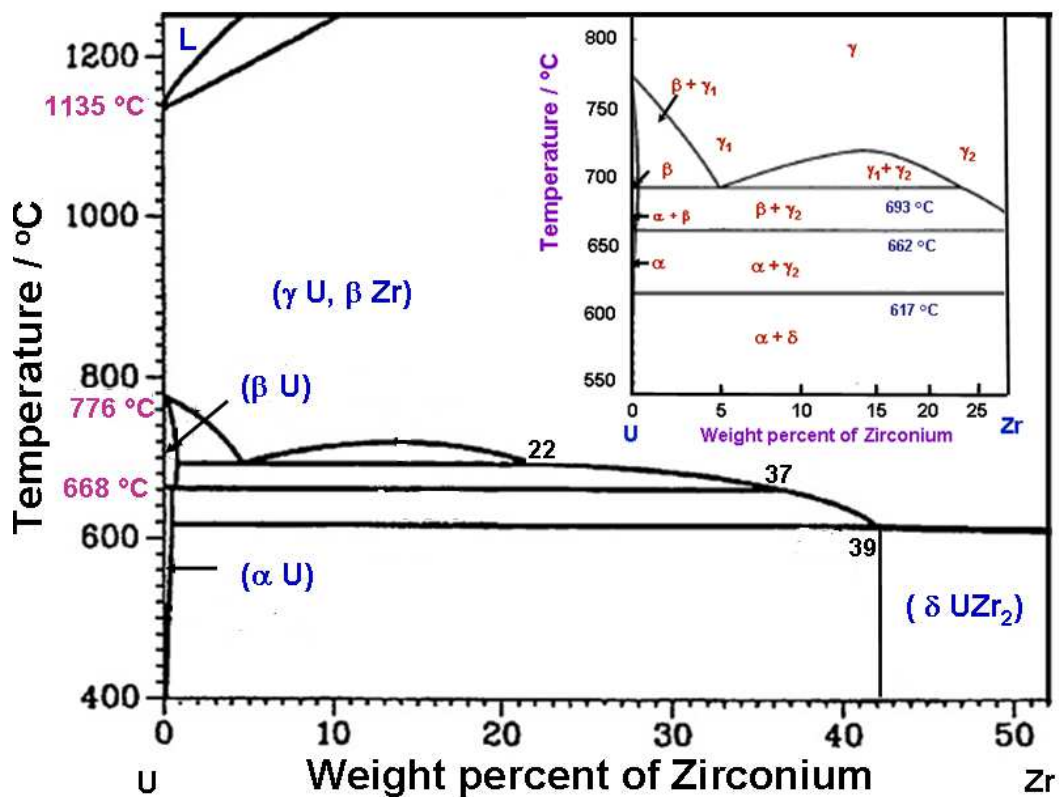


Fig.5.2. Equilibrium diagram of U-Zr system. The expanded view on uranium rich side is shown as inset for better clarity

high angle reflections rather difficult to be detected unambiguously. The lattice parameters of the α phase estimated from present XRD results are given in **table 5.1**.

The typical optical microstructure of annealed sample of U-2 wt.% Zr alloy is presented in **figure 5.3(a)**. Before proceeding further, it may be added that U-2wt.% Zr is

taken as typical case study candidate for highlighting the important findings of this study; for other compositions, the results are presented in either graphical or tabulated forms. From **figure 5.3(a)**, the fine cellular morphology of α phase outlined within the prior γ -phase grain boundary is immediately apparent. In addition, a Widmanstatten like side plate morphology emanating from prior γ grain boundary is also seen at some places in

Composition	<i>a</i> (nm)	<i>b</i> (nm)	<i>c</i> (nm)
U	0.28507	0.58661	0.49602
U-2 wt.% Zr	0.28616	0.58565	0.49648
U- 5 wt.% Zr	0.28652	0.58548	0.49688
U-10 wt.% Zr	0.28702	0.58503	0.49702

microstructure (**figure 5.3(b)**). Such type of microstructures were reported earlier in U rich U-Zr alloys, and was taken to be indicative of the formation of martensitic α' phase [2-4]. Further, it is also interesting to note the appreciable change in microstructure morphology that develop upon slow cooling (1 K min^{-1}) from γ -phase. In **figure 5.3(c)** and **figure 5.3(d)**, the secondary electron image and the X-ray map of 1 K min^{-1} cooled sample of U-2 wt.% Zr alloy are shown. It is instructive to note the presence of strong Zr enrichment along the grain boundary of relatively large α -grains or cells. It is clear that the preferential formation of $\delta\text{-UZr}_2$ all along the grain boundary during slow cooling, has given rise to such enrichment. It is also useful to note that some $\delta\text{-UZr}_2$ particles are also present inside of the α -grains. In addition, it is also found that with decreasing cooling rate, the cells have a sufficiently coarsened appearance (**figure 5.3(c)**), and are

decorated with thicker grain boundaries. The typical microhardness of the annealed U-2 wt.% Zr alloy is found to be about 380 VHN. With increasing Zr content, the hardness of annealed microstructure is found to increase, up to about 420 VHN for 10 wt.% Zr composition. Further, the hardness is also found to increase with cooling rate. The increase in hardness is also attended by a concomitant refinement of microstructure that is, a decrease in cell spacing.

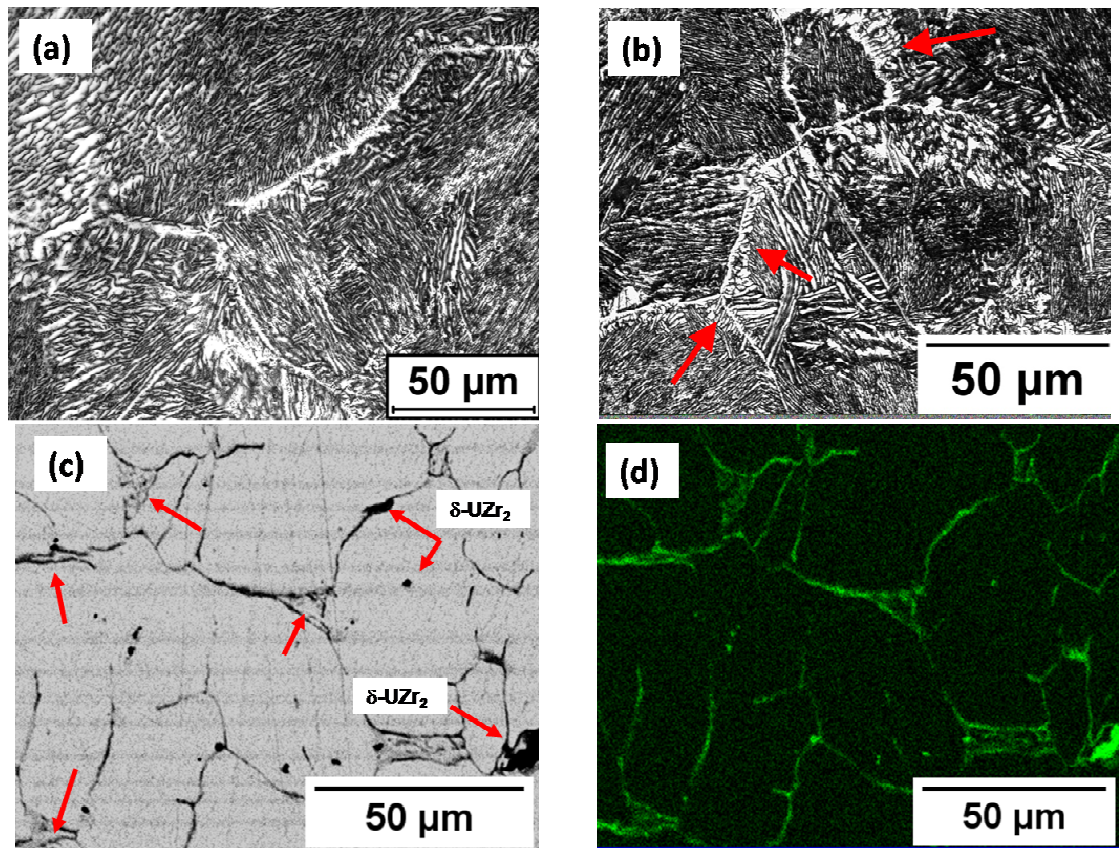


Fig.5.3(a). A typical optical microstructure of annealed U-2 wt.% Zr alloy and in this the fine cellular morphology of α phase is clearly outlined within the prior γ -phase; **(b).** The Widmanstatten side-plate like morphology, emanating from select prior γ grain boundary is shown (arrow markers); **(c).** The secondary electron image of U-2 wt.% Zr alloy cooled at 1 K min^{-1} from 1273 K (1000°C) and in this, large equiaxed of α -cells can be readily witnessed; **(d).** X-ray map of 1 K min^{-1} cooled sample and from this a clear Zr enrichment along grain boundary region, together with the preferential formation of $\delta\text{-UZr}_2$ at select locations (arrow markers) can be noticed

5.3.2 Phase changes and transformation temperatures

Figure 5.4 shows the typical DSC profile obtained at 10 K min^{-1} heating/cooling rate on

annealed U-2wt.% Zr alloy. For other compositions, the relevant thermogram data are collated in **figure 5.5**. For the purpose of clearly elucidating the nature of various on-heating/cooling induced phase changes, the U-2 wt.% Zr alloy has been taken as typical case study candidate. It is clear from **figure 5.4**, that a total of four distinct phase transformation events take place on heating in U-Zr alloys. Postponing the detailed explanation of these events to a latter section, it may be said that the sequence of these

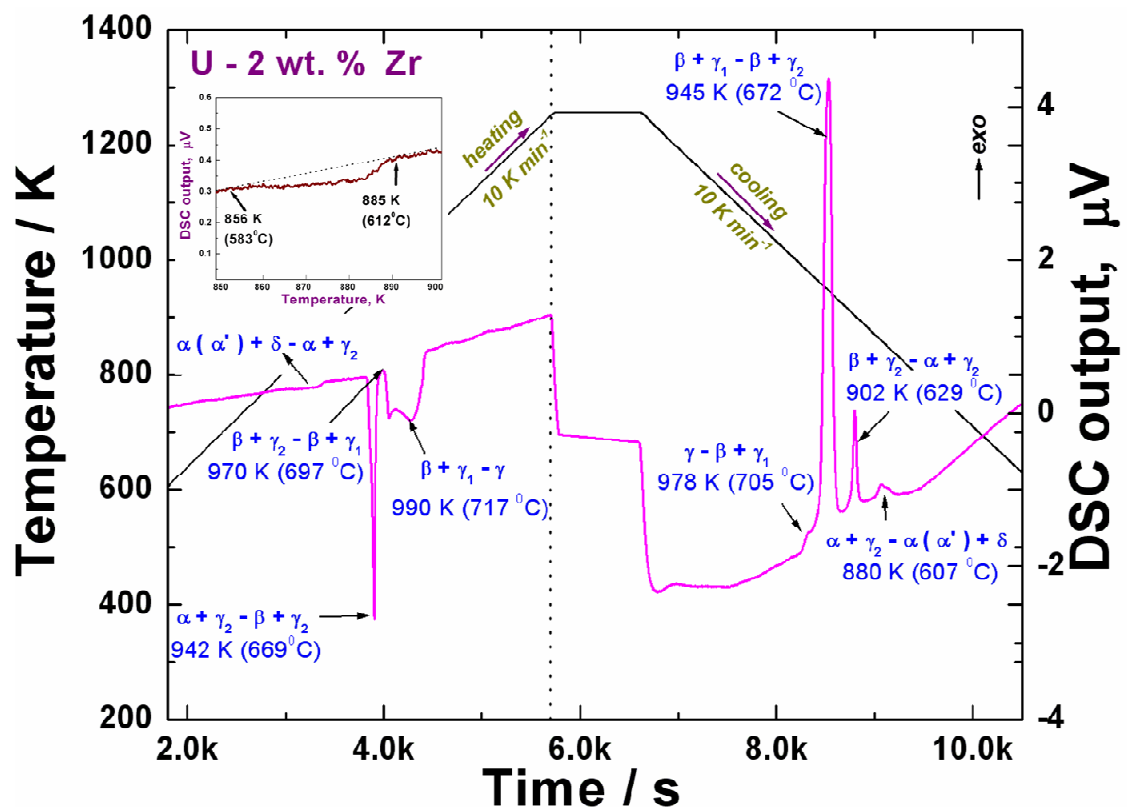


Fig.5.4. DSC thermogram obtained for U- 2wt.% Zr alloy at 10 K min⁻¹. An expanded view of the first composite endothermic thermal arrest arising due to the co-occurrence of martensitic relaxation and δ -UZr₂ dissolution is also shown as inset.

phase changes is in accordance with the phase diagram shown in **figure 5.2**. The first endothermic thermal arrest which begins at 856 K (583°C) and ends at 885 K (612°C) is actually a composite one. An expanded view of the composite nature of this first thermal event is projected as an inset in **figure 5.4**. If the starting microstructure is taken to be

either α' -martensite or a mixture of (predominantly) equilibrium α -orthorhombic phase and a small fraction of δ -UZr₂ (see, phase diagram in **figure 5.2**); then the first thermal arrest could arise from either of the following events:

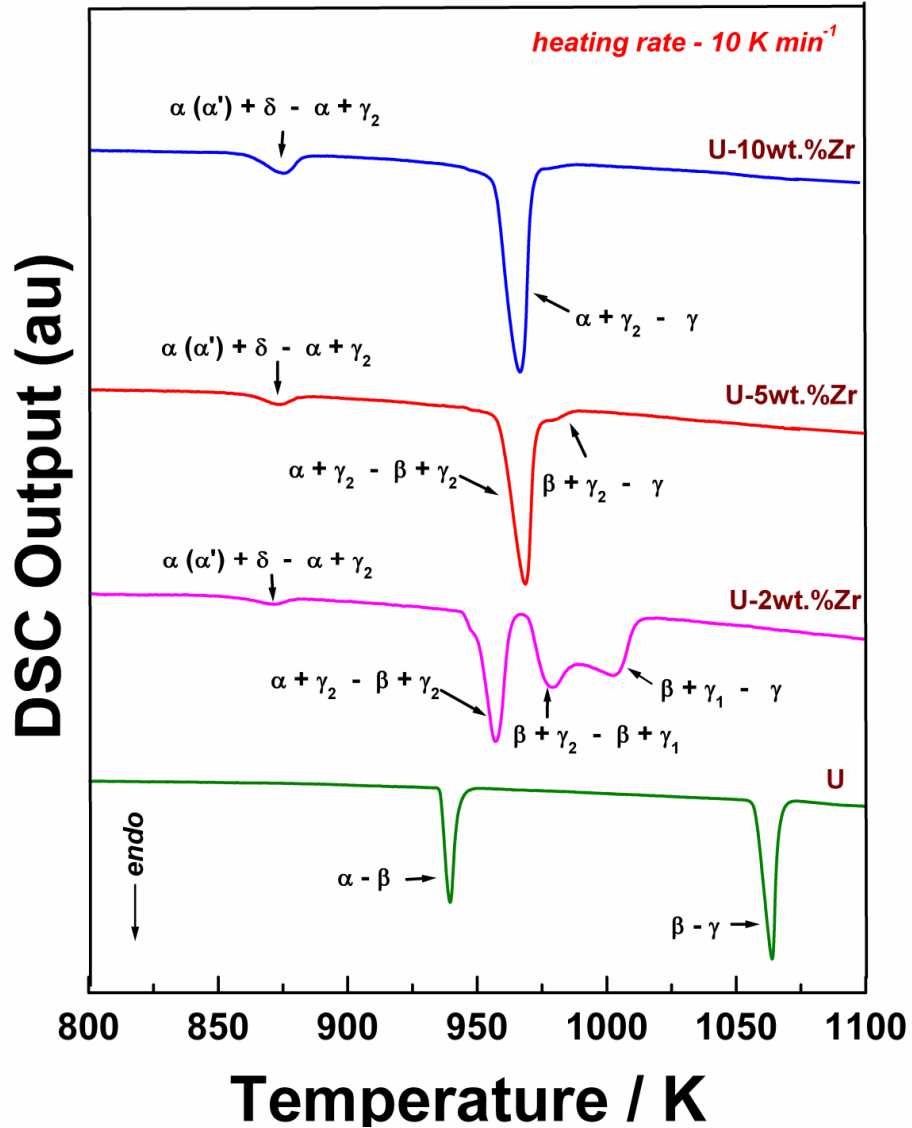


Fig.5.5. On heating DSC thermograms obtained at 10 Kmin⁻¹ for U, 0, 2, 5 & 10wt.% Zr alloys are stacked together.

- (i) $\alpha' \rightarrow \alpha$; that is α' -martensite relaxation (in case of martensite as the starting microstructure),
- (ii) $\alpha_{eq} + \delta \rightarrow \alpha_{eq} + \gamma_2$; the (gradual) peritectoidal dissolution of δ -UZr₂ phase (if starting microstructure contains $\alpha_{eq} + \delta$).

The structural relaxation of α' -martensite in U rich U-Zr alloys is generally reported to take place between 840 and 862 K (570-589°C) [6, 7]. However, the peritectoidal dissolution of δ -UZr₂ also occurs at a closely spaced temperature interval, namely around 890 K (617°C) [9, 10] (see **figure 5.2**), if equilibrium dissolution conditions are assumed to prevail. In either case, there is a clear possibility of overlap of these two on-heating transformation events, if the starting microstructure contains some martensitic α' , diffusional α and δ -UZr₂. Of these, the peritectoid transformation is bound to occur with feeble thermal effect, if the phase fraction of δ -UZr₂ is rather small. The other contribution arising from $\alpha' \rightarrow \alpha$ -relaxation becomes meaningful, only if the relaxation enthalpy is somewhat appreciable, that is within the detection capability of DSC. In literature, it is widely reported that $\gamma \rightarrow \alpha'$ -martensite formation during cooling is easily facilitated for even moderate cooling rates [3, 7, 8, 10-12]. Thus for example, the critical cooling rate for the formation of 100% α' -martensite is estimated to be about 60 K min⁻¹ for U-2wt.% Zr alloy [12]. It decreases however for alloys of higher Zr content; for U-10wt. % Zr alloy, even cooling at the rate of 10 K min⁻¹ can result in near 100 % martensite transformation [12]. In the present study it has been observed (**figure 5.3(a,b)**) that the starting microstructure contained predominantly α -phase (possibly with a small α' -martensite fraction), together with grain boundary δ -UZr₂ phase. Nevertheless, it cannot be said that equilibrium amount of δ -UZr₂ would have precipitated during cooling after the high temperature annealing treatment. It is estimated by the application of lever rule, that about 4.2% by volume of UZr₂ should be present in U-2wt.% Zr alloy at room temperature. This is scarcely sufficient to unambiguously record the presence of δ -phase by conventional XRD. Notwithstanding this limitation, it is likely that both martensitic relaxation of α' and δ -UZr₂ dissolution had actually occurred together upon heating, and this contributes to the composite character of the

first on-heating thermal arrest seen in **figure 5.4**. The relative competition between martensite relaxation and δ -UZr₂ dissolution will be addressed separately in one of the ensuing sections.

Continuing with the enumeration of DSC results, we may note that the second peak observed at 942 K (669°C) is due to the eutectoid reaction, $\alpha+\gamma_2\rightarrow\beta+\gamma_2$ (see, phase diagram in **figure 5.2**). The third thermal arrest is again a composite peak arising from two reactions: the monotectoid one, $\beta+\gamma_2\rightarrow\beta+\gamma_1$ and finally the $\beta+\gamma_1\rightarrow\gamma$ phase transformation [13-15, 9-12]. In fact, the tailing part of this composite peak corresponds to the formation of single phase γ from $\beta+\gamma_1$. It may be added that the offset temperature of the monotectoid and the onset temperature of the latter phase transition are rather close for U-2wt.% Zr composition (**figure 5.2**). This is further accentuated by kinetic or diffusional lag due to sluggish Zr diffusion, which enhances the overlapping occurrences of these two phase changes in a standard thermal analysis profile. The overlap is more keenly observed at higher heating rates and especially in higher Zr content alloys, where the sluggish nature of Zr diffusion attests its presence in clear terms. Only a very slow heating scan can portray these two thermal arrests distinctly in such cases. This fact will again be deliberated upon in detail while discussing the kinetic aspects of phase change in a latter section of this manuscript.

During the cooling part of the thermal cycle, all the four phase transformations discussed above have been observed with varying degrees of under cooling. Thus, the first peak occurring at 978 K (705°C) is associated with the formation of $\beta+\gamma_1$ phase from single phase γ after reaching the onset of $(\gamma_1+\gamma_2)$ miscibility gap. This reaction is represented as $\gamma\rightarrow\gamma_1+\beta$, and is reflected as a very small hump in the DSC trace. The second step observed at 945 K (672°C) is the completion of β formation upon reaching the horizontal eutectoid invariant line. The appropriate transformation is represented as:

$\gamma_1 + \beta \rightarrow \beta + \gamma_2$. The third peak at 902 K (629°C) is due to the formation of α phase from β through the reaction, $\beta + \gamma_2 \rightarrow \alpha + \gamma_2$. The α -phase formation is complete only when the temperature reaches about 880 K (607°C); that is the peritectoid line, at which point the

Table 5.2				
Measured transformation start (T_s), finish (T_f) temperatures for various solid state and melting transformations and corresponding transformation enthalpy (ΔH) are listed for 2, 5, 10 wt.% Zr alloys				
Composition	Transformation Reaction	Transformation start T_s (K)	Transformation finish T_f (K)	Enthalpy of transformation ΔH $J g^{-1}$
U	$\alpha \rightarrow \beta$	933	942	12.7
	$\beta \rightarrow \gamma$	1057	1067	21.8
	Melting		1401	88.2
U-2 wt. Zr	$\alpha' + \delta \rightarrow \alpha + \gamma_2$	853	888	1.2
	$\alpha + \gamma_2 \rightarrow \beta + \gamma_2$	944	958	14.2
	$\beta + \gamma_2 \rightarrow \beta + \gamma_1$	969	982	11.9
	$\beta + \gamma_1 \rightarrow \gamma$	988	1010	11.1
	Melting	1426	1455	97.4
U-5 wt.%Zr	$\alpha' + \delta \rightarrow \alpha + \gamma_2$	855	886	1.85
	$\alpha + \gamma_2 \rightarrow \beta + \gamma_2$	954	966	16.7
	$\beta + \gamma_2 \rightarrow \beta + \gamma_1$	968	985	16.3
	$\gamma_1 + \gamma_2 \rightarrow \gamma$	995	1007	2.5
	Melting	1446	1509	112.9
U-10 wt.%Zr	$\alpha' + \delta \rightarrow \alpha + \gamma_2$	858	889	3.7
	$\alpha + \gamma_2 \rightarrow \beta + \gamma_2$	956	966	36.2
	$\beta + \gamma_2 \rightarrow \beta + \gamma_1$	969	978	8.0
	$\gamma_1 + \gamma_2 \rightarrow \gamma$	996	1008	8.5
	Melting	1644	1650	128.8

UZr_2 phase starts to come out of $\alpha + \gamma_2$. This last step constitutes the fourth thermal arrest.

It is useful to highlight the point that the temperature at which the precipitation of δ - UZr_2

starts is fairly close to the equilibrium peritectoid line of UZr_2 dissolution, that occurs during heating cycle. As mentioned before, a similar set of experiments were also carried out for other compositions (U-5, 10 wt. % Zr) under the same experimental conditions. In **figure 5.5**, these different on-heating DSC traces obtained on $U-xZr$ ($x=0, 2, 5, 10$ wt. %) alloys are compared. It may be added that at 10 K min^{-1} heating rate, some of the transformations are not well resolved in 5 and 10 wt. % Zr alloys, as these intermediate transitions are skipped during 10 K min^{-1} heating cycle. The transformation temperature data obtained during slow heating at 3 K min^{-1} have been reported separately in **table 5.2**. It may further be added that at such slow scan rate only, all the transformations evidenced by phase diagram (**figure 5.2**) are distinctly observed in all the three alloy compositions. Before proceeding to discuss further, attention is paid to discuss the co-occurrence of $\alpha' \rightarrow \alpha$ and $\alpha + \delta \rightarrow \alpha + \gamma_2$ reactions upon slow heating in U-2 wt.% Zr alloy.

5.3.3. Co-occurrence of UZr_2 dissolution and martensite relaxation

According to Lagerberg, Bauer and Duffey *et al* [10, 16, 17], the equilibrium UZr_2 dissolution temperature in U rich U-Zr alloys is estimated to be around $890 \pm 10\text{ K}$ ($617 \pm 10\text{ }^\circ\text{C}$). In U-2wt.% Zr alloy, Basak *et al.*, [6] have observed the dissolution of UZr_2 at a lower temperature of 862 K (589°C) using dilatometry. But, Basak *et al.* have attributed the corresponding dilatometric inflection to martensitic relaxation of α' phase [6]. Meanwhile, Akabori *et al.*, [18, 19] have observed in U-1.98 wt.% Zr alloy using differential thermal analysis (DTA), a peak at 857 K (584°C). This has however been attributed to UZr_2 dissolution. Recently, Kaity *et al.*, in their DSC study on U-6wt.% Zr alloy have observed a peak at 842 K ($569\text{ }^\circ\text{C}$) [8]. Again they interpreted it is due to $\alpha \rightarrow \alpha'$ -martensitic relaxation. According to the currently accepted phase diagram, the UZr_2 dissolution takes place at 890 K (617°C) under equilibrium conditions. Keeping in mind all the above reported diversity with regard to the possible co-occurrence or overlap

of two distinct phase transformation events upon heating, an attempt has been made to resolve this issue in the present study.

In a separate series of experiments, three different starting microstructures have been produced on U-2wt.% Zr alloy. To begin with, a sample has been taken to 1273 K (1000°C), and held at this temperature for 5h, followed by cooling at the rate of 99 K min⁻¹ to room temperature in DSC. Subsequently, a second sample of roughly the same mass has been equilibrated at 1273 K (1000°C) for 5h and directly quenched in water. The long equilibration at high temperature has been done to promote grain growth, which facilitates athermal $\gamma \rightarrow \alpha'$ -martensite transformation. In a third experiment, the sample

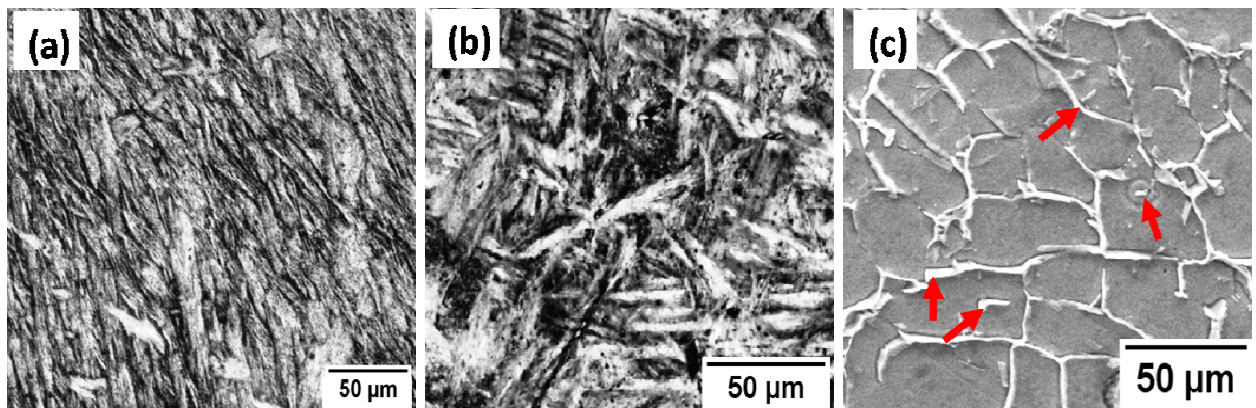


Fig.5.6(a). Microstructures of 99 K min⁻¹ cooled U-2wt.%Zr alloy revealing α' martensitic structure, **(b).** Microstructure of water quenched sample of U-2wt.%Zr, showing fine acicular needles of α' martensite, **(c).** SEM micrograph of 0.1 K min⁻¹ slow-cooled sample of U-2wt.%Zr alloy showing the presence of equilibrium α_{eq} and grain boundary δ -UZr₂ (arrows).

after annealing at 1273 K (1000°C) for 5h has been cooled very slowly at the rate of 0.1 K min⁻¹. It is believed that this very slow cooling is adequate enough to ensure thermodynamic equilibrium of the alloy, as it traverses through different phase transformation domains and result in the formation of equilibrium α -orthorhombic phase.

The microstructures of 99 K min⁻¹ cooled (**figure 5.6(a)**) and water quenched sample (**figure 5.6(b)**) indicated the presence of α' -martensite. The 0.1 K min⁻¹ slow-

cooled sample showed on the other hand the presence of equilibrium α and more importantly, grain boundary δ -UZr₂ phase (**figure 5.6(c)**). The microhardness value of α' -martensite is found to be 466 VHN. The 0.1 K min⁻¹ cooled sample having large equiaxed grains of α -phase, showed a microhardness value of 336 VHN.

In a fresh set of DSC experiments, the 99 K min⁻¹ cooled sample having α' -martensite as the starting microstructure has been heated in DSC at 1 K min⁻¹. The

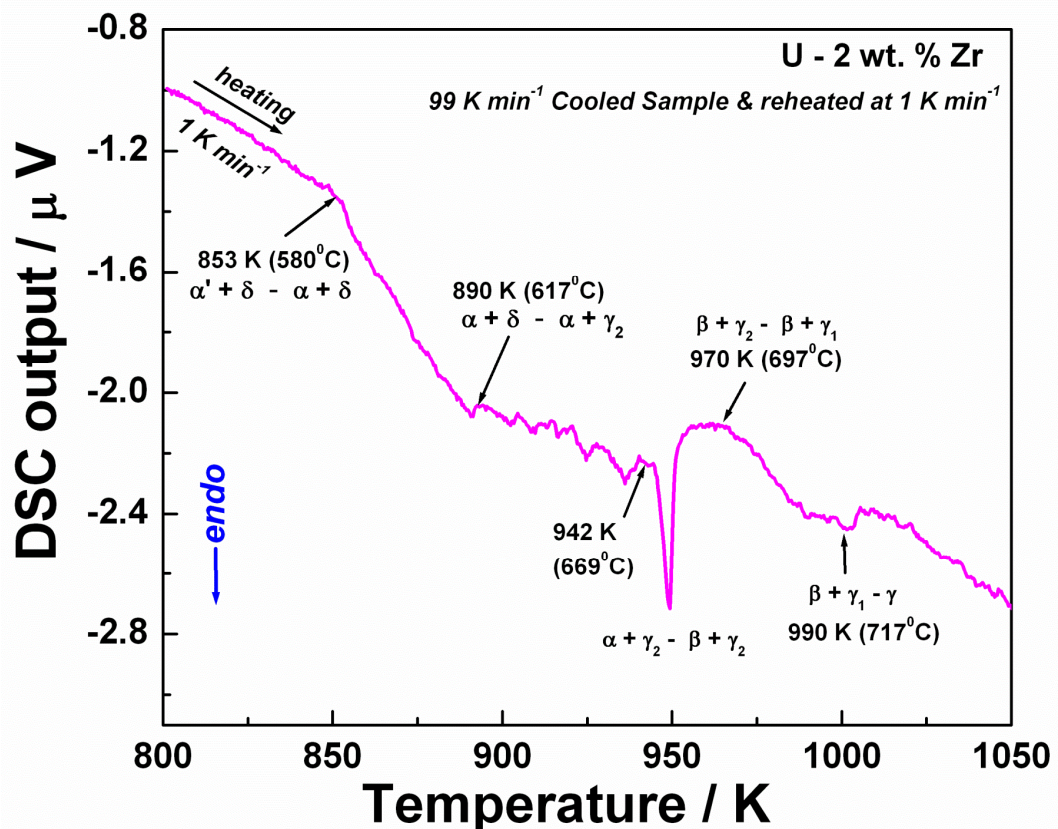


Fig.5.7(a). The on-heating DSC thermogram obtained at 1 K min⁻¹ on 99 K min⁻¹ sample of U-2wt.%Zr alloy. The occurrence of both martensitic relaxation and δ -UZr₂ dissolution are clearly noticed.

resulting DSC profile is shown in **figure 5.7 (a)**. This figure indicates clearly the presence of two distinct thermal events arising from both martensite relaxation and δ -UZr₂ dissolution at a closely spaced temperature interval of 853 K (580°C) to 890 K (617°C) respectively. The presence of two thermal events brings out the fact that a

complete suppression of the diffusive formation of δ -UZr₂ phase could not be realized even in the case of Zr-lean U-Zr alloys, at a fairly moderate cooling rate of 99 K min⁻¹. Although, the starting microstructure in this case possessed a distinct lath martensite morphology, (**figure 5.6(a)**), the presence of δ -UZr₂ cannot be ruled out, as it could still be present as a thin interlath particles or lamellae, making it thus undetectable at optical and normal SEM levels of resolution. Further, as mentioned earlier that, the

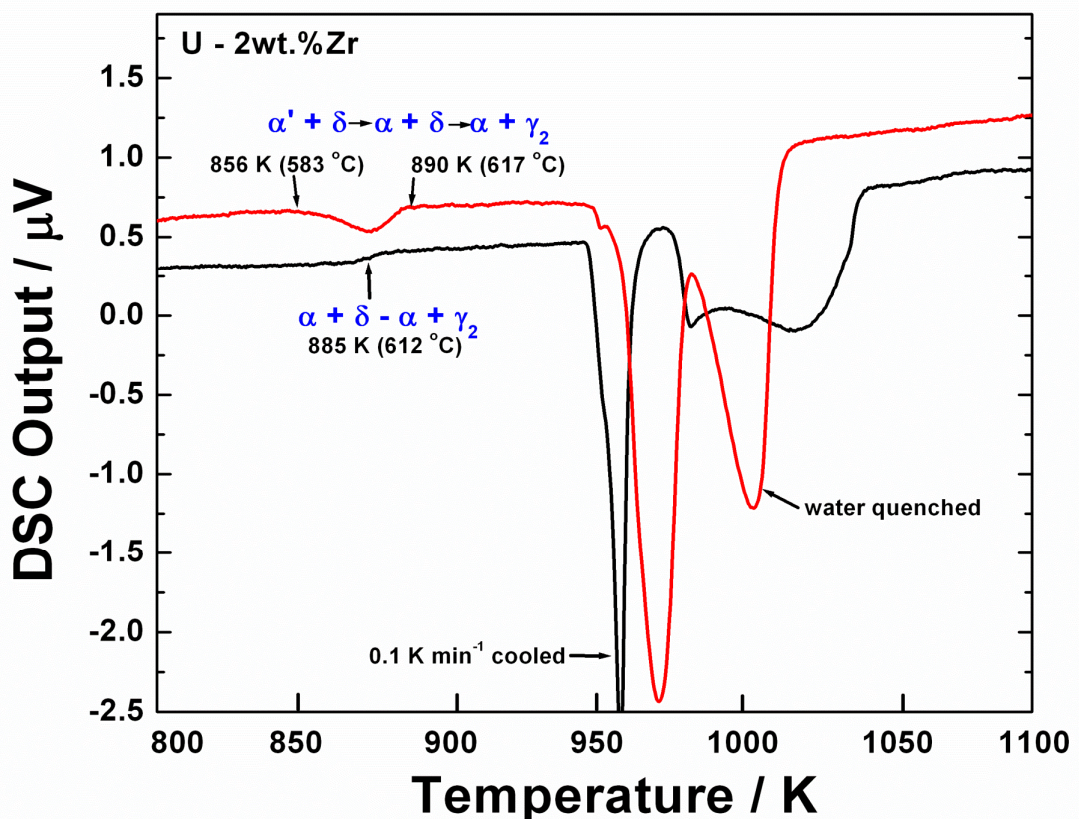


Fig.5.7(b). The on-heating DSC thermogram obtained on water quenched and 0.1 K min⁻¹ slow cooled samples of U-2wt.%Zr alloy.

volume fraction of δ -UZr₂ being small (~4.2%) in U-2 wt.% Zr alloy, it is equally difficult to be detect this phase by conventional XRD in U-2 wt.%Zr alloy. At this point, it is also instructive to recall the earlier observation of Mckeown *et al.*, who had shown that δ -phase is present even in as-cast microstructure of U-10wt.% Zr, in the form of fine nanometric lamellae [1].

In **figure 5.7(b)** the DSC profiles obtained on water-quenched and cooled sample are compared. It is clear that the WQ sample evinces a comparatively large endothermic peak area, whose enthalpy effects come from both martensite relaxation and UZr_2 dissolution. It is also useful to note that this thermal event associated with α' -relaxation is initiated at a lower temperature of about 856 K (583°C) and ends at about 890 K (617°C). The DSC trace of the 0.1 K min^{-1} sample on the other hand, revealed only a small step like inflection in the base line that is indicative of meager change in enthalpy associated with the dissolution of (a small volume fraction) $\delta\text{-UZr}_2$ phase. Further, this inflection is also found to occur at a higher temperature of 885 K (612°C), which is in fact very close to the equilibrium peritectoid temperature of 890 K (617°C) (see, **figure 5.2**). Thus, in the final analysis, it emerges that a complete suppression of $\gamma \rightarrow \alpha'$ -martensite formation in U-Zr alloys requires the employment of very slow cooling rates of the order of 0.1 K min^{-1} as observed in this case. For any other moderate or reasonably high cooling rates, the $\gamma \rightarrow \alpha'$ formation readily co-occurs along with the equilibrium $\gamma \rightarrow \alpha_{\text{eq}} + \delta\text{-UZr}_2$ formation. The relative extents of these two reactions, and hence the nature of the thermal analysis profile is a strong function of Zr content, and cooling history from single γ -phase field. It is generally the case that the volume fraction of $\delta\text{-UZr}_2$ is rather small in Zr-lean alloys, which makes it rather hard to be detected clearly in regular DSC experiments. Nevertheless, its presence is attested in the sensitive dynamic calorimetric trace obtained in the present study, in the form of composite thermal arrest. In the current study, this has been demonstrated only for U-2 wt. % Zr alloy; but it is a straight forward matter to carry out similar experiments on alloys of higher Zr content. Since the phase fraction of $\delta\text{-UZr}_2$ phase increases with Zr-content of alloy, the enthalpy effect associated with its dissolution is also more increasingly reflected in the DSC

profiles of high Zr alloys. This is evident in **figure 5.5**, where the DSC profiles of U-0, 2, 5, 10 wt. % Zr are collated together.

5.3.4. Effect of heating and cooling rate on phase transformations

Since heating and cooling rate variations play a crucial role in determining the kinetic pathways of alloy phases [9, 11, 3, 4], a set of DSC runs covering a spectrum of heating/cooling rates in the range, 5-50 K min⁻¹, was performed on each composition. It may be mentioned that each run was performed with a fresh sample, under nearly identical experimental conditions. In **figure 5.8**, the DSC profiles obtained on U-2wt.%

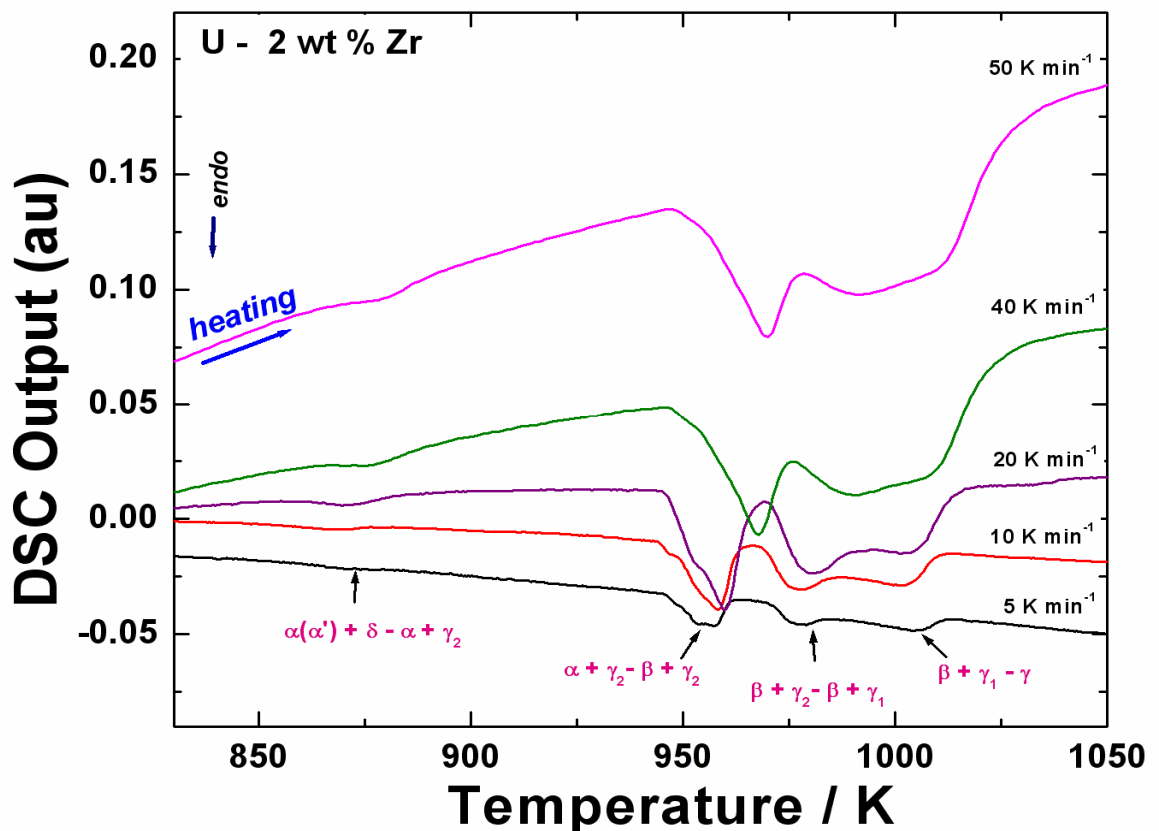


Fig.5.8. DSC thermogram obtained as function of heating rate (5-50 K min⁻¹) for U-2 wt.% Zr alloy are presented.

Zr for different heating rates (5–50 K min⁻¹) are shown; in **figure 5.9** the corresponding cooling cycle profiles are collated. It may be noted that the figures are self-explanatory, as various thermal arrests are clearly annotated. However, it is obvious that with

increasing heating rate, the separation between the finish temperature of $\alpha \rightarrow \beta$ and the start temperature of $\beta \rightarrow \gamma$ transformation is getting narrowed rather gradually (**figure 5.8**). For heating rates higher than about 40 K min^{-1} , the two thermal events overlap. A similar phenomenon is also noticed during cooling cycle (**figure 5.9**). Further, in the case

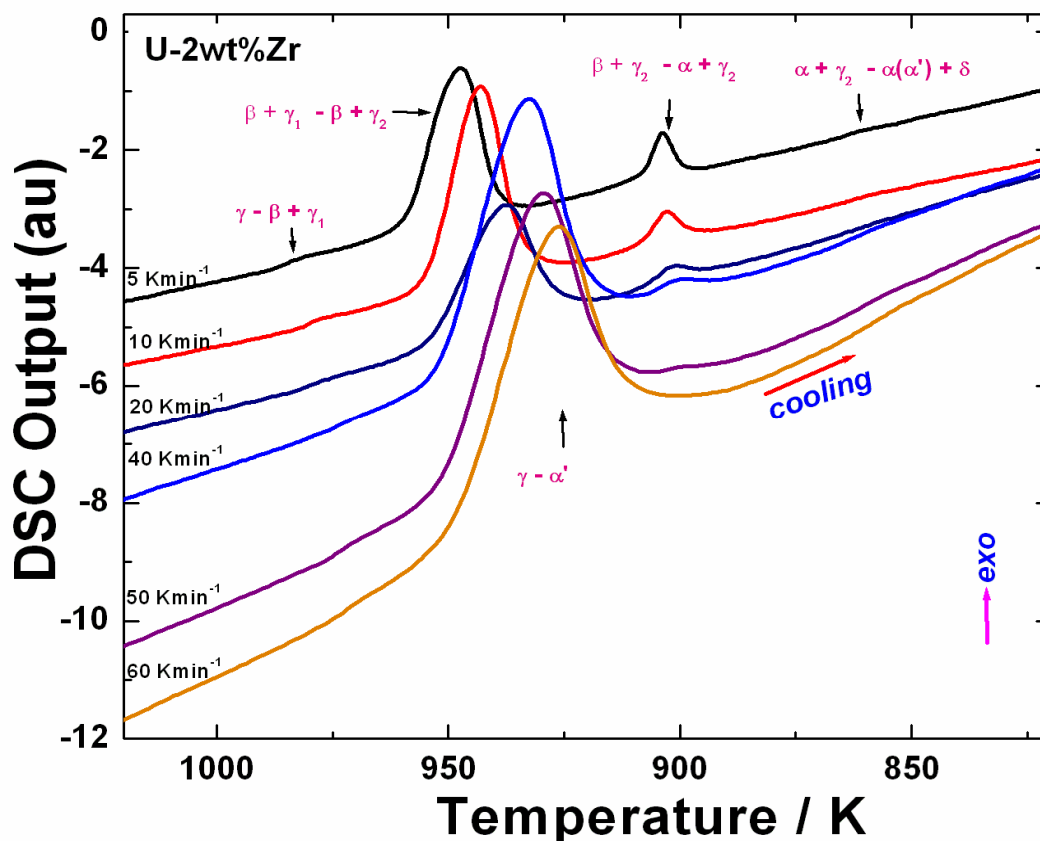


Fig.5.9. DSC thermogram obtained as function of cooling rate ($5\text{-}50 \text{ K min}^{-1}$) for U-2 wt.% Zr alloy are presented.

of U-2 wt.%Zr alloy, for cooling rates exceeding about 60 K min^{-1} , there is a clear possibility of direct $\gamma \rightarrow \alpha'$ -martensite phase change, as is also observed earlier by Hills *et al* [4]. It may be noted that with increasing cooling rate, the degree of undercooling experienced by γ phase also becomes higher. This results in the increase of the driving force for the decomposition of γ -phase [10]. However, the diffusion of Zr and U becomes increasingly sluggish with increasing under cooling, which ultimately favours $\gamma \rightarrow \alpha'$ -martensite transformation. But one interesting feature that merits special attention in

figure 5.8, is that the dissolution of δ -UZr₂ is observed at all heating rates and further, the dissolution temperature does not change significantly with heating rate. A similar behavior has also been observed in the case of U-5, 10 wt. % Zr alloys, since the results for higher Zr content follow the same trend, and therefore, these results are not being presented here in order to avoid space proliferation. Finally, one may also add that in case of pure uranium, there is no direct $\gamma \rightarrow \alpha'$ -martensite transition possible, even under very fast cooling rates. This aspect had already been discussed in detail in our earlier work [20].

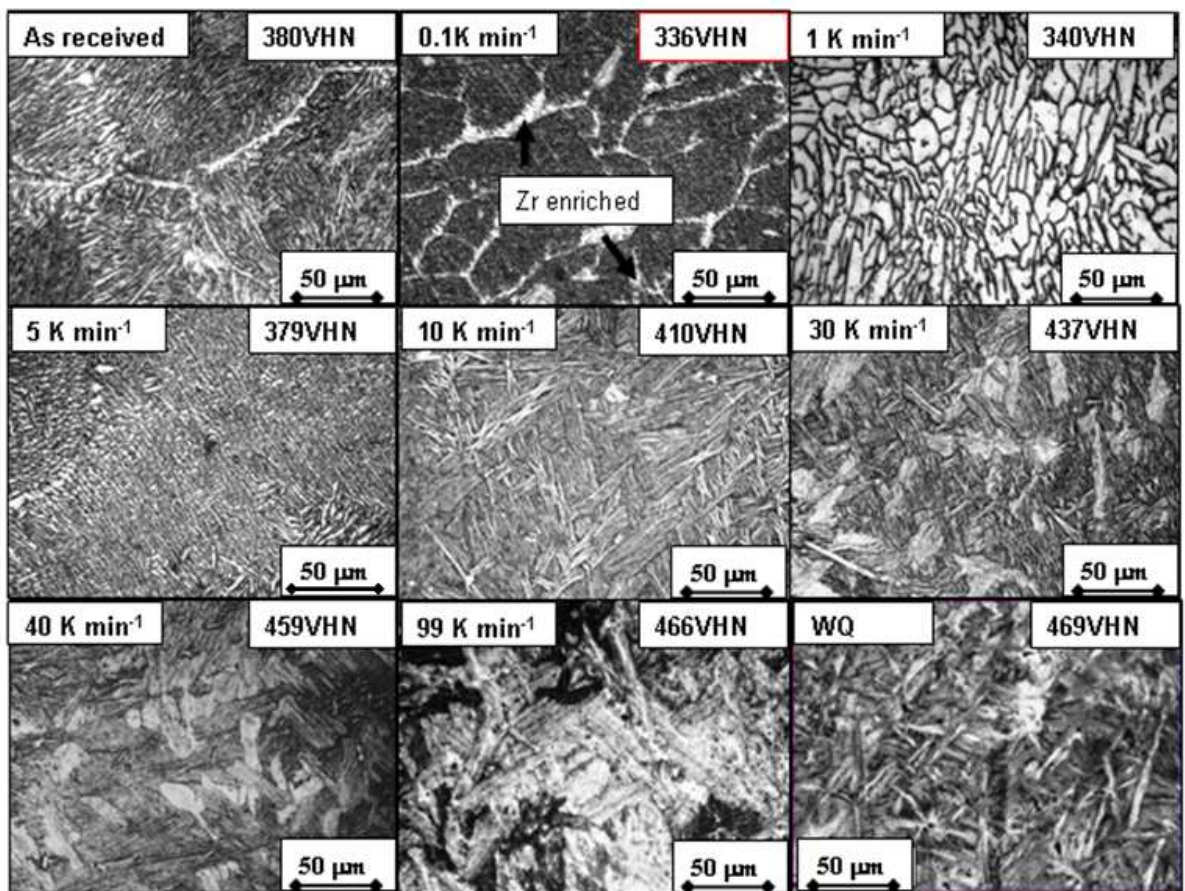


Fig.5.10. The effect of cooling rate on microstructure in U-2 wt.% Zr alloy. Individual micrographs are arranged in the order of increasing cooling rate

5.3.5. *Effect of cooling rate on microstructural morphology*

The effect of cooling rate on microstructure is depicted in **Fig. 5.10**, for U-2wt. % Zr alloy. The individual micrographs in **Fig. 5.10**, are arranged in the order of increasing cooling rate, from 0.1 to 99 K min⁻¹. The corresponding variation in microhardness has also been labeled on each micrograph. This collage reveals that with increasing cooling rate, there is a significant change in the microstructural morphology, from that of equiaxed α (0.1 K min⁻¹) to an acicular α' martensitic type (WQ). In the case of slow cooled sample, the enrichment of Zr along grain boundary, due to δ -UZr₂ formation has already been discussed elsewhere in this report (see, **figure 5.3(c) & 5.3(d)**).

5.3.6 *Continuous heating and cooling transformation diagrams*

The heating and cooling dependencies of various solid state transformations (transformation start -T_S and transformation finish -T_f temperatures)are nicely brought out in the form of continuous heating (CHT) and cooling (CCT) transformation diagrams, shown in **figure 5.11 (a)** and **figure 5.11 (b)**, respectively for U-2wt.% Zr alloy. It is clearly evident from the CHT diagram (**figure 5.11(a)**) that separation between $\alpha \rightarrow \beta$ transformation finish and the beginning of $\beta \rightarrow \gamma$ transformation is getting narrower for higher heating rates. Similarly, one can see from CCT diagram (**figure 5.11 (b)**) that for cooling rates exceeding about 40-60 K min⁻¹, the two successive phase changes $\gamma \rightarrow \beta$ and $\beta \rightarrow \alpha$ heavily overlap. In a similar fashion the continuous heating and cooling transformation diagrams (CHT & CCT) for U-5 & 10 wt.% Zr alloys are also obtained and presented in **figure 5.12 (a)**, **figure 5.12 (b)**, **figure 5.13 (a)** and **figure 5.13 (b)** respectively. Further, the direct possibility of $\gamma \rightarrow \alpha'$ -martensite formation at high cooling rates is also evident from CCT diagrams for all the three compositions. The critical cooling rates needed for effecting $\gamma \rightarrow \alpha'$ -displacive phase transformation are estimated to be, 60, 20 & 10 K min⁻¹ respectively for 2, 5 and 10 wt. %Zr alloys.

5.4. Discussion

As mentioned earlier, the physical metallurgy of U-Zr alloys has been investigated quite extensively in the past. Yet, to the best of our knowledge, the number of comprehensive

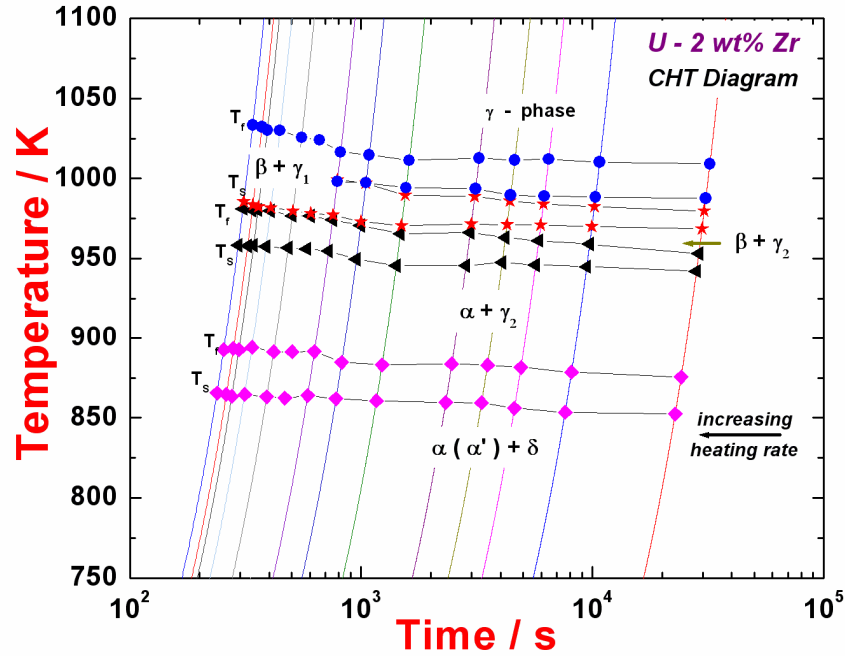


Fig.5.11(a). Continuous heating transformation (CHT) diagram for U-2wt.%Zr alloy

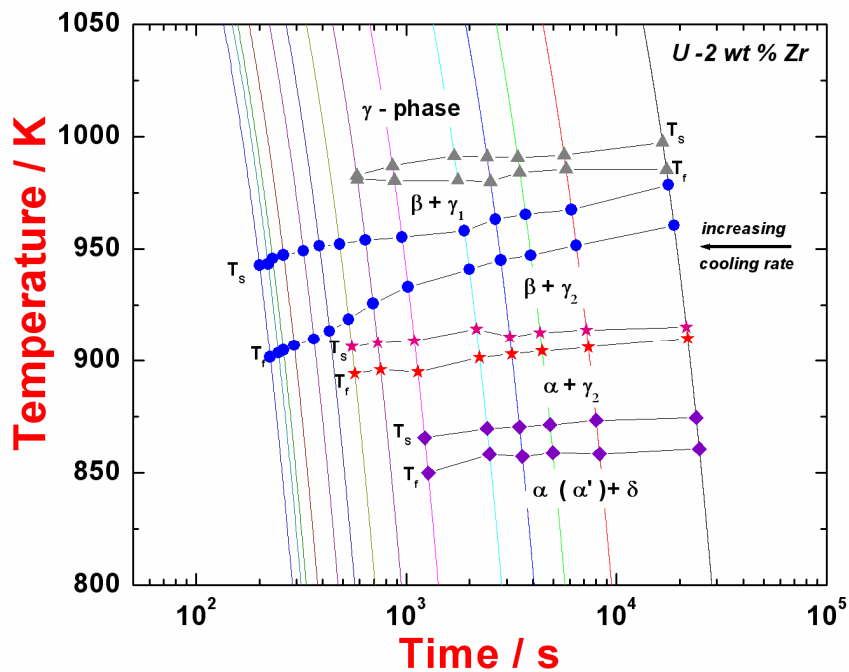


Fig.5.11(b). Continuous cooling transformation (CCT) diagram for U-2wt.%Zr alloy.

calorimetry investigations on this important nuclear binary system is comparatively rather minimal, and almost very few in the past ten years. Accurate high temperature dynamic calorimetry can offer two principal advantages.

In addition to the fact that it can serve to establish the sequence of phase changes as a

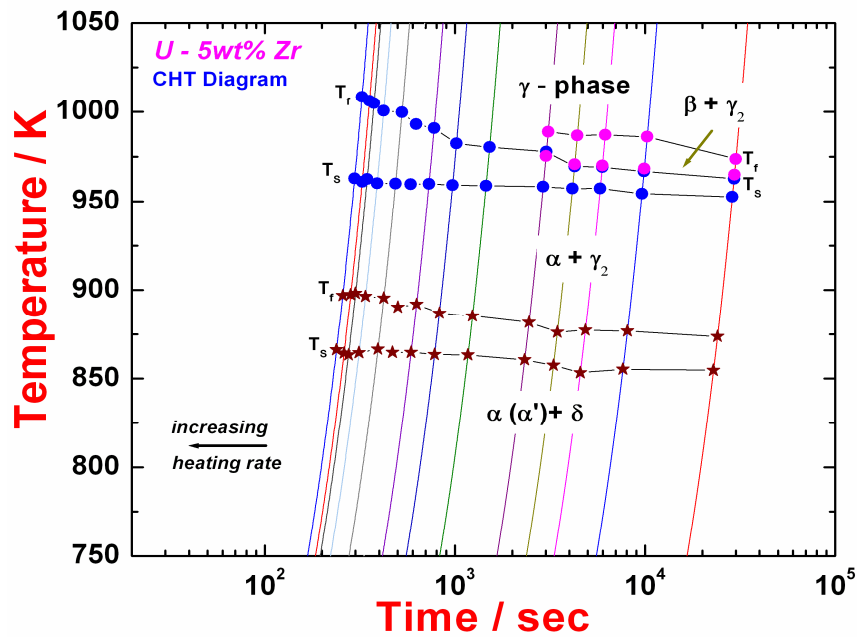


Fig.5.12(a). Continuous heating transformation (CHT) diagram for U-5wt.%Zr alloy.

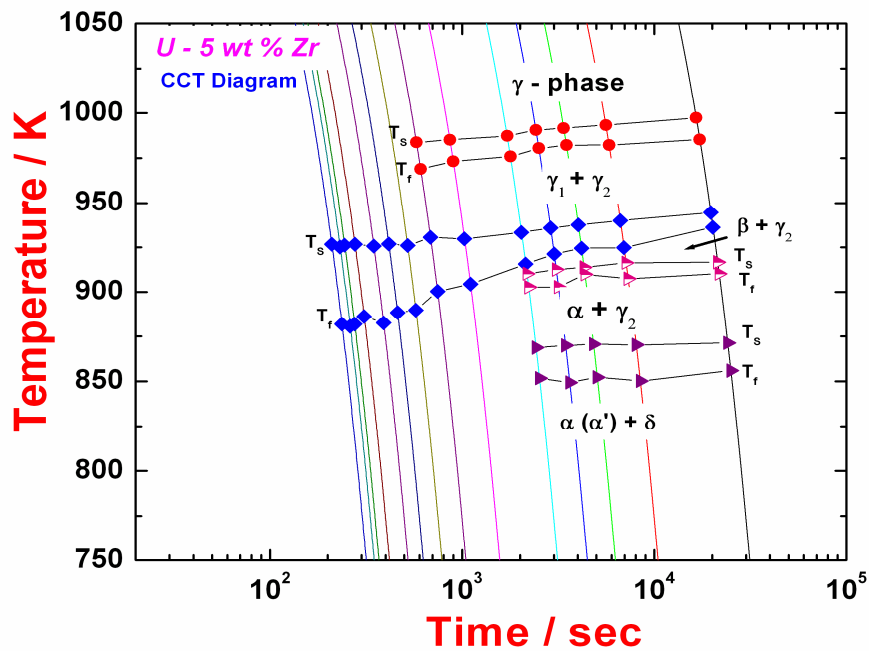


Fig.5.12(b). Continuous cooling transformation (CCT) diagram for U-5wt.%Zr alloy.

function of temperature, and providing accurate thermodynamic data on associated phase changes, it can also be used to obtain valuable information on transformation kinetics.

The calorimetry results become even more appealing, when they are supplemented with metallographic characterization of transformed sample microstructure, as had been done here. In the present study, fairly accurate data on various solid state transformation temperatures, together with enthalpies of phase transformation have been obtained on three U-Zr alloys. The results are in good agreement with most of the values reported in literature [6-20] and also in line with the recent assessment of phase equilibria [5]. However, to the extent we have surveyed the open literature; experimental estimates of enthalpies of various solid state phase changes as a function of Zr content are scarce. In this sense, the enthalpy data reported in **table 5.2**, constitute a valuable (additional) input for future optimization of U-Zr and other higher order systems.

One of the principal outcomes of this study is the clear enunciation of the role of composition and cooling rate from high temperature γ -bcc phase, in deciding the course of phase evolution. The possible coexistence of α_{eq} or α' -martensite and δ -UZr₂ phase in annealed U rich U-Zr alloys (with Zr content up to 20wt. %) and more importantly their separate attestation upon subsequent heating has not been unambiguously established in literature. This is partially because one needs to employ a combination of techniques to resolve this issue. Further, in Zr-lean alloys, the equilibrium phase fraction of δ -UZr₂ being small, it often remains undetected in conventional analysis. If one estimates the phase fraction of UZr₂ phase in U-2wt.% Zr from equilibrium diagram (**figure 5.2**), it is around 4.2% and this will be more for higher Zr alloys. Hence, in principle the presence of δ -UZr₂ phase must be confirmed by XRD. However, if one compares carefully the 2θ positions for δ -UZr₂ and α -orthorhombic phase in a wide range of 2θ spectrum, it can be found that they are almost the same for many principal reflections. There are of course, a

few weak non overlapping high angle reflections that are intrinsic to δ -UZr₂ phase, but their intensity being small, they often go unnoticed in a general purpose analysis. In a recent transmission electron microscopy study, Mckeown *et al.*, [1] has clearly confirmed the presence of UZr₂ phase in the as-cast structure of U-10 wt.% Zr alloy. According to this study, the UZr₂ phase has lamellar structure with an average lamellae width of the

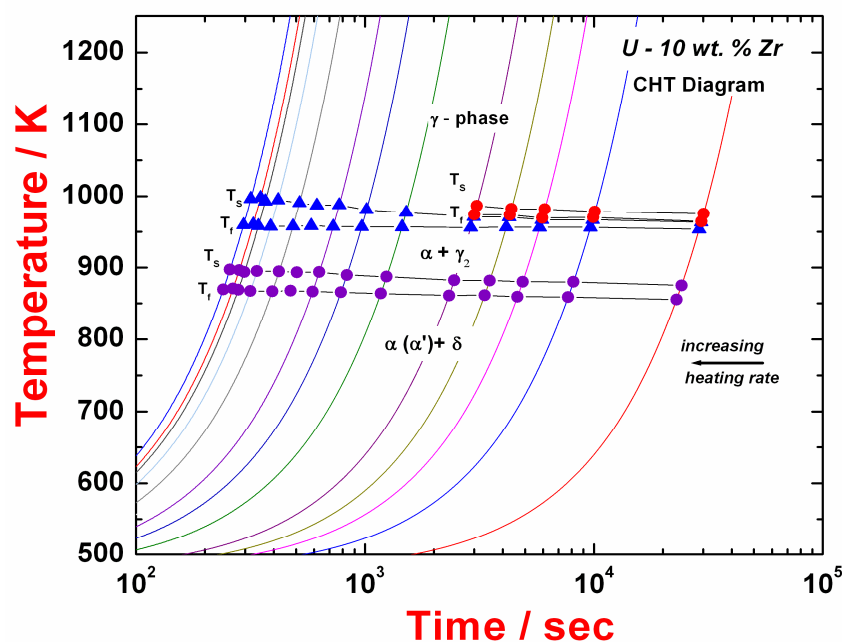


Fig.5.13(a). Continuous heating transformation (CHT) diagram for U-10wt.%Zr alloy.

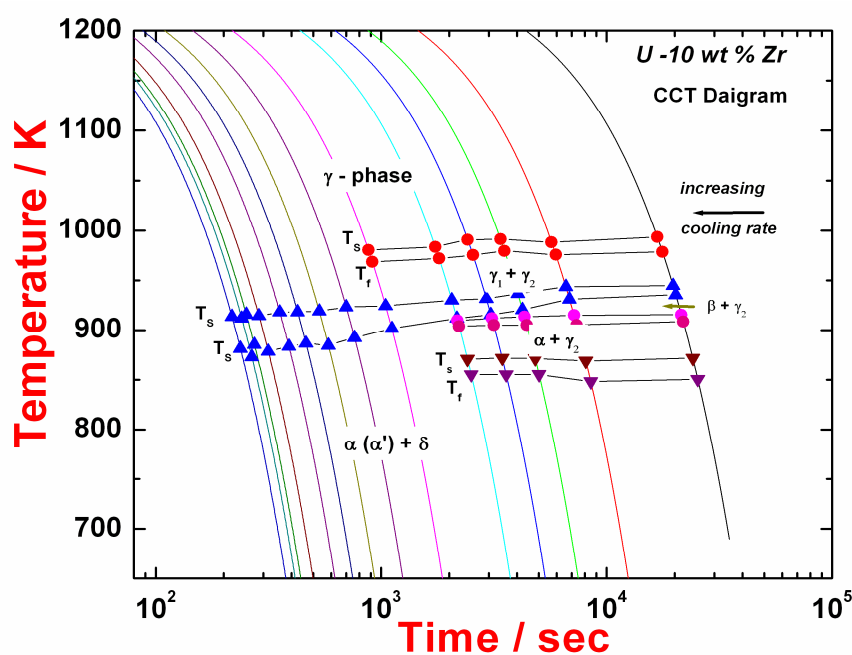


Fig.5.13(b). Continuous cooling transformation (CCT) diagram for U-10wt.%Zr alloy.

order of 20 nm. Again it is not possible to characterize such feature using scanning electron microscopy, as has been observed in the present study as well. But then, if one has to detect the presence of δ -UZr₂ either with or without the accompanying presence of martensitic α' -phase, it is necessary to devise specific heating and cooling rate combinations, to establish the individual presence of $\gamma \rightarrow \beta \rightarrow \alpha$ and $\gamma \rightarrow \alpha'$ transformations separately. At the end of normal annealing cycle with slow furnace cooling (furnace switched off), one often ends up with a mixture of α_{eq} , α' and small δ -UZr₂ phases, due to the mixed mode of γ -bcc decomposition. This finding is important as it has some bearing on the microstructure development of complex U-Zr-Pu base alloys that actually constitute the kernel of metal fuel. The presence of other alloying additions, besides impurities will influence the decomposition kinetics of γ phase in U-base alloys, by the way of modifying the diffusive mobility values.

As for transformation kinetic aspects are concerned, the experimentally obtained, baseline subtracted DSC peak profile of a phase transformation can be de-convoluted to obtain quantitative information about the extent of phase transformation X as a function of time (t), or temperature (T) for a given heating or cooling rate ($\beta = dT/dt$) (instructive to recall from **chapter 3**).

$$X(T) = \frac{\int_{T_s}^T (\varphi(T) dT)}{\int_{T_s}^{T_f} (\varphi(T) dT)}. \quad (5.1)$$

Where the integral in the numerator $\int_{T_s}^T \varphi(T) dT$ represents the partial area under the transformation peak in the temperature domain $T-T_s$, while the denominator $\int_{T_s}^{T_f} \varphi(T)dT$, stands for total peak area for entire transformation range, T_s to T_f . Further, a quantitative modeling of the transformation kinetics, namely, $X(T)$ versus $T(\beta)$ data for fixed heating rate β , is also possible, by invoking a suitable conceptual formalism for the non isothermal transformation kinetics [20]. In the present study, for modeling the

kinetics of $\alpha \rightarrow \beta$ transformation in the light of experimental DSC data, the popular, often used Kolmogorov-Johnson-Mehl-Avrami (KJMA) model has been employed [20-27]. In

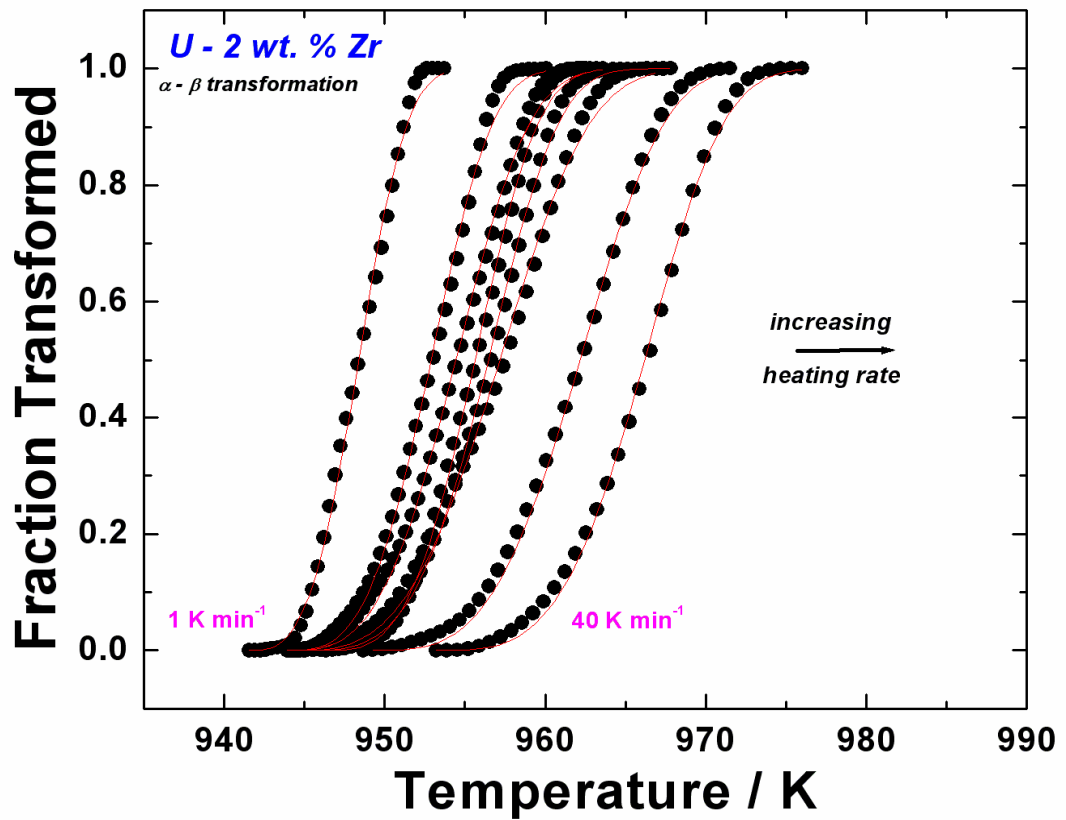


Fig.5.14. Phase fraction versus temperature data obtained for $\alpha \rightarrow \beta$ on-heating transformation in U-2wt.%Zr alloy. The KJMA model fit is shown as continuous line, passing through experimental data points, shown as filled circles.

simple terms, assuming site saturation nucleation, the non isothermal KJMA model for the diffusional transformation kinetics can be expressed as follows (refer to **chapter 3**).

$$X(T) = 1 - \exp \left\{ -k_o^n \left[\frac{R(T-T_s)^2}{q Q_{eff}} \right]^n \right\}. \quad (5.2)$$

The above equation assumes that all the potential nucleation sites (of equal potency) are already available at the beginning of the transformation. q is heating rate in K s^{-1} , R is the universal gas constant, T_s is onset temperature in Kelvin, k_o is the frequency factor, n is the empirical overall transformation exponent, whose theoretical value (ranging from 0.5 to 4) depends on whether the transformation is bulk diffusion or interface controlled and growth proceeds in one, two or three dimensions [20-26]. Q_{eff} is the apparent activation

energy for the transformation process. In a strict sense Q_{eff} reflects the suitably weighted

Table 5.3				
Estimated effective activation energy Q_{eff} for $\alpha \rightarrow \beta$ phase transformation kinetics as function of heating rate, for U-0, 2,5& 10 wt. % Zr alloys				
Composition	Heating Rate K min ⁻¹	n	k	Q_{eff} kJ mol ⁻¹
U	3	2.8±0.02	$2.2 \times 10^{11} \pm 0.2 \times 10^{11}$	176±2
	5	2.5±0.03	$2.9 \times 10^{11} \pm 0.1 \times 10^{11}$	174±1
	7	2.7±0.01	$3.9 \times 10^{11} \pm 0.3 \times 10^{11}$	176±1
	10	2.7±0.04	$7.3 \times 10^{11} \pm 0.6 \times 10^{11}$	182±2
	20	2.4±0.02	$1.1 \times 10^{12} \pm 0.7 \times 10^{11}$	186±1
	30	3.1±0.02	$1.4 \times 10^{12} \pm 0.9 \times 10^{11}$	188±2
	40	2.8±0.05	$1.8 \times 10^{12} \pm 0.8 \times 10^{11}$	190±1
U-2 wt. Zr	3	1.8±0.01	$1.5 \times 10^{13} \pm 0.4 \times 10^{12}$	220±2
	5	1.8±0.01	$8.8 \times 10^{12} \pm 0.1 \times 10^{12}$	215±1
	7	1.7±0.02	$3.7 \times 10^{12} \pm 0.2 \times 10^{12}$	204±2
	10	1.8±0.02	$1.3 \times 10^{13} \pm 4.5 \times 10^{12}$	214±1
	20	1.8±0.02	$3.8 \times 10^{12} \pm 0.5 \times 10^{12}$	201±2
	30	1.8±0.02	$7.4 \times 10^{12} \pm 0.7 \times 10^{12}$	207±1
	40	1.7±0.02	$1.1 \times 10^{13} \pm 1.5 \times 10^{12}$	208±2
U-5 wt. Zr	3	1.2±0.01	$2.5 \times 10^{13} \pm 0.5 \times 10^{12}$	223±1
	5	1.2±0.01	$9.1 \times 10^{13} \pm 2.5 \times 10^{12}$	230±3
	7	1.2±0.02	$1.2 \times 10^{14} \pm 8.5 \times 10^{12}$	229±1
	10	1.2±0.02	$2.5 \times 10^{13} \pm 7.5 \times 10^{12}$	219±2
U-10 wt. Zr	3	0.9±0.01	$1.1 \times 10^{15} \pm 8.5 \times 10^{13}$	251±3
	5	1.1±0.02	$6.8 \times 10^{14} \pm 1.5 \times 10^{13}$	242±2
	7	1.1±0.01	$6.9 \times 10^{14} \pm 2.5 \times 10^{13}$	248±2
	10	0.9±0.01	$4.4 \times 10^{14} \pm 4.5 \times 10^{13}$	240±1

average of the activation barrier for nucleation and growth. As such, it has to be treated as function of the extent of transformation $X(T)$ as well [20]; however, in the present case, these complications are avoided and instead is taken as constant through the entire transformation. The experimental $X_{\beta}(T)$ data for $\alpha \rightarrow \beta$ phase change in U-2wt.% Zr alloy have been fitted using Eq. (5.2), by means of a standard non-linear optimization routine. The fit along with the experimental $X_{\beta}(T)$ data are shown in **figure 5.14**. The figure shows that both experimental data and the KJMA model fit are in good agreement. The

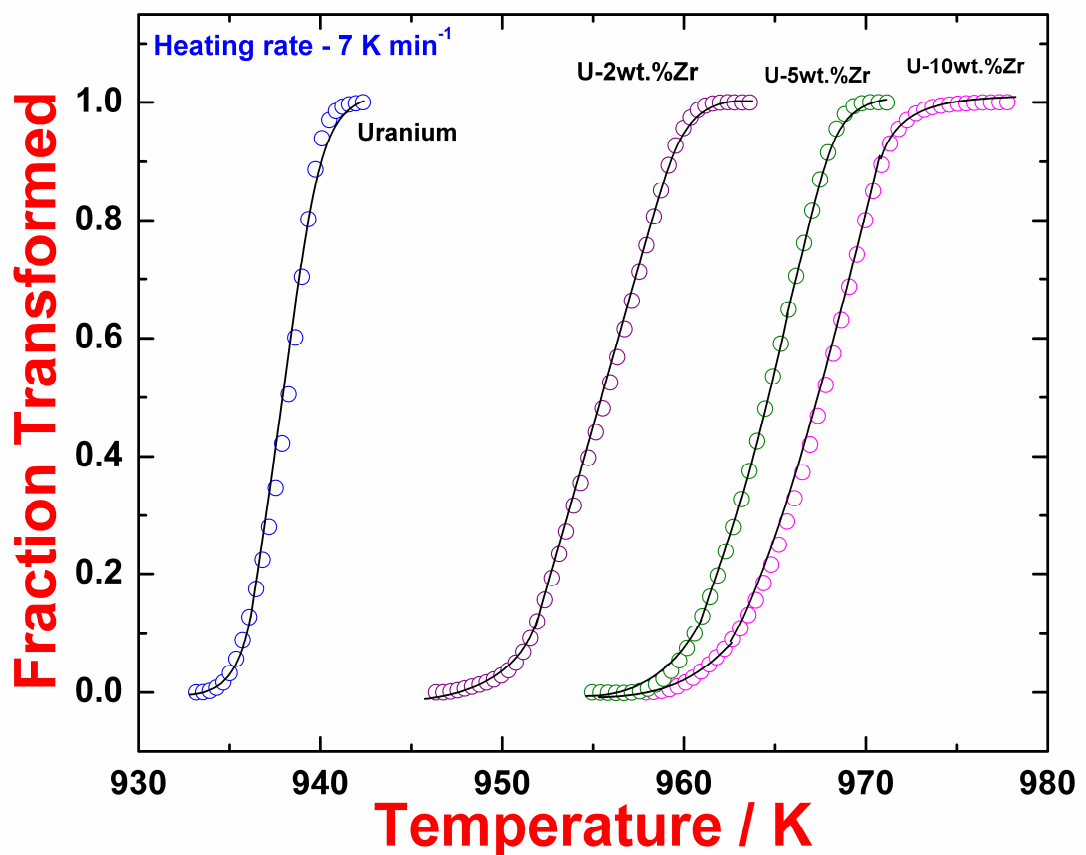


Fig.5.15. Phase fraction versus temperature data obtained for $\alpha \rightarrow \beta$ on-heating transformation in U-0, 2, 5 & 10 wt.%Zr alloys. The KJMA model fit is shown as continuous line, passing through experimental data points, shown as open circles.

estimated kinetics parameters, namely Q_{eff} , k_o and n for $\alpha \rightarrow \beta$ phase change are tabulated in **table 5.3**. Similar exercise has been performed in case of other alloy compositions and the corresponding fraction curve and fitted data using KJMA for different U-Zr alloys

obtained at given heating rate of 7 K min^{-1} are shown in **figure 5.15**. The estimated kinetic data are listed in **table 5.3**. It can be seen from the tabulated data that with increasing Zr content of alloy, the effective activation energy Q_{eff} , is increasing. This is in line with the observation that solid state diffusion becomes progressively more sluggish with increasing Zr-content, which is one of the reasons, as to why $\gamma \rightarrow \alpha'$ - displacive transformation is favored rather easily in high Zr containing U-Zr alloys. The activation energy for $\alpha \rightarrow \beta$ transformation in the case of U is found to be in the range of 174-190 kJ mol^{-1} and it is in good agreement with the reported activation energy for self diffusion of U in α -U matrix, which is about of the order of 168 kJ mol^{-1} [28]. For U-2, 5 & 10 wt.% Zr alloys the activation energy is found to be in the range of 200-250 kJ mol^{-1} . To the author's knowledge, experimental inter-diffusivity data on U-Zr alloys are not available in open literature for low temperature orthorhombic structure. However, for γ -bcc alloys, the activation energy of Zr diffusion has been reported to be much lower, that is in the range 90-150 kJ mol^{-1} , for Zr content in the range of 10- 50 wt.% [28-31]. On the other hand, in the case of U-2.5 wt. % Cr and U-1wt.% Pt alloys, the reported activation energy for $\beta \rightarrow \alpha$ transformation is of the order of 190 and 135 kJ mol^{-1} respectively [32, 33]. A comparison with these sparse data suggests that the activation energy obtained in the present study for different U-Zr alloys is fairly reasonable and in expected order. However, more research needs to be carried on this important issue. The transformation exponent (n) obtained in the present study for pure uranium is in the range, 2.58-3.05 which signifies that the polymorphic transformation is interface controlled [20]. But in the case of U-2 wt. % Zr alloys n varies in the range of 1.7-1.9 and this indicate that the transformation is controlled by diffusion with continuous nucleation process [34]. However in the case of U-5 & 10 wt. % Zr alloys n varies in the range of 0.9-1.2 and this

indicate that the transformation is controlled by diffusion with site saturation nucleation process.

In an early study, Hills *et al.*, [4] have investigated the change in microstructural morphology in U-0.97 to 27.7 wt.% Zr alloys by end-quench method. A general phase refinement with increasing cooling rate was observed. However, the effect of controlled cooling rate on microstructure evolution, as observed in the present study has not been reported earlier. In the present study, it is established that very slow cooling from γ -phase is required for obtaining α_{eq} , along with grain boundary δ -UZr₂. It is quite likely that the preferential segregation of Zr to prior γ -boundaries might have been instrumental in enhancing the local super saturation and hence in catalyzing the heterogeneous nucleation of δ -UZr₂. The enrichment of Zr along grain boundary has been supported by X-ray map shown in **figure 5.3(d)**. Further, at very slow cooling rates, the growth of α_{eq} is also facilitated as sufficient time is provided for the development of regular equiaxed grain structure.

In the present study, it is found that upon increasing the cooling rate, the α -cells become finer; and with further increase, a Widmanstatten like side plate morphology is seen to develop. However, beyond a threshold cooling rate of about 60 K min⁻¹ (U-2wt.% Zr) the microstructure significantly changes from cellular to lath like morphology, indicating possibly the formation of α' -martensite. Further increase in cooling rate results in the refinement of α' -colony size, with many intersections occurring between newly formed laths. For large enough cooling rate, such as water quenching, we see very many fine acicular α' -needles, populating thickly the entire specimen [4]. The change in microstructure upon increased cooling rate has also been reflected in the increase of hardness values. It is clear that thermal history and composition taken together decide the course of phase transformations and microstructure evolution in U-Zr alloys.

5.5. Conclusions

- (i) Calorimetric characterization of transformation sequence, transformation temperatures and enthalpy have been made for U-xZr (x=0, 2, 5, 10 wt.%) alloys. The reported transformation temperatures and enthalpy of transformation have accuracy of the order of ± 2 K and 5% respectively.
- (ii) Upon slow heating of an annealed sample of U-2 wt.% Zr alloy, the following phase transformation sequence is found to take place: $\alpha(\alpha') + \delta\text{-UZr}_2 \rightarrow \alpha_{\text{eq}} + \gamma_2 \rightarrow \beta + \gamma_2 \rightarrow \beta + \gamma_1 \rightarrow \gamma$. For U-5 wt.% Zr and U-10 wt.% Zr alloys, the corresponding sequence is found to be, $\alpha(\alpha') + \delta\text{-UZr}_2 \rightarrow \alpha_{\text{eq}} + \gamma_2 \rightarrow \beta + \gamma_2 \rightarrow \gamma_1 + \gamma_2 \rightarrow \gamma$.
- (iii) In case of annealed U-Zr alloys, it is found that upon heating, both $\delta\text{-UZr}_2$ dissolution and α -martensitic relaxation occurs in a concomitant fashion. However, if the initial microstructure consists of $\alpha_{\text{eq}} + \delta\text{-UZr}_2$, then the major thermal effect arises from $\delta\text{-UZr}_2$ dissolution.
- (iv) A clear enumeration of the effect of cooling rate from high temperature single γ -phase, and alloy composition in influencing the decomposition modes has been made. It is found that for slow cooling rates, of the order of 0.1 K min^{-1} or less, it is possible to obtain equilibrium α -orthorhombic phase along with grain boundary $\delta\text{-UZr}_2$ phase. However, with increasing cooling rate, it becomes difficult to nucleate α and $\delta\text{-UZr}_2$, due to sluggish Zr diffusion. This favors the formation of α' -martensitic phase directly from γ through a displacive mode.
- (v) The critical cooling rate required for $\gamma \rightarrow \alpha'$ direct displacive transformation is found to decrease with increasing Zr content. For U-2, 5, and 10 wt.% Zr alloys, it is found to be of the order of, 60, 20, 10 K min^{-1} respectively.
- (vi) Based on present dynamic calorimetry results, continuous heating and cooling transformation diagrams have been obtained for U-2, 5 & 10 wt.% Zr alloys.

- (vii) Significant change in the microstructure morphology with increasing cooling rates has been found. The morphology changes from equiaxed α_{eq} orthorhombic phase to acicular α'_m -martensite needles, with increase in cooling rate from 0.1 K min^{-1} to severe water quenching.
- (viii) The apparent activation energy for $\alpha \rightarrow \beta$ on-heating phase transformation showed an increase with increasing the Zr content which implies that with increasing Zr content the diffusion of Zr in uranium matrix become difficult. Further, the kinetics of $\alpha \rightarrow \beta$ phase change in the case of uranium is controlled by interface mobility however in the case of U-2, 5 & 10 wt.% Zr alloys it is controlled by Zr-diffusion in α' -phase.

5.6. References

1. T. Mckeown, S. Irukuvarghula, S. Ahn, M. A. Wall, L. L. Hsiung, S. McDeavitt and P. E. A. Turuchi, *J. Nucl. Mater.*, 436 (2013)100.
2. G. Lagerberg, *J. Nucl. Mater.*, 9 (1962) 261.
3. A. Viro, *J. Nucl. Mater.*, 5(1962)109.
4. R. F. Hills, B. R. Butcher, B. W. Howlett and D. Stewart, *J. Nucl. Mater.*, 16(1965) 25.
5. H. Okamoto, *J. Phase Equilibria*, 28 (2007) 499.
6. C. B. Basak, G. J. Prasad, H. S. Kamath and N. Prabhu, *J. Alloys Compd.*, 480 (2009) 857.
7. C. B. Basak, R. Keswani, G. J. Prasad, H. S. Kamath and N. Prabhu, *J. Alloys Compd.*, 471 (2009) 544.
8. S. Kaity, J. Banerjee, M. R. Nair, K. Ravi, S. Das, T. R. G. Kutty, Arun Kumar and R. P. Singh, *J. Nucl. Mater.*, 427 (2012) 1.
9. S. T. Zegler, USAEC Rep. ANL-6055, 1962.
10. G. Lagerberg, *J. Nucl. Mater.*, 9 (1962) 261.
11. C. B. Basak, G. J. Prasad, H. S. Kamath and N. Prabhu, *J. Alloys Compd.*, 471 (2009) 544.
12. Arun Kumar Rai, S. Raju, Haraprasanna Tripathy, R. N. Hajra and M. Vijayalakshmi, *Trans. Ind. Inst. Met.*, 66 (2013) 387.
13. D. Summers-Smith, *J. Inst. Met.* 83 (1954-55) 277.
14. B. W. Howlett and A. G. Knapton, paper P/1469, Proc. 2nd U. N. International Conference on Peaceful use at Geneva, 6 (1958) 104.
15. F. A. Rough and A. A. Bauer, Battelle (USA) Report BMI-1300, 1958.
16. A. A. Bauer, Battelle (USA) Report BMI-1350, 1959.
17. J. F. Duffey, and C. A. Bruch, *Trans. AIME*, 212 (1958) 17.

18. M. Akabori, A. Itoh, T. Ogawa, F. Kobayashi and Y. Suzuki, *J. Nucl. Mater.*, 188 (1992) 249.
19. M. Akabori, T. Ogawa, A. Itoh and Y. Morii, *J. Phys. Condens. Matter.*, 7 (1995) 8249.
20. Arun Kumar Rai, S. Raju, B. Jeyaganesh, E. Mohandas, R. Sudha, and V. Ganesan, *J. Nucl. Mater.*, 383 (2009) 215.
21. F. Liu, F. Sommer and E. J. Mittemeijer, *Int. Mater. Rev.*, 52 (2007) 193.
22. P. Kruger, *J Phys. Chem. Solids*, 54 (1993) 1549.
23. E. J. Mittemeijer, *J. Mat. Sci.*, 27 (1992) 3977.
24. G. Ruitenberg, E. Woldt and A. K. Petford, *Thermochim. Acta*, 378 (2001) 97.
25. Y. C. Liu, F. Sommer and E. J. Mittemeijer, *Acta Mater.*, 54 (2006) 3383.
26. R. Massih and L. O. Jernkvist, *Modell. Simul. Mater. Sci. Eng.*, 17 (2009) 055002.
27. S. Malinov, Z. Guo, W. Sha, and A. Wilson, *Metall. Trans A*. 32 (2001) 8798.
28. Y. Adda and A. Kirianenko, *J. Nucl. Mater.*, 6 (1962) 135.
29. T. Ogata, M. Akabori, A. Itoh and T. Ogawa, *J. Nucl. Mater.*, 232 (1996) 125.
30. M. Akabori, A. Itoh, T. Ogawa and T. Ogata, *J. Alloys Comp.*, 271-3 (1998) 597.
31. W. Li, R. Hu, Y. W. Cui, H. Zhong, H. Chang, J. Li and L. Zhou, *J. Nucl. Mater.*, 407 (2010) 220.
32. W. J. Kitchingman, K. M. Pickwick, I. G. Brown and R. J. Edwards, *J. Nucl. Mater.*, 18 (1966) 219.
33. R. D. Townsend and J. Burke, *J. Nucl. Mater.*, 17 (1965) 215.
34. R. A. Vandermeer, *Proceedings of the Third Army Materials Technology Conference held at Vall, Colorado, USA, February 1974*, p. 259.

Chapter 6

Investigation of Phase Equilibria of Fe-U System using Calorimetry

6.1. Introduction

According to the literature survey presented in **chapter 1** on Fe-U binary system it emerges that the metallurgy of this system has been well studied in past [1-19], nevertheless some ambiguities still persist in the context of transformation temperatures of invariant reactions [1-19]. In order to address these issues to some extent, a differential scanning calorimetry based characterization of high temperature phase equilibria and phase transformation kinetics in $\text{Fe}_{100-x}\text{U}_x$ binary alloys, with x varying from 0 to 95 mass % U has been undertaken. In the present study accurate measurement of transformation temperatures pertaining to: (i) $\alpha\text{-Fe}\rightarrow\gamma\text{-Fe}\rightarrow\delta\text{-Fe}$ polymorphic phase change, (ii) $\text{UFe}_2+\gamma\text{-Fe}\rightarrow\text{L}$ and $\text{U}_6\text{Fe}+\text{UFe}_2\rightarrow\text{L}$ transformations and (iii) melting has been made as a function of uranium concentration. The measured transformation temperatures are used to construct the binary Fe-U phase diagram, which showed general agreement with the latest assessment. The heat of transformation for various invariant reactions and solid state transformations has been obtained from DSC results as a function of U content. It must be added here that the novelty of this work is that these measured data will act as valuable source of information for rigorous phase equilibria assessment through CALPHAD method.

The experimental details related to alloy synthesis, annealing treatments and composition analysis (**table 2.2**) are already presented in **chapter 2**. In addition, the experimental procedure of DSC experiments, metallography and SEM are also presented in the **chapter 2**. Therefore the following account covers results and discussion part only.

6.2. Results

6.2.1. Transformation temperatures measured as function of U content in Fe-U alloys

In **figure 6.1**, the typical DSC thermo-gram for Fe-5 mass % U alloy recorded during heating/cooling cycle at 3 K min^{-1} is presented. This composition is taken as the

typical one for highlighting the sequence of phase changes that occur in Fe-U alloys. In deference to limited space, the individual DSC traces for other alloy compositions are not shown here, except for the fact that in **figure 6.2**, the DSC profile bears clear testimony to the presence of single phase Fe₂U. It may be noted that according to the currently

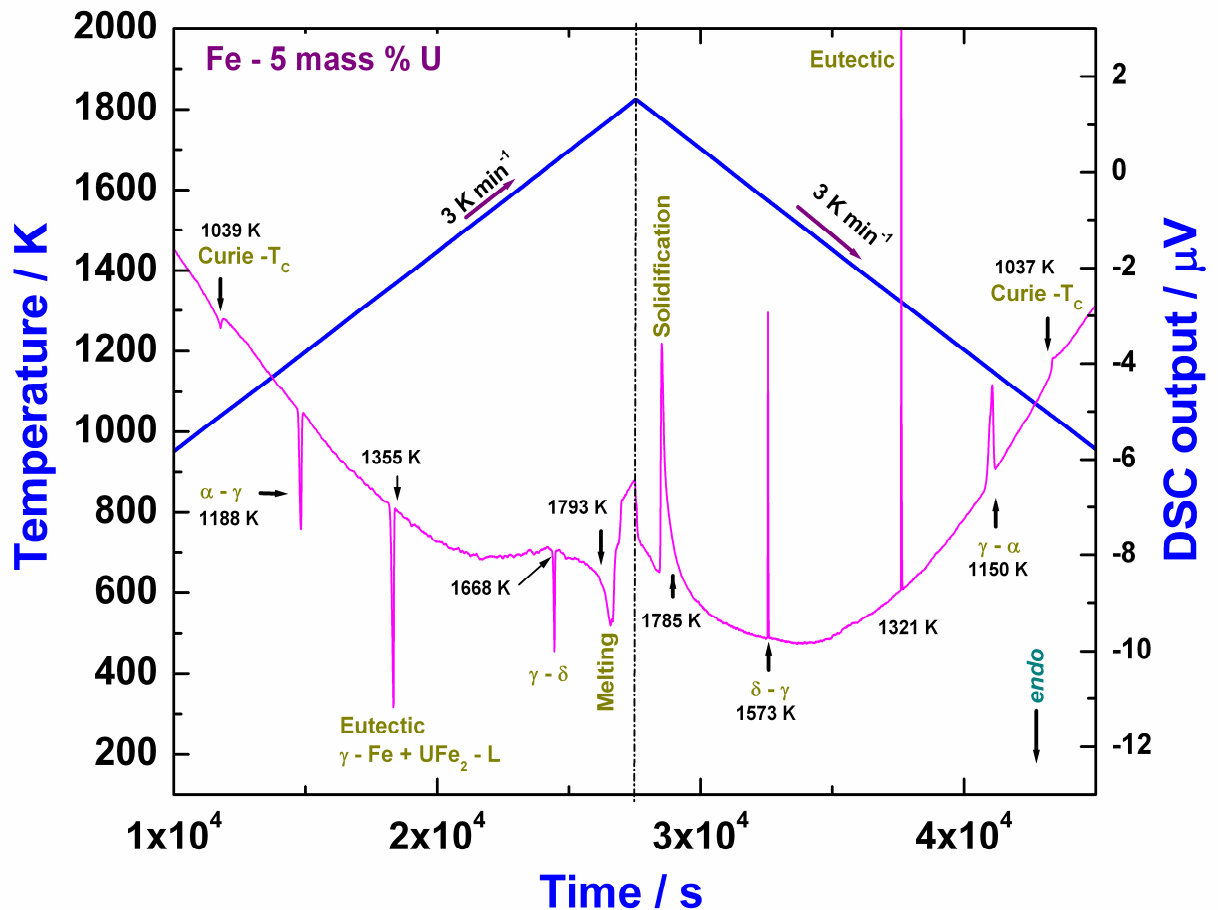


Fig. 6.1. The DSC thermo-gram obtained on Fe-5 mass% U alloy at scan rate of 3 K min⁻¹

accepted version of Fe-U equilibrium diagram [3, 6], the Fe-5 mass %U alloy exists as α-Fe+ Fe₂U two phase mixture at room temperature. Since there are three allotropic phase changes associated with iron, in addition to the magnetic phase change as a function of increasing temperature therefore a total of five endothermic thermal events must be observed upon slow heating. This is fully evident from **figure 6.1**. The first small endothermic peak observed at 1039 K corresponds to the magnetic transformation of α-

iron solid solution phase. The second peak located at 1188 K is due to $\alpha(\text{bcc}) \rightarrow \gamma(\text{fcc})$ allotropic phase change of Fe-rich solid solution. Upon further heating, a third transformation thermal arrest is seen to occur at 1355 K which marks the onset of $\gamma\text{-Fe} + \text{UFe}_2 \rightarrow \text{L}$ reaction. Subsequent to this transformation, the $\gamma\text{-Fe}(\text{fcc}) \rightarrow \delta\text{-Fe}(\text{bcc})$ phase change is observed at 1668 K. The on-heating transformation sequence is completed by

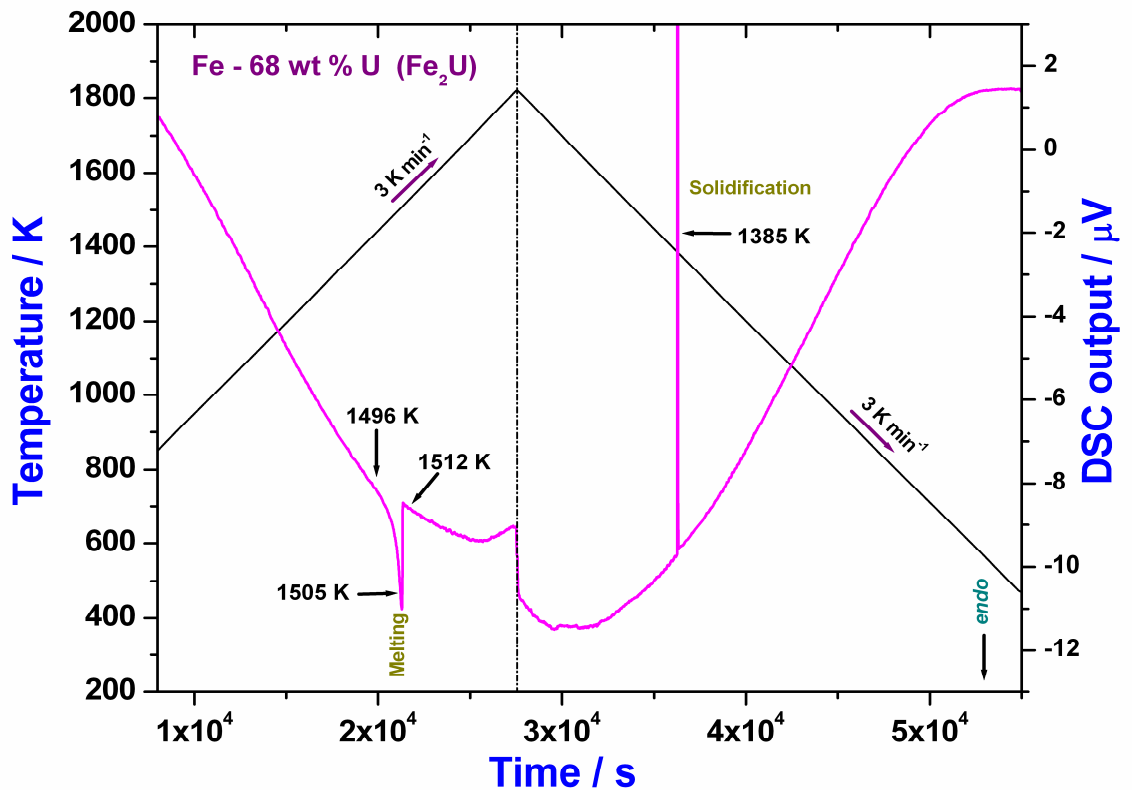


Fig. 6.2. DSC thermo-gram obtained for Fe_2U alloy at 3 K min^{-1}

the fifth dominant endothermic melting peak placed at 1793 K. This corresponds to $\delta\text{-Fe}(\text{bcc}) \rightarrow \text{L}$ transformation. All the phase changes observed during heating cycle are traced back during cooling as well, but with distinct under cooling effects. Similar experiments have been carried out for other Fe-U compositions, including Fe_2U intermetallic (figure 6.2) and one composition close to FeU_6 intermetallic compound. In table 6.1, the measured transformation temperatures for different alloy compositions are compiled.

Composition (mass % U)	Curie Temperature (K)	α-Fe$\rightarrow\gamma$-Fe (K)	Fe₂U+ γ-Fe \rightarrow L (K)	γ-Fe $\rightarrow\delta$-Fe (K)	Liquidus (K)
0	1043	1185		1663	1811
5	1039	1188	1355	1668	1793
8	1043	1184	1357	1666	1747
10	1043	1179	1353	1669	1735
15	1042	1189	1357	1663	1708
20	1041	1178	1352	1667	1687
25	1040	1185	1353	1662	1681
30	1041	1190	1354	--	1573
35	1041	1189	1349	--	1520
40	1039	1191	1354	--	1503
45	1042	1193	1346	--	1423
			Fe₂U+ γ-Fe \rightarrow L		
50	1043	1178	1357	--	1401
55	1045	1188	1354	--	1410
60	--	1195	1347	--	1463
65	--	1188	1351	--	1486
68.1 (Fe ₂ U)	--	--	--	--	1505
			Fe₂U + FeU₆\rightarrow +L		
70			994		1500
75			988		1473
80			995		1353
85			991		1268
			Fe₂U+FeU₆\rightarrowL		
90			992		1043
95			1001		1064
100	α-U$\rightarrow\beta$-U	β-U$\rightarrow\gamma$-U			
	940	1046			1405

6.2.2 $\gamma\text{Fe}+\text{Fe}_2\text{U} \rightarrow\text{L}$ and $\text{FeU}_6+\text{Fe}_2\text{U} \rightarrow\text{L}$ transformation characteristics

In **figure 6.3**, the measured variation of the eutectic temperatures with U-content is graphically portrayed. It can be seen that notwithstanding the compositional effects, which certainly influence the kinetics of phase change, the transformation temperatures measured in the current study, 1357 \pm 5 K for the of $\gamma\text{-Fe} + \text{Fe}_2\text{U} \rightarrow\text{Liquid}$ reaction and 1001 \pm 5 K for the $\text{FeU}_6+\text{Fe}_2\text{U} \rightarrow\text{L}$ reaction are fairly in agreement with the reported values in literature [3-8]. In addition, the measured variations in the enthalpy of three principal on-heating transformations namely, (i) melting, $\delta \rightarrow\text{L}$, (ii) $\gamma \rightarrow\delta$ and (iii) $\gamma\text{-Fe} +$

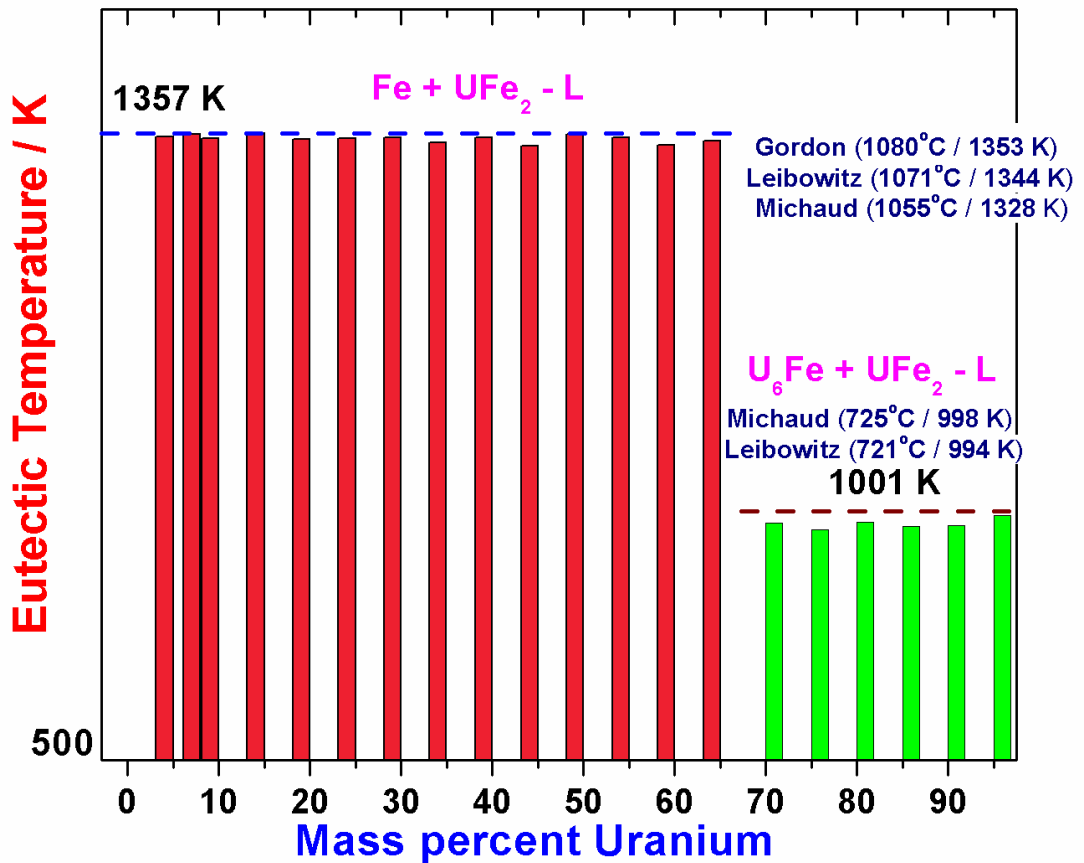


Fig. 6.3. The variation of $\text{UFe}_2+\gamma\text{-Fe} \rightarrow\text{L}$ and $\text{UFe}_2+\text{U}_6\text{Fe} \rightarrow\text{L}$ transformation temperatures with uranium content along with select literature data

$\text{Fe}_2\text{U} \rightarrow\text{L}$, are graphically depicted in **figure 6.4** for alloys of different U content. It can be seen that starting from pure Fe-side, the addition of U results in a progressive decrease

in the enthalpy of melting; this is however compensated by an increasing contribution from the enthalpy of eutectic transformation, which reaches the maximum at the exact eutectic composition. In the current study, the eutectic composition on Fe-rich side is identified to be close to 47 mass %U. The associated eutectic reaction enthalpy is estimated to be 19969 ± 1736 J mol of atoms⁻¹. To the best of author's knowledge, no previous experimental measurements of this quantity are reported in open literature. It

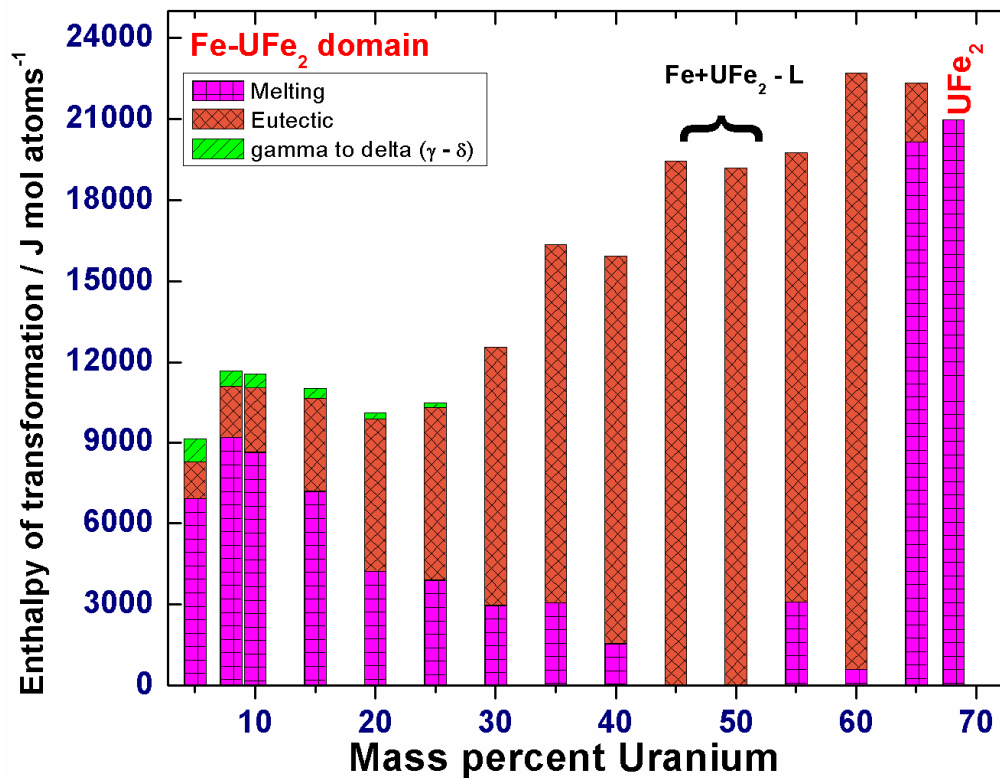


Fig. 6.4. The variation in enthalpies of (i) melting, (ii) $UFe_2 + \gamma\text{-Fe} \rightarrow L$ and (iii) $\gamma\text{-Fe} \rightarrow \delta\text{-Fe}$ transformations with uranium content.

also emerges from **figure 6.4**, that the share of melting enthalpy increases for alloys lying on the right side of eutectic composition, and it reaches the maximum value of 20983 ± 2098 J mol of atoms⁻¹, for Fe_2U . In the recent, Chatain *et al* [3] has estimated the melting enthalpy for UFe_2 to the order of 43715 J mol of atoms⁻¹, which apparently is based on the previous heat capacity measurements of Labroche *et al.*, [14].

Nevertheless, Chatain *et al.*, remark that there could possibly be a slight underestimation of the enthalpy of melting of UFe_2 compound [3]. In **figure 6.5**, the measured enthalpies of eutectic and melting reactions for alloys in the Fe_2U to FeU_6 intermediate composition regime are graphically plotted. In this region, the melting enthalpy decreases with increasing U-content and the maximum melting enthalpy of $36448 \pm 3608 \text{ J mol of atoms}^{-1}$ is measured for Fe-70 mass% U alloy. For the second eutectic, $\text{Fe}_2\text{U} + \text{FeU}_6 \rightarrow \text{L}$ (~ 89

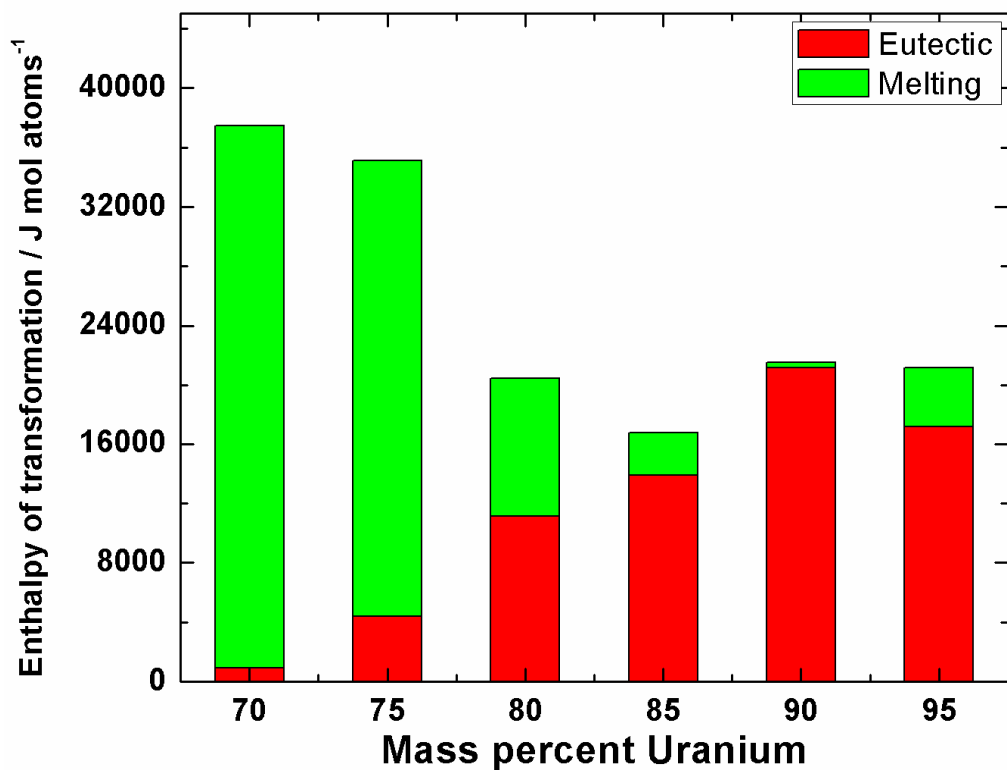


Fig. 6.5. The variation in enthalpies of (i) melting and (ii) $\text{U}_6\text{Fe} + \text{UFe}_2 \rightarrow \text{L}$ transformations with uranium content

mass.% U), the measured transformation enthalpy is $20250 \pm 2113 \text{ J mol of atoms}^{-1}$. Unfortunately, the present authors are not aware of any other independent experimental estimates of the enthalpy of this second eutectic transformation. In **table 6.2**, the measured transformation enthalpies are summarized for different alloys.

6.2.3. Construction of Fe-U phase diagram using current data and reported literature

The temperatures of phase changes as observed for different alloys during heating

cycle (**figure 6.1 & 6.2; table 6.1**) are used to construct the Fe-U phase diagram. This is shown in **figure 6.6**, which also contains important data drawn from select previous research as well. In order to enhance the appeal of **figure 6.6**, the temperature axis is presented in both K and °C units. For plotting the liquidus line, the measured peak temperatures of the melting thermal arrest have been used in place of the onset

Table 6.2				
Measured phase transformation enthalpies as a function of alloy composition are listed. The measured values are accurate to $\pm 10\%$.				
Alloy composition (mass % U)	$\gamma\text{-Fe} \rightarrow \delta\text{-Fe}$ (J mol of atoms ⁻¹)	$\gamma\text{-Fe} + \text{Fe}_2\text{U} \rightarrow \text{L}$ (J mol of atoms ⁻¹)	$\text{FeU}_6 + \text{Fe}_2\text{U} \rightarrow \text{L}$ (J mol of atoms ⁻¹)	Melting (J mol of atoms ⁻¹)
			-	
5	871	1335	-	6911
8	536	1903	-	9162
10	544	2358	-	8588
15	379	3407	-	7129
20	198	5605	-	4220
25	138	6353	-	3867
30		9569	-	2899
35		13197	-	3051
40		14327	-	1529
45		19423	-	10
50		19180	-	23
55		16589	-	3086
65		2112	-	20116
68 (Fe ₂ U)				20983
70			842	36451
75			4327	30679
80			11092	9219
85			13745	2877
90			21179	359
95			16986	3888

temperature. This is done in order to reduce the uncertainty in precisely fixing the onset temperature. Alternately, it is possible to adopt the onset temperature of solidification thermal arrest recorded during slow cooling scan as an equivalent measure of liquidus temperature. However, the differential degree of under cooling encountered in alloys of

different composition even at a constant slow cooling rate of 3 K min^{-1} has rendered this measure somewhat less rigorous. Despite this limitation, the peak temperatures of melting as observed in this study for slow heating scan are found to be in good agreement with the liquidus line projected in the currently assessed Fe-U phase diagram [3] and also with some of the previously reported experimental data [4-9]. It may be

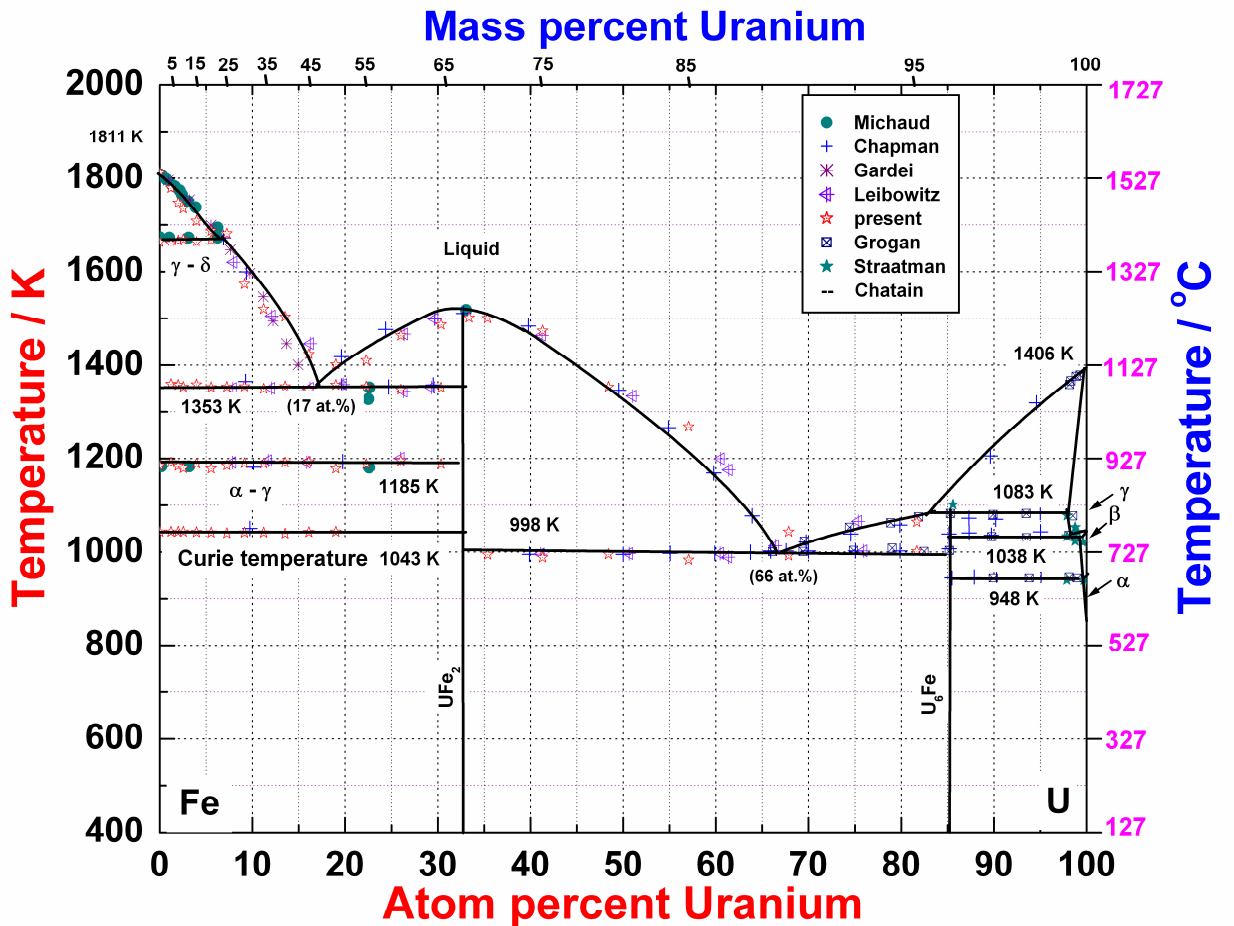


Fig 6.6. The Fe-U binary phase diagram constructed using present measurements along with other reported data are also included in the figure for comparative purpose

noted in general terms that an uncertainty of the order of $\pm 5 \%$ is generally attributed to thermal analysis determination of solid-liquid and solid-solid phase change temperatures [20-22]. Considering this point, our present estimates of eutectic transformation

temperatures and the liquidus line may be taken to be no more accurate than ± 5 and 12 K respectively. This is clearly brought out in **figure 6.6**, wherein the previous estimates of liquidus points that are co-plotted with the present data, exhibit a good agreement with present measurements. The on-heating melting temperatures (T_m/K) obtained in this study for different alloy compositions have been combined with the literature data to yield the following analytical representation with regard to the dependence on U-content X_U , given in atom percent.

$$T_m/K = 1813.2 - 27.08 X_U + 1.157 X_U^2; \quad \text{for } (0 \leq X_U \leq 7.5) \quad (6.1)$$

$$T_m/K = 1672.19 + 8.072 X_U - 1.793 X_U^2; \quad \text{for } (7.6 \leq X_U \leq 17) \quad (6.2)$$

$$T_m/K = 690.52 + 47.51 X_U - 0.685 X_U^2; \quad \text{for } (17 \leq X_U \leq 33) \quad (6.3)$$

$$T_m/K = 1505 + 8.349 X_U - 0.229 X_U^2; \quad \text{for } (35 \leq X_U \leq 66) \quad (6.3)$$

$$T_m/K = 778.87 + 2.913 X_U - 0.0075 X_U^2; \quad \text{for } (66 \leq X_U \leq 85) \quad (6.4)$$

$$T_m/K = -7351.67 + 166.064 X_U - 0.787 X_U^2; \quad \text{for } (85 \leq X_U \leq 98) \quad (6.5)$$

6.3 Solid state transformation kinetics

In **figure 6.7**, the DSC peak profiles obtained at 3 K min^{-1} for $\alpha\text{-Fe} \rightarrow \gamma\text{-Fe}$ transformation for three alloy compositions namely 5, 8 and 10 mass % U are shown. From the ratio of the partial area to the total peak area spanned in the transformation onset to offset temperatures, the fractional extent of transformation as a function of temperature is readily obtained. The calculation of fraction area is already discussed in more detail in **chapter 3**. The fraction curve is plotted in **figure 6.8**, wherein the sigmoidal character of the transformation is evident. Following the earlier work on the kinetic modeling of phase changes in uranium [21], the kinetics of diffusional $\alpha\text{-Fe} \rightarrow \gamma\text{-Fe}$ transformation is modelled after the site saturation approximation of Kolmogorov-Johnson-Mehl formalism [23]. Modeling of transformation kinetics is already discussed in detail in **chapter 3** and it is instructive to recall that according to Liu *et al.*, [24], the

fractional extent of transformation $f(T)$ under nonisothermal conditions may be represented as follows.

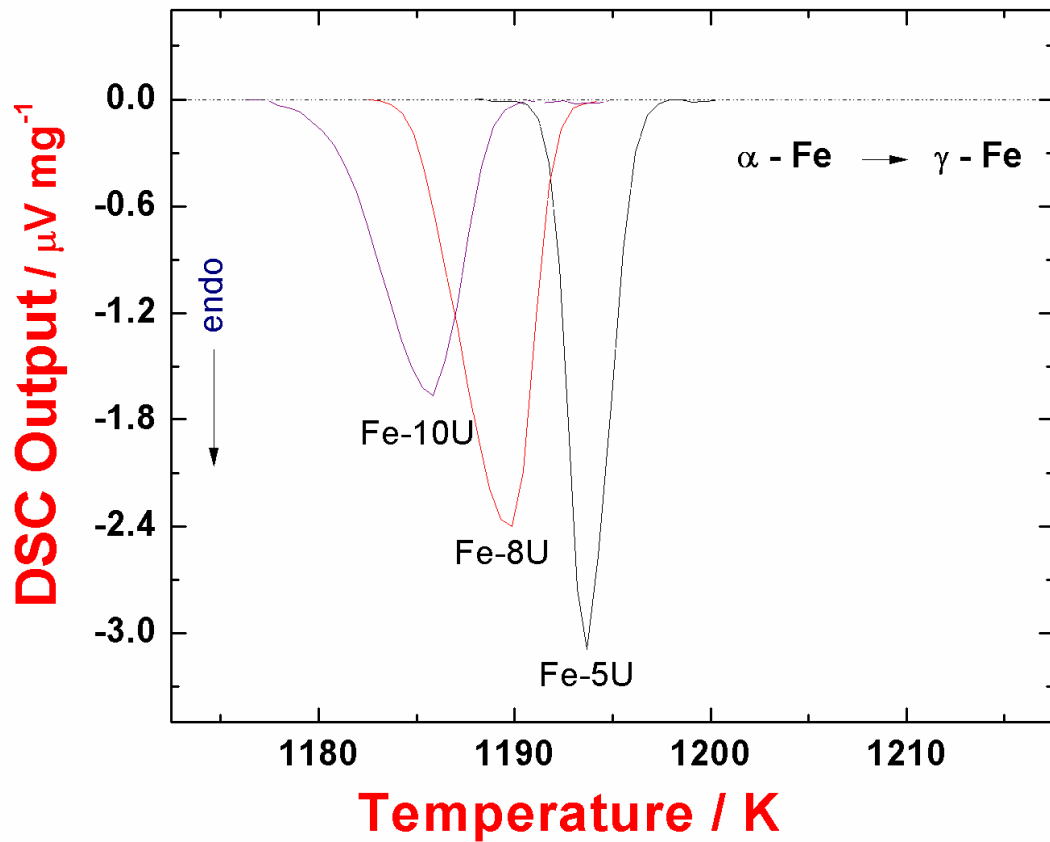


Fig. 6.7. DSC peak profiles for the α -Fe \rightarrow γ -Fe phase transformation in Fe-5U, Fe-8U and Fe-10U alloys are stacked together.

$$X(T) = 1 - \exp \left[-k^n \left\{ \frac{R(T - T_s)^2}{\beta Q_{eff}} \right\}^n \right]. \quad (6.6)$$

Where, k_0 is the kinetic prefactor, Q_{eff} is the apparent or effective activation energy for the overall transformation, n is the empirical transformation exponent, β is heating rate ($K s^{-1}$), T_s is transformation start temperature in Kelvin and R is the gas constant. The experimental data obtained in the present study namely $f(T)$ are fitted to Eq. (6.6) by the method of non linear least square regression. The values of the fit parameters are listed in

table 6.3. A value of 150 kJ mol^{-1} is obtained for Q_{eff} . It emerges from a comparison of the present estimate of Q_{eff} with the recent inter diffusion study on U-Fe binary system by Huang et al. [25], and also based on the earlier study of Pavlinov *et al* [26]., that Q_{eff} is in the expected range for the diffusional processes taking place in uranium-transition metal alloys.

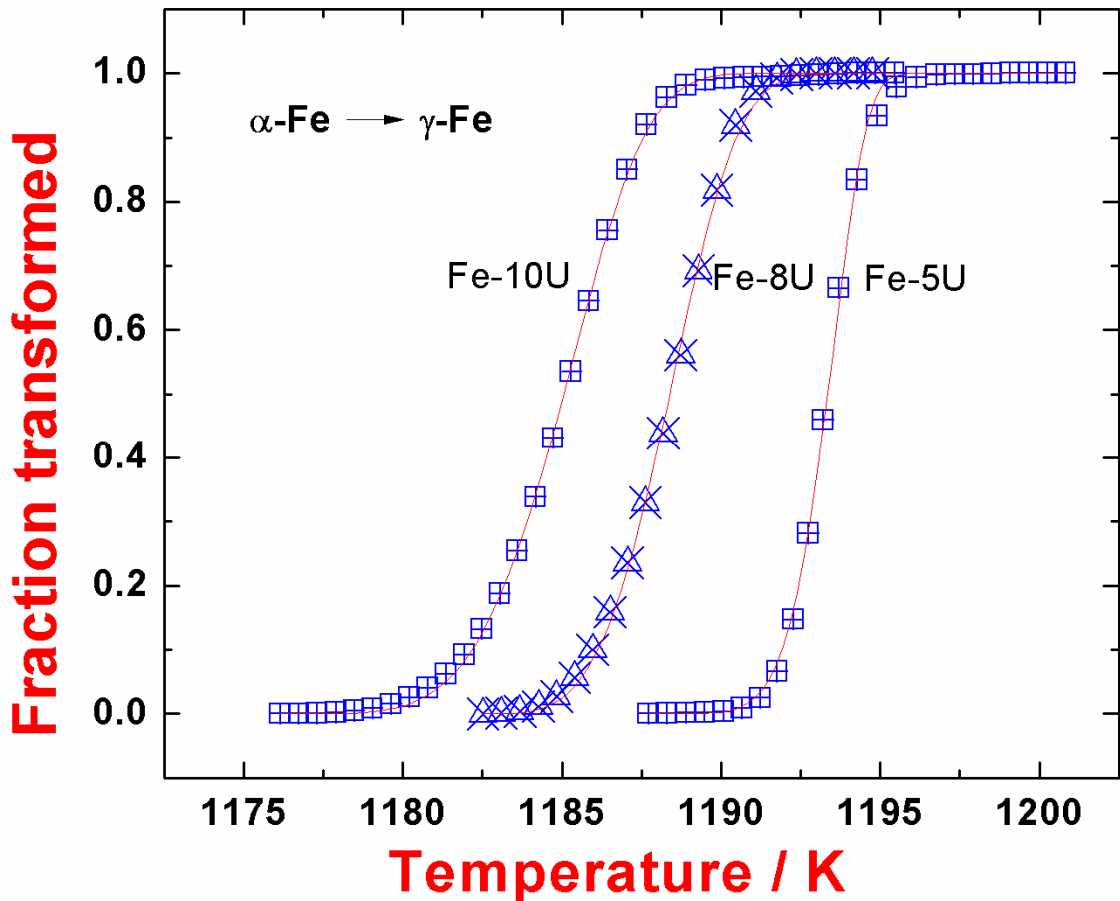


Fig. 6.8. The fractional extents of $\alpha\text{-Fe} \rightarrow \gamma\text{-Fe}$ phase transformation in Fe-5U, Fe-8U and Fe-10U alloys as a function of temperature are graphically illustrated

6.4. Characterization of solidification microstructure development

In **figure 6.9**, a collage of secondary electron micrographs of the solidification microstructure is presented for different alloy compositions spanning the range, 5-80 mass % U. It may be noted that all the alloys are subject to identical heating/cooling schedules in DSC. It is interesting to note the change in microstructural morphology as

the eutectic composition is gradually approached. It is generally known that eutectic microstructural morphology is decided by the interplay of several factors, such as, solidification (cooling) rate that determines the interfacial velocity through under cooling below the liquidus, nucleation difficulties associated with the complex intermetallic compound, presence of impurities, liquid-solid interface energy and its anisotropy *etc*

Table 6.3			
Kinetic parameters obtained by fitting the experimental α -Fe \rightarrow γ -Fe transformation data to KJMA model are tabulated.			
Alloy Composition (mass % U)	Apparent Activation Energy Q_{eff} (kJ mol ⁻¹)	Avrami exponent n	k_0 (s ⁻¹)
5	150 ± 1	3.2 ± 0.2	8.7 ± 0.9×10 ⁷
8	149 ± 2	1.8 ± 0.1	8.4 ± 2.1×10 ⁷
10	149 ± 1	2.2 ± 0.1	4.2 ± 0.3×10 ⁷
15	149 ± 2	2.3 ± 0.1	2.5 ± 0.4×10 ⁷
20	149 ± 1	1.8 ± 0.1	3.3 ± 0.3×10 ⁷
30	150 ± 2	1.8 ± 0.1	1.2 ± 0.1×10 ⁷
35	150 ± 1	2.6 ± 0.1	1.7 ± 0.1×10 ⁷

[27]. It is generally held that of the two phases involved in any eutectic reaction, if heterogeneous or sympathetic nucleation of one phase is induced over the other, then typical rod or lamellar morphology is expected with well-defined orientation relationships [27]. If on the other hand, the two phases nucleate independently for reasons of drastic difference in crystal structure and interfacial energy, then complex or anomalous eutectic morphology is witnessed [27]. Thermodynamically, such situations are governed by the magnitude of the entropy of melting ($\Delta^{\circ}S_m$), the degree of under

cooling below liquidus and in addition to the volume fraction of the phases involved [27].

In the case of $L \rightarrow \text{Fe}_2\text{U} + \gamma\text{-Fe}$ eutectic reaction, the nucleation of Fe_2U –Laves phase from liquid is somewhat difficult owing to its complex crystal structure and a wide difference in the composition of nuclei as compared to the matrix of $\gamma\text{-Fe}$ phase. It's entropy of melting is also fairly appreciable ($41.96 \text{ J mol}^{-1} \text{ K}^{-1}$). Therefore, for the $L \rightarrow \text{Fe}_2\text{U} + \text{Fe}$ eutectic, the Fe_2U phase is observed as the intercellular film. The matrix Fe -

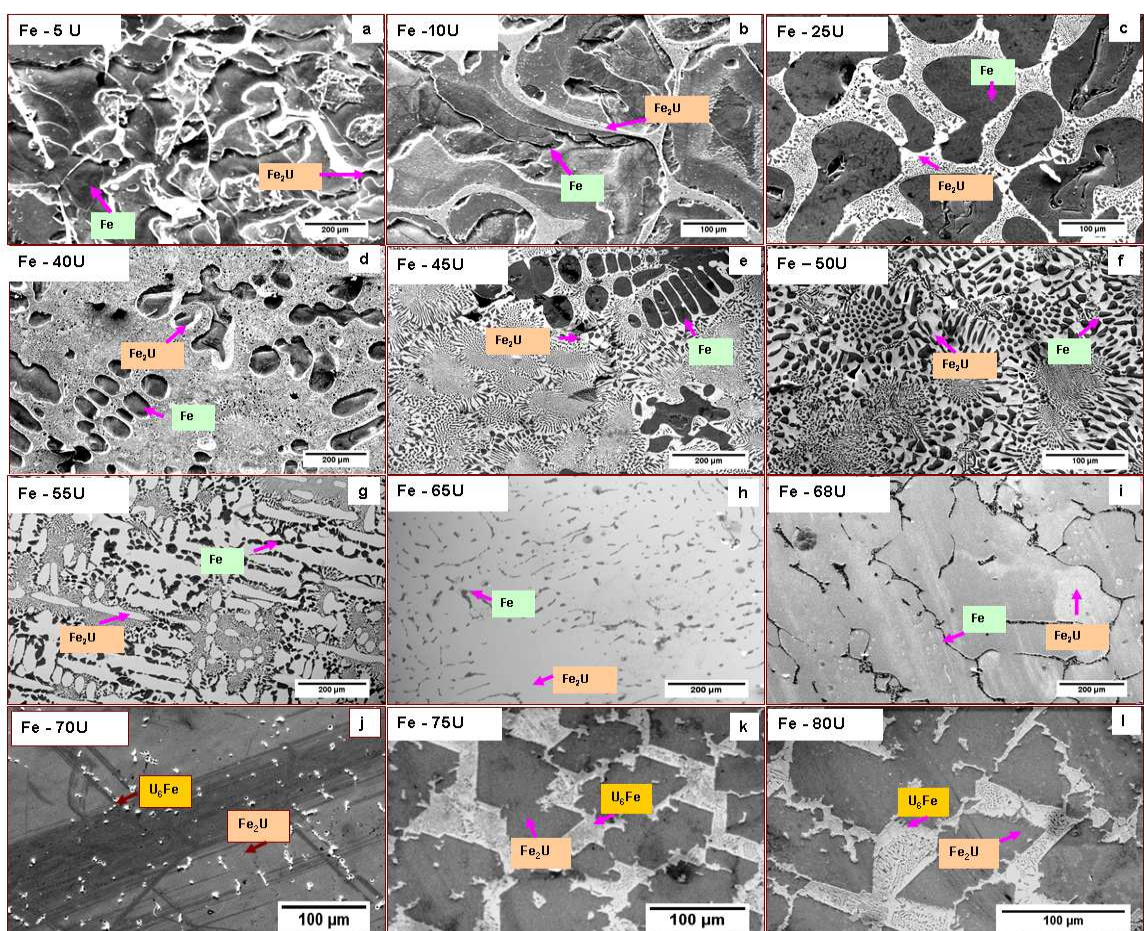


Fig. 6.9. A collage of SEM micrographs for different Fe-U alloy compositions is presented

rich phase appears as blocky white etching grains with rounded or non faceted shape (figure 6.9(a)–(c)). It can also be seen that as one moves close to the eutectic composition, the change in the nature of eutectic colony is more distinctly revealed. The

presence of so-called ‘halo’—or the white envelope of Fe_2U surrounding the primary $\alpha\text{-Fe}$ phase which appears as black embedded regions in **figure 6.9 (e)-(f)**, is indeed typical of many eutectics [27]. For compositions very close to the stoichiometric Fe_2U , large

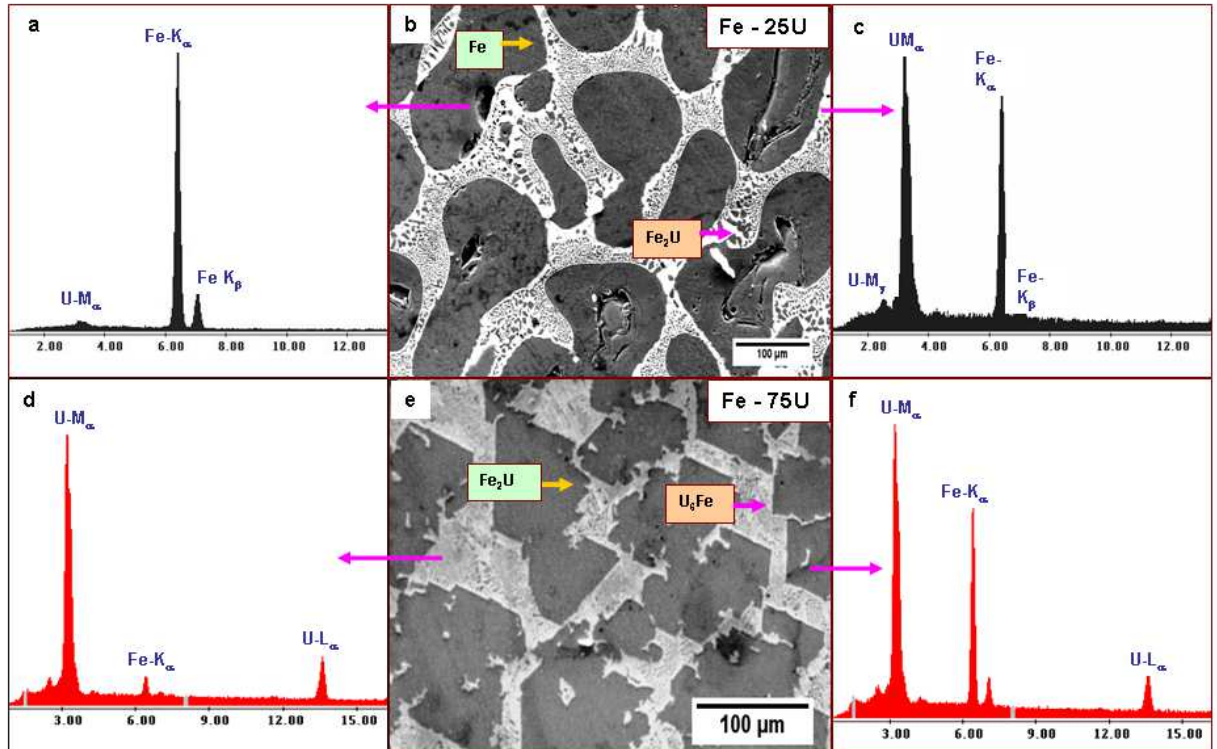


Fig. 6.10. The EDS spectra along with SEM microstructure taken for phase identification in Fe-25 mass % U and Fe-75mass % U alloys are presented. From the EDS spectra the presence of distinct phases, such as Fe, Fe_2U and U_6Fe can be clearly identified

primary grains of Fe_2U , surrounded by continuous intergranular network of eutectic mixture are noticed (**figure 6.9 (h)-(i)**). A similar, but more clearly revealing microstructural development has been witnessed in the case of the eutectic solidification of alloys with compositions, Fe-70, 75 & 80 mass % U. For 70 mass % U alloy which is rather close to Fe_2U intermetallic, the minority FeU_6 phase appears as small white inclusions embedded in the large grainy matrix of Fe_2U (**figure 6.9 (j)**). With further increase in the U-content of the alloy, the volume fraction of FeU_6 phase exhibits an increase, and this phase forms with a distinct morphology, as may be seen from **figure 6.9 (k)** and (i). In **figure 6.10 (a-f)**, the EDS spectra obtained from different phases that

constitute the solidification microstructures of select Fe-U alloys have been graphically portrayed.

6.5. Discussion

In the present study, an attempt has to trace the temperature and composition dependent phase evolution in Fe-U binary system using dynamic calorimetry technique. Although the literature on Fe-U system contains many thermal analysis studies [4-9], the present study has significantly augmented the existing knowledge base. In addition to establishing precisely the on-heating transformation temperatures, useful data with regard to transformation enthalpies have also been obtained. Taken together, the transformation enthalpy data generated for different alloys represent valuable additional inputs that facilitate greatly the optimization of Fe-U phase equilibria especially, when combined with accurate first principles calculations of phase stability at low temperatures.

A critical appraisal of transformation temperature data as shown in **table 6.1** reveals that for Fe-rich alloys, the measured transition temperatures for both $\alpha \rightarrow \gamma$ and $\gamma \rightarrow \delta$ phase changes of terminal solid solution phase did not show appreciable variation with U content. Obviously, this is due to the low solubility of uranium in iron even at high temperatures. As the alloy composition is extended from pure iron to Fe₂U side, it is observed that the Fe+Fe₂U \rightarrow L transformation temperature is found to vary only a little (1346-1357 K) for alloys of different U-content. This attests to the fact that present experiments are conducted at near equilibrium conditions. As stated before, the small variation found for the eutectic temperature measured for different alloys is well within the typical scatter band and uncertainty limit of thermal analysis investigations. Further, the average of Fe+Fe₂U \rightarrow L transition temperature measured in the present study is found to be close to the value of 1353 K reported by Gordon *et al.*, [5] and that of 1344 K assessed by Leibowitz *et.al.* [6]. However, the value 1328 K reported by Michaud [9] is

significantly lower than the present measurement. It may be mentioned that the recent assessment of Fe-U phase equilibria by Chatain *et al.*, also recommends 1353 K for the γ -Fe+Fe₂U→L transformation temperature [3].

As for the second eutectic reaction involving Fe₂U and FeU₆ is concerned, the present measurements indicate that for alloys of different U content, it is observed to be in the range of 988–1001 K, which is reasonably close to the values of 998 K, reported by Michaud [9] and 994 K reported by Leibowitz *et al.* [6]. In the recent assessment by Chatain *et al.*, the value of 998 K has been recommended for the Fe₂U + FeU₆→L reaction [3]. In literature, there are only few experimental values reported for enthalpies of different phase changes encountered in Fe-U system. This is probably because of the situation that the earlier phase diagram studies [4-7, 9] employed basic versions of thermal analysis as the major technique which do not readily yield for reliable calibration of enthalpy effects. In the present investigation however, it is possible to obtain fairly reliable and consistent estimates of enthalpy changes for all the investigated compositions. It is also possible to employ dynamic calorimetry technique for obtaining high temperature heat capacity values, which are valuable additional information for performing an integrated thermodynamic assessment of U-Fe system.

6.6. Conclusions

- (i) Comprehensive characterisation of high temperature phase equilibria in Fe-U binary has been performed using differential scanning calorimetry.
- (ii) The eutectic transformation involving Fe₂U and γ -Fe occurs at 1357±5 K, and at a composition of 47 mass % U. The transformation enthalpy is estimated to be 19969±1736 J mol of atoms⁻¹.
- (iii) The eutectic reaction involving Fe₂U and FeU₆ occurs at 1001±5 K, with an enthalpy of 20250±2113 J mol of atoms⁻¹.

- (iv) Liquidus temperatures have been measured for $\text{Fe}_{100-x}\text{U}_x$ binary alloys ($x= 0$ to 95 mass %). These are found to be in good overall agreement with the currently assessed Fe-U equilibrium diagram.
- (v) The melting enthalpy of Fe_2U intermetallic is found to be $(20983 \pm 2098 \text{ J mol of atoms}^{-1})$ with associated entropy of $41.96 \text{ J mol}^{-1} \text{ K}^{-1}$
- (vi) The Fe-U eutectic alloys solidified with a non-faceted colony microstructure.

6.7. References

1. K. Nakamura, T. Ogata, M. Kurata, T. Yokoo and M. A. Mignanelli, *J. Nucl. Mater.*, 304 (2002) 63.
2. M. Kurata, T. Ogata, K. Nakamura, and T. Ogawa, *J. Alloys Compd.*, 271-273 (1998) 636.
3. S. Chatain, C. Guéneau, D. Labroche, J. Rogez, and O. Dugne, *J. Phase Equilibria*, 24 (2003) 122.
4. P. Gordon and A.R. Kaufmann, *Trans. AIME*, 188 (1950) 182.
5. J. D. Grogan, *J. Inst. Met.*, 77 (1950) 571.
6. L. Leibowitz and R.A. Blomquist, *J. Nucl. Mater.*, 184 (1991) 47.
7. L. R. Chapman and C. E. Holcombe, Jr., *J. Nucl. Mater.*, 126 (1984) 323.
8. J.A. Straatmann and N.F. Neumann, *Mallinckrodt Chem. Reports*, MCW-1487, Weldon Spring, MO, (1964).
9. G. G. Michaud, *Can. Met. Quarterly*, 5 (1966) 355.
10. N. Swindells, *J. Nucl. Mater.*, 18 (1966) 261.
11. P. Gardie, G. Bordier, J. J. Poupeau and J. Le Ny, *J. Nucl. Mater.*, 189 (1992) 85.
12. P. Chiotti, V.V. Akhachinskij, I. Ansara and M.H. Rand, *The Chemical Thermodynamics of Actinide Elements and Compounds, Part 5, The Actinide Binary Alloys*, IAEA, Vienna, (1981), p. 114.
13. O. Kubaschewski, *Proceedings of the Symposium on Thermodynamics of Nuclear Materials*, IAEA, Vienna, (1962) p. 219.
14. D. Labroche, J. Rogez, S. Chatain, and O. Dugne: 10th IUPAC Conference on High Temperature Materials Chemistry, Jülich, Germany, (2000) p. 123.
15. M. P. Antony, R. Babu, C. K. Mathews and U. V. Varada Raju, *J. Nucl. Mater.*, 233 (1995) 213.

16. M. P. Antony, R. Babu, C. K. Mathews, and U. V. Varada Raju, *J. Nucl. Mater.*, 228 (1996) 154.
17. H. Okamoto, *Phase Diagrams of Binary Alloys*, (1993) 129.
18. T.B. Massalski, *Binary Alloy Phase Diagrams*, 2nd ed., ASM International, Materials Park, OH, (1990).
19. M. Kanno, *J. Nucl. Mater.*, 51 (1974) 24.
20. S. Raju, B. Jeyaganesh, A. Banerjee and E. Mohandas: *Mater. Sci. Engg. A*, 465 (2007) 29.
21. Arun Kumar Rai, S. Raju, B. Jeyaganesh, E. Mohandas, R. Sudha and V. Ganesan, *J. Nucl. Mater.*, 383 (2009) 215.
22. S. Raju, B. Jeya Ganesh, Arun Kumar Rai, R. Mythili, S. Saroja, E. Mohandas, M. Vijayalakshmi, K.B.S. Rao and Baldev Raj, *J. Nucl. Mater.*, 389 (2009) 385.
23. E. J. Mittemeijer and F. Sommer, *Int. J. Mater. Res.*, 102 (2011) 784.
24. F. Liu, F. Sommer and E. J. Mittemeijer, *Int. Mater. Rev.*, **52** (2007) 193.
25. K. Huang, Y. Park, E. Ewh, B. H. Sencer, J. R. Kennedy, K. R. Coffey and Y. H. Sohn, *J. Nucl. Mater.*, 424 (2012) 82.
26. L. V. Pavlinov, A. I. Nakonechnikov and V. N. Bykov, *J. Nucl. Energy*, 20 (1966) 1027.
27. G. A. Chadwick, *Metallography of Phase Transformations*, Butterworth, London, (1972), pp 1-294.

Chapter 7

Measurement & Modelling of Thermophysical Properties of UFe_2 and URh_3 Intermetallics

7.1. Introduction

In the present chapter, the results of measurement and modelling of thermophysical properties of two important uranium-transition metal based intermetallic compounds UFe_2 & URh_3 are presented and discussed.

A study on high temperature thermal properties of UFe_2 is relevant in both basic and applied contexts. From the point of view of understanding the physics of magnetism in alloys of actinide and d-band elements, UFe_2 has been attracting enormous attention from physics quarters, especially in terms of precise characterisation of its low temperature structural, electrical, and magnetic properties, using a variety of experimental techniques [5-10]. In addition, extensive theoretical studies of the ground state electronic structure and high pressure equation of state (EoS) using a variety of *ab-initio* or density functional methods have also been carried out on UFe_2 [11-16]. However, to the best of our knowledge, there are only few experimental studies devoted to the elucidation of high temperature phase stability of UFe_2 , especially using calorimetry [17-23]. On the applied front, the comprehensive knowledge of the thermal properties of UFe_2 , the most stable intermetallic in U-Fe binary system is a vital prerequisite in understanding the effects of high temperature interaction between stainless steel clad and U-Pu-Zr metallic fast reactor fuel [24]. The high temperature metallurgical compatibility between fuel and clad is crucially dependent on the thermodynamic and kinetic aspects of UFe_2 formation at the clad-fuel interface [24].

The thermodynamic characterization of intermetallics of uranium metal with d-block transition elements, especially Pt, Rh, Ru, Pd, Ir etc., are of interest from the point of view of understanding and modelling the fuel-fission product behavior at high temperatures [1-4, 25-30]. In view of the restricted solubility of Pt-group elements in uranium, these compounds are often present as insoluble residues in dissolved spent fuel [2]. There have been extensive studies in the past on thermodynamic and physical

metallurgy characterization of various U-X (X = Transition metal) alloys [1-4, 25-30]. Among all, URh₃ is one of the most important intermetallics which have been extensively characterized in recent times. However, the available data on phase diagram, crystal chemistry and high temperature thermodynamics are somewhat incomplete and in some cases even uncertain [1-4, 25-30].

Therefore in the present study, evaluation of thermo physical properties of UFe₂ and URh₃ intermetallics have been undertaken based on experiment and modeling. Before proceeding further, in the next section a brief description of available information related to thermal properties of both compounds are presented.

7.2. Thermal stability and thermophysical property of UFe₂ and URh₃ compounds: a brief summary

The intermetallic UFe₂ crystallizes in cubic MgCu₂ type Laves phase structure (Fd3m) with a lattice parameter value in the range of 0.7058 to 0.7061 nm [5, 6, 20]. This phase is almost stoichiometric and is stable right up its melting point 1505±5 K [22]. There have been many investigations on the magnetic behavior of this compound and it has been established that UFe₂ exhibits itinerant type of ferromagnetism below 165 K [6-8, 10, 14-16]. The formation enthalpy of UFe₂ has been determined to a fair degree of consistency by different groups, and found to be in the range of 32.6 to-63 kJ mol⁻¹ [24, 31]. Campbell has estimated the thermal functions of UFe₂ over the temperature range of 300-1000 K, by invoking Neumann-Kopp's law of additivity of heat capacity, and resorting to the estimation of $\Delta^{\circ}H_f$ the standard formation enthalpy through an empirical correlation between and the radius ratio, R_A/R_B of AB₂ compounds [18]. In addition, Labroche *et al.*, have measured using adiabatic calorimetry the heat capacity up to near melting temperature [21]. The data from this direct heat capacity measurement have been used by Chatain *et al.*, in their recent phase equilibria assessment of binary Fe-U system [22]. To the best of the authors' knowledge, no other experimental data exist

for temperature dependent enthalpy or heat capacity values for temperatures higher than 1000 K. As for the cohesive and equation of state (EoS) properties of UFe_2 are concerned, Itie *et al.*, have reported isothermal hydrostatic pressure (P)-volume (V) data using diamond anvil high pressure set-up [5], from which isothermal bulk modulus B_0 and its derivative B_0' have been extracted using Murnaghan equation of state [32, 33]. However, it may be added that the number of actual (P - V) data points cited in their investigation is rather small to permit a rigorous and unambiguous estimation of the basic EoS (equation of state) parameters, namely, bulk modulus B_0 , its isothermal pressure derivative B_0' , and equilibrium volume at zero pressure condition V_0 . A few first principle calculations of ground state electronic structure and zero Kelvin equation of EoS quantities have also been reported for UFe_2 [13-16]. However, it is observed that the agreement between these diverse theoretical estimates *vis a vis* the experimental values is not really satisfactory. The elastic properties of UFe_2 have been estimated based on ultrasonic wave velocity measurements by Sorokina *et al.* [19]. In addition, Yamanaka *et al.*, has recently attempted a robust estimation of adiabatic bulk modulus, Debye temperature (θ_D) and room temperature thermal expansion *etc.* for UFe_2 , [20]. There is certain degree of mismatch between these ultrasonic estimates of bulk modulus, Grüneisen parameter (γ_G) and those estimated from isothermal P - V data after standard de-convolution procedures [5, 15, 19]. In deference to limited space, a detailed account of these issues is not presented here.

URh_3 has face centered cubic crystal structure (cF4; $\text{Pm}\bar{3}\text{m}$) and have highest melting temperature of about 1973 K among all the four stoichiometric intermetallic compounds namely URh_3 , U_3Rh_5 , U_3Rh_4 that exist in U-Rh system. In literature very little thermodynamic information exists for this compound. In fact, the available thermodynamic data for URh_3 covers only a limited temperature range, although its melting temperature is fairly high, about 1973 K [1-4, 25, 2]. Cordfunke *et al.* have

measured the enthalpy increment ($H_T - H_{298.15}$) up to 840 K [25]. On the theoretical front, there exist a few zero Kelvin calculations of electronic band structure and total energy as a function of volume for URh₃ intermetallic [34-37]. Recently, the elastic properties of URh₃ have been estimated from ultrasonic wave velocity measurements [20]. Besides these, it appears that there are no experimental data on most of the fundamental physical properties such as thermal expansivity, thermal conductivity and bulk modulus as a function of temperature.

Nevertheless, it may be summarized, that there is a critical need for assessment of thermophysical and thermodynamic data for UFe₂ and URh₃ compounds. In view of this situation, we have undertaken a fresh investigation of high temperature thermal properties of UFe₂ and URh₃ in this study. In particular, the enthalpy increment ($H_T - H_{298.15}$) is measured for both UFe₂ and URh₃ as a function of temperature, up to 1473 K, using inverse drop calorimetry. Experimental results obtained in this study have been jointly analysed with the estimated and measured intermediate temperature data of Campbell [18] and Cordfunke *et al.* [25] for both compounds respectively, so as to arrive at a more comprehensive experimental dataset over an extended range of temperature. Further, the experimental heat capacity data obtained in this study have been critically analysed for its internal thermodynamic consistency in terms of an integrated modelling approach which involves the use of quasi-harmonic Debye-Grüneisen formalism for calculating and predicting the thermal properties [32, 33, 38-40]. As an off-shoot of this analysis, consistent theoretical estimates of thermal expansivity have also been obtained for both UFe₂ and URh₃. It may be appropriate to mention here that such an integrated approach involving a judicious combination of experiment and modelling protocols has been gaining currently in the recent thermophysical or calorimetry studies of diverse materials [41-43]. In the following sections the results of the current study are presented.

7.3 Structure and microstructural characterization of UFe₂ and URh₃

The details about alloy synthesis and annealing treatment for UFe₂ and URh₃ compounds are already presented in **chapter 2**. In order to confirm the homogeneity of the both compounds, different characterization techniques which include XRD, metallography, SEM and DSC have been employed and the corresponding results are presented below.

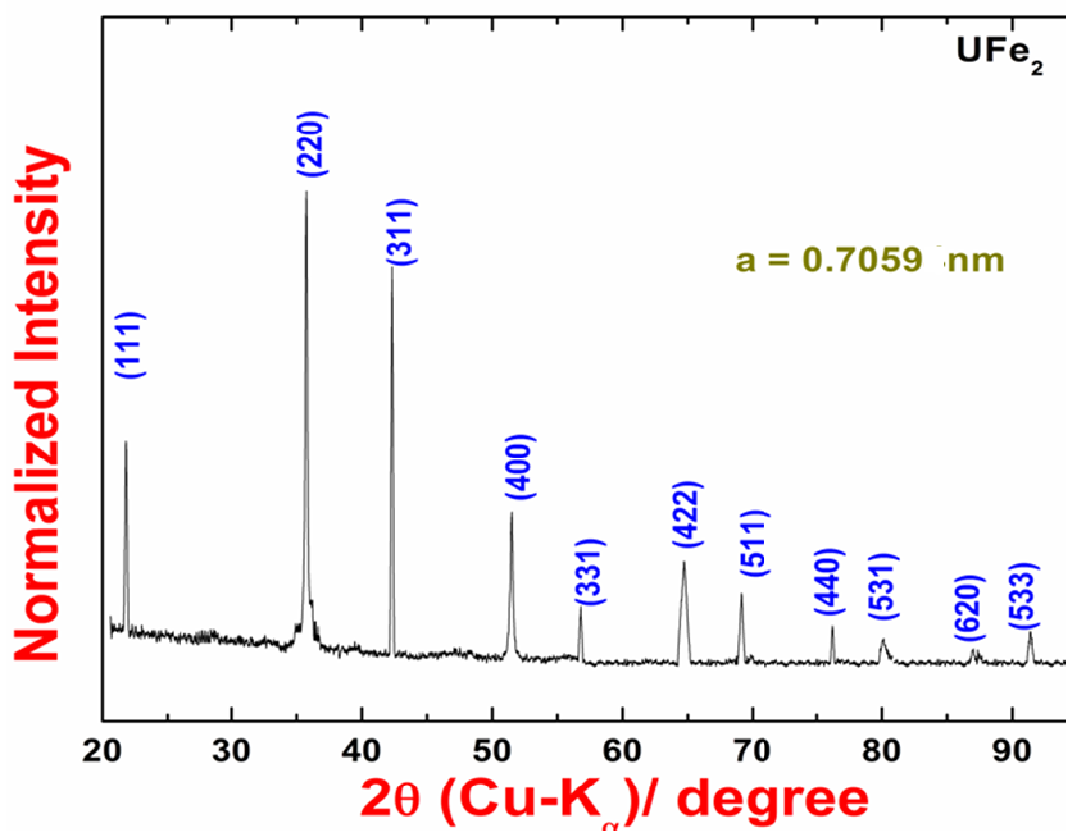


Fig. 7.1: XRD profile of UFe₂ showing presence of cubic-MgCu₂ type crystal structure

The XRD profile of homogenized UFe₂ alloy is presented in **figure 7.1**, which bears evidence to the presence of cubic-MgCu₂ type crystal structure. The lattice parameter after standard data analysis is estimated to be 0.7059 ± 0.0005 nm, which is in good agreement with the reported values, which range between 0.7058 to 0.7061 nm [5, 6, 20]. The XRD profile did not reveal the presence of any second phase. In order to

confirm the phase purity of the sample, a small piece of alloy weighing about 100 mg has been slowly heated at the rate of 3 K min⁻¹ up to 1547°C (1820 K) in a heat flux

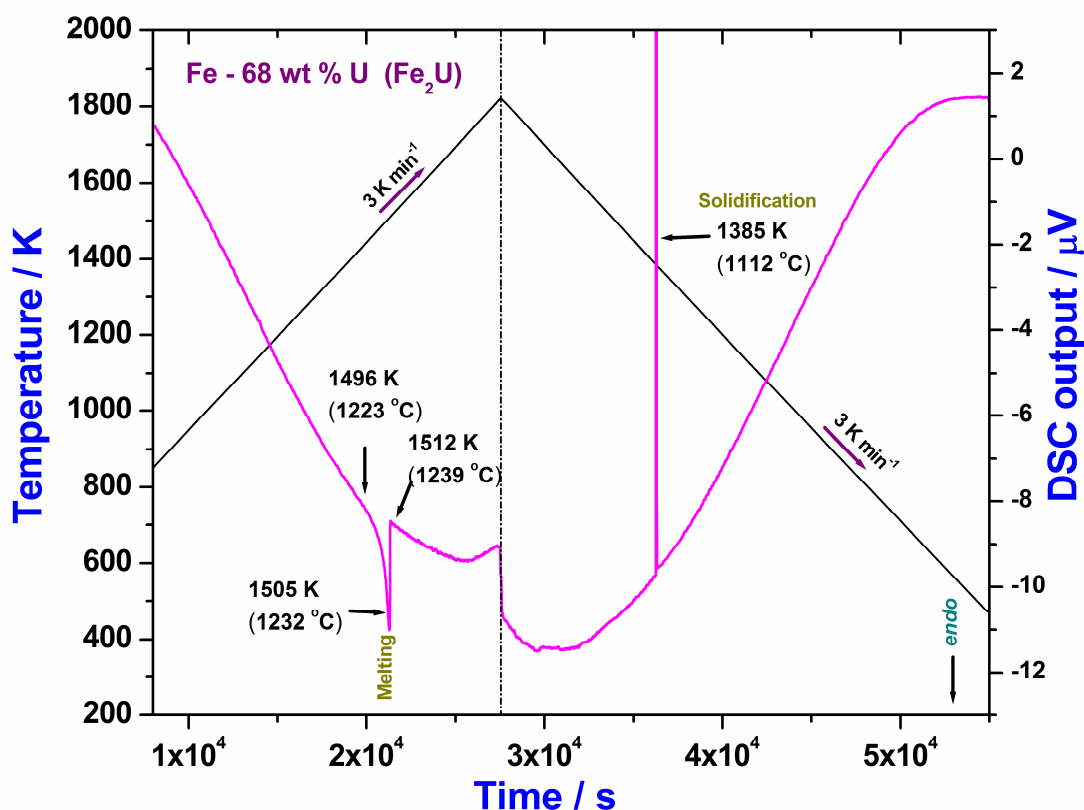


Fig. 7.2. The on-heating and cooling DSC profile for UFe₂ taken at 3 K min⁻¹ scan rate

DSC instrument (*Setaram setsys1600*) and the corresponding thermo-gram is shown in **figure 7.2**. The DSC profile is indicative of the presence of only the melting and solidification transitions of UFe₂ upon heating and cooling cycles respectively. The measured melting temperature is found to be around 1232 ± 2°C (1505 ± 2 K) which is in good agreement with the reported value of 1505±5 K [22]. However during the cooling cycle, there is an under cooling to the tune of 100 K is found, which arises from the difficulties associated with the nucleation of UFe₂ possessing complex crystal structure. In **figure 7.3**, the back scattered SEM image (**figure 7.3a**) along with the U and Fe elemental X-ray maps (**figure 7.3b & c**) of the annealed sample are shown. It appears from the SEM micrograph that a very small amount of the terminal iron solid solution

phase is present along the grain boundaries of UFe_2 . It may be added at this juncture that the solubility of U in Fe is almost negligible [22]. The grain boundary film like presence of the iron rich phase is due to the eutectic reaction, $L \rightarrow \gamma\text{-Fe} + \text{UFe}_2$ [22]. Nevertheless,

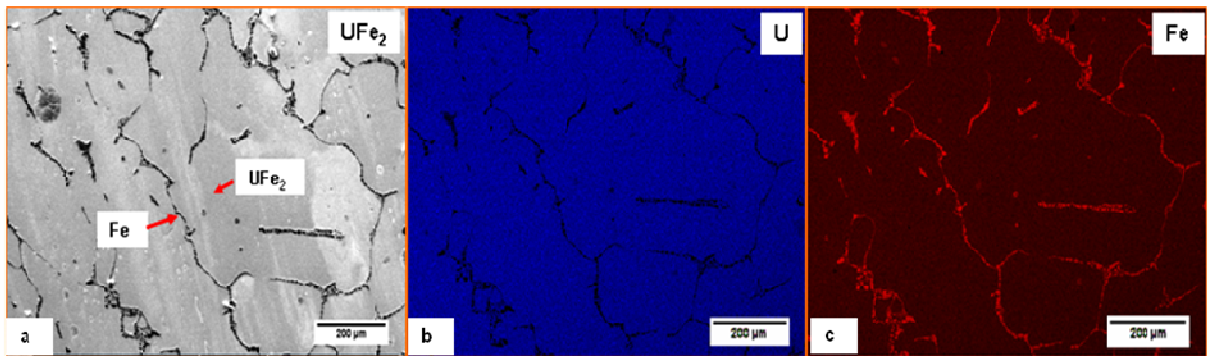


Fig.7.3. (a). SEM micrograph of the annealed UFe_2 alloy, (b). Elemental X-ray map of U, (c). Elemental X-ray map of Fe

the fraction of the iron phase present is very small and as a result, it had escaped detection in both DSC and XRD. Since UFe_2 is a line compound with very little homogeneity range [22], it is indeed difficult to prepare the ideal single phase UFe_2 ; the invariable presence of the pro-eutectic solid solution phase, namely pure iron in the present case is unavoidable. Notwithstanding this, the alloy used in this study revealed a fair degree of compositional homogeneity, which is evident from the x-ray map (**figure 7.3b &c**).

The XRD profile as shown in **figure 7.4** clearly reveals the presence of cubic (Cu_3Au type) URh_3 phase. The lattice parameter estimated after standard data analysis is found to be 0.3988 ± 0.0007 nm, which is in good agreement with the reported value of 0.399 nm in literature [20]. In **figure 7.5**, the back scattered SEM image along with the elemental X-ray mapping of 1273 K/5h annealed sample is shown. This structure seen is typical of the as-cast uranium alloys which solidify through a eutectic reaction with coarse primary dendrites. The SEM-EDX analysis performed over many grains chosen at random showed that there is no appreciable change in the characteristic x-ray

line intensities of U-L α and Rh- L α lines throughout the sample. This suggested a fair degree of alloy homogeneity. The elemental X-ray mapping showed only mild

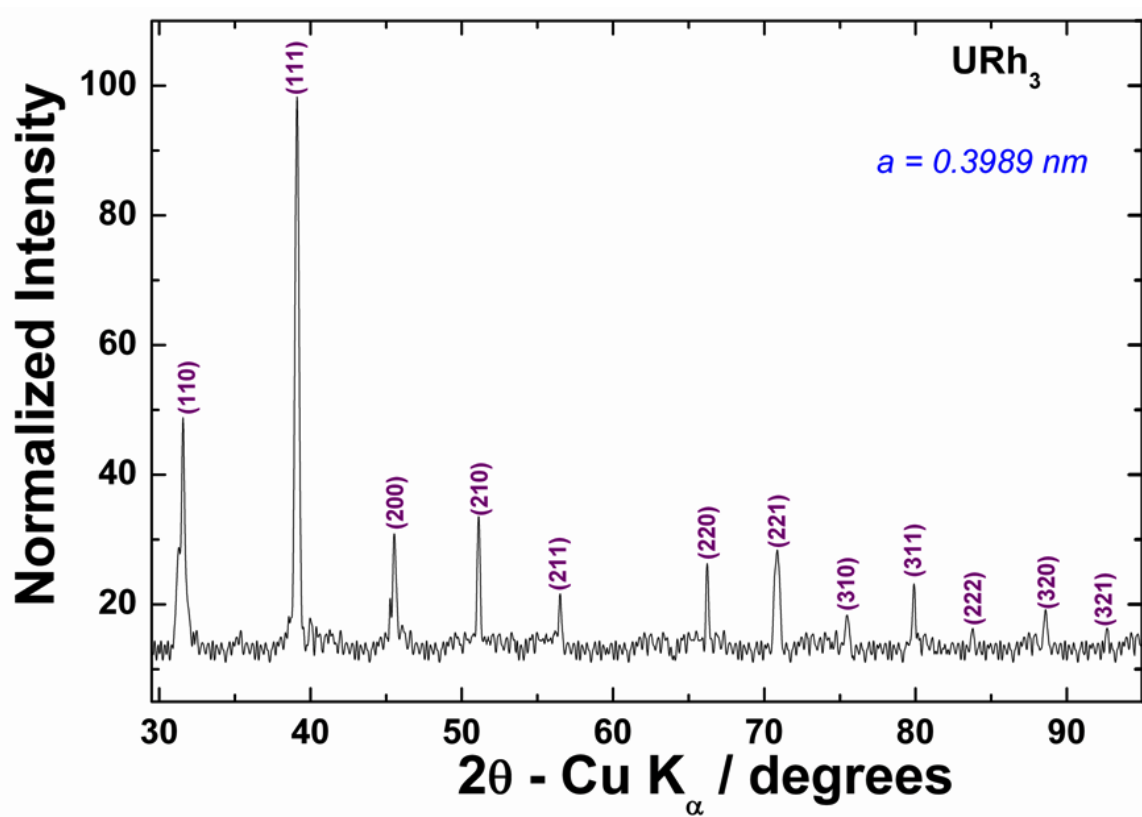


Fig. 7.4. XRD profile of URh₃ conforming to face centered cubic structure

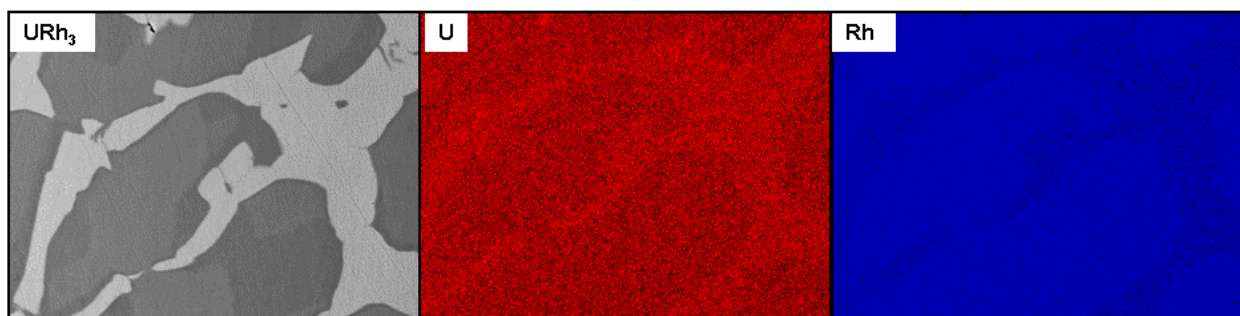


Fig. 7.5. SEM BSE image along with by elemental X- ray mapping of U & Rh atoms

differences of U and Rh atom density distribution throughout the sample. In view of this, it is concluded that the possible presence of a second phase other than URh₃ phase is almost absent. The average micro-hardness of this alloy measured using Leitz micro-hardness tester with 100 g load is found to be 653 VHN.

7.4. Enthalpy increment measurements

The enthalpy increment data as a function of temperature for both homogenized UFe_2 and URh_3 compounds has been measured using inverse drop calorimetry. The experimental procedure is already discussed in **chapter 2**, therefore here only result part will be discussed for both the compound in the next sections

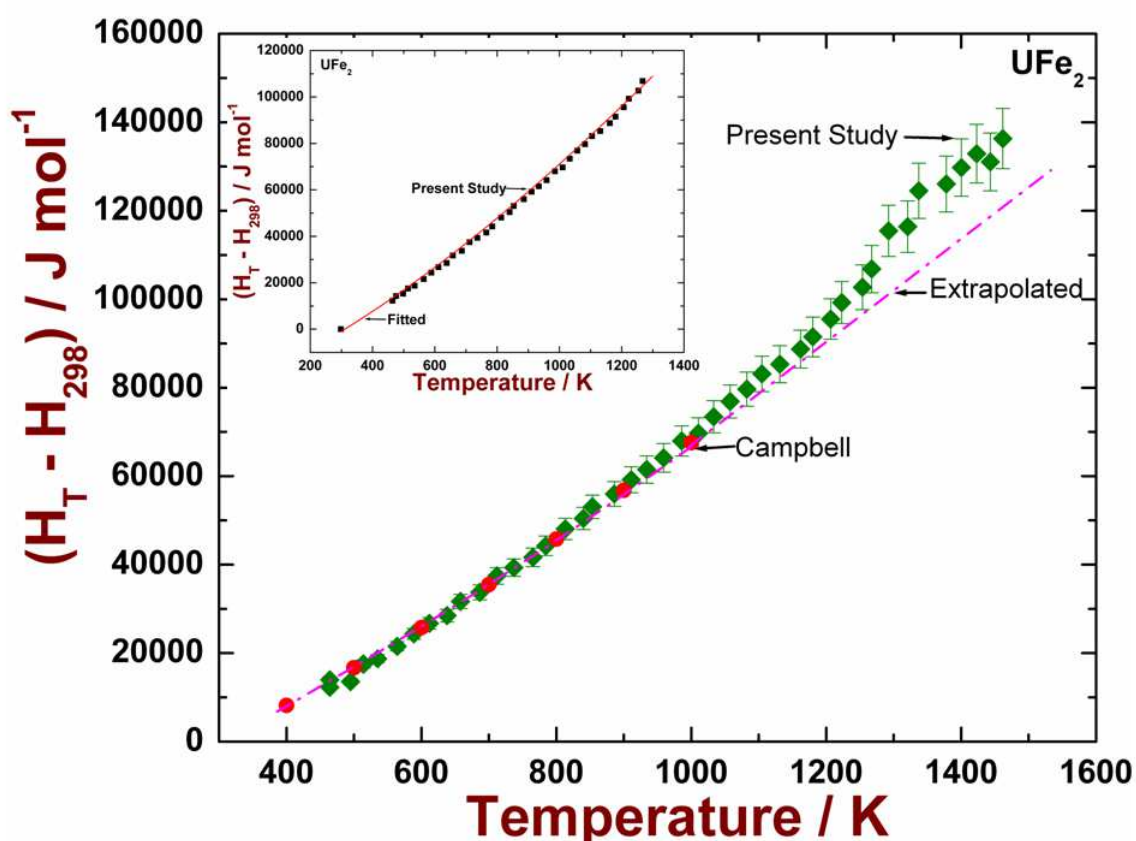


Fig. 7.6: Temperature variation of enthalpy increment data obtained in this study along with reported data of Campbell. The inset shows the fit to the present experimental data

7.4.1. Enthalpy increment data ($H_T - H_{298.15}$) for UFe_2

In **figure 7.6**, the enthalpy increment data ($H_T - H_{298.15}$) measured as a function of temperature up to 1473 K along with previous experimental data of Campbell is presented [18]. It is clearly observed that the present measurements evince an excellent degree of agreement with the estimated data of Campbell up to 1000 K, which is the maximum temperature of study by Campbell [18]. However, for temperatures exceeding 1000 K, the current experimental data deviates clearly from the extrapolated behavior of

Campbell. This suggests that at high temperatures, the possible role of lattice anharmonicity, in addition to the linear electronic contribution ($\sim T$) may assume considerable importance in deciding the actual course of the temperature dependence of thermal quantities. The present measurements do not cover up to the melting transition of UFe_2 . However, going by the steeply rising trend of enthalpy and therefore the heat capacity with temperature, it is likely that melting of UFe_2 will be associated with a λ -type sharp discontinuity in the heat capacity at T_m .

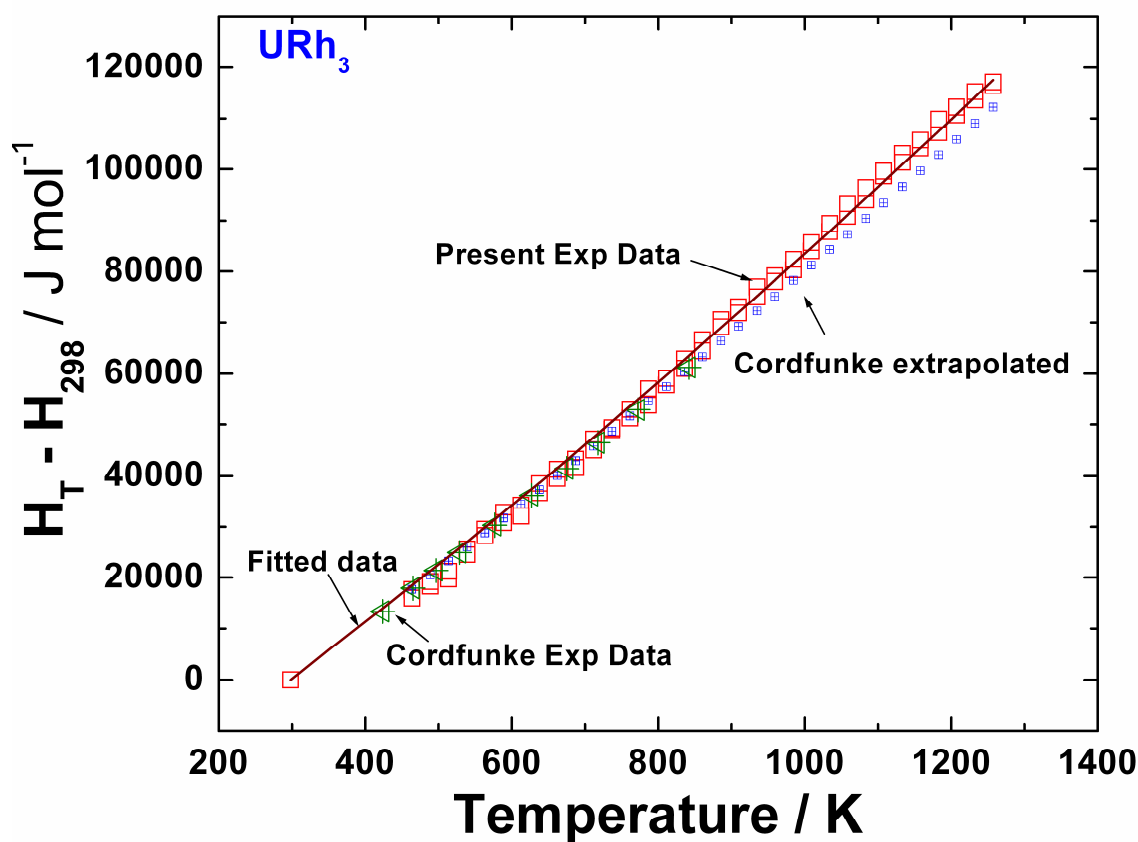


Fig. 7.7. Enthalpy increment data for URh_3 obtained in present study is compared with the data of Cordfunke's experimental and extrapolated data

7.4.2. Enthalpy increment data ($H_T - H_{298.15}$) for URh_3

In **figure 7.7** the temperature variation of measured enthalpy increment ($H_T - H_{298.15}$) is graphically portrayed. Since URh_3 is a line compound which is stable up to 1973 K [29], the enthalpy increment data measured up to 1273 K in present study do not show any

abrupt inflection which mark the incidence of any phase change. **Figure 7.7** also contains the earlier experimental as well the extrapolated data of Cordfunke *et al* [25]. It is observed that the present measurements evince an excellent degree of agreement with the previous data due to Cordfunke *et al*, up to 840 K, the maximum temperature of measurement in the previous study [25]. But the extrapolated data at high temperature do not match with the present experimental data and it could be attributed due to the anaharmonicity. In order to obtain the heat capacity the present data has been analyzed using nonlinear regression analysis and it is given in the next section.

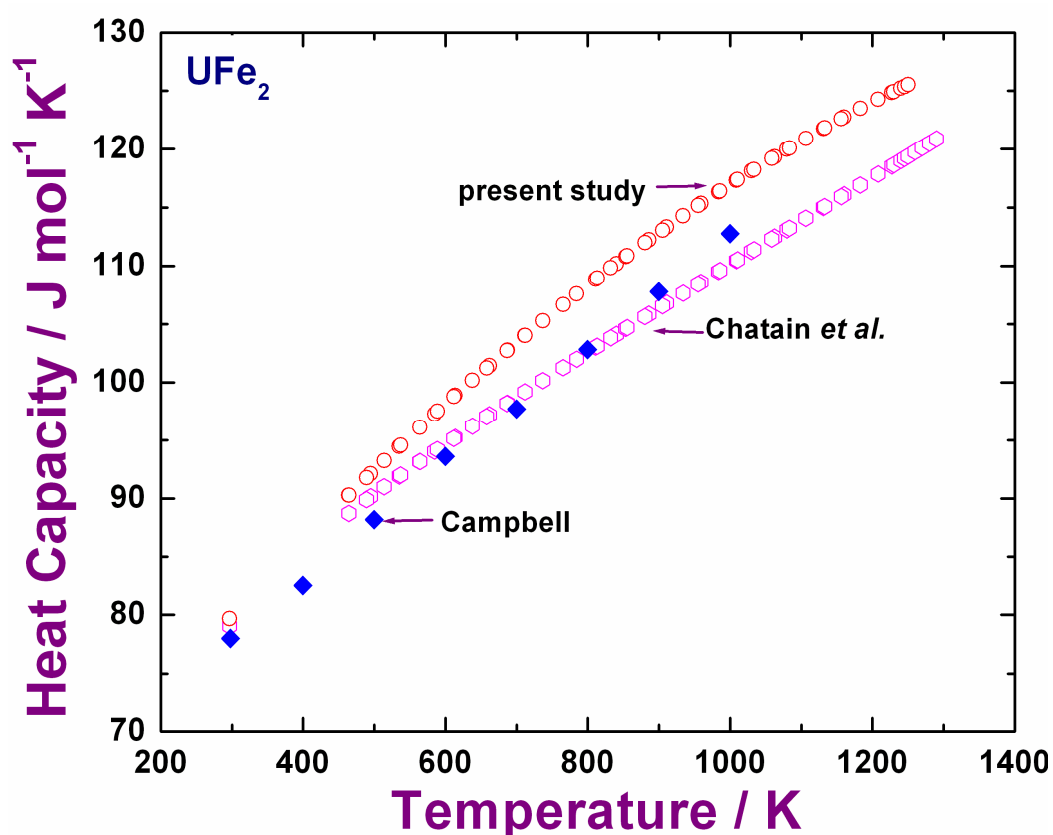


Fig. 7.8. Temperature variation of heat capacity for UFe_2 compound

7.4.3. Analytical analysis of enthalpy increment data of UFe_2 & URh_3

The enthalpy increment data measured for both compounds in the present study have been fitted to the following standard Mayer-Kelly like expressions using the method of non-linear least square regression [44].

$$(H_T - H_{298.15} / J. mol^{-1})_{UFe_2} = AT + BT^2 + C/T + D. \quad (7.1)$$

$$(H_T - H_{298.15} / J. mol^{-1})_{URh_3} = A'T + B'T^2 + C'/T + D'. \quad (7.2)$$

In the above expressions, T is the absolute temperature in Kelvin. The corresponding values of the fit-coefficients for UFe₂ are: A (J mol⁻¹K⁻¹) = 78.5±0; B (J mol⁻¹ K⁻²) = 0.0181± 0.00141; C (J mol⁻¹ K) = 5.05638 × 10⁵ ± 1.1242× 10⁴, D (J mol⁻¹) = -30325.66 ± 2564.31.37. The R² value for the fit is found to 0.9933. The experimental enthalpy increment data fitted using Eq. (7.1) for UFe₂ is shown as inset in **figure 7.6**. Similarly the fit coefficients for URh₃ are A' (J mol⁻¹K⁻¹) = 106.25 ±0, B' (J mol⁻¹ K⁻²) = 0.01177± 0.0051, C' (J mol⁻¹ K) = 10.0455 × 10⁵ ± 4.897× 10³, D' (J mol⁻¹) = -35493.29 ± 1030.37, R² (Fit) = 0.9987. The fitted data for URh₃ using Eq. (7.2) is already plotted in **figure 7.7** along with the experimental data. It must be added that in fitting the experimental enthalpy data to Eq. (7.1 & 7.2), the value of coefficients A and A' have been suitably adjusted to reproduce the accepted room temperature value of Cp at 298.15 K, namely 78.79 and 103 J mol⁻¹ K⁻¹ for UFe₂ and URh₃ respectively [44]. Further, Eq. (7.1 & 7.2) also complies with the condition that at T=298.15 K, the value of H_T-H_{298.15} goes to zero.

In **figure 7.8**, the heat capacity C_p obtained by differentiating Eq. (7.1) is plotted along with earlier data of Campbell and the assessed values of Chatain *et al* [18, 22]. As mentioned before, the heat capacity data adopted in the assessment of Chatain *et al.* were based on adiabatic calorimeter measurements by Labroche *et al.*, [21]. It can be seen that there is a good agreement between present C_p data with that of Campbell and Chatain *et al.* [18, 22] at low temperature; however at high temperature Campbell data is not in good agreement with present Cp data.

In **figure 7.9**, the present C_p obtained from the derivative of Eq. (7.1) is compared with the reported values of Cordfunke *et al* [25]. It is clear that a fair degree of agreement is readily obtained in the region of overlapping temperature of measurements. However, at higher temperatures, the present data showed a small but distinct upward deviation

from the extrapolated behavior of the Cordfunke *et al.*, data [25]. This deviation at high temperature could be due to anharmonic contribution to the heat capacity.

The heat capacity data obtained for both compound in the present study have been theoretically modelled in a holistic manner by employing the framework of quasi-harmonic Debye-Grüneisen treatment of temperature effects. As an off-shoot of the heat capacity modelling, we have also obtained internally consistent estimates of volume thermal expansion as a function of temperature. The modelling of the result obtained in the present study under the scheme of Debye-Grüneisen formalism is discussed in the next section.

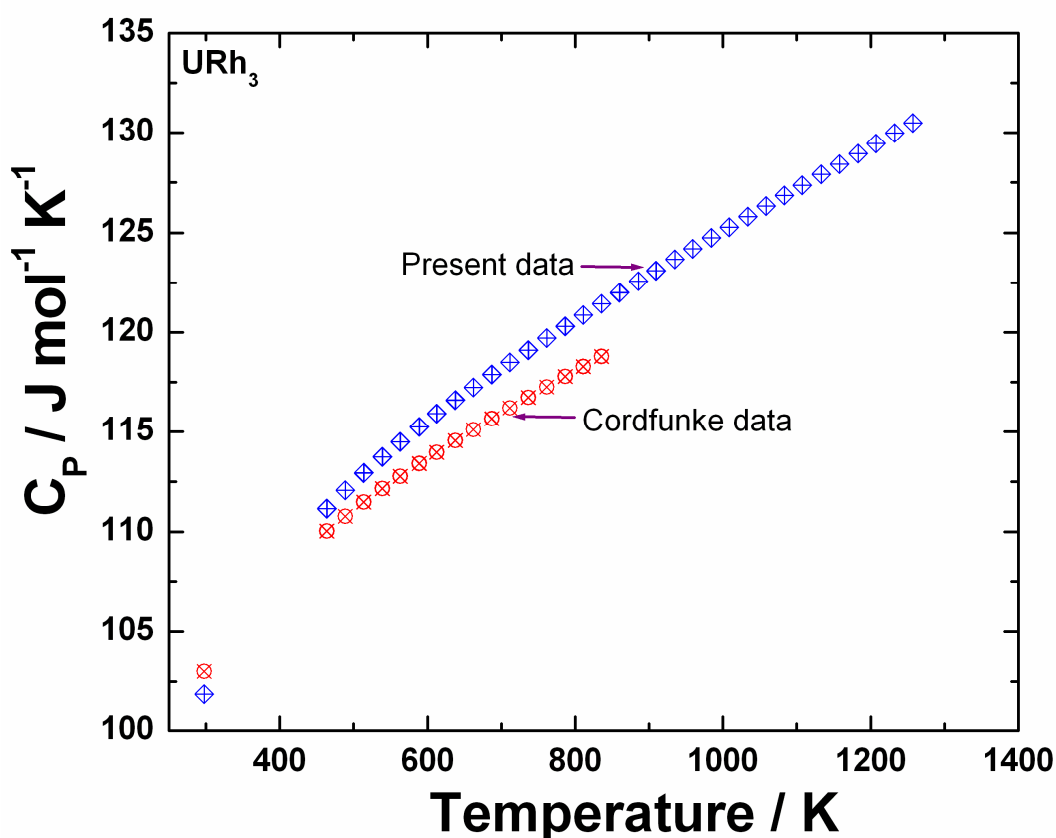


Fig. 7.9. Temperature variation of heat capacity for URh₃ compound

7.5. Integrated Modelling of heat capacity and thermal expansion for UFe₂ and URh₃: quasi harmonic Debye-Grüneisen formalism

Notwithstanding the extensive research on experimental and theoretical fronts of

actinide-transition metal systems, it is generally the case that a complete thermodynamic description of integral thermodynamic quantities in terms of pressure (P), volume (V) and temperature (T) coordinates, namely the *equation of state* (EoS) is still lacking [1-4, 25-30]. It is possible to theoretically estimate thermal properties of condensed phases to varying degrees of technical sophistication depending on the intricacies of the physical chemistry of the system under study and also in direct relation to the available information on fundamental cohesive properties of the system [45]. In the present study, we adopt the Debye-Grüneisen quasi harmonic formalism for getting a consistent first-order estimate of the heat capacity and thermal expansion at high temperatures by having the knowledge of certain thermodynamic input data [32, 33, 38-40]. A brief familiarizing account of this model is already being discussed in the **chapter 3**. In this chapter the result parts only are discussed for both UFe_2 and URh_3 .

7.6. Evaluation of thermophysical properties of UFe_2

From **chapter 3** it clear that under Debye-Grüneisen formalism the volume of a condense phase can be written as follow

$$V_T = V_o \left\{ \left[\frac{E_{vib}}{(Q_o - rE_{vib})} \right] + 1 \right\}. \quad (7.3)$$

In above equation E_{vib} is vibrational contribution to the energy and in the present study it has been calculated using Debye theory with a given Debye temperature, $\Theta_D = 190$ K [6].

The other two parameters can be expressed as follows.

$$Q_o = B_o V_o / \gamma_o \quad (7.4)$$

$$r = (B'_T - 1) / 2. \quad (7.5)$$

Where B_o , V_o , γ_o and B'_T are isothermal bulk modulus, molar volume, Grüneisen parameter and pressure derivative of bulk modulus at reference temperature. In order to calculate the volume using *Eq. (7.3)* one needs to have correct input parameters listed above. These parameters either can be obtained from reported literature or can be

estimated. The various input parameters which have been either taken from the literature or calculated in the present study are listed in **table 7.1** for UFe₂. The estimation of isothermal bulk modulus, its pressure derivative and Grüneisen parameter have been carried out in the present study and discussed in the next section.

Lattice parameter at room temperature/nm	0.7059 0.7063 0.7057 0.7041 at 4.2 K 0.7057	Measured in present study at RT Yamanaka <i>et al.</i> [20] Itie <i>et al.</i> [5] Andreev <i>et al.</i> [6] Andreev <i>et al.</i> [6]
B_T at 300 K / GPa	239 220 201 194	Itie <i>et al.</i> , (diamond anvil cell measurement) [5] Eriksson <i>et al.</i> (calculated from first principles) [13] Present Study; estimated from P - V data of Itie <i>et al.</i> [5] From Laves Phase systematic in present study
B_S at 300 K / GPa	156 134	Vaez <i>et al.</i> calculated using first principle [15] Yamanaka <i>et al.</i> (sound velocity measurement) [20]
B_T'	3 5.17 9.93	Itie <i>et al.</i> [5] Present Study Vaez <i>et al.</i> , calculated using first principle [15]
C_P at 298.15 / J mol ⁻¹ K ⁻¹	78.79	Campbell [18]
Θ_D / K	178 190	Yamanaka <i>et al.</i> (sound velocity measurement) [20] Andreev <i>et al.</i> [6]
C_V at 298.15 / J mol ⁻¹ K ⁻¹	75.67	Calculated using $\Theta_D = 190$ K
γ_G	2.25 2.13	Using bulk modulus derivative in present study using thermodynamic properties in present study
Γ_e / J mol K ⁻²	55×10^{-3}	Naegele <i>et al.</i> [10]
α_v at 298.15 K / K ⁻¹	3.12×10^{-5}	Present Study estimated from low temperature volume
S^0 at 298.15 K / J mol ⁻¹ K ⁻¹	104.7	Campbell <i>et al.</i> [18]

7.6.1. Evaluation of B_T , B_T' and γ_G for UFe₂

Isothermal bulk modulus and its pressure derivative for UFe₂ have been determined both experimentally and theoretically [5, 13, 15, 19, 20], but there is some inconsistency between diverse estimates. Thus for example, Itie *et al.*, were the first to

measure P - V data for UFe_2 by employing the diamond anvil cell technique [5]. Their derived 298.15 K isothermal bulk modulus B_T and its pressure derivative values are about 239 GPa and 3 respectively, using Murnaghan equation of state. Subsequently using first principle calculations, Eriksson *et al.*, [13] have evaluated the isothermal bulk modulus to be 220 GPa for the (experimental) lattice parameter of 0.7060 nm. A similar calculation performed by Vaez *et al.* recently [15] yielded the isothermal bulk modulus to a value of 156 GPa and its pressure derivative to be 9.93, together with the lattice parameter of $a = 0.6986$ nm. Moreover, the experimental adiabatic bulk modulus value reported by Yamanaka *et al.*, is found to be 134 GPa with the quoted lattice parameter $a = 0.7058$ nm [20]. It is well known that adiabatic bulk modulus has to be larger than its isothermal counterpart, $B_s > B_T$; this is however violated by the experimental estimate of Yamanaka *et al.* [20]. At this point, it is instructive to add comment about the intricacies involved in the comparison of theoretical and experimental values of cohesive properties. Thus, for example Vaez *et al.* have recently calculated using pseudo-potential based density functional methods, the zero Kelvin cohesive properties of UFe_2 and PuFe_2 [15]. This calculation highlighted the importance of incorporating subtle physical effects like spin-orbit coupling, the exchange-correlation effects in the local density or generalized gradient approximation etc. However, their predicted isothermal bulk modulus and its pressure derivative deviated significantly from experimental estimates. It may be added that for fixed choice of DFT parameters, the theoretical values of cohesive properties are extremely sensitive to the choice of the equilibrium volume or the so-called minimum volume at which the EoS properties are calculated. It appears that Vaez *et al.* [15] have calculated their EoS properties for the theoretical minimum volume obtained in their study, but unfortunately, this estimate itself is off by 1% from the corresponding experimental molar volume measured at 298.15 K.

In order to obtain a reliable estimate of isothermal bulk modulus and its partial derivative, we have adopted two separate strategies which are discussed below. In the first scheme, we took recourse to a reanalysis of the P - V data given by Itie *et al* [5]. Their

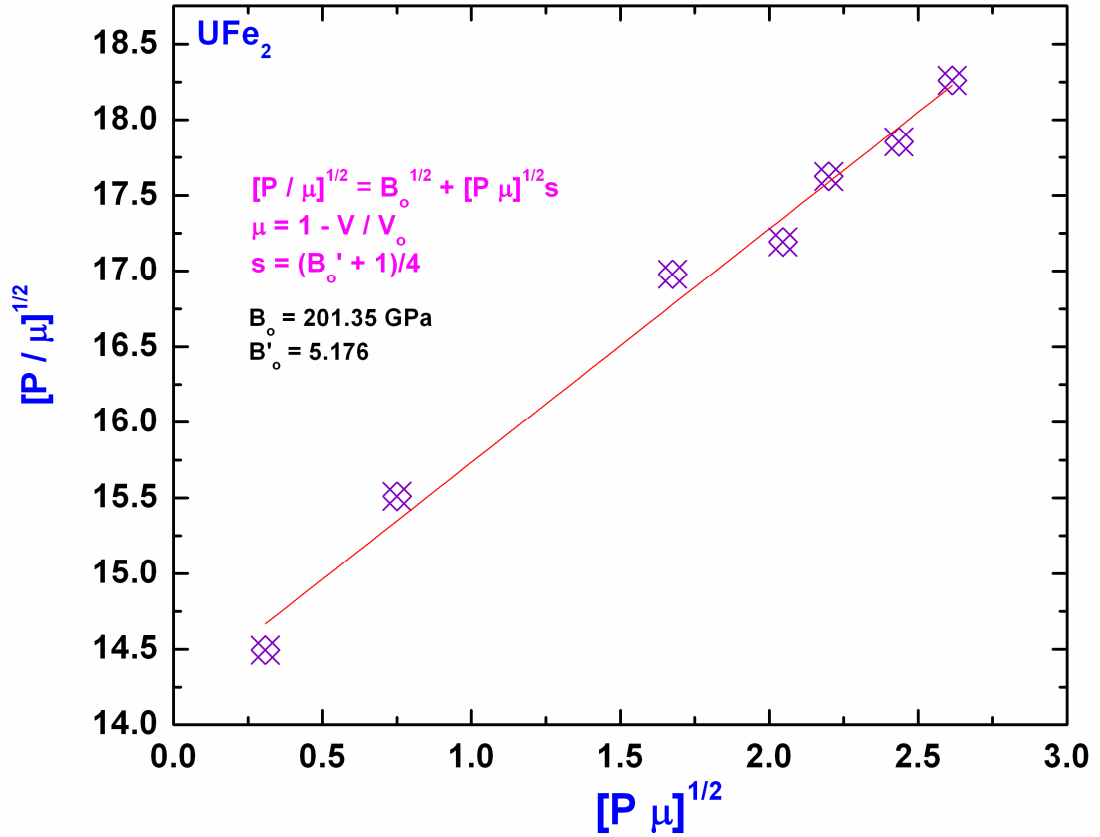


Fig. 7.10. Linearization of isothermal pressure-volume data of Itie *et al*.

data read from the graph are linearized using the scheme of Smith [46]. In **figure 7.10**, the linear scaling of the Itie *et al*. [5], data is shown. The linear form of Murnaghan EoS which is already discussed in **chapter 3** is given below [46].

$$P/\mu = (B_T)^{1/2} + s[P\mu]^{1/2}. \quad (7.6)$$

In the above equation, $\mu = 1 - V/V_o$ and $s = (B'_T + 1)/4$; V_o is the volume at atmospheric pressure, V is volume at any pressure P . According to Eq. (7.6), the value of B_T at 298.15 K turns out to be 201 GPa and $B'_T = 5.17$. These values are considered more reliable than the ones quoted by Itie *et al.*, [5], as they are obtained after proper linearization procedure which any consistent P - V data must follow [46].

In the second scheme, we have collected the data on isothermal bulk modulus and corresponding lattice parameter for different intermetallic compounds of AB₂ type having cubic C15 type structure. These data are listed in **table 7.2** [47-52]. As already

Table 7.2			
Listing of the bulk modulus and lattice parameter values for select C15 laves phases taken from literature			
Compounds	Lattice parameter (nm)	Isothermal Bulk Modulus B_T (GPa)	Reference
CaAl ₂	0.8035	56	[47]
GdAl ₂	0.7905	80	[47]
YAl ₂	0.7855	86	[47]
ScAl ₂	0.7582	92	[47]
ZrZn ₂	0.7394	123	[47]
TiCr ₂	0.6993	201	[47]
UFe ₂	0.7058	194	Present study
UCo ₂	0.6992	217	[5]
UAl ₂	0.7777	83	[49]
UMn ₂	0.7165	168	[50]
PuFe ₂	0.7194	157	[48]
ZrCr ₂	0.7131	177	[52]
NbCr ₂	0.6918	229	[51]

discussed in the **chapter 3**, that the bulk modulus and corresponding molar volume for many iso-structural elements and even compounds are related through following relations

$$B_T V^n \cong \text{constant. (with } n=1 \text{ in the present case)} \quad (7.7)$$

This trend is illustrated in **figure 7.11** for cubic laves phase compounds. The following linear relation is obtained with an rms variation of ~11 GPa.

$$B_T = 0.01163/V - 245.19 \quad (7.8)$$

Considering a molar volume of $2.64708 \times 10^{-5} \text{ m}^3 \text{ mol}^{-1}$ for UFe₂ phase obtained in the present study, a bulk modulus of 194 GPa is calculated for UFe₂ from Eq. (7.8). This is rather close to the value 201 GPa obtained from the linearization scheme of experimental *P-V* data. Therefore, it is concluded that the correct value of isothermal bulk modulus of UFe₂ should be around 201 ± 10 GPa. The other important quantity required for calculating the temperature dependence of volume is the Grüneisen parameter. The

Grüneisen parameter in terms of macroscopic physical properties has been calculated using the following relation

$$\gamma_G = \alpha_v V_o B_T / C_v = \alpha_v V_o B_S / C_p \quad (7.9)$$

Substitution of the values of $\alpha_v = 3.11 \times 10^{-5} \text{ K}^{-1}$, $V_o = 2.64 \times 10^{-5} \text{ m}^3 \text{ mol}^{-1}$, $B_T = 201 \times 10^9 \text{ Nm}^{-2}$ and $C_v = 74.67 \text{ J mol}^{-1} \text{ K}^{-1}$ at $T = 298.15 \text{ K}$ in Eq. (7.9), a value of 2.13 is obtained

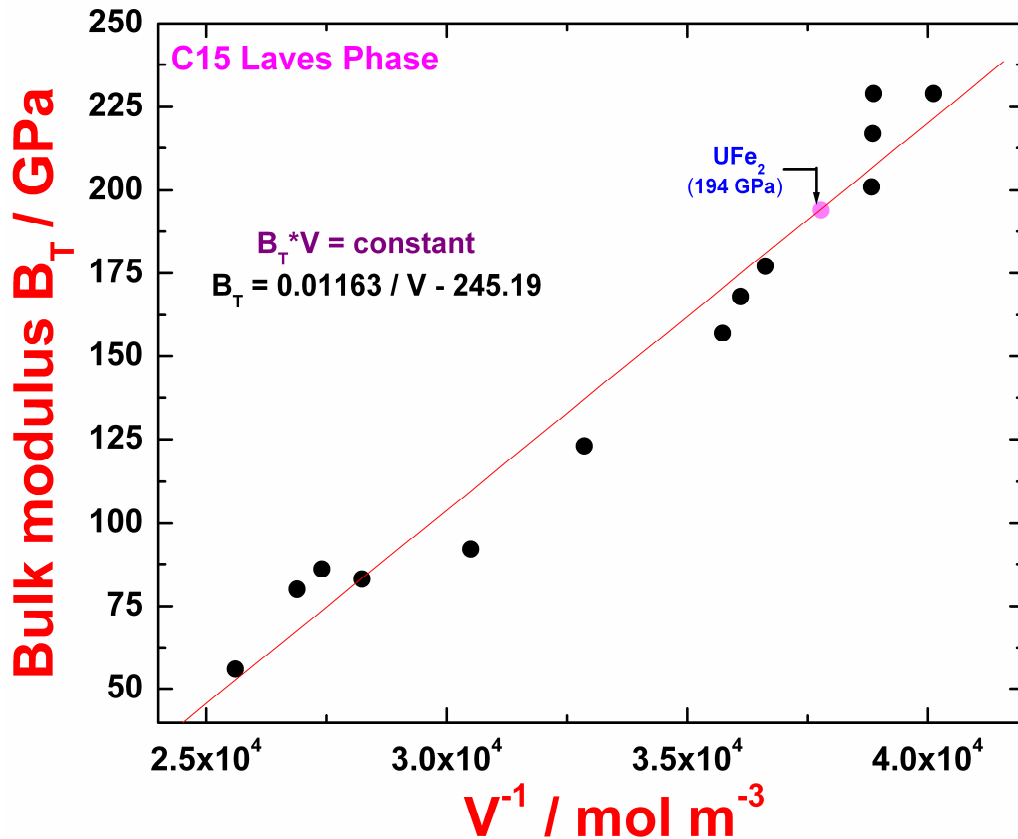


Fig. 7.11. Bulk modulus vs. molar volume for the C15-cubic laves phases

for γ_G . On the other hand, employing Slater's empirical formula relating γ_G with B'_T

$$\gamma_G = \frac{1}{2} (dB_T/dP) - 1/6. \quad (7.10)$$

We get $\gamma_G = 2.25$, with $B'_T = 5.17$. It may be added that Slater's approximation is valid when Poisson's ratio is taken to be independent of pressure [33]. Notwithstanding this limitation, it may be seen that both estimates of γ_G are in good mutual agreement.

7.6.2 Calculation of thermal expansivity and heat capacity data

Having thus, estimated all the required quantities, the temperature dependence of volume has been calculated for UFe_2 in the temperature range of 0–1273 K. The calculation has been made by taking $B_T = 201$ GPa, $B'_T = 5.17$ and $\gamma_G = 2.25$ to maintain internal consistency. The calculated volume as function of temperature is shown as an inset in **figure 7.12** along with the experimental data of Andreev *et al.* that are available

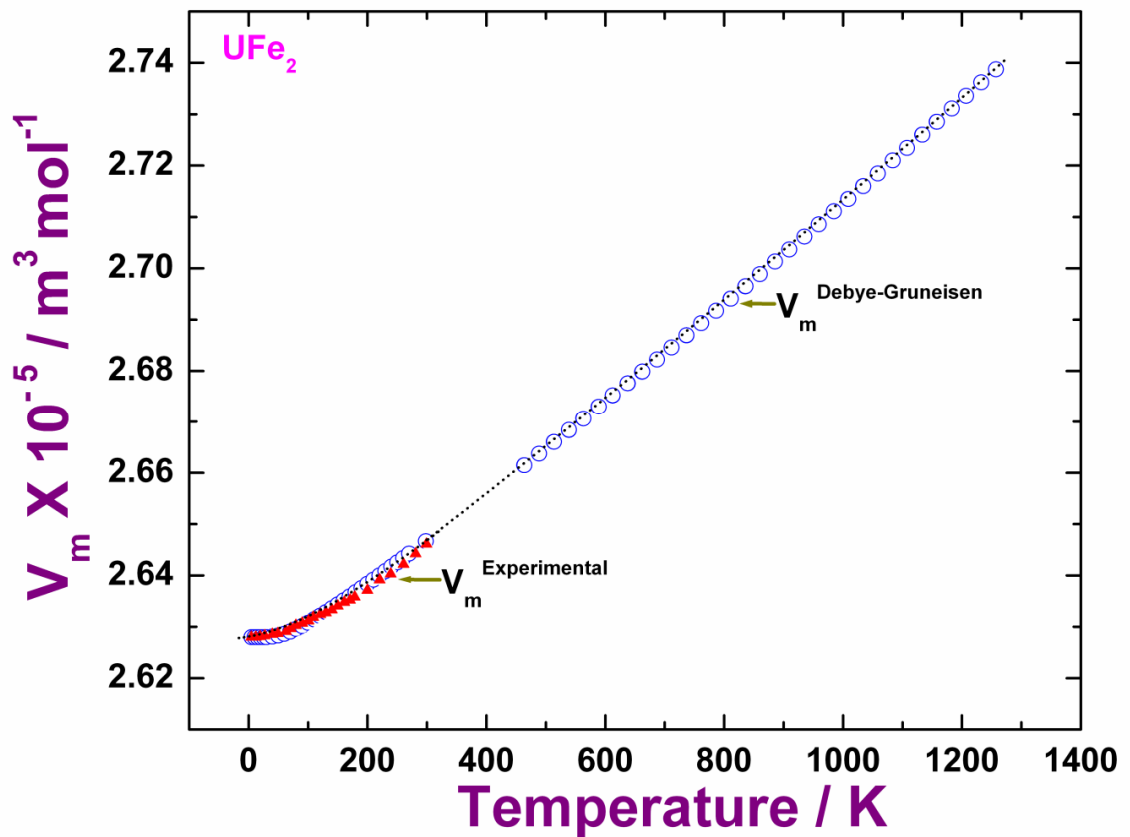


Fig. 7.12. Molar volume as a function of temperature obtained using Debye-Grüneisen scheme and compared with experimental data of reported up to 300 K by Andreev *et al.*

only up to 300 K [6]. It is evident that both experimental and calculated molar volumes exhibit a good agreement at low temperature. Further by taking the derivative of Eq. (7.3) with respect to temperature, it is possible to calculate volume thermal expansivity data as well. The calculated volume thermal expansivity compares well with the

available experimental data at low temperatures [6]. In **figure 7.13**, comparison of experimental and estimated volume thermal expansivity is made.

Further dilatational and the electronic contributions to heat capacity have been estimated from the following relation

$$C_P \approx C_V^h (1 + \alpha_V \gamma_G T) + \Gamma_e T \quad (7.11)$$

The last term, $(\Gamma_e T)$ accounts for the small, linear electronic contribution to the heat capacity. $\Gamma_e = 55 \times 10^{-3} \text{ J mol}^{-1} \text{ K}^{-2}$, the coefficient of electronic heat capacity is taken from

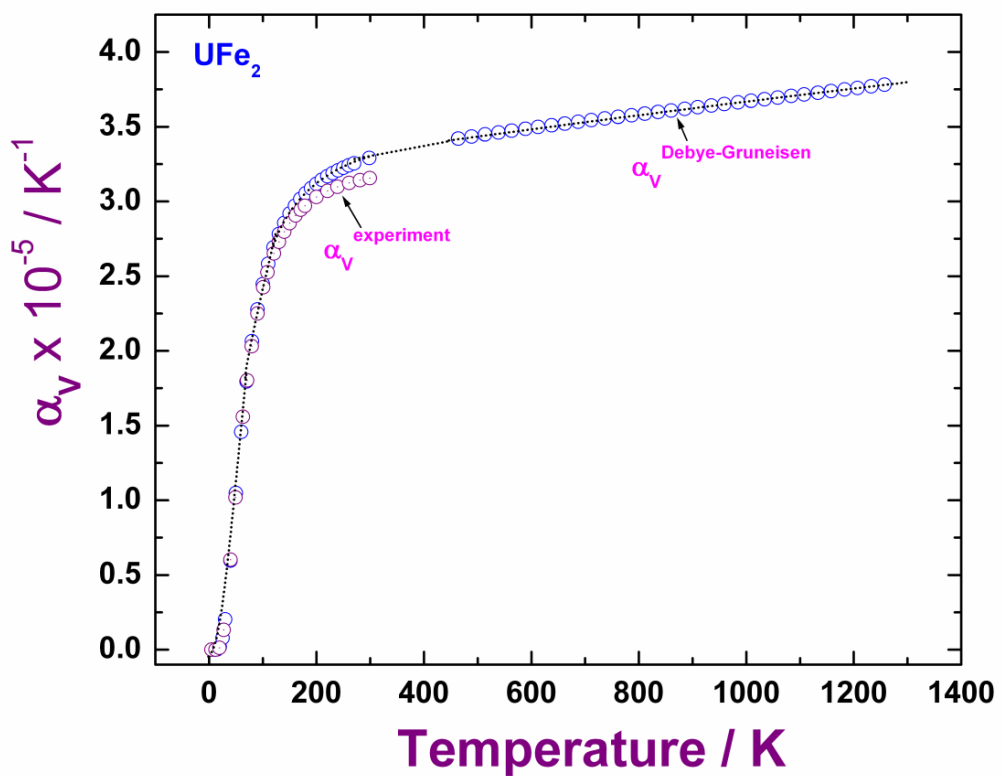


Fig. 7.13. Calculated variation of volume thermal expansivity with temperature along with the Andreev *et al.*

the work of Naegele [10]. The calculated C_p using Debye-Grüneisen formalism including the dilatational correction is plotted in **figure 7.14**, along with experimental values. It can be seen that the agreement between experimental and model values is indeed good.

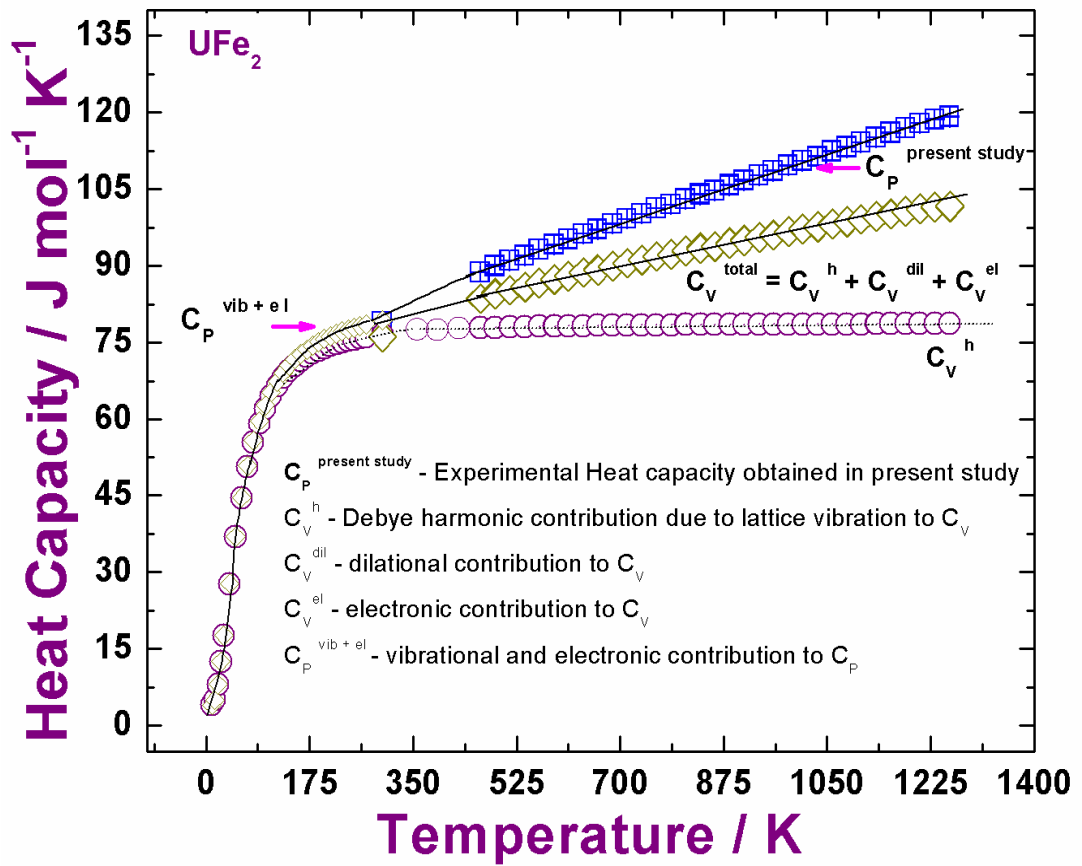


Fig. 7.14. Experimental heat capacity data obtained in the present study are compared with the calculated values using Debye-Grüneisen framework

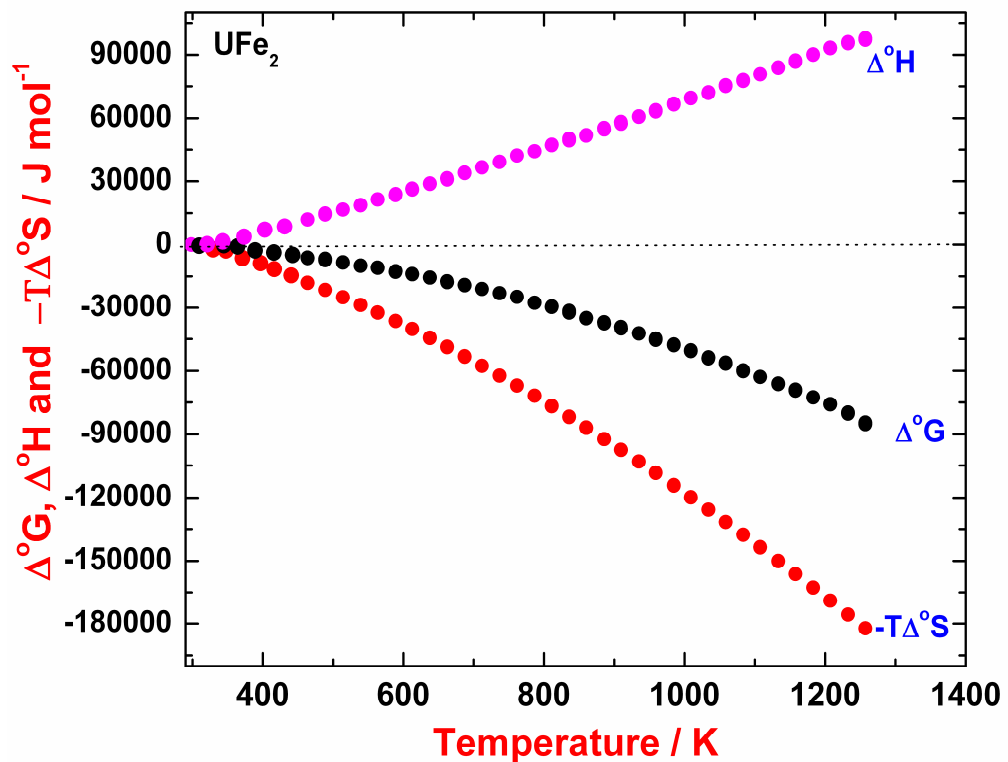


Fig. 7.15. Temperature variation of $\Delta^\circ H$, $\Delta^\circ G$ and $\Delta^\circ S$, estimated in the current study

7.6.3. Estimation of Δ^0H , Δ^0S and Δ^0G for UFe_2

Having known $C_p(T)$, the temperature dependent entropy values $S(T)$ may be calculated in the standard manner by using the following equation.

$$S(T) = S_o(298.15\text{ K}) + \int_{298.15}^T C_p dT. \quad (7.12)$$

Where S_o , is the entropy value at 298.15 K ($104.7\text{ J mol}^{-1}\text{ K}^{-1}$) is taken from Campbell [18]. Once Δ^0H and $S(T)$ are known, it is rather straight forward to compute Δ^0G , the standard Gibbs energy as a function of temperature. In **figure 7.15** the temperature dependence of Δ^0H , Δ^0S , Δ^0G for UFe_2 are plotted up to 1273 K.

7.7. Calculation of thermophysical properties of URh_3

For URh_3 the calculation of different thermophysical properties has been carried out in the same way as adopted for UFe_2 . The various input parameters required to

Table 7.3 Values of input parameters used in the Debye-Grüneisen model for URh_3 .		
Lattice parameter and molar volume	$a = 0.3989\text{ nm}$, $V_m = 0.3834 \times 10^{-4}\text{ m}^3\text{ mol}^{-1}$	Measured in present study
B_T	261 GPa 216 G Pa	Yamanaka <i>et al</i> from sound velocity [20] Kathirvel <i>et al.</i> (calculated from first principles) [53]
B_S	280 GPa	Calculated using the expression $C_p/C_v = B_S/B_T$
B'	5.6	Kathirvel <i>et al.</i> (calculated from first principles) [53]
Θ_D	297 K	Cordfunke <i>et al.</i> [25]
$C_p(298.15)$	$103\text{ J mol}^{-1}\text{ K}^{-1}$	Cordfunke <i>et al.</i> [25]
$C_v(298.15)$	$99.29\text{ J mol}^{-1}\text{ K}^{-1}$	Calculated using $\Theta_D = 297\text{ K}$
γ_G	2.90 2.63	Estimated from thermodynamic properties Estimated form bulk modulus derivative
Γ_e	$14.4 \times 10^{-3}\text{ J mol K}^{-2}$	Dunlap <i>et al.</i> [54]
$\alpha_v(298.15\text{ K})$	$2.78 \times 10^{-5}\text{ K}^{-1}$ $2.74 \times 10^{-5}\text{ K}^{-1}$	Yamanaka <i>et al.</i> [20] Present Study
$S_o(0K)$	$152\text{ J mol}^{-1}\text{ K}^{-1}$	Cordfunke <i>et al.</i> [25]

calculate the temperature dependence of volume for URh_3 compound using Eq. (7.3) are

listed in **table 7.3**. The vibrational contribution to energy for URh₃ has been calculated using Debye theory with $\Theta_D=297$ K reported by Cordfunke *et al.* [25]. Further the values of B_T , B' and γ_G are taken to be 261 GPa, 5.6 and 2.90 respectively. The temperature dependence of volume calculated using Eq (7.3) under Debye-Grüneisen scheme is presented in **figure 7.16**. Since there exist, no prior published data on the high

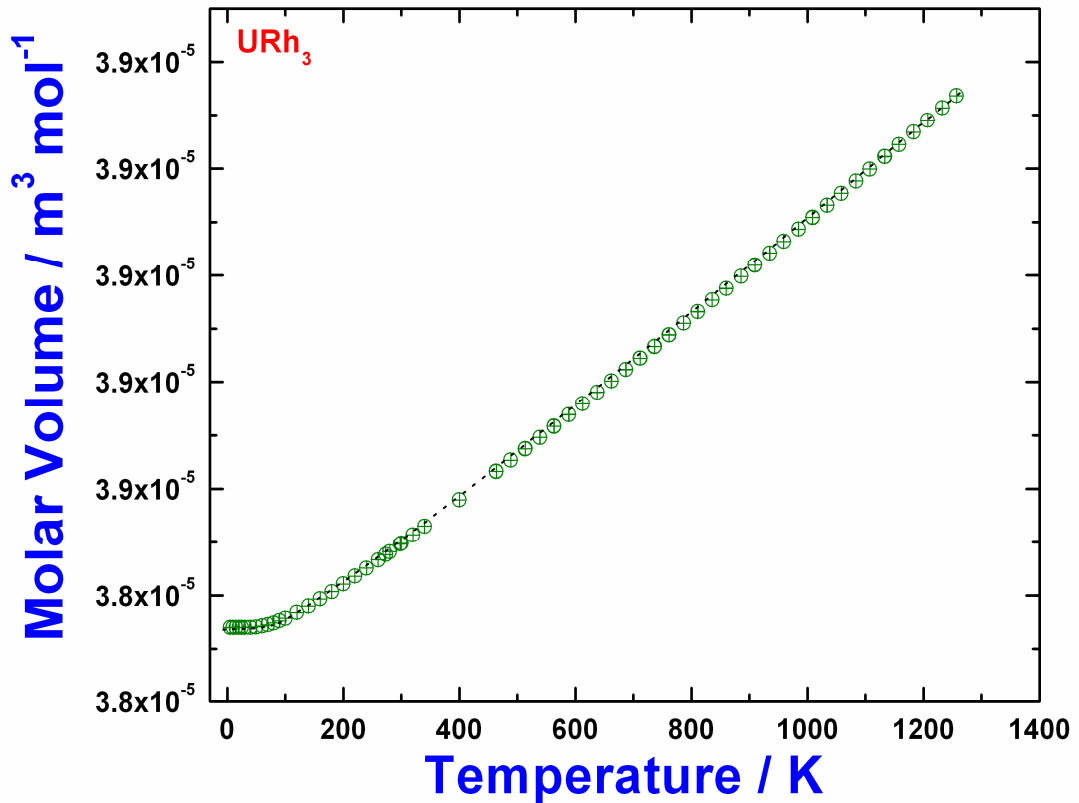


Fig. 7.16. Temperature dependence of molar volume obtained using Debye-Grüneisen scheme for URh₃

temperature thermal expansion of URh₃, we have also obtained a self-consistent estimate of probable thermal expansivity α_v from the temperature derivative of Eq. (7.3). The estimated $\alpha_v(T)$ data is plotted in **figure. 7.17**. The estimated thermal expansivity at room temperature is found to be $2.74 \times 10^{-5} \text{ K}^{-1}$.which is good agreement with literature data reported by Yamanaka *et al* [20]. With the knowledge of temperature dependence of thermal expansivity and Grüneisen constant for URh₃, the dilatational contribution to heat capacity has been calculated using Eq. (7.11). In this calculation the value of

electronic coefficients Γ_e is taken to be $14.4 \times 10^{-3} \text{ J mol K}^{-2}$ from the work of Dunlop

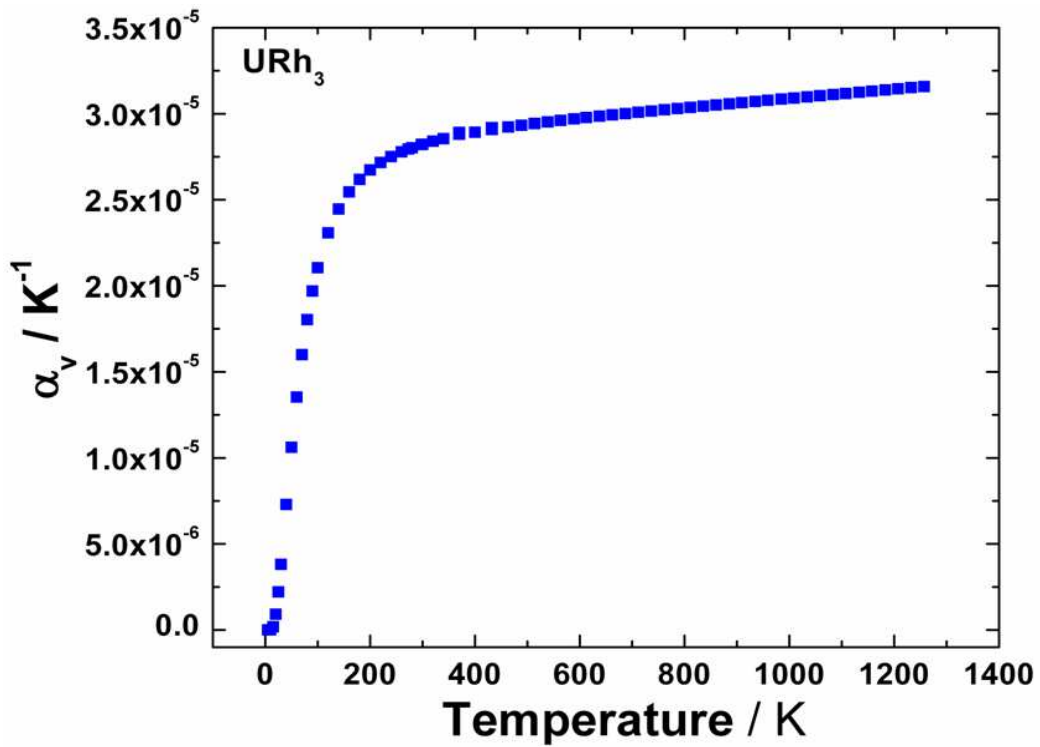


Fig. 7.17. Calculated variation of volume thermal expansivity with temperature for URh_3

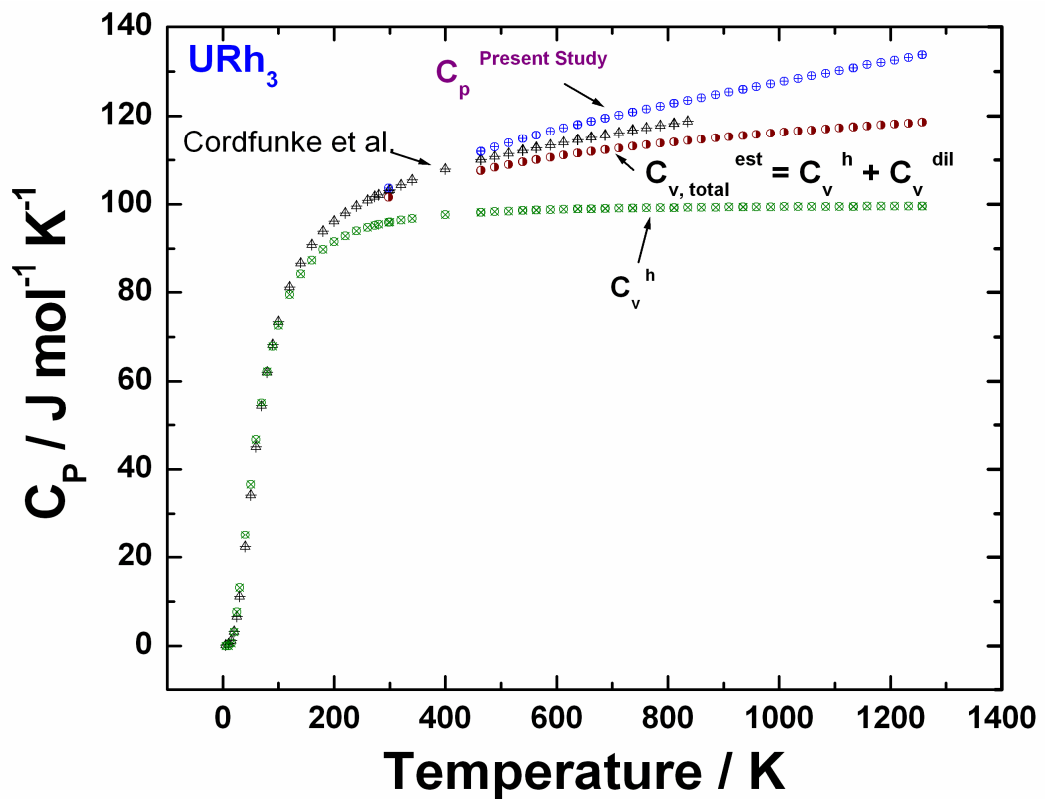


Fig. 7.18. Experimental heat capacity data obtained in the present study are compared with the calculated values using Debye-Grüneisen framework for URh_3

[54]. The calculated C_v and the dilatational correction are shown in **figure 7.18**, together with experimental C_p values for the temperature range 0-1273 K. It can be seen that the agreement is indeed good between the simulated and the experimental results. Once the temperature dependence of C_p is obtained in the temperature range of 0-1273 K, using Eq. (7.11) the entropy $S(T)$ has been calculated with the value of $S_0 = 152 \text{ J mol}^{-1} \text{ K}^{-1}$ reported by Cordfunke *et al* [25] at 0 K. Thereafter the temperature dependence of Δ^0G is obtained for URh_3 . In **figure 7.19** the temperature variation of computed thermodynamic quantities Δ^0H , Δ^0S , Δ^0G from 0 to 1273 K are presented. It can be seen that there is a

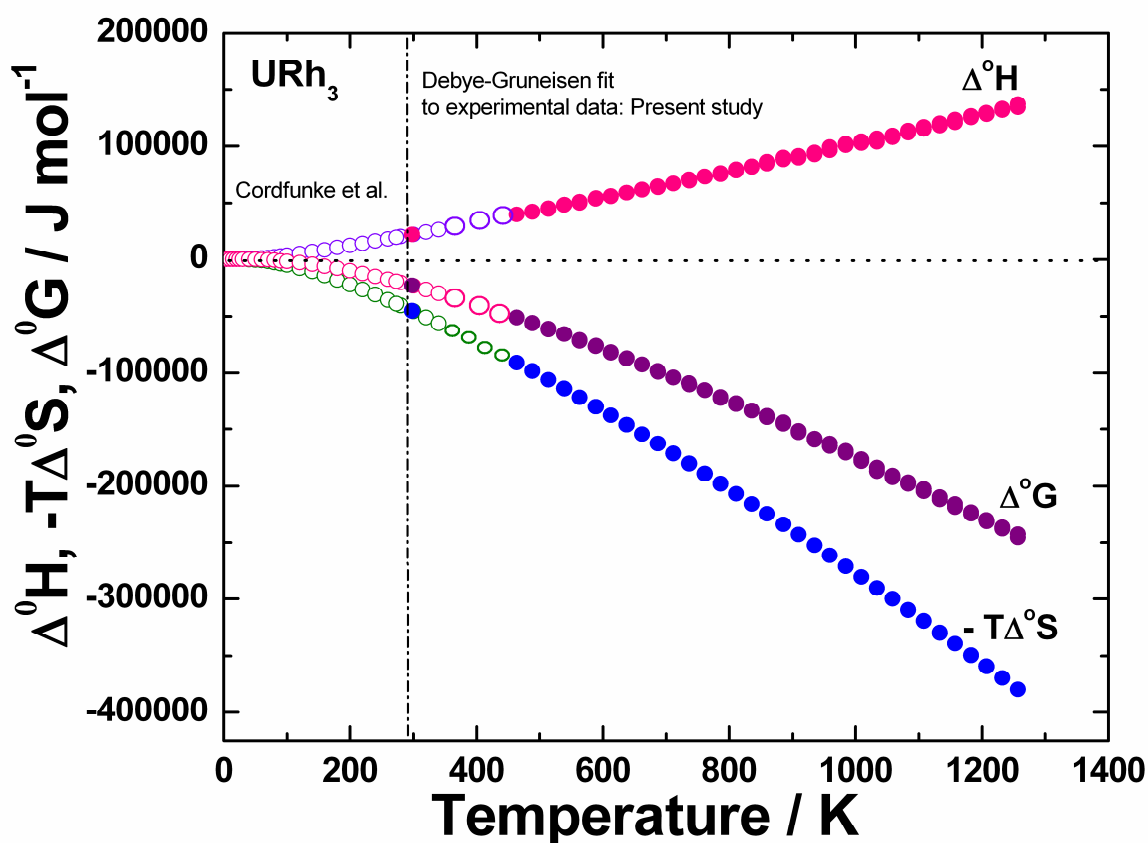


Fig. 7.19. Temperature variation of Δ^0H , Δ^0G and Δ^0S , for URh_3

nice continuity maintained between the low temperature values of Cordfunke *et al.* [25] and the high temperature values obtained in this study. Taken together, these values constitute the most comprehensive set of thermodynamic properties available so far on

URh₃ compound.

7.8. Conclusions

- (i) The high temperature thermodynamic stability of UFe₂ and URh₃ intermetallic compounds have been characterized by drop calorimetry based enthalpy increment measurements up to 1473 and 1273 K. respectively.
- (ii) The specific heat as a function of temperature has been obtained from the measured enthalpy data and the same has been successfully modelled by quasiharmonic Debye-Grüneisen formalism. In this way both harmonic and dilatational contribution to heat capacity are successfully estimated to first order of approximation for both the compounds. The calculated and experimental data are found to be in good agreement.
- (iii) In addition, a consistent estimate of temperature dependent volume thermal expansivity data has also been obtained in this study for both compounds.
- (iv) The thermodynamic properties namely, $\Delta^{\circ}H$, $\Delta^{\circ}S$ and $\Delta^{\circ}G$ are estimated as a function of temperature in the range, 0-1273 K both compounds.

7.9. References

1. C. B. Alcock, *J. Nucl. Mater.*, 167 (1989) 7.
2. H. Kleykamp, *Proc. of the Symp. on Behavior and Chemical State of Irradiated Ceramic Fuels* Vienna, IAEA, Vienna (1974) p. 157.
3. H. Kleykamp, *Pure & Appl. Chem.*, 63 (1991) 1401.
4. H. Kleykamp, *J. Nucl. Mater.*, 201 (1993) 193.
5. J. P. Itie, J. S. Olsen, L. Gerward, U. Benedict and J. C. Spirlet, *Physica B*, 139&140 (1986) 330.
6. A. V. Andreev and R. Z. Levitin, *J. Alloys Compd.*, 337 (2002) 18.
7. Lebech, M. Wulff, G. H. Lander, J. Rebizant, J.C. Spirlet and A. Delapalme, *J. Phys. Condens. Matter.*, 1 (1989) 10229.
8. T. K. McGuire and R. H. Herber. *Sol. St. Commun.*, 48 (1983) 393.
9. L. Paolasini, B. Hennion, A. Panchula, K. Myers and P. Canfield, *Phys. Rev. B*, 58 (1998) 12125.
10. J. R. Naegele, *Physica B*, 130 (1985) 52.
11. A. P. Goncalves, M. S. Henriques, J. C. Waerenborgh, L. C. J. Pereira, E. B. Lopes, M. Almeida, S. Maskova, L. Havela, A. Shick, Z. Arnold, D. Berthebaud, O. Tougait and H. Noel., *Matter. Sci. Engg.*, 9 (2010) 012090.
12. D. J. Lam and A. W. Mitchell, *J. Nucl. Mater.*, 44 (1972) 279.
13. O. Eriksson, B. Johansson, H. L. Skriver and M. S. S. Brooks, *Physica B*. 1144 (1986) 32
14. L. Paolasini, R. Caciuffo, B. Roessli and G. H. Lander, *Physica. B*, 241-243 (1997) 681.
15. Z. N. A. Vaez, *J. Supercond. Nov. Magn.*, 24 (2001) 603.
16. V. N. Antonov, B. N. Harmon and A. N. Yaresko, *Phys. Rev. B*, 68 (2003) 214424(1)

17. O. Kubaschewski, Proceedings of the Symposium on Thermodynamics of Nuclear Materials held by the IAEA at Vienna, 21-25 May; 1962.
18. G. M. Campbell, *Met. Trans. A*, 8 (1977) 1493.
19. T. P. Sorokina, G. M. Kvashnin and A. M. Kapitonov, *Phys. Met. Metall.*, 66 (1988) 164.
20. S. Yamanaka, K. Yamada, T. Tsuzuki, T. Lguchi, M. Katsura, Y. Hoshimo and W. Saiki, *J. Alloys Compd.*, 271-273 (1998) 549.
21. D. Labroche, J. Rogez, S. Chatain, and O. Dugne, High temperature materials chemistry. 10 Int. IUPAC Conference. Julich Germany, (2000) 123.
22. S. Chatain, C. Guéneau, D. Labroche, J. Rogez, and O. Dugne, *J. Phase Equilibria*, 24 (2003) 122.
23. M. P. Antony, R. Babu, C. K. Mathews and U. V. Raju, *J. Nucl. Mater.*, 223 (1995) 213.
24. K. Nakamura, T. Ogata, M. Kurata, T. Yokoo and M. A. Mignanelli, *J. Nucl. Mater.*, 304 (2002) 63.
25. E. H. P. Cordfunke, R. J. M. Konings and E. F. Westrum, *J. Nucl. Mater.*, 167 (1989) 205.
26. Yuji Arita, Naohiko Sasajima and Tsuneo Matsui, *J. Nucl. Mater.*, 247 (1997) 232.
27. H. W. Chiswick; *Metallurgy and Fuels*, Progress in Nuclear Energy, Series V. Vol 3 Pergamon, New York (1961).p. 23.
28. Rajendra Prasad, Y. S. Sayi, J. Radhakrishna, C. S. Yadav, P. S. Shankaran and G. C. Chhapru. *J. Alloys Compd.*, 199 (1993) 141.
29. J. J. Park, *J. Res. Nat. Bur. Stand.*, 72 A (1968) 11.
30. O.S. Ivanov, T.A. Badaeva, R.M. Sofronova, V.B. Kishenevskii, and N.P. Kushnir, *Phase Diagrams of Uranium Alloys*, Nauka, Moscow (1972).

31. J. H. Zhu, C. T. Liu, L. M. Pike and P. K. Liaw, *Intermetallics.*, 10 (2002) 579.
32. D. C. Wallace, *Thermodynamics of crystals*. New York: Wiley; 1972.
33. O. L. Anderson, *Equation of state of solid for Geophysics and Ceramic Science*. New York: Oxford University press; 1995.
34. G. W. Crabtree, B.D. Dunlap and D.D. Koelling, *Physica B*, 135 (1985) 38-40.
35. Tamio Ogouchi, *J. Magn. Magn. Mat.*, 61 (1986) 233-245
36. Börje Johansson, Olle Eriksson, M.S.S. Brooks and Hans L. Skriver, *Inorg. Chim. Acta*, 40 (1987) 59–66.
37. M. G. Naraine and H. B. Bell, *J Nucl. Mater.*, 50 (1974) 83-90.
38. T. H. K. Barron, J. G. Collins, G. K. White, *Thermal expansion of solids at low temperature*, *Adv. Phys.*, 29 (1980) 609.
39. R. Jose, S. Raju, R. Divakar, E. Mohandas, G. Panneerselvam, M. P. Antony, and K. Sivasubramanian, *J. Nucl. Mater.*, 317 (2003) 54.
40. Arun Kumar Rai, Haraprasanna Tripathy, B. Jeyaganesh and S. Raju. *J. Nucl. Mater.*, 427 (2012) 378.
41. D. Sedmidubsky, J. Leitner, P. Svoboda, J. Sofer and J. Machacek, *J. Therm. Anal. Calorim.*, 95 (2009) 403.
42. J. Leitner, K. Ruzicka, D. Sedmidubsky and P. Svoboda, *J. Therm. Anal. Calorim.*, 95 (2009) 397.
43. V. Mankad, S. K. Gupta, H. R. Soni, P. K. Jha, *J. Therm. Anal. Calorim.*, 107 (2012) 45.
44. K. Yamaguchi and K. Itagaki, *J. Therm. Anal. Calorim.*, 69 (2002) 1059-1066.
45. S. L. Shang, Y. Wang and Z. K. Liu, *Comp. Mater. Sci.*, 47 (2010)1040.
46. G. S. Smith, *Phys. Lett. A*, 140 (1989) 431.
47. B. Mayer, H. Anton, E. Bott. M. Methfessel, J. Sticht, J. Harris and P. C. Schmidt, *Intermetallics*, 11 (2003) 23.

48. M. Wulff, G. H. Lander, J. Rebizant, J.C. Spirlet, B. Lebech, C. Broholm and P. J. Brown, *Phys. Rev., B*, 37 (1988) 5577.
49. P. C. H. Sahu and N. V. Chandra Shekar, *PRAMANA*, 54 (2000) 685.
50. A. Lindbaum, S. Heathman, T. L. Bihan and P. Rogl, *J. Alloys Compd.*, 298 (2000) 177.
51. A. Kellou, T. Grosdidier, C. Coddet and H. Aourag, *Acta Mater.*, 53(2005)14596.
52. K. Foster, J. E. Hightower, R. G. Leisure and A. V. Skripov, *Philos. Mag. B*, 80 (2000) 1667.
53. V. Kathirvel, Sharat Chandra, N. V. Chandra Shekar, P. Ch. Sahu and S. Moorthy Babu, *J Phys., Conference Series*, 215 (2010) 012115.
54. B. D. Dunlap, G. W. Crabtree, J. D. Jorgensen, H. A. Kierstead, D. D. Koelling, W. K. Kwok, D. J. Lam, S. K. Malik, A. W. Mitchell and S. C. Strite, *Phys. Rev. B*, 39 (1989) 5640.

Chapter 8

Summary and Further Avenues of Research

8.1. Summary of the present study

The scope of the present thesis is characterization of phase stability and phase transformation characteristics of U-Zr, U-Fe, UFe₂ and URh₃ alloy systems using calorimetry and modelling. This study has been undertaken to evaluate many important thermokinetics and thermo physical property data for the three different alloy systems of uranium. For the present study the differential scanning calorimetry and drop calorimetry are used as major experimental tools which are supplemented by the metallographic and XRD characterization. The major finding of this thesis works are summarized as follows.

(i). In the case of pure uranium, the transformation temperatures for both $\alpha \leftrightarrow \beta$ and $\beta \leftrightarrow \gamma$ transformations measured using DSC exhibit a strong non-linear variation with the heating or cooling rate. Further for small heating rates, the DSC profile for the $\alpha \rightarrow \beta$ transformation contains a shoulder, which feature is however absent for larger heating rates. This shoulder like feature arises in the case of $\alpha \rightarrow \beta$ for small heating rates is due the relative competition between heterogeneous and homogeneous nucleation event occurring together because of very large grain size of α -U. The kinetics of both the on-heating phase changes, namely, $\alpha \rightarrow \beta$ and $\beta \rightarrow \gamma$ are described well by a standard KJMA formalism for the nucleation and growth process and the relevant kinetics parameters has been obtained for both the transformation. However on cooling the $\gamma \rightarrow \beta$ and $\beta \rightarrow \alpha$ phase changes do not follow the conventional KJMA model. Both $\gamma \rightarrow \beta$ and $\beta \rightarrow \alpha$ transformations are found to be non diffusional in nature and they adopt either martensitic or massive mode depending on the cooling rate.

(ii). For U-xZr ($x= 2, 5, 10$ wt.%) alloys, the accurate measurement of transformation temperatures and enthalpy of transformations have made using DSC. In the present study with the help of DSC results, the actual sequence of transformation in all the three alloys is clearly established. In case of annealed U-Zr alloys, it is found that upon heating, both

δ -UZr₂ dissolution and α -martensitic relaxation occurs in a concomitant fashion. However, if the initial microstructure consists of $\alpha_{eq} + \delta$ -UZr₂, then the major thermal effect arises from δ -UZr₂ dissolution alone. Further, a clear effect of cooling rate and alloy composition on the decomposition mode of high temperature γ phase has been observed in the present study. It is found that for slow cooling rates, of the order of 0.1 K min⁻¹ or less, it is possible to obtain equilibrium α -orthorhombic phase along with grain boundary δ -UZr₂ phase. However, with increasing cooling rate, it becomes difficult to nucleate α and δ -UZr₂, due to sluggish Zr diffusion. This favors the formation of α' -martensitic phase directly from γ through a displacive mode. In addition, using DSC the critical cooling rate for $\gamma \rightarrow \alpha'$ direct displacive transformation are obtained for U-2, 5, and 10 wt.% Zr alloys in the present study. Based on present DSC results, continuous heating and cooling transformation diagrams (CHT & CCT) have been obtained for all the three alloys. Further the $\alpha \rightarrow \beta$ phase change is controlled by Zr-diffusion in α -phase. The apparent activation energy for $\alpha \rightarrow \beta$ phase change obtained using KJMA formalism showed an increase with increasing the Zr content.

(iii). In the case of Fe-U system, a comprehensive characterisation of high temperature phase equilibria in Fe-U binary has been carried out using DSC. The various solvus, solidus and liquidus temperatures have been measured for Fe_{100-x}U_x binary alloys ($x=0$ to 95 mass %) at very slow heating rate of 3 K min⁻¹. These are found to be overall in good agreement with the currently assessed Fe-U equilibrium diagram. The enthalpy of transformation for various invariant reaction, solid state transformations and melting have been obtained from the DSC results as a function of U content. The novelty of this work is that these measured thermodynamic data on binary Fe-U system will acts as valuable source of information for reliable phase equilibria assessment or calculation

through CALPHAD method for higher order system such as U-Zr-Fe-Pu complex system.

(iv). The other major findings are, accurate measurement of enthalpy increment as a function of temperature in temperature range of 463-1257 K for UFe_2 and URh_3 intermetallics. The specific heat as a function of temperature has been obtained from the measured enthalpy data and the same has been successfully modelled by quasi-harmonic Debye-Grüneisen formalism. In this way both harmonic and dilatational contribution to heat capacity are successfully estimated to first order of approximation for both the compounds. The calculated and experimental data are found to be in good agreement.

8.2. Further avenues of research

This thesis reports an extensive characterization of phase stability and phase transformation kinetics on U-Zr, Fe-U alloys, UFe_2 and URh_3 intermetallics using calorimetric measurements and modeling. It has been realized that there is plenty of scope to extend this study along following lines.

(i). The extension of present thermo-kinetic analysis on U, and U-2, 5 & 10 wt. % Zr alloys to obtain reliable values for many parameters like interface energy, mobility, that are currently lacking for U-Zr system for α -U and β -U phases.

(ii). Further study of transformation kinetics aspect in U-Zr system at atomic level using the transmission electron microscopy and synchrotron based XRD.

(iii). Measurement of thermal expansivity, and thermal diffusivity data on U, and U-2, 5 & 10wt. % Zr alloys, followed by an integrated analysis thereof.

(iii). CALPHAD based optimization of Fe-U phase diagram in light of present data on transformation temperature and enthalpy of formation.

(iv). Extension of research on U-Cr system in context to metal fuel and ferritic steel clad interaction, because Cr is the second (next to Fe) major element present in ferritic based clad material for future fast reactors.

Publications related to Ph.D work

(i) Journal

1. Effect of heating and cooling rate on the kinetics of allotropic phase changes in uranium: A differential scanning calorimetry study Arun Kumar Rai, S. Raju, B. Jeyaganesh, E. Mohandas, R. Sudha and V. Ganesan, *J. Nucl. Mater.*, 383(2009) 215-225.
2. Measurement and Modelling of High Temperature Thermodynamic Properties of URh₃ Alloy, Arun Kumar Rai, Harapasanna Tripathy, B. Jeya Ganesh and S. Raju, *J. Nucl. Mater.*, 427 (2012) 378-383.
3. Phase Transformation Studies in U-xZr (x= 2, 5, 10 wt.%) Alloys Using Dynamic Calorimetry, Arun Kumar Rai, S. Raju, Harapasanna Tripathy, R. N. Hajra and M. Vijayalakshmi, *Trans. Ind. Inst. Met.*, 66 (2013) 387-390.
4. A Calorimetric Study of High Temperature Phase Stability in Fe-U Alloys, Arun Kumar Rai, S. Raju, and M. Vijayalakshmi, *J. Nucl. Mater.*, 432 (2013) 520-528.
5. Measurement of Thermal Properties of UFe₂ by Calorimetry and Modelling Using Debye-Gruneisen Quasi-harmonic Formalism, Arun Kumar Rai and S. Raju, *J. Therm. Anal. Calorim.*, 112 (2013) 73-82.
6. Calorimetric Study of Phase Stability and Phase Transformation in U-xZr (x = 2, 5, 10 wt.%) Alloys, Arun Kumar Rai, S. Raju, R. N. Hajra and Harapasanna Trpathy, communicated to *Metallurgical and Materials Transactions A* (2014).

(ii) Conference Proceedings

1. Characterization of phase stability and phase change behavior in U-2wt.% Zr alloy: A differential scanning calorimetry study, **Arun Kumar Rai**, S. Raju, B. Jeyaganesh and V. Ganesan Proc. of National Conf. on THERMANS 2010, Kurukshetra University, March 8-10, 2010, pp. 77-79.

2. Measurement and modelling of high temperature thermodynamic properties of actinide alloys, S. Raju, **Arun Kumar Rai** and Haraprasanna Triapthy, Proc. of the Second International Conf. on Advances in Nuclear Materials (ANM-2011), BARC Mumbai, 9-11 Feb. 2011, pp. 92-95
3. Measurement of Thermal Properties of UFe_2 by Calorimetry and Modelling Using Debye-Gruneisen Quasi-harmonic Formalism, **Arun Kumar Rai** and S. Raju, Proc. of International Conf. on THERMANS 2012, BARC Mumbai, Jan 31-Feb 4, 2012, pp. 82-84.

CONTENTS

Abstract of Synopsis	vii-ix
List of Figures	x-xv
List of Tables	xvi-xvii
Chapter 1	
Introduction: Literature Survey	1-43
1.1	Choice of U-Pu-Zr alloys as metal fuel for fast reactor application 2
1.2	Relevance of study of phase stability and phase transformation kinetics in uranium based actinide alloys in the context to the metallic fuel 5
1.3	Alloying behavior of uranium with transition metals 9
1.4	Scope of the present study 13
1.5	Study of phase equilibria and phase transformations in U-Zr System 13
1.5.1	General description of phases and equilibrium reactions 13
1.5.2	Solid state transformation kinetics 25
1.5.3	Thermodynamic modeling of phase equilibria 27
1.6	Phase equilibria and phase transformation studies on Fe-U system 28
1.7	Phase equilibria studies on U-Rh system. 31
1.8	Organization of the thesis 33
1.9	References 37-43
Chapter 2.	
Experimental Methodology	44-79
2.1	Details about alloy synthesis, composition and heat treatment 46

2.2	Major experimental techniques: Calorimetry	49
2.2.1	Principle of calorimeter	49
2.2.2	Classification of calorimeters	49
2.3	Differential scanning calorimetry (DSC)	51
2.3.1	General principle	51
2.3.2	Power compensating DSC	52
2.3.3	Heat flux DSC	53
2.4	Basic components of Setaram Setsys 1600 DSC	54
2.4.1	High temperature furnace	54
2.4.2	Measurement head – DSC probe	55
2.4.3	Vacuum pump, gas circuit, chill water cooling circuit	56
2.4.4	Mass flow controller (MFC)	57
2.5	Experimental procedure	57
2.5.1	Determination of phase transformation temperatures	59
2.5.2	Determination of transformation enthalpy	60
2.5.3	Calibration of DSC	60
2.5.4	Temperature calibration	61
2.5.5	Peak area calibration	62
2.6	Inverse drop calorimeter	63
2.6.1	High temperature furnace	65
2.6.2	Measurement head – drop transducer	66
2.6.3	Multi-sample introducer and the drop tube	67
2.6.4	Gas, vacuum, chill-water circuit and controller	67
2.6.5	Experimental procedure	68
2.6.6	Temperature and heat calibration of drop calorimeter	70
2.6.7	Estimation of enthalpy	71
2.6.8	General observation of result of drop calorimeter	72
2.6.9	Limitation of drop calorimeter	73
2.7	Optical metallography studies	73

2.7.1	Grain size measurement	74
2.7.2	Microhardness measurement	75
2.8	Scanning electron microscopy (SEM) study	75
2.9	X-ray diffraction (XRD) Study	76
2.10	References	77

Chapter 3

Theoretical Aspects of Phase Transformation Kinetics and Evaluation of Thermo-Physical Properties

		80-109
3.1	Basic glimpse of kinetics of phase transformation	81
3.2	Isothermal and non-isothermal transformations	83
3.3	Kinetics model for nucleation & growth type transformation	84
3.4	Rate of transformation	85
3.5	Transformation mechanism: nucleation and growth	87
3.5.1	Nucleation modes	87
3.5.2	Growth modes	89
3.5.3	Effect of impingement on growth	91
3.5.4	Overall transformation kinetics	92
3.5.5	Formulation of Kolmogrov-Johnson-Mehl and Avrami model for isothermal and non-isothermal transformations	93
3.6	Determination of kinetics parameter from DSC results	96
3.7	Martensitic Transformation: Koistinen- Marburger Relation	97
3.8	Quasi harmonic theory	99
3.8.1	Evaluation of vibrational energy	104
3.8.2	Estimation of isothermal bulk modulus and its pressure derivative	104
3.8.3	Estimation of Grüneisen parameter	105
3.8.4	Calculation of thermal expansivity and heat	106

	capacity	
3.9	References	107

Chapter 4

Investigation of Effect of Heating/Cooling Rates on Phase Transformation in Uranium using Calorimetry

		110-142
4.1	Introduction	111
4.2	Experimental details	113
4.3	Results	113
4.3.1	Preliminary characterization	113
4.3.2	Transformation peak profiles and transformation temperatures	114
4.3.3	Transformation plots	119
4.3.4	Empirical description of transformation kinetics	120
4.3.5	Transformation kinetics upon cooling	126
4.4	Discussion	129
4.4.1	Nucleation modes and the role of heating rate	129
4.4.2	Kinetics parameters : heating rate dependence of Q_{eff}	133
4.4.3	Other general aspects	137
4.5	Conclusions	138
4.6	References	140

Chapter 5

Calorimetric Investigation of Phase stability and Kinetics in U-x wt. % Zr (x=0, 2, 5&10wt. %) Alloys

		143-176
5.1	Introduction: genesis of the present study	144
5.2	Experimental details	144
5.3	Results	145
5.3.1	X-ray diffraction and microstructure	145
5.3.2	Phase changes and transformation temperatures	148
5.3.3	Co-occurrence of UZr_2 dissolution and martensitic	154

	relaxation	
5.3.4	Effect of heating and cooling rate on phase transformations	159
5.3.5	Effect of cooling rate on microstructural morphology	162
5.3.6	Continuous heating and cooling transformation diagrams	162
5.4	Discussion	163
5.5	Conclusions	172
5.6	References	175

Chapter 6

Investigation of Phase Equilibria of Fe-U System using Calorimetry

177-197

6.1	Introduction	178
6.2	Results	178
6.2.1	Transformation temperatures measured as function of U content in Fe-U alloys	178
6.2.2	$\gamma\text{-Fe}+\text{Fe}_2\text{U}\rightarrow\text{L}$ and $\text{FeU}_6+\text{Fe}_2\text{U}\rightarrow\text{L}$ transformation characteristics	182
6.2.3	Construction of Fe-U phase diagram using current data and reported literature	184
6.3	Solid state transformation kinetics	187
6.4	Characterization of solidification microstructure development	189
6.5	Discussion	193
6.6	Conclusions	194
6.7	References	196

Chapter 7

Measurement & Modelling of Thermophysical Properties of UFe_2 and URh_3 Intermetallics

198-229

7.1	Introduction	199
7.2	Thermal stability and thermophysical property of UFe ₂ and URh ₃ compounds: a brief summary	200
7.3	Structure and microstructural characterization of UFe ₂ and URh ₃	203
7.4	Enthalpy increment measurements	207
7.4.1	Enthalpy increment data (H _T -H _{298.15}) for UFe ₂	207
7.4.2	Enthalpy increment data (H _T -H _{298.15}) for URh ₃	208
7.4.3	Analytical analysis of enthalpy increment data of UFe ₂ & URh ₃	209
7.5	Integrated modelling of heat capacity and thermal expansion for UFe ₂ and URh ₃ : quasi harmonic Debye-Grüneisen formalism	211
7.6	Evaluation of thermophysical properties of UFe ₂	212
7.6.1	Evaluation of B _T , B' _T and γ _G for UFe ₂	213
7.6.2	Calculation of thermal expansivity and heat capacity data	218
7.6.3	Estimation of Δ ⁰ H, Δ ⁰ S and Δ ⁰ G for UFe ₂	221
7.7	Calculation of thermophysical properties of URh ₃	221
7.8	Conclusions	225
7.9	References	226

Chapter 8

Summary and Further Avenues for Research Work

230-235

8.1	Summary of the present study	231
8.2	Further avenues of research	233
	Publications related to Ph.D work	234

Abstract of Synopsis

Increased interest in metallic fuels for liquid metal (sodium) cooled fast reactors has ignited a reassessment of available thermodynamic data, study of phase stability and transformations kinetics for some of the uranium based alloys. In the present study, investigations have been carried out on three uranium-transition metal systems, namely, U-Zr, U-Fe and U-Rh.

The knowledge of the physical metallurgy and phase transformation characteristics of uranium and its alloys, especially zirconium is of interest in harnessing metal fuelled fast reactor technology. Selection of Zr over other alloying additions is because it has low absorption coefficient for neutron, acts as inter diffusion barrier between fuel and clad material and it has 100% solid solubility in high temperature bcc phase of U. The critically assessed information on phase diagram of U-Zr system is seminal to an understanding of the behavior of the U-Pu-Zr based metallic fuel. Albeit extensively investigated in the past, our understanding of the phase stability and transformation characteristics on U-Zr alloys is still far from complete. The nature of stable and metastable phase fields that emerge upon cooling from high temperature γ -(bcc) phase is extremely sensitive to cooling rate, Zr content, holding temperature and time in the γ -phase field. Both conventional diffusive nucleation and growth and martensitic modes of transformations have been observed in this system upon cooling from the high temperature γ -phase. Accordingly, the microstructures that develop as a result of phase changes also vary from being fine cellular to massive martensite, depending on cooling rate and Zr content.

A study on U-Fe binary system is of interest from the point of view of understanding the high temperature metallurgical interaction of uranium containing metallic fuels with nuclear grade austenitic or ferritic steel clad during actual reactor operation. In order to understand the chemical compatibility of metal fuel with clad material, we need to have reliable information related to phase equilibria on Fe-U. Within the spirit of CALPHAD methodology, a more reliable assessment of the higher order system such as U-Pu-Fe-Zr is possible only, if reliable information on constituent ternary, binary and unary systems is available.

In addition, during fission, the composition of the fuel is not going to remain the same because of the generation of fission products, like Pt, Rh, Ru, Pd, Ir, *etc.* The

presence of such foreign transition metal solutes influences the thermokinetic stability and hence performance of fuel. . In view of the restricted solubility of Pt-group elements in uranium, there is a very high possibility of formation of UM_n intermetallics, where $M= Pd, Rh$ and Ru , and $n=3$. These compounds have very high melting temperature and are left as insoluble residue after the dissolution of spent fuels during reprocessing. Therefore, the knowledge of stability and phase equilibria of the uranium-fission product systems, such as URh_3 , UPd_3 are also necessary to ascertain the thermodynamic status of fuel during operating conditions.

In this regard, the present investigation has been designed towards a comprehensive characterization of phase stability and phase transformation kinetics in U, U-Zr, U-Fe alloys and URh_3 intermetallics using static (Inverse Drop Calorimeter) and dynamic (Differential Scanning Calorimeter-DSC) calorimetry techniques. Further the results of calorimetry experiments are supplemented with data gathered from metallography and X-ray diffraction techniques.

Using differential scanning calorimetry, the complete phase transformation sequence up to melting have been measured at slowest heating rate of 3 K min^{-1} for U, U-2, 5 & 10 wt.% Zr alloys. In the case of uranium the following solid state phase transformation sequence is observed: α (orthorhombic) \rightarrow β (tetragonal) \rightarrow γ (bcc) during heating cycle. On the other hand, in the case of U-2wt.% Zr alloy, the transformation sequence is: $\alpha(\alpha'$ -distorted orthorhombic) $+\delta-UZr_2 \rightarrow \alpha+\gamma_2 \rightarrow \beta+\gamma_2 \rightarrow \beta+\gamma_1 \rightarrow \gamma$. For alloys of 5 and 10 wt.% Zr, the additional presence of a miscibility gap (γ_1 U rich bcc + γ_2 Zr rich bcc) in the high temperature γ (bcc) phase region resulted in the following transformation sequence: $\alpha(\alpha')+\delta-UZr_2 \rightarrow \alpha+\gamma_2 \rightarrow \beta+\gamma_2 \rightarrow \gamma_1+\gamma_2 \rightarrow \gamma$. Further, it has been demonstrated in the case of U-2, 5 & 10 wt.% Zr alloys, that depending on the nature of starting microstructure, namely whether it is α' -martensite, $\alpha_{eq}+\delta-UZr_2$, or a mix of $\alpha'+\alpha_{eq}+\delta-UZr_2$ phases, the relative extents of two possible co-occurring transformation modes (α' -martensite relaxation and dissolution of $\delta-UZr_2$) differs. It has been noticed that the co-occurrence of these two events gives rise to a composite thermal arrest in the normal on-heating DSC profile. In addition, the decomposition of high temperature γ (bcc) phase as a function of cooling rate and Zr-content has been studied using DSC and metallography. It has been observed that it is not possible to obtain 100% of α_{eq} phase along with equilibrium amount of $\delta-UZr_2$, if the cooling rate

is more than 0.1 K min^{-1} . The cooling rate from high temperature $\gamma(\text{bcc})$ is found have a strong influence on microstructure evolution as well.

The kinetic aspects of $\alpha \rightarrow \beta$ and $\beta \rightarrow \gamma$ transformations that occurs on heating have been modelled using Kolmogorov-Johnson-Mehl-Avrami (KJMA) formalism. It has been observed that in the case of uranium, the transformation kinetics is interface controlled, however, in the case of U-2, 5 & 10 wt.% Zr alloys, the kinetics is controlled by the diffusion of Zr in α' -orthorhombic phase. The continuous heating and cooling transformation diagrams have also been obtained for U-2, 5 & 10 wt.% Zr alloys in the present study.

In the case of Fe-U system, the reevaluation of phase equilibria has been made based on present calorimetric measurements. With the help of DSC experiments, accurate measurements of transformation temperatures pertaining to: (i) $\alpha\text{-Fe} \rightarrow \gamma\text{-Fe} \rightarrow \delta\text{-Fe}$ polymorphic phase change, (ii) $\text{UFe}_2 + \gamma\text{-Fe} \rightarrow \text{L}$ and $\text{U}_6\text{Fe} + \text{UFe}_2 \rightarrow \text{L}$ transformations and (iii) melting have been made as a function of uranium content, in the range of 5-95 wt.%. A total of 20 alloy compositions were melted for this purpose. The compositions and temperatures of eutectic invariant reactions that occur in Fe-U binary system are reestablished using the present DSC results. In addition, the measured transformation temperatures are also used to construct the binary Fe-U phase diagram. In addition, the heat of transformation for various solid state transformations and melting have been obtained as a function of U content. These are fresh additions to the existing literature on Fe-U alloys.

Further, using drop calorimetry, the enthalpy increment ($H_T - H_{298.15}$) data have been generated for UFe_2 and URh_3 intermetallics as a function of temperature, up to 1473 K. Experimental results obtained in this study have been analysed analytically to obtain the heat capacity data for both compounds. Further, the experimental heat capacity data have been modelled using Debye-Grüneisen formalism for calculating the thermal expansivity and heat capacity data for both UFe_2 and URh_3 in the range of 0-1473 K. It may be added that the thermal expansivity estimated for these compounds will fill a gap in the thermophysical database of UFe_2 and URh_3 systems.

List of Figures

Figure No.	Figure Captions	Page No.
Fig. 1.1	Crystal Structure of α -uranium	10
Fig. 1.2	Three layer that constitute the crystal structure of β -uranium	11
Fig. 1.3	BCC crystal structure of γ -uranium	11
Fig. 1.4	Equilibrium phase diagram of U-Zr system given by Okamoto [29]	19
Fig. 1.5	Crystal structure of α -Zr with AB type layer stacking	21
Fig. 1.6	Crystal structure of δ -UZr ₂ phase	21
Fig. 1.7	Fe-U equilibrium phase diagram	30
Fig. 1.8	Equilibrium phase diagram of U-Rh system	32
Fig. 2.1	Schematic representation of power compensated DSC	52
Fig. 2.2	Schematic representation of heat flux DSC	52
Fig. 2.3	Experimental setup of heat flux DSC used in the present study	53
Fig. 2.4	(a). Setaram high temperature DSC furnace, (b). Heat flux DSC plate-rod	55
Fig. 2.5	DSC thermogram obtained during heating cycle for uranium	59
Fig. 2.6	Temperature calibrations with Al and Cu	61
Fig. 2.7	Schematic of enthalpy increment variation with temperature	65
Fig. 2.8	The experimental setup of inverse drop calorimeter used in the present study	66
Fig. 2.9	Schematic representation of inverse drop calorimeter	67
Fig. 2.10	Snapshot of the drop experiment output ΔV vs t	69
Fig. 2.11	Illustration of the temperature variation of Q for a typical experimental schedule and calibration constant (inset)	71
Fig. 3.1	A schematic of different kinetic path ways offered by three different cooling histories is shown. Paths A and B stand for transformations occurring under isothermal and linear cooling conditions, where as the path C represents a step wise cooling	82

with small incremental isothermal holds. Note that in all the three paths A, B and C the net reduction in Gibbs energy Δ^0G is the same.

Fig. 3.2	Schematic of DSC peak profile used for calculating phase fraction	96
Fig. 3.3	Phase fraction curve obtained using <i>Eq. (3.38)</i>	97
Fig. 4.1	SEM micrograph obtained for uranium annealed at 800°C for 10h	113
Fig. 4.2	EDX spectrum from the particle shown by arrow in figure 4.1	114
Fig. 4.3	XRD pattern obtained for uranium annealed at 800°C for 10h	115
Fig. 4.4	A typical DSC profile obtained for uranium at the scan rate of 3 K min ⁻¹	116
Fig. 4.5(a)	The DSC profiles for the $\alpha \rightarrow \beta$ transformation obtained at lower heating rates are stacked together (1-30 K min ⁻¹).	117
Fig. 4.5(b)	The DSC profiles for the $\alpha \rightarrow \beta$ transformation obtained at higher heating rates are stacked together (40-99 K min ⁻¹)	117
Fig. 4.6	The non-linear variation of the transformation start (T_s), peak (T_p) and finish (T_f) temperatures with heating / cooling rate for $\alpha \leftrightarrow \beta$ and $\beta \leftrightarrow \gamma$ transformations	118
Fig. 4.7(a)	DSC profiles for the $\gamma \rightarrow \beta$ transformation during cooling	119
Fig. 4.7(b)	DSC profiles for the $\beta \rightarrow \alpha$ transformation during cooling	120
Fig. 4.8(a)	The transformation plot for $\alpha \rightarrow \beta$ transformation	121
Fig. 4.8(b)	The transformation plot for $\beta \rightarrow \gamma$ transformation	121
Fig. 4.9(a)	The transformation plot for $\gamma \rightarrow \beta$ transformation	122
Fig. 4.9(b)	The transformation plot for $\beta \rightarrow \alpha$ transformation	122
Fig. 4.10	The variation of heating rate normalised Arrhenius rate constant (k/β) with β for $\alpha \rightarrow \beta$ transformation	134
Fig. 4.11	The variation of heating rate normalised Arrhenius rate constant (k/β) with β for $\beta \rightarrow \gamma$ transformation	135
Fig. 4.12	The heating rate dependence of the width of the transformation zone ($T_f - T_s$) for the $\alpha \rightarrow \beta$ transformation	136
Fig. 4.13	The heating rate dependence of the width of the	137

- transformation zone (T_f-T_s) for the $\beta \rightarrow \gamma$ transformation
- Fig. 5.1** X-ray diffraction patterns obtained on U-0, 2, 5 & 10 wt.% Zr alloys. 145
- Fig. 5.2** Equilibrium diagram of U-Zr system. The expanded view on uranium rich side is shown as inset for better clarity 146
- Fig. 5.3** **(a)**. A typical optical microstructure of annealed U-2 wt.% Zr alloy and in this the fine cellular morphology of α phase is clearly outlined within the prior γ -phase; **(b)**. The Widmanstatten side-plate like morphology, emanating from select prior γ grain boundary is shown (arrow markers); **(c)**. The secondary electron image of U-2 wt.% Zr alloy cooled at 1 K min^{-1} from 1273 K (1000°C) and in this, large equiaxed of α -cells can be readily witnessed; **(d)**. X-ray map of 1 K min^{-1} cooled sample and from this a clear Zr enrichment along grain boundary region, together with the preferential formation of $\delta\text{-UZr}_2$ at select locations (arrow markers) can be noticed 148
- Fig. 5.4** DSC thermogram obtained for U- 2wt.% Zr alloy at 10 K min^{-1} . An expanded view of the first composite endothermic thermal arrest arising due to the co-occurrence of martensitic relaxation and $\delta\text{-UZr}_2$ dissolution is also shown as inset. 149
- Fig. 5.5** On heating DSC thermograms obtained at 10 Kmin^{-1} for U, 0, 2, 5 & 10wt.% Zr alloys are stacked together. 150
- Fig. 5.6** **(a)** Microstructures of 99 K min^{-1} cooled U-2wt.%Zr alloy revealing α' martensitic structure, **(b)**. Microstructure of water quenched sample of U-2wt.%Zr, showing fine acicular needles of α' martensite, **(c)**. SEM micrograph of 0.1 K min^{-1} slow-cooled sample of U-2wt.% Zr alloy showing the presence of equilibrium α_{eq} and grain boundary $\delta\text{-UZr}_2$ (arrows). 155
- Fig. 5.7(a)** The on-heating DSC thermogram obtained at 1 K min^{-1} on 99 K min^{-1} sample of U-2wt.%Zr alloy. The occurrence of both 156

	martensitic relaxation and δ -UZr ₂ dissolution are clearly noticed.	
Fig. 5.7(b)	The on-heating DSC thermogram obtained on water quenched and 0.1 K min ⁻¹ slow cooled samples of U-2wt.%Zr alloy.	157
Fig. 5.8	DSC thermogram obtained as function of heating rate (5-50 K min ⁻¹) for U-2 wt.% Zr alloy are presented.	159
Fig. 5.9	DSC thermogram obtained as function of cooling rate (5-50 K min ⁻¹) for U-2 wt.% Zr alloy are presented.	160
Fig. 5.10	The effect of cooling rate on microstructure in U-2 wt.% Zr alloy. Individual micrographs are arranged in the order of increasing cooling rate	161
Fig. 5.11(a)	Continuous heating transformation (CHT) diagram for U-2 wt. % Zr alloy	163
Fig. 5.11(b)	Continuous cooling transformation (CCT) diagram for U-2 wt.% Zr alloy.	163
Fig. 5.12(a)	Continuous heating transformation (CHT) diagram for U-5 wt.% Zr alloy.	164
Fig. 5.12(b)	Continuous cooling transformation (CCT) diagram for U-5 wt.% Zr alloy.	164
Fig. 5.13(a)	Continuous heating transformation (CHT) diagram for U-10 wt.% Zr alloy.	166
Fig. 5.13(b)	Continuous cooling transformation (CCT) diagram for U-10 wt.% Zr alloy	166
Fig. 5.14	Phase fraction versus temperature data obtained for $\alpha \rightarrow \beta$ on-heating transformation in U-2wt.%Zr alloy. The KJMA model fit is shown as continuous line, passing through experimental data points, shown as filled circles	168
Fig. 5.15	Phase fraction versus temperature data obtained for $\alpha \rightarrow \beta$ on-heating transformation in U-0, 2, 5 & 10 wt.%Zr alloys. The KJMA model fit is shown as continuous line, passing through experimental data points, shown as open circles	170
Fig. 6.1	The DSC thermogram obtained on Fe-5 mass% U alloy at	179

	scan rate of 3 K min ⁻¹	
Fig. 6.2	DSC thermogram obtained for Fe ₂ U alloy at 3 K min ⁻¹	180
Fig. 6.3	The variation of UFe ₂ +γ-Fe→L and UFe ₂ +U ₆ Fe→L transformation temperatures with uranium content along with select literature data	182
Fig. 6.4	The variation in enthalpies of (i) melting, (ii) UFe ₂ +γ-Fe→L and (iii) γ-Fe→δ-Fe transformations with uranium content	183
Fig. 6.5	The variation in enthalpies of (i) melting and (ii) U ₆ Fe+UFe ₂ →L transformations with uranium content	184
Fig. 6.6	The Fe-U binary phase diagram constructed using present measurements along with other reported data are also included in the figure for comparative purpose	186
Fig. 6.7	DSC peak profiles for the α-Fe→γ-Fe phase transformation in Fe-5U, Fe-8U and Fe-10U alloys are stacked together.	188
Fig. 6.8	The fractional extents of α-Fe→γ-Fe phase transformation in Fe-5U, Fe-8U and Fe-10U alloys as a function of temperature are graphically illustrated	189
Fig. 6.9	A collage of SEM micrographs for different Fe-U alloy compositions is presented	191
Fig. 6.10	The EDS spectra along with SEM microstructure taken for phase identification in Fe-25 mass % U and Fe-75mass % U alloys are presented. From the EDS spectra the presence of distinct phases, such as Fe, Fe ₂ U and U ₆ Fe can be clearly identified	192
Fig. 7.1	XRD profile of UFe ₂ showing presence of cubic-MgCu ₂ type crystal structure	203
Fig. 7.2	The on-heating and cooling DSC profile for UFe ₂ taken at 3 K min ⁻¹ scan rate	204
Fig. 7.3	(a). SEM micrograph of the annealed UFe ₂ alloy, (b). Elemental X-ray map of U, (c). Elemental X-ray map of Fe	205
Fig. 7.4	XRD profile of URh ₃ conforming to face centered cubic structure	206

Fig. 7.5	SEM BSE image along with by elemental X- ray mapping of U & Rh atoms	206
Fig. 7.6	Temperature variation of enthalpy increment data obtained in this study along with reported data of Campbel. The inset shows the fit to the present experimental data	207
Fig. 7.7	Enthalpy increment data for URh ₃ obtained in present study is compared with the data of Cordfunke's experimental and extrapolated data	208
Fig. 7.8	Temperature variation of heat capacity for UFe ₂ compound	209
Fig. 7.9	Temperature variation of heat capacity for URh ₃ compound	211
Fig. 7.10	Linearization of isothermal pressure-volume data of Itie et al	215
Fig. 7.11	Bulk modulus vs. molar volume for the C15-cubic laves phases	217
Fig. 7.12	Molar volume as a function of temperature obtained using Debye-Grüneisen scheme and compared with experimental data of reported up to 300 K by Andreev et. al	218
Fig. 7.13	Calculated variation of volume thermal expansivity with temperature along with the Andreev <i>et. al</i>	219
Fig. 7.14	Experimental heat capacity data obtained in the present study are compared with the calculated values using Debye-Grüneisen framework	220
Fig. 7.15	Temperature variation of $\Delta^{\circ}H$, $\Delta^{\circ}G$ and $\Delta^{\circ}S$, estimated in the current study	220
Fig. 7.16	Temperature dependence of molar volume obtained using Debye-Grüneisen scheme for URh ₃	222
Fig. 7.17	Calculated variation of volume thermal expansivity with temperature for URh ₃	223
Fig. 7.18	Experimental heat capacity data obtained in the present study are compared with the calculated values using Debye-Grüneisen framework for URh ₃	223
Fig. 7.19	Temperature variation of $\Delta^{\circ}H$, $\Delta^{\circ}G$ and $\Delta^{\circ}S$, for URh ₃	224

List of Tables

Table No.	Table Captions	Page No.
Table 1.1	Listing of different related studies on U-Zr system	13
Table 1.2	Crystallographic data for different phases in U-Zr system	20
Table 1.3	Invariant reactions in U-Zr system	22
Table 1.4	Phase equilibria information of Fe-U system	28
Table 2.1	The chemical composition of the U-0, 2, 5 & 10 wt.%Zr alloy as determined using ICP-AES. The quoted figure for Zr is in wt.% and rest are in weight ppm basis	47
Table 2.2	Chemical composition of reactor grade uranium and pure iron used in synthesis of Fe-U alloys	48
Table 3.1	Listing of different kinetics parameters under isothermal and isochronal condition	95
Table 4.1	Listing of the kinetics parameters estimated for the $\alpha \rightarrow \beta$ transformation using Eq. (4.4).	124
Table 4.2	Listing of the kinetics parameters estimated for the $\beta \rightarrow \gamma$ transformation using Eq. (4.4)	125
Table 4.3	Listing of the kinetics parameters estimated for $\gamma \rightarrow \beta$ and $\beta \rightarrow \alpha$ transformation using Eq. (4.5) & (4.6)	127
Table 5.1	Listing of lattice parameters of α -orthorhombic phase for U-0, 2, 5&10 wt. Zr % alloys obtained in the present study	147
Table 5.2	Measured transformation start (T_s), finish (T_f) temperatures for various solid state and melting transformations and corresponding transformation enthalpy (ΔH) are listed for 2, 5, 10 wt.% Zr alloys	153
Table 5.3	Estimated effective activation energy Q_{eff} for $\alpha \rightarrow \beta$ phase transformation kinetics as function of heating rate, for U-0, 2,5& 10 wt. % Zr alloys	169
Table 6.1	The on-heating transformation temperatures measured in the present study for different Fe-U alloys	181

Table 6.2	Measured phase transformation enthalpies as a function of alloy composition are listed. The measured values are accurate to $\pm 10\%$.	185
Table 6.3	Kinetic parameters obtained by fitting the experimental $\alpha\text{-Fe}\rightarrow\gamma\text{-Fe}$ transformation data to KJMA model are tabulated.	190
Table 7.1	List of various thermophysical properties taken from the literature and evaluated in present study	213
Table 7.2	Listing of the bulk modulus and lattice parameter values for select C15 laves phases taken from literature	216
Table 7.3	Values of input parameters used in the Debye-Grüneisen mode for URh_3	221